



TECHNISCHE
UNIVERSITÄT
WIEN



Dissertation

Advanced concepts of THz resonant-tunnelling-diode oscillators

Petr Ouředník

A thesis submitted in partial fulfillment for the
degree of Doctor of Philosophy

in the

Fakultät für Elektrotechnik und Informationstechnik
Technische Universität Wien

Supervisor: Univ. Prof. Michael Feiginov

January 2023

“For a successful technology, reality must take precedence over public relations, for nature cannot be fooled.”

Richard P. Feynman, *Personal Observations on the Reliability of the Shuttle*, 1986

“I think there’s nothing cooler than being a lone wolf. Except at wolf picnics when you don’t have a partner for the wolf wheelbarrow races.”

Norm Macdonald

“ ... To be sure, all this costs us all a good deal of money. This year’s space budget is three times what it was in January 1961, and it is greater than the space budget of the previous eight years combined. That budget now stands at \$5,400 million a year—a staggering sum, though somewhat less than we pay for cigarettes and cigars every year. Space expenditures will soon rise some more, from 40 cents per person per week to more than 50 cents a week for every man, woman and child in the United States, for we have given this program a high national priority—even though I realize that this is in some measure an act of faith and vision, for we do not now know what benefits await us. But if I were to say, my fellow citizens, that we shall send to the moon, 240,000 miles away from the control station in Houston, a giant rocket more than 300 feet tall, the length of this football field, made of new metal alloys, some of which have not yet been invented, capable of standing heat and stresses several times more than have ever been experienced, fitted together with a precision better than the finest watch, carrying all the equipment needed for propulsion, guidance, control, communications, food and survival, on an untried mission, to an unknown celestial body, and then return it safely to earth, re- entering the atmosphere at speeds of over 25,000 miles per hour, causing heat about half that of the temperature of the sun—almost as hot as it is here today—and do all this, and do it right, and do it first before this decade is out—then we must be bold. ... ”

John F. Kennedy, *We choose to go to the Moon*, 1962

“Zkuste to bez drátů, milý Marconi.” In English: “Dear Marconi, try it without the wires.”

Jára da Cimrman, *An advice to Guglielmo Marconi*, from Czech absurd comedy *Jára Cimrman ležící, spící*.

Acknowledgements

I would like to gratefully thank my supervisor, Univ. Prof. Michael Feiginov, for his guidance during my doctoral studies and helpful advice when writing this thesis. Indeed, it was his influence that shifted my point of view on many problems to new levels. I would also like to thank him for his always open doors, nonetheless the problem.

Thanks are also owed to all members of my research group. They listened many times to my nonsensical rambling about the problems that I was having and were there every time to offer me their support. Specifically, I thank Thomas Hackl, who has done a great deal of work on the first published scientific article relevant to this thesis. I thank Christian Spudat and Dinh-Tuan Nguyen for their advice regarding the devices' fabrication and their deep humanity. To Gabriele Picco, who showed me and to my group a modest behavior of a great mind. To Bob Mirkhaydarov for his personality, for which an example can be that once during our conversation, he started by asking me what my hopes and dreams were and ended with him telling me he could bench press 90 kg. To Zehn Luo for showing me what a perfect doctoral student should look like. And to my office mate, Zoltán Jéhn, who has invited me to his wedding and will pay for my travels and the stay.

Further, I would like to thank the Center for Micro- and Nanostructures personnel for providing the clean-room facilities that allowed me to fabricate the here-reported devices. Specifically, I thank Dr. Werner Schrenk, who has built and is keeping the clean room capable of operating at a high standard. Additionally, I would like to thank all cleanroom users for their helpful on-site advice. I thank the Technische Universität Wien and Austria for the opportunity for the studies that were given to me. I would like to thank the Austria Science Fund FWF, which funded our research in the project with the number P30892-N30.

I want to thank Miriam Giparakis for making Vienna feel more like my home and for the nice-nice support during my studies. Finally, I would like to thank my family, my mother, father, sister, brother, grandfather, and grandmother, and the broader members of the family that provided for me and gave me what I shall pass on one day again to the next generation.

Petr Ouředník, 2023

Contents

| | |
|--|-------------|
| Acknowledgements | v |
| Table of content | viii |
| Abstract | 1 |
| 1 Introduction | 3 |
| 1.1 Outline of the thesis | 3 |
| 1.2 Oscillators | 4 |
| 1.3 The terahertz gap | 6 |
| 1.3.1 Applications of THz waves | 6 |
| 1.3.2 Challenges of the sources in the THz gap | 7 |
| 1.4 THz sources | 8 |
| 1.4.1 Devices exploiting the negative differential conductance | 8 |
| 1.4.2 THz lasers | 11 |
| 2 Resonant-Tunneling-Diode Oscillators | 13 |
| 2.1 Introduction to resonant-tunneling-diode oscillators | 14 |
| 2.2 Resonant-tunneling diodes | 14 |
| 2.2.1 Principle of resonant-tunneling diodes | 15 |
| 2.2.2 Technical realization | 18 |
| 2.2.3 Parameters of RTDs | 20 |
| 2.3 State-of-the-Art of the RTD oscillators | 21 |
| 2.3.1 Standard RTD oscillators | 21 |
| 2.3.2 Chip-sized RTD oscillators | 31 |
| 2.3.3 Design considerations for the RTD oscillators | 34 |
| 2.4 Frequency limitation of RTD oscillators | 37 |

| | | |
|----------|--|-----------|
| 2.4.1 | Contact parasitics | 37 |
| 2.4.2 | Frequency dependence of the RTD conductance | 41 |
| 3 | Analysis of RTD oscillators | 47 |
| 3.1 | Small-signal analysis of an oscillator with NDC | 48 |
| 3.2 | Relation between the large-signal and small-signal analysis | 53 |
| 3.3 | Large-signal analysis | 54 |
| 3.3.1 | General method | 54 |
| 3.3.2 | Third-order I-V curve approximation | 57 |
| 3.3.3 | Real I-V curve | 59 |
| 3.3.4 | Effect of the oscillations on the I-V curve | 63 |
| 3.3.5 | Limiting cycle | 65 |
| 3.4 | Power generation mechanism | 68 |
| 3.5 | Output power and its limitation | 71 |
| 3.6 | Conclusions | 74 |
| 4 | Double-RTD Oscillator | 75 |
| 4.1 | Sub-THz chip-size double-RTD oscillator with patch antenna | 76 |
| 4.1.1 | Operation principle | 76 |
| 4.1.2 | 1.6 nm RTD | 78 |
| 4.1.3 | Analysis of the oscillators | 78 |
| 4.1.4 | Fabrication of the devices | 81 |
| 4.1.5 | Oscillators' performances | 86 |
| 4.1.6 | Patch antenna loss assessment | 90 |
| 4.1.7 | Summary for the sub-THz patch antenna oscillators with bridges | 90 |
| 4.2 | Bridge-less double-RTD oscillator beyond 1 THz | 91 |
| 4.2.1 | Conical vias | 92 |
| 4.2.2 | 1.0 nm RTD | 94 |
| 4.2.3 | Fabrication of the optimized devices | 94 |
| 4.2.4 | Performance of the optimized design | 95 |
| 4.2.5 | Comparison with the chip-sized RTD oscillators | 97 |
| 4.2.6 | Losses in the dielectric | 98 |
| 4.2.7 | Summary for the THz patch-antenna DRTD oscillators | 101 |
| 4.3 | FMCW and OCT application of RTD oscillators | 102 |
| 4.3.1 | RTD oscillator frequency tunability | 102 |
| 4.3.2 | Frequency response linearization | 103 |
| 4.3.3 | FMCW Radar | 106 |
| 4.3.4 | Summary for the FMCW and OCT RTD oscillator source | 106 |
| 4.4 | Measurement system | 107 |

| | | |
|----------|--|------------|
| 5 | Large signal RTD dynamics | 111 |
| 5.1 | Static and dynamic RTD models | 112 |
| 5.1.1 | Static RTD model | 113 |
| 5.1.2 | LS dynamic RTD model | 114 |
| 5.2 | RTD dynamics in phase space, “full model” (FM) | 117 |
| 5.3 | RTD LS equivalent circuit | 118 |
| 5.4 | Reconstruction of the phase map, “simplified model” (SM) | 121 |
| 5.5 | Connection between the LS response and the SS relaxation time constant | 123 |
| 5.6 | High-frequency (HF) response | 125 |
| 5.7 | Second-subband current | 126 |
| 5.8 | Discussion on acceleration of LS response | 128 |
| 5.9 | Dynamic response at the bias point of the highest NDC | 129 |
| 5.10 | Conclusion | 130 |
| 6 | Thesis Conclusions | 133 |
| | Bibliography | 137 |
| | List of publications | 151 |
| | Curriculum Vitae | 153 |

Abstract

One of the topics the thesis is focused on is the concept of chip-sized double-resonant-tunneling diode (RTD) patch antenna oscillators capable of operating in the sub-THz and THz frequency regions. The concept offers the advantages of simplicity, compactness, high isolation of the oscillator from the external biasing circuitry, and substantial output powers comparable with the output powers of more complex chip-sized oscillators. Implementing this concept into a practical design with 1.6 nm barrier RTDs resulted in an output power of $10 \mu\text{W}$ at the fundamental frequency of 525 GHz and $70 \mu\text{W}$ at 330 GHz. These results represent an order-of-magnitude increase in the output power compared to previous reports on patch-antenna RTD oscillators. In addition, the oscillators were fabricated using only optical lithography.

Further, from the analysis of the designed oscillators' limiting factors, the hindering mechanisms for achieving higher frequencies were identified in the inductance of the slant bridges connecting the RTDs and the patch antenna and in the parasitics of the used RTD. Therefore, conical vias replacing the slant bridges and 1.0 nm barrier RTDs were used in the design's next iteration, reducing the influences of those parasitics. These changes resulted in the oscillator operating with an output power of $9 \mu\text{W}$ at the fundamental frequency of 1.09 THz, $15 \mu\text{W}$ at 0.98 THz, and up to $27 \mu\text{W}$ at the lower frequencies of 620-660 GHz. These parameters are close to the state-of-the-art level for all other types of RTD oscillators at around 1 THz. We further demonstrate that there is much room for further improvement of the parameters of these oscillators.

The constructed oscillators were used as sources for sub-THz FMCW radar and optical coherent tomography. These two examples represent potential real-life applications of RTD oscillators. For these applications, an RTD oscillator operating at 680 GHz, with a bandwidth of 38 GHz, and output power of $23 \mu\text{W}$ provided a spatial resolution of 4 mm. The frequency tuning of the RTD oscillator was done by the sweep of its bias voltage. The shape of the sweep needed to be corrected to increase the system's accuracy.

Next, we show that the theoretical maximum output power of a simple RTD oscillator is fundamentally limited by the radiation conductance of its antenna and by a maximum RTD

voltage swing for which the RTD still shows negative conductance. As such, this maximum output power marks an upper bound for the RTD oscillators. The RTD current peak density and the RTD capacitance then influence how close we can get to this bound. The value of the upper bound gives us a tool for comparing the theoretical performance of different antennas.

Lastly, the thesis presents a model for analyzing dynamic large-signal characteristics of double-barrier RTDs. The model is based on analyzing dynamical trajectories in phase space, defined by the RTD bias and electron density in the RTD quantum well. We demonstrate that the large-signal admittance of RTDs can be accurately represented with a simple equivalent circuit composed of a capacitor, inductor, and two resistors (RLRC). These circuit elements correspond to large-signal relaxation time, geometrical RTD capacitance, and low- and high-frequency resistors. The same structure of the circuit was previously derived to model small-signal RTD admittance; however, in the large-signal case, the model's parameters depend on the AC-signal amplitude. Further, we show that the large-signal RTD relaxation time can be shorter or longer than the small-signal one. For the RTD oscillators, a shorter RTD relaxation time increases the gain of the RTD at high frequencies, which allows one to get higher output power at these frequencies. The availability of an accurate, general, but relatively simple, physics-based model for analyzing large-signal RTD dynamics removes one of the main obstacles to the further improvement of sub-THz and THz RTD oscillators. This model allows one to drop the quasi-static approximation of the RTD parameters in the large-signal analysis of the RTD oscillators. We also show that the model's parameters can be estimated, relying only on a directly measurable DC I-V curve and on a few other RTD parameters, which could be easily estimated with simple DC calculations.

Chapter 1

Introduction

1.1 Outline of the thesis

In the first chapter, we introduce the THz frequency range and the emerging applications operating at frequencies of this region. We describe the fundamental obstacles to the construction of THz sources and summarize the basic types of these sources. The second chapter is dedicated to the description state-of-the-art of RTD oscillators. We introduce there the operational principle, basic parameters, and technical realization of RTDs. Further, we describe the historical development of RTD oscillators. We conclude the chapter with the estimation of the maximum operating frequency of the RTD oscillators. In the third chapter, we describe the small-signal and large-signal analysis of the RTD oscillators. The analyses lead to the estimation of the oscillation frequency and of the output power of the oscillators. Further, we describe the origin of the power generation from the RTD and explain the self-rectification process that changes the I-V curve of an oscillating RTD. The chapter is concluded with the derivation of the upper bound of the output power achievable with the RTD oscillators. The fourth chapter describes the design of double-RTD patch antenna oscillators and presents their results. Additionally, we present in the chapter a possible real-life application of the RTD oscillators, used as a source for FMCW radars or for optical coherence tomography applications. In the fifth chapter, we put forward a model for analyzing dynamic large-signal characteristics of double-barrier RTDs. We present a simple RLRC model which can accurately represent the large-signal admittance of the RTD. Further, we show that the response of the RTD to the dynamical changes of the bias can be slower or faster than anticipated from its small-signal characteristics. We conclude the thesis in the sixth chapter.

1.2 Oscillators

At the museum of clocks in Vienna is a broad selection of different types of clocks. One of the exhibits is a mechanical clock from 1699 constructed by Jakob Joachim Oberkircher, and it served in St. Stephen's Cathedral. It is an impressive machine, yet, its basic principle is straightforward. There is a pendulum acting like a quasi-harmonic oscillator, where its length determines the oscillation frequency. The pendulum is connected through an escapement gear (a specifically shaped cog) by a shaft to a hanging weight, which gravity pulls down. The swinging pendulum then periodically allows the weight to drop down. The weight movement unwinds a rope that rotates the escapement gear with a frequency proportional to the pendulum oscillation frequency multiplied by the number of the teeth of the cog. The escapement gear pushes and thus accelerates the pendulum in the direction of the swings, compensating for the deceleration due to frictional losses. Hence, the change in the weight's potential energy is used to cover frictional losses. The rotation of the shaft then moves the hands of the clock. Another example of an oscillator can be water clocks or heat engines, which shows that artificial oscillators have been built for centuries.

In the end, all artificial oscillators, with more or less abstraction, work on the above-described principle. The description of the clock fits all dissipative oscillators, where an external energy source covers the energy losses to produce steady oscillations. Every oscillator is formed by a resonating part determining its oscillation frequency (such as a pendulum or an electric resonant circuit), source of energy to cover for the losses (potential energy such as a water level height or an electric potential of a battery), and element that allows converting the source energy into the oscillating energy (the escapement gear shape or particularly shaped an I-V curve of an electronic device).

In this thesis, we deal with electromagnetic oscillators that have found applications in far broader ranges than mechanical clocks. The electric oscillators are used, e.g., to transform energy from one form to another (e.g., DC electric motor), to provide a reference clock for the world (atomic MASER clock), or, as this thesis partially describes, to generate electromagnetic waves. As only the changes of the electromagnetic field carry energy in the free space over far distances, the oscillators, which by their definition are producing the changes, are practically used everywhere in our information age. The generation of electromagnetic waves is of particular interest because of their capability to transfer large amounts of information over long distances (communications) or to provide the signal source for spectroscopy and reflectometry.

Here we give a brief history of the development of electrical oscillators for generating electromagnetic waves. One can see that the parameters in the development's focus were to raise the oscillation frequency, raise output power, decrease the oscillator's sizes, and increase the oscillator's simplicity. These oscillators have been studied since the 19th century when Heinrich Hertz developed the first radio wave transmitter using an induction coil and a spark gap, see [1]. When the voltage on the gap increases above a threshold the arc starts and the electrical resistance

of the gap significantly decreases. The current-voltage characteristic of such a circuit would then show so-called negative differential resistance, which means that the current decreases with increasing voltage. The negative differential resistance (or, when appropriate; negative differential conductance) is the central part of all oscillators, and this term will be used in this thesis extensively. We should also mention that the induction coil instrument (used to generate the sparks) that Hertz used was also an electrical oscillator. The problem with the spark system is that it cannot sustain continuous wave operation and needs to be operated in a pulsed regime. This problem was overcome using an arc converter, where the arc was never quenched. The oscillation frequencies of the last spark oscillators were in the range of tens to lower hundreds of kHz, and the output powers reached over 100 kW.

Vacuum tubes were invented at the beginning of the 20th century. Triodes (tubes with a single grid) could have easily oscillated because of a parasitic capacitance (Miller capacitance) between the anode and the grid that was able to create positive feedback. Early tetrodes (two grid tubes) then showed negative differential resistances and could have been used in the oscillators when appropriately connected to an LC tank circuit. Another worth mentioning vacuum tube capable of oscillation is a cavity magnetron. In the cavity magnetron, the traveling electrons from the cathode to the anode are because a transversal magnetic field is applied to them, traveling on a spiral path. The anode is in the form of split ring resonators. As the anode resonators are being excited by the arriving electron, the field in them oscillates at the resonance frequency given by the geometrical shape of the cavities. The magnetrons are still being used today, e.g., in radars and microwave ovens. The magnetrons can work up to 95 GHz, with an average output power of tens of kW, see [2]. For other oscillating tubes, see, e.g., [1].

With the advent of semiconductor devices in the 1950s and 60s, transistor oscillators were introduced, which work on a similar principle as the triodes and tetrodes. New semiconductor diodes (two terminal devices) that exhibited negative differential resistance were invented along with the transistors. As the semiconductor devices' dimensions approach nano-metric scales, also their parasitics are lower, and thus their oscillation frequency can be increased. On the other hand, the small dimensions then limit the maximum generated power. In the 1960s, the first Lasers were developed, which started to cover the infrared and visible light range of electromagnetic radiation, see, e.g., [3]. The principles developed in these two decades are still being used nowadays, and most modern electronic devices utilize them.

One of the semiconductor devices that is particularly suitable for high-frequency applications is the resonant-tunneling-diode (RTD), which lies at the center point of this thesis. What makes the RTDs so attractive is the fact that they exhibit negative differential resistance in the so-called terahertz gap. Therefore, they represent a potential candidate for electrical oscillators in the high-frequency range.

1.3 The terahertz gap

The terahertz (or THz) gap represents a frequency range in which the active electronic and photonic devices are still not yet matured. The frequency range of the THz gap is defined from 0.1 THz to 10 THz, which corresponds to wavelengths of 3 mm (millimeter waves) to 30 μm (far infrared), see e.g. [4], [5].

1.3.1 Applications of THz waves

The THz waves are interesting for various applications, both for scientific purposes and for applications with which we may soon have contact in our daily lives.

The scientific application lies mainly in deep space exploration, where low-noise THz detectors are necessary. By measuring the THz radiation spectrum, we can analyze the molecular content of far galaxies, as spectral lines of many molecules lie in the THz range. The light from the very far galaxies is red-shifted and lies in the THz range. Also, we can detect galaxies hiding behind dust clouds, as the long wavelengths of THz waves can penetrate those. These experiments help our understanding of the beginning of our universe, see [6].

THz waves are starting to be extensively used in biomedical sciences, as the radiation is non-ionizing and highly sensitive mainly to the water content of the samples. Both the sources and detectors can be utilized in this field. The THz waves are used for tomography, e.g., for Ex vivo breast and skin cancer detection or in dentistry to probe the decay of teeth. The application for cancer treatment is also being considered, see [7].

THz spectroscopy is used in biological sciences to detect and recognize molecules of, e.g., hazardous substances or proteins. The THz spectroscopy is typically used with the help of meta-materials, which selectively amplify the spectroscopic response, see [8].

The radars at these frequencies are attractive as the THz radiation is non-ionizing while allowing for high resolution due to the large bandwidth. Radars in the THz range serve in security applications, e.g., at airports for scanning passing by persons to detect dangerous objects they might carry, see [9]. However, the fast enough scanning and signal processing for these applications still need to be improved. Recently, a system capable of scanning persons walking at a speed of 4 km/h was developed, see [10]. Another possible application is scanning mail, as the paper envelopes are nearly transparent to the THz radiation, while the dangerous items ordinarily reflect and scatter the THz waves.

The THz waves can also be used for a quality check of the fabricated materials, see [11]: In this specific case, to check the quality of the polymeric compounds. Alternatively, they can be used in agriculture for crops or food inspection, see, e.g., [12].

The usefulness of the THz waves for telecommunications is being considered. For example feasibility of utilizing sub-THz frequencies for the 6G networks is discussed in [13]. However, telecommunication using THz frequencies is a topic in its early stages, and the literature shows more a vision than a concept. However, e.g., compact oscillators operating in the sub-THz range

were used to transport broadband signal (several tens of Gb/s) over a short distance (a couple of meters) and were reported in [14].

For most of the above-stated applications, we need suitable THz sources to provide the THz radiation. However, these sources suffer from specific problems, as explained in the following subsection.

1.3.2 Challenges of the sources in the THz gap

The development of THz sources faces fundamental obstacles. As the THz-gap is being closed by photonic and electronic devices, we can categorize the challenges accordingly. The photonic devices generate electromagnetic waves from the electron transitions between electronic bands within the active material. The transitions can be either spontaneous or stimulated. On the other hand, electronic devices produce oscillations from a periodic movement of electrons in a single band. The acceleration of the charge then produces electromagnetic waves. We start by describing the problems on the photonic side, and then we follow with the description of the problem on the electronic side.

The photonic side

The photon energy range corresponding to the frequency band of the THz gap lies between 0.4 meV and 40 meV. The magnitude of these energies leads to a fundamental problem. The active photonic devices are almost exclusively made from III-V semiconductors, i.e., semiconductors composed of alloys of the third and fifth atomic groups. The III-V semiconductors are polar, meaning that there is an ionic bond between the atoms. The polarity allows for optical phonons to exist. The optical phonons are vibrations of the semiconductor lattice, where the neighboring atoms oscillate out of phase. Their dispersion characteristic in the dispersion diagram (angular frequency versus the wave vector) intersects the dispersion line of photons. The intersection allows for the optical phonons and photons to be coupled, as both the energy and the momentum are conserved during the absorption/emission.

For example, the optical phonon energies for GaAs (the fundamental material for high-speed electronics and photonics) are 33.2 meV and 36.1 meV for transversal (TO) and longitudinally (LO) optical modes, respectively. These energies correspond to frequencies of 8.4 THz and 9.2 THz. The frequency band between these frequencies is called the Reststrahlen band, see [15]. In this frequency band, the real part of the dielectric constant is negative. Therefore, the electromagnetic waves cannot propagate in this band through the crystal, as their wave vector is complex. All other used III-V semiconductors show similar behavior at similar frequencies.

There is another problem, which originates from the relatively small energy of the THz photons. To build a semiconductor laser, one needs to have an energy separation between two levels in the band structure equal to the THz photon energy and a higher number of electrons that can emit than the number of electrons that can absorb the radiation (population inversion).

However, because the THz photon energy is so low, which means that the energy of the two states is very similar, it is difficult to maintain the population inversion because of scattering effects on higher temperatures than cryogenic (kT at 300 K is ≈ 25.7 meV), see [16], [17].

The Reststrahlen band and the small separation of the states limit the photonics devices to work only at high-frequencies (short wavelengths).

The electronic side

The electronic devices are limited by the everywhere-present RC circuit having an RC time constant. The RC circuit behaves as a lowpass filter, limiting the devices to work only at low frequencies. Such a circuit allows the currents to bypass the active devices, thus limiting the maximum operating frequencies and output powers. The RC circuit originates from parasitic elements of the physical device; the Ohmic losses and parasitic capacitances. The only suitable solution for this problem is to minimize the parasitics by, e.g., using simple devices that limit the parasitics' effect or minimize the devices' dimensions.

1.4 THz sources

For a comparison of THz sources, see Fig. 1.1. In the comparison, we state only the advantageous candidates for compact sources, i.e., not tabletop systems. The figure shows the gap between the electronic and photonic sources at around 1 THz. We should note that this comparison is rather subjective, as it compares devices in the pulsed and continuous wave regime or room temperature devices and devices requiring cooling to cryogenic temperatures. However, it still does capture the power descending towards the higher frequencies for the electronic devices and the power descending towards the lower frequencies for the photonic devices. For a further detailed comparison of various THz sources, see, e.g., [18], [19].

1.4.1 Devices exploiting the negative differential conductance

The negative differential conductance (NDC) (or resistance (NDR), depending on the context) is the central part of electronic oscillators. The NDC covers for the losses in the electrical resonators and thus enables the generation of steady oscillations. On an NDC, the current decreases with the voltage rise, which is an inverse behavior of a resistor.

No passive device can have negative conductance (resistance) at zero bias. However, devices that show the NDC when biased exist. This means that the devices exhibit negative differential conductance only locally; meanwhile, they are passive globally. That is why the device needs to be biased into the NDC region by an external energy source. The connection of the device with NDC and the bias source then effectively create an electronic part, which shows negative conductance for changes in the applied voltage, thus negative differential conductance.

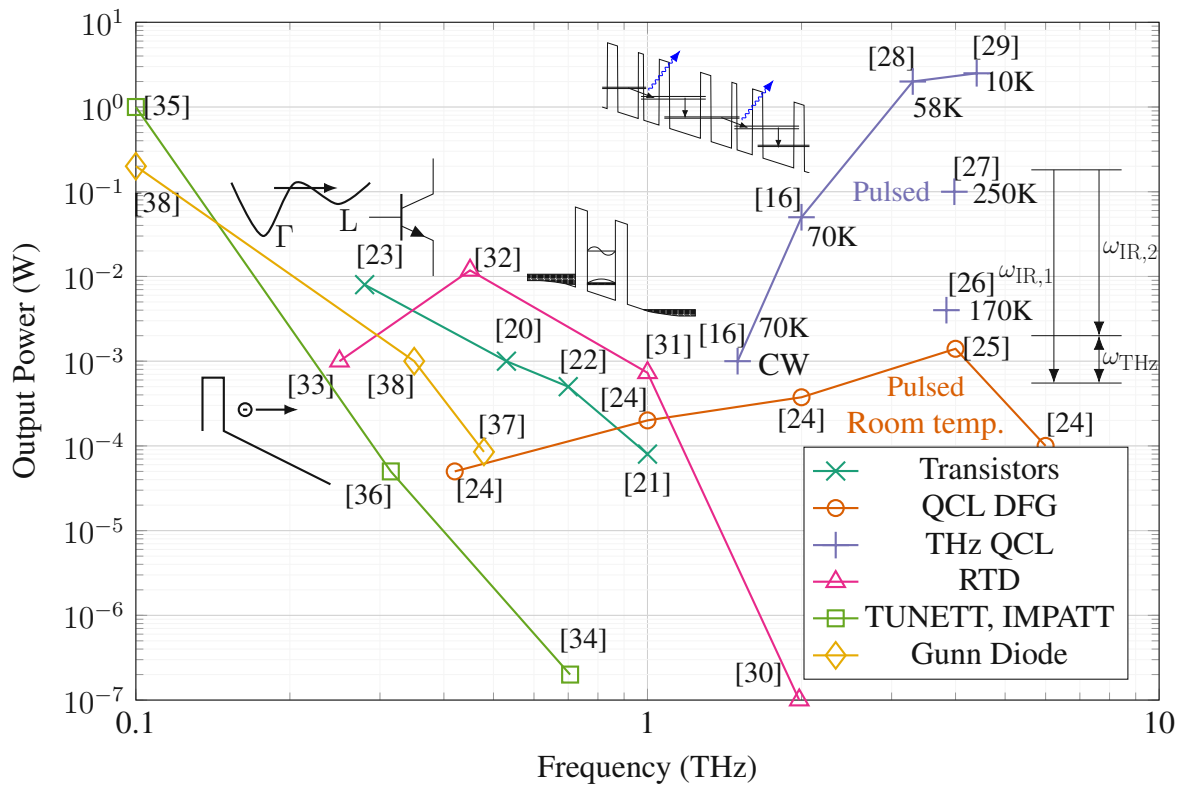


Figure 1.1: Comparison of THz-wave sources that have the potential to be used in compact THz applications. The photonic sources (THz QCL and QCL DFG) cover the high frequencies, and the electronic sources (the rest of the listed devices) cover the low frequencies. The THz QCLs need to be cooled down. The powers for the THz-QCL and the QCL-DFG correspond to the peak power of a pulsed operation (if not explicitly stated otherwise). In contrast, the powers for the other devices that work on the electronic principle correspond to the continuous wave (CW) power. The figure shows the THz-Gap being closed from both sides. For a brief description of here shown devices, see the next sections.

The state-of-the-art devices with NDC can be operated in the sub-THz and THz range in a continuous wave regime and at room temperature. In the following subsections, we list their types.

Esaki, Gunn and other diodes

Esaki diodes (or also Tunnel diodes) are composed of a connection of highly n- and p-doped semiconductors. For small biases, the electrons from the conduction band of the n-doped part can tunnel, due to the alignment of the bands, to the valence band of the p-doped part. With increasing the bias voltage, the bands get progressively more and more misaligned, and thus the current flow decreases. The decrease of the current with increasing voltage results in the NDC. Esaki diodes have a high capacitance of the depleted region and therefore are limited by the RC constant due to the contacts' parasitic resistance, see [39]. The maximum fundamental oscillation frequency achieved with GaAs tunnel diode is 103 GHz, see [40], and the theoretical prediction of around 200 GHz, see [41], was never experimentally demonstrated.

Gunn diodes are composed of a heavily n-doped semiconductor except for a short region (ones of μm) which is only lightly doped. The NDC originates from the increase of the electrons' effective mass when the electrons are injected from the Γ -valley into the L-valley (in the case of GaAs Gunn diodes). This injection is caused by an acceleration of the electrons by a relatively strong electric field in the lightly doped region, which is generated by the applied bias. The highest reported achieved frequency is 450 GHz with an output power of 23 μW . However, this frequency corresponds to the third harmonic of the free-running oscillator [35]. The prediction of the oscillation frequencies of Gunn diodes composed out of GaN report 3 THz, see [42]. However, one should take these results with caution because they are still left to be experimentally confirmed for more than twenty years.

Impact ionization avalanche transit-time diode (IMPATT), tunnel-injection transit-time (TUNNETT), and barrier-injection transit-time (BARITT) are other two-terminal devices exhibiting NDC in the sub-THz range. All these diodes work on a principle of injecting the carriers into an intrinsic semiconductor, where the carriers are accelerated by an electric field and travel with saturation speed (the bias maintains an electric field). The intrinsic region length is such that the current reaching the collector is 180 degrees phase shifted in reference to the driving AC voltage, which results in NDC behavior for the AC signal. The above-stated diodes differ in the injection types [43]. TUNNETT diode in a waveguide achieved oscillation frequency 706 GHz, with an output power of 0.2 μW [34].

Transistors

Contrary to diodes, transistors are three-terminal devices and thus offer better flexibility theoretically when building oscillators. When a positive feedback loop is established, either through external circuitry or through the transistor's inverse transmission, the transistor acts as a two-terminal device with NDC, which can compensate for the losses in the resonant circuit, see, e.g., [1]. Resonant circuits are parts of the feedback circuit, as they can shift the phase between the input and the output signal. Because the feedback is frequency selective, the transistor oscillators do not suffer from the low-frequency instability as the diodes.

The main parameter of transistors when building an oscillator is their f_{max} , which corresponds to the maximum achievable oscillation frequency. It is a frequency for which the transistor's transducer unilateral gain is 1. However, in practice, it is not easy to achieve this limit, see [44].

There are different types of high-speed transistors used in oscillators: heterojunction bipolar transistors, see [22], high electron-mobility transistors, see [20], [21], or classical metal oxide transistors, see [23]. The transistor oscillators are ordinarily designed to operate in arrays and generate signals with higher harmonics (typically the second or third harmonic), which are sub-sequentially radiated. For their performance, see Fig. 1.1.

Resonant-tunneling diodes

Resonant-tunneling diodes (RTDs) are devices exploiting resonant-tunneling of electrons through a double-barrier structure (eventually through a multiple-barrier structure). The I-V curves of RTDs show negative differential conductance similar to the Esaki diodes. It has been shown they can operate in oscillators up to 1.98 THz, see [30], and output powers of 11.8 mW at frequency 450 GHz, see [32]. As the RTDs play an integral part in this thesis, we describe them in more detail in Chapter 2.

1.4.2 THz lasers

Quantum cascade lasers (QCLs) are photonic devices in which it is the stimulated emission that generates electromagnetic radiation. QCLs are hetero-structures and super-lattices of quantum wells and barriers. The width of the wells defines the energies of the discrete states that the electrons can occupy. The transition of the electrons between the states then emits photons, which results in electromagnetic radiation. The wells and barriers are periodically repeated in many periods (tens to hundreds of periods) and, if biased, create a cascade. A single electron injected from the top of the cascade then undergoes many transitions and generates in every period one photon with an identical wavelength. If the QCL is situated in a cavity, then the resonating electromagnetic waves trigger the stimulated emission, and the QCL starts lasing. The QCLs are well matured in the infrared and far-infrared range, see, e.g., [45]. However, in the THz range, they suffer from the above-mentioned thermal excitation of the carriers.

The infra-red QCL designs were optimized and simplified, which allowed the QCLs to operate in the THz range (THz QCL). However, these still need to be cooled down far below zero degrees Centigrade, see [16]. Recently, breakthroughs allowed the build of THz QCLs cooled down by Peltier elements, allowing further minimization of the QCL systems, see [26], [46]. If cooled down to cryogenic temperatures, these THz QCLs show in pulsed regime peak output powers up to 2.5 W and can cover the frequency range from 1.5 to 6 THz, see, e.g., [28], [29].

Another principle of utilizing QCL for generating THz waves is the difference frequency generation (DFG). This principle uses a QCL generating two lasing modes with differing wavelengths. The frequency difference between the modes corresponds to a frequency in the THz range. At the same time, the QCL active region exhibits strong nonlinearity, capable of mixing the two modes into the electromagnetic radiation at the difference frequency, see [47]. The used QCL operates in the infrared range, where it does not require cryogenic cooling, and thus QCL-DFG can generate THz waves at room temperature. These sources can work even in the sub-THz range, although with very small output power. QCL-DFGs operating in the frequency range from 0.42 THz to 6 THz and with a maximal output power of 1.4 mW in the pulsed mode were demonstrated, see [24], [25].

THz sources with frequency multiplication

A possible solution for generating the sub-THz waves is to use non-linear elements to generate higher harmonics of an applied harmonic signal. Schottky diodes are made from metal-semiconductor contacts, have a non-linear I-V characteristic, and can be used as high-speed devices. The efficiency of the higher harmonics with the number of harmonics is limited; thus, creating a chain of multipliers is necessary to obtain considerable output power. Schottky multiplier chains have shown capability to produce approximately 900 mW at 0.1 THz, 1 mW at 1 THz, and 20 μ W at 2.7 THz, see, e.g., [48], [49]. However, these systems are rather bulky, require high input powers, and might require cooling.

Optically pumped sources

Similarly to QCL-DFG devices, the THz radiation can be generated by mixing two signals with different optical wavelengths, where their frequencies differ by the wanted frequency of the THz signal. The signal in the THz range is generated by focusing the optical signals onto a non-linear semiconductor, which mixes their frequencies and produces the difference frequency. The nonlinearity of the semiconductor is caused by photoconductivity. Typically, a broadband antenna (e.g., bow tie antenna) is situated on the surface of the semiconductor and is split into two arms by a gap in its middle. The antenna's separated arms are biased, and the optical signal is focused on the gap where the exposed photoconductive semiconductor lies. The difference in the frequency of the signals composes a beat signal, periodically changing the conductivity of the gap. The currents on the antenna generated by the bias and the optical beat then radiate the THz waves. The output power can reach 1.5 mW, and the system can operate from low frequencies of tens of GHz up to approximately 2 THz, with output power in the range of tens of μ W at 1 THz, see [50].

Other THz sources

Another principle for the THz wave generation is to use a femtosecond laser and use the produced pulse on the photoconductive antenna described in the previous section. The short femtosecond pulse contains a broad spectrum of frequencies in the THz region, which is radiated by the antenna. This system operates only in the pulsed regime. For details, see [51].

Additionally to the above-stated source are the following: glow-bar, discharge tubes, free-electron lasers, optically pumped gas lasers, and vacuum tubes. For details about these, see, e.g., [18] or other relevant literature reviewing THz sources.

Chapter 2

Resonant-Tunneling-Diode Oscillators

All electronic oscillators work on the principle that an active device compensates for losses in a resonant circuit, which allows for oscillations in the circuit with a steady amplitude. As the losses are represented with resistors with positive resistance, components with the negative differential conductance (NDC) locally represent resistors with negative resistance and thus can compensate for the losses. For example, two-terminal devices such as gas discharge tubes have been used in oscillators since 1922 [52]. Another worth mention examples are tunnel diode and Gunn diode oscillators operating at microwave frequencies. In the end, also for transistor oscillators, the transistors, which are three-terminal devices, are connected to the circuit so that they compensate for the losses in the resonant circuit, which is equivalent to the description of the effects of the negative resistance. Therefore, already before the advent of resonant-tunneling-diodes (RTDs) oscillators, there was already broad knowledge about electrical oscillators.

Nevertheless, the RTDs can operate on the THz frequencies, and because the output power generated by the RTD is fundamentally limited, the concept still had to be adjusted. At high frequencies, losses of the conductive materials and dielectrics from which the oscillator is built increase, resulting in decreased output power. Therefore, it is a good practice to avoid building oscillators with long waveguides and rather couple out the generated oscillations as soon as possible to the free space. That is why it is beneficial to use a resonant antenna, as both the resonator, which defines the oscillation frequency and the radiator, which directly radiates the generated waves.

2.1 Introduction to resonant-tunneling-diode oscillators

The benefits of using the RTDs as the active elements in oscillators are that they can be operated in the THz range in the continuous wave regime and at room temperature, which allows us to build compact, high-performance THz sources.

RTD oscillators are composed of: an RTD, which is the active element having the NDC, i.e., the gain; a resonator, which determines the oscillation frequency; from a biasing circuitry and an external bias source, which provides the energy to the oscillator; and from an antenna, that provides the generated oscillation to the outer world. In state-of-the-art oscillators, the resonator and the antenna are combined in a resonant antenna that directly radiates the generated electromagnetic waves. However, this trend might be changing to the separation of the resonator and the radiator; see further details in section 2.3.

RTD oscillators are typically free-running oscillators. However, as such, they can suffer from phase noise, which would degrade their performance in real-life applications, see [53]. Thus, experiments with injection locking the oscillator to a reference oscillator with a low phase noise were performed which reduces the phase noise of the RTD oscillators, see [54], [55]. The RTD oscillators were also operated in the harmonic mode, where it was a higher harmonic of the base oscillation frequency that was used as the output frequency (a concept that is mainly used in transistor oscillators), see [56].

As the RTD oscillators should be applicable in real-life applications, several parameters are essential when researching and comparing them. These parameters are, among others, the oscillation frequency, the output power, the DC-to-RF efficiency, their physical size, their ease of use, and whether the frequency of the output signal is the fundamental harmonic.

Some of the already reported examples of the RTD oscillator used in real-life applications are: use in radar sensors and optical coherent tomography systems, see [57], [58]; communications, see [14], [59], [60]; or imaging [61], [62]. Only recently, an RTD oscillator operating in a comb-like mode was reported, see [63], which might allow using the RTD oscillators for broadband sensing applications.

2.2 Resonant-tunneling diodes

Theoretically, the resonant-tunneling-diodes were proposed in the 1960s based on the Esaki diode [64]. However, the development of RTDs came together with the start of the molecular-beam-epitaxy (MBE) method [65] and with the works of Chang, Tsu, and Esaki. At first, they predicted resonant tunneling in hetero-structures, see [66], and then fabricated and measured the first RTD, see [67], that showed the negative differential conductance (NDC). The materials used for the conducting layers and the barriers were GaAs and AlGaAs, respectively. However, this result was achieved at 77 K, the boiling temperature of liquid nitrogen. An RTD having NDC at

room temperature was developed in 1985, see [68], which was possible due to the changes in the layers and the improved quality of the MBE's grown films.

2.2.1 Principle of resonant-tunneling diodes

Resonant-tunneling diodes are two-terminal electrical components that exhibit the NDC. RTDs work on the resonant-tunneling principle, which occurs in double (or multiple barriers) structures. The space between the barriers composes a quantum well (QW), where the allowed energy levels of the charge carriers are quantized. The quantization creates subbands in the QW. See Fig. 2.1 for a graphical illustration of the operational principle of double barrier RTDs. The double barrier structure is highly transparent for the carriers with an energy matching the energy of the quantized state and highly opaque for the others, see, e.g., [69], [70]. A direct analogy for this phenomenon is the Fabry-Perot resonator, constructed out of two semi-reflective mirrors with relatively high reflectivity facing each other. The light waves can pass the Fabry-Perot resonator only when it is in resonance with the resonant cavity composed of the mirrors and the space between them.

Double-barrier RTD is composed of a double-barrier band structure, which is uniform in a plane (2D structure), and contacts that provide carriers capable of resonant tunneling through the structure. As most of the RTDs are designed to work with carriers occupying the conduction band, we will further speak about the charge carriers as electrons that are traveling in the conduction band. The electrons in the contacts are distributed according to the Fermi-Dirac statistic, filling the contacts' states up to the Fermi level. The contacts are called the emitter and the collector, which is based on the direction of the electron transport in reference to the double-barrier structure. Because the RTDs are uniform in the two dimensions of the plane that is transversal to the electron transport, the quantum confinement between the barriers takes place only in the longitudinal dimension, and thus only those electrons with longitudinal momentum that matches the energy of the quantized states can tunnel through. The longitudinal quantization allows the electrons with various transversal momenta, but still matching the longitudinal momentum, to fulfill the resonant condition and tunnel through the structure, e.g., [70], [71]. Although exotic RTDs with multiple wells also exist (e.g., triple-barrier RTDs), here we only describe the single well structures.

The current density flowing through the RTD is proportional to the tunneling rate of the electrons tunneling through the double-barrier structure and to the available number of electrons that fulfill the resonant condition. The tunneling rate depends on the thickness of the barriers and on the width of the well and can be determined from the solution of the Schrödinger equation. The number of electrons that match the resonant condition is proportional to the energy difference between the Fermi level of the emitter and the energy level of the bottom of the corresponding subband, see [70].

For the zero bias, the electron transport between the contacts surrounding the double barrier

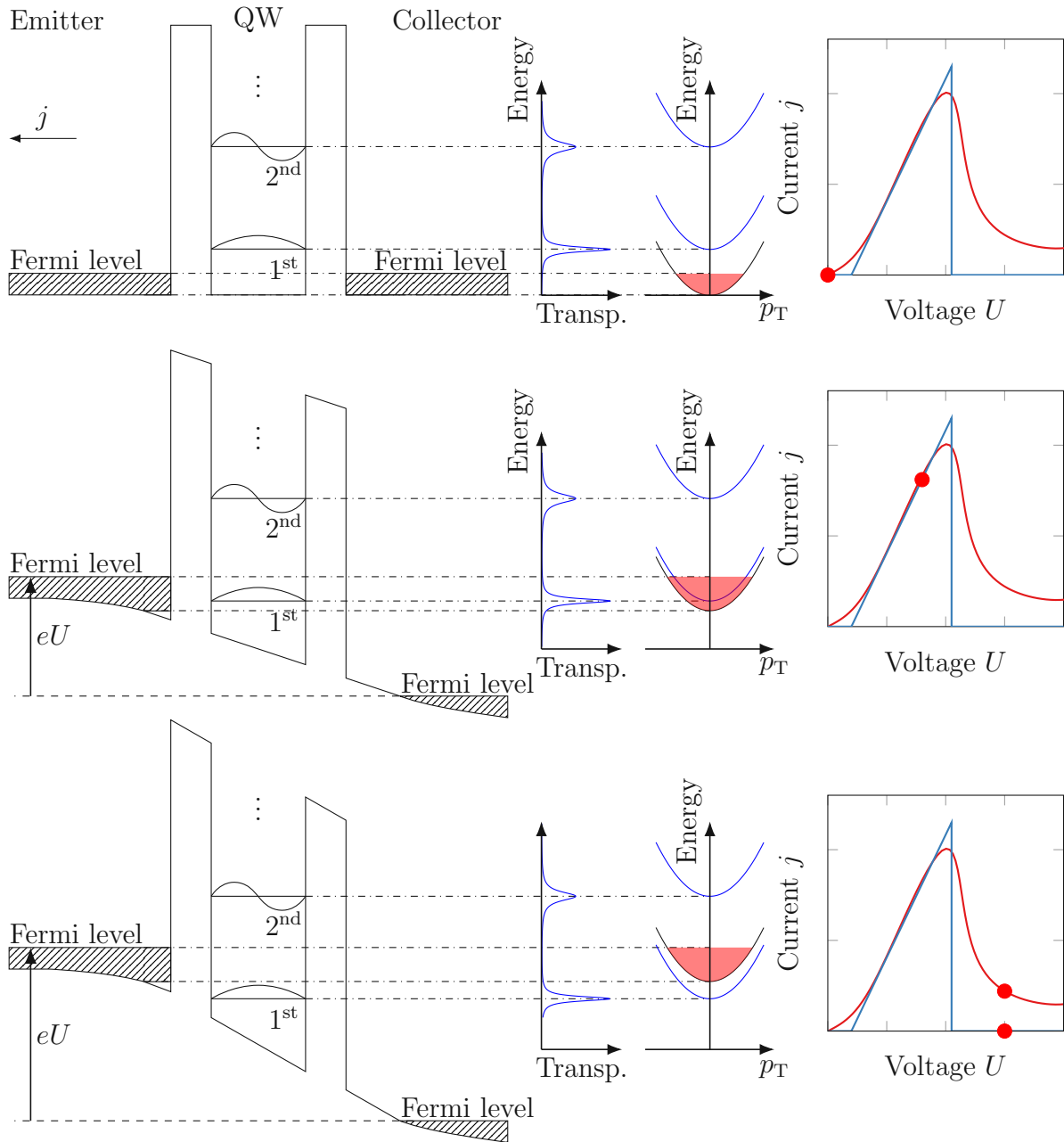


Figure 2.1: The operation principle of RTDs. Diagrams from top to bottom differ in the applied voltage on the example RTD. The first column of the pictures shows the sketches of the conduction band diagram of the RTD. The second column shows the dependency on the transparency of the double barrier structure. The third column shows the dispersion diagrams for the transversal direction, where the filled part corresponds to the filled states in the emitter. The fourth column shows the I-V curve of the RTD, where we show in red an idealized I-V at zero Kelvins without any scattering and an example of a real I-V curve; the red points mark the bias points from the corresponding figures. For simplicity, we neglect the space-charge effect of the electron in the QW. For further details about the space-charge effects, see Chapter 5. Mind the conventional direction of the current which is opposite to the electron transport.

structure is in equilibrium. However, when we apply bias to the RTD, we disturb this equilibrium. With the bias voltage increase, we mutually shift the quasi Fermi-levels of the contacts, and because of this imbalance, the current through the RTD can start to flow.

With further increase of the bias, the RTD current also increases. This is happening because simultaneously with the change of the energy difference between quasi Fermi-levels of the contacts, we change the relative energy difference between the bottom of the QW ground subband and the Fermi levels of the contacts. For the emitter, the bottom of the ground subband shifts below the emitter's Fermi level, and for the collector, the collector's Fermi-level shifts below the bottom of the QW ground subband. As the energy difference between the Fermi level of the emitter and the bottom of the ground subband increases, the number of available electrons fulfilling the resonant condition in the emitter increases. Similarly, in the collector, the number of electrons fulfilling the resonant condition decrease. These two effects increase the magnitude of the electron transport from the emitter to the collector, which results in the increase of the current flowing through the RTD. The rise of the RTD current is approximately linear with the rise of the applied bias.

The current raises with the bias until the energy level of the QW ground subband matches the energy level of the emitter's conduction band, where suddenly there are no available electrons for the tunneling, which results in a sudden stop of the current flow. Theoretically, this transition between the peak current and the state where no current flows is sharp. In real RTDs, the resonant energies of the subbands are broadened from a finite lifetime of the electrons in the QW and various scattering effects. Because of this broadening, there is a certain spread of energies for the electrons that can tunnel through the structure. So as the ground subband energy level reaches the conduction band of the emitter, some electrons are still available to tunnel through. Therefore, the transition between the peak current and no current is smoothed out. This region is the part of the I-V curve where the RTD shows the NDC; with increasing voltage, the current decreases.

As there are additional (excited) subbands in the QW with higher energies than the ground one, with further bias increase, we shift the band diagram such that the number of electrons that can tunnel through those increases. Thus, the RTD current can rise again after the current drop. In real RTDs, the minimal current following the NDC region never goes to strict zero because of the current conducted by these excited subbands and by thermally excited electrons that can fly over the barriers. The point of the smallest current in the I-V curve after the NDC region between the first current peak (due to the ground subband) and the second current peak (due to the excited subbands) is called the valley current.

Notice from Fig. 2.1 that on the collector side of the RTD, with the increasing bias, a region that is depleted of electrons arises. This region is called the depletion region. Its length is bias-dependent and influences the capacitance of the RTD. The electrons constituting the RTD current need to travel through it.

2.2.2 Technical realization

To construct the RTDs, one needs to be able to create a device with the band diagram shown in Fig. 2.1. Semiconductor heterostructures give one flexibility in designing various shapes of the band diagram in the longitudinal direction. Semiconductor heterostructures arise from the controlled application of various semiconductive materials in one structure. Typically layers of varying semiconductors are sequentially deposited (e.g., grown by an MBE) one on another. There are heterojunctions between the layers, which create discontinuities in the band diagram. The barriers of the RTD are made out of a semiconductor with a larger bandgap than the semiconductor from which the well and the contacts are made. From the ordered deposition of these layers, we obtain the RTD. Along with the different band gaps, the band alignment between the layers is also important in the overall band structure. The typical conduction band discontinuity of the barriers is at around 1 eV, see e.g. [72], [73].

The used semiconductors are ordinary alloys of the III-V semiconductors, such as GaAs, InGaAs, AlAs, AlGaAs, GaN, AlN, InAs, InSb, etc. The concentrations of the elements in the alloys can also vary. The variety of the available materials gives flexibility in the designs. Typically, alloys containing aluminum are used for barriers because of their larger band gap. For high-frequency devices, semiconductors with high mobility of electrons and high saturation velocity are favored for the QW and the contacts. Not all of these materials are compatible because of their differing lattice constants. Thus they either need to be lattice-matched (adjusted concentration of the alloys to match the lattice constant). Alternatively, only small thicknesses of strained layers can be deposited, with a thickness smaller than the critical thickness (thickness of the strained semiconductor at which the lattice relaxes). It is important to have lattice-matched layers because the dislocations caused by the layers' relaxations increase the electron scattering and thus reduce the devices' performance.

The emitter and the collector are doped by shallow n-type dopants, which raise the contacts' conductivity. Additionally, doping in the emitter increases the number of electrons (raises the Fermi level in the emitter) that can tunnel through the RTD, which increases the peak current. For the III-V semiconductors, a typical n-type dopant is silicon. See Fig. 2.2 for an example layer stack-up forming an RTD and the corresponding band diagram.

The RTDs are two-dimensional structures; thus, their final area can be scaled by fabrication processes, which results in the truncation of the two transversal dimensions. The RTD current, capacitance, and current-related parameters are scaled together with the area of the RTD. The smallest working area of the RTD is limited because, for the tiny areas, the edge effect, which is bending the band diagram in the lateral dimension and influencing the quantized states, starts to dominate. Theoretically, for very small areas, we would get a quantum dot. The minimum size depends on the RTD layers. As a rule of thumb, these effects start if the RTD has a smaller diameters than ≈ 100 nm.

Because the RTD is a layered structure, if processed to be a column, it remembers a mesa

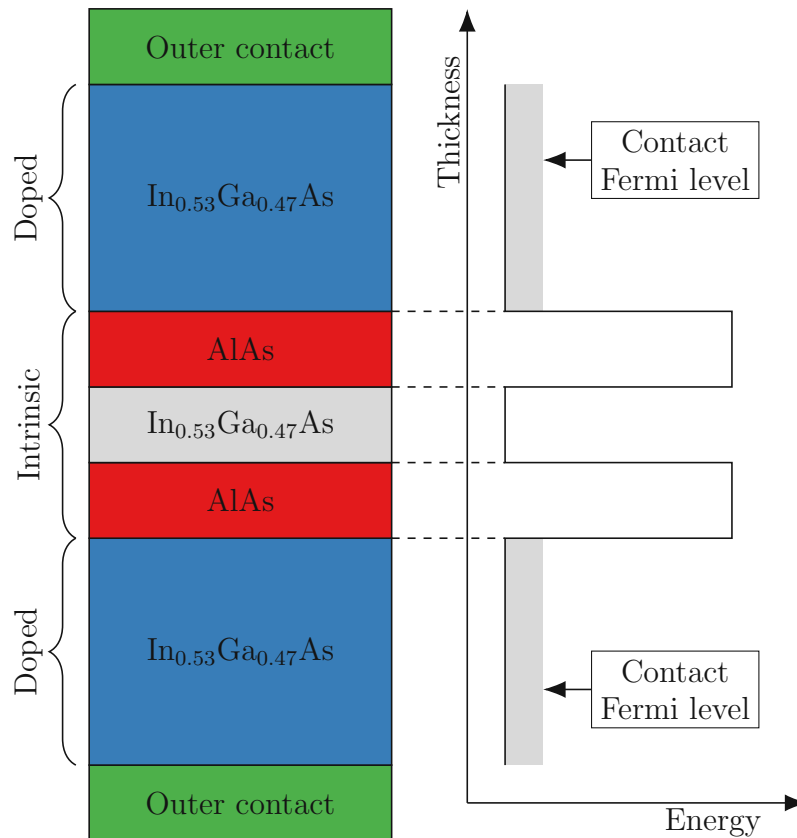


Figure 2.2: An example of an RTD layer stack up, with $\text{In}_{0.53}\text{Ga}_{0.47}\text{As}$ and AlAs layers, and its corresponding conduction band diagram.

mountain, where from the side, one can see the layers of the mountain. Thus, the processed RTD column is called a mesa.

In the emitter and the collector of the RTD resides an accumulated charge if we apply bias to the RTD. This charge separation corresponds to the capacitance of the RTD. Together with a parasitic resistance of the RTD originating from its contacts, the capacitance forms an RC circuit that fundamentally limits the RTDs' maximum operation frequency by its time constant.

Nowadays, the standard material of high-speed RTDs is InGaAs for the conductive layers and AlAs for the barriers. For more details, see the next section, as the development of high-speed RTD was connected to the RTD oscillators. The state-of-the-art RTDs are almost exclusively grown layer by layer on a semiconductor substrate by the MBE. However, RTDs grown by the metalorganic vapor phase epitaxy (MOVPE) were also reported, see [74].

We should add that there is research dealing with GaN/AlN RTDs. GaN material offers high thermal stability of the devices and high saturation velocity of the traveling electrons. With these benefits, GaN RTDs also bring drawbacks, such as growth difficulties, small peak-to-valley current ratios when compared to $\text{InGaAs}/\text{AlAs}$ RTDs, or band structure bending that results in high operational voltages, see [75], [76]. RTD oscillator build with GaN RTD was reported in [77], with the oscillation frequency of ≈ 1 GHz. However, experiments on the switching time of GaN RTDs suggest that the devices might have the potential to be able to operate at millimeter

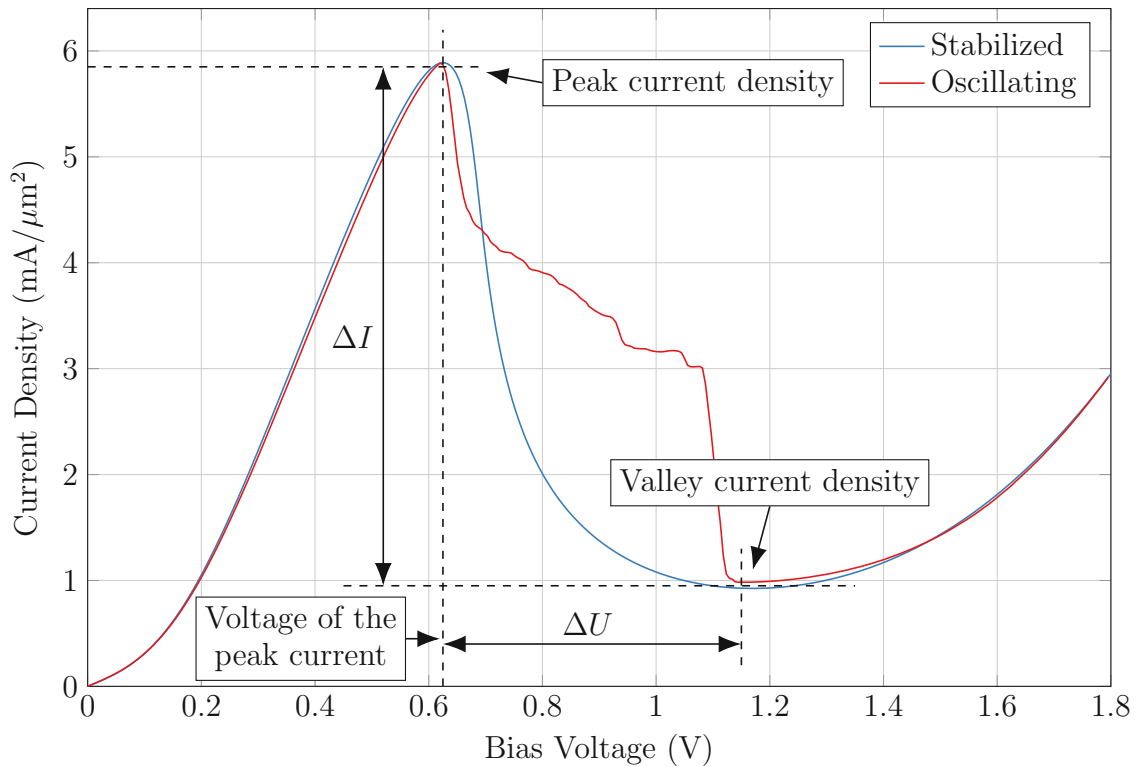


Figure 2.3: An experimental example of an I-V curve of an RTD studied in [80]. The oscillating case corresponds to the measured data of a fabricated device, and the stabilized case corresponds to a result obtained from a simulation of the RTD with the same nominal parameters as the fabricated device. Due to the NDC, the fabricated device oscillates during the measurement, which hides the NDC's actual shape due to a self-rectification effect. For details about the shape of the oscillating I-V, see Chapter 3.

waves, see [76], [78]. For additional information about the GaN RTDs, see [79].

2.2.3 Parameters of RTDs

Important equivalent parameters of RTDs in the context of RTD oscillators are the following: the peak current density j_p , the ratio between the peak current and the valley current (PVCR), the difference between the peak the valley current ΔI , the voltage difference between the peak current and the valley current ΔU , and the voltage of the peak current density. These parameters are defined on an I-V curve of an RTD in Fig. 2.3.

To obtain the equivalent parameters, one needs to perform DC measurements of the RTD's I-V curve. Because of the NDC of the RTDs, the RTDs are ordinary oscillating during the measurement. This is caused by the measurement system's parasitics, which create the resonant circuit and allow the RTD to oscillate. In that case, one obtains an I-V curve similar to the oscillating version shown in Fig. 2.3. One needs to stabilize the RTD to obtain a smooth version of the I-V curve, but the stabilization requires additional considerations and is not straightforward to achieve. The equivalent parameters, on the other hand, are useful because, for their determination, one does not need the stabilized curve, and they can be used for the

rough analysis of the oscillator. The current difference ΔI and the voltage difference ΔU are approximately giving the magnitude of the NDC because the conductance $G \approx -\Delta I/\Delta U$. G influences the maximal oscillation frequency and the output power. The voltage difference between the peak and the valley ΔU also determines the output power. The voltage of the current peak and the peak current density then influence the DC-to-RF efficiency. These two parameters, together with the thermal conductivity of the used material system of the RTD, influence the maximum RTD area for which a thermal breakdown due to power dissipation does not occur. For further details about the parameters, see Chapter 3.

In the optimal case for analyzing the RTD oscillators, the stabilized I-V curve and the RTD capacitance as a function of the voltage are known. This allows one to use, e.g., SPICE circuit simulator for the analysis, see [81]. However, those parameters are fully known only on quite rare occasions. Moreover, these parameters are frequency dependent and nonlinear. For further details, see Chapter 5.

We can roughly attribute the above-stated equivalent RTD parameters to the RTD physical parameters. An increase in the barrier height decreases the current due to the thermionic excitation of the electrons. However, it also decreases the peak current. A decrease in the barrier thickness increases the RTD's current density. An increase in the doping in the contacts also increases the current density. However, it also may disproportionately increase the valley current and thus decrease PVCR. The increase of the well's width decreases the voltage of the peak current density but also increases the valley current because the energy separation between the ground subband and the excited subband with it decreases.

2.3 State-of-the-Art of the RTD oscillators

2.3.1 Standard RTD oscillators

This section briefly describes the RTD oscillators in a (mostly) chronological order. For a more detailed summary of RTDs used for RTD oscillators, see, e.g., [71]. We state here only those RTD oscillators operating on the fundamental harmonic. For a plot of achieved oscillation frequencies and output powers of here presented oscillator, see Fig. 2.4. For a summary of the here-stated parameters, see Tables 2.1 and 2.2 at the end of this section.

We note here a couple of standard design practices in RTDs that we do not explicitly state in the following sections if not necessary. Usually, the RTDs have thin (ones of nm) spacers that separate the barriers from the dopants of the contacts. Additionally, the RTD collector contains a thicker undoped spacer (ones to tens of nm), which lowers the RTD capacitance and increases the ΔU parameter of the RTD. Contact layers usually surround the RTDs with layers that have very high doping levels (ones of 10^{19} cm^{-3}) that lower the serial and contact resistance of the RTDs.

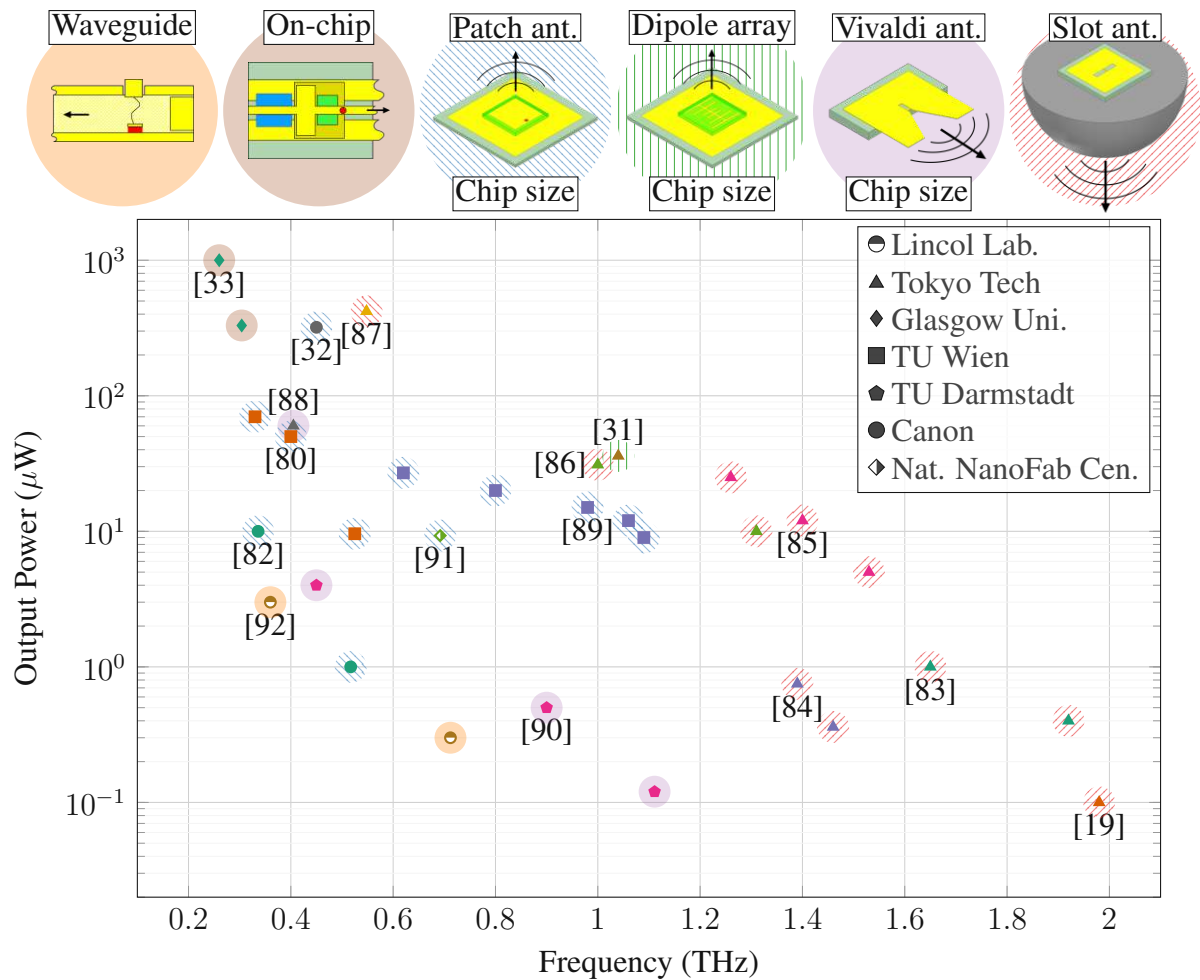


Figure 2.4: Oscillation frequencies and output powers of RTD oscillators operating at the fundamental harmonic. Results for arrays of oscillators are not shown. The variants of the marks correspond to the institutions in which the oscillator was achieved. The colors then group the points to the reference number, which are shown in the square brackets near the marks. The shadings of the points then correspond to the types of oscillators shown above the figure and are described in more detail further in the text.

First RTD oscillator

The first free-running RTD oscillator was constructed by using a coaxial cable 1984, in Lincoln Laboratories, see [93]. The RTD was made out of $\text{GaAs}/\text{Al}_{0.3}\text{Ga}_{0.7}\text{As}$ the quantum well was not doped (as was usual in prior RTDs), both the barrier thickness and the width of the well were 5 nm, and doping of the layers surrounding the barriers was $1 \times 10^{18} \text{ cm}^{-3}$. The samples were processed as follows. The wafer, on which the RTD layers were grown by an MBE, was cleaved into small samples. Then metallic electrode was evaporated and structured, which defined the mesa sizes that were consequently etched. The second contact with the RTD was made on the bottom side of the sample, onto which a metallic electrode was deposited. The diameter of mesas was, on average, $3 \mu\text{m}$ (area of $7 \mu\text{m}^2$). The current density of the RTD was $0.06 \text{ mA}/\mu\text{m}^2$, and the peak-to-valley current ratio (PVCr) was 2.8 (-) at 100 K. The samples were mounted onto a conductor, which terminated the outer conductor of the coaxial line on one of its ends.

The electrical connection to the top metallic layer of the mesas was made by a gold whisker connected to the coaxial cable's inner conductor. The enclosing of the resonant cavity was accomplished by a capacitive stub between the inner and the outer conductor of the coaxial line. The generated waves were leaking through the stub to the coaxial line and were subsequently measured. The biasing of the RTD was also done through the coaxial line, and the biasing circuit was decoupled using a bias tee. The RTD needed to be cooled down to 200 K for the circuit to oscillate (PCVR at 200 K was not stated). The highest obtained frequency at this temperature was 8.2 GHz with the output power of $5 \mu\text{W}$.

Room temperature RTD oscillators

The first free room temperature RTD oscillator was then constructed in 1985, see [68], where the configuration of the resonator was the same as described above. In this work, the RTD was adjusted by lowering the doping level of the layer surrounding the barriers to $5 \times 10^{16} \text{ cm}^{-3}$. This might have decreased the current through the second resonant current in the valley region, as the Fermi level in the emitter decreased, and thus it might have increased the PVCRC, which was maximally 1.5 (-) at room temperature. The peak current density was $0.016 \text{ mA}/\mu\text{m}^2$. The RTD layers were otherwise identical to those in the previous work. However, the quality of the growth might have also played a role. The achieved oscillation frequency was 80 MHz, and the output power was approximately $20 \mu\text{W}$.

In further, we report only the room-temperature RTD oscillators. In the subsequent works, the RTD barriers were grown out of pure AlAs, which shows a larger barrier height, and thus the barriers better suppress the thermionic current. Placing the RTD into a small rectangular waveguide resulted in the oscillation frequency of 200 GHz with the output power of $20 \mu\text{W}$, see [94]. A whisker wire was used to contact the RTD mesas, similarly as in the previous work; however, in this work, the whisker was installed to the cavity directly through a bias tee. The whisker thus served for the RTD biasing and as a probe coupling the RTD into the cavity. A shiftable back-short then tuned the cavity. For the configuration, see Fig. 2.5. The material of the RTD was GaAs/AlAs, with barrier thickness of 1.7 nm, width well width of 4.5 nm, and doping level of $2 \times 10^{17} \text{ cm}^{-3}$, which resulted in peak current density of $0.4 \text{ mA}/\mu\text{m}^2$, and PVCRC of 3.5 (-).

Further thinning the barrier to the width of 1.1 nm led to the RTD having a peak current density of $1.5 \text{ mA}/\mu\text{m}^2$ and PVCRC of 1.5 (-). Using the RTD in the rectangular cavity resulted in the oscillation frequency of 420 GHz with the output power of $0.2 \mu\text{W}$, see [95].

High-frequency waveguide RTD oscillator

The change of the RTD materials made another step towards higher frequencies. Replacing the GaAs layers with InAs and the barrier material AlAs by AlSb resulted in an RTD capable of sustaining oscillations at 712 GHz with the output power of $0.3 \mu\text{W}$, see [92]. Electron mobility is

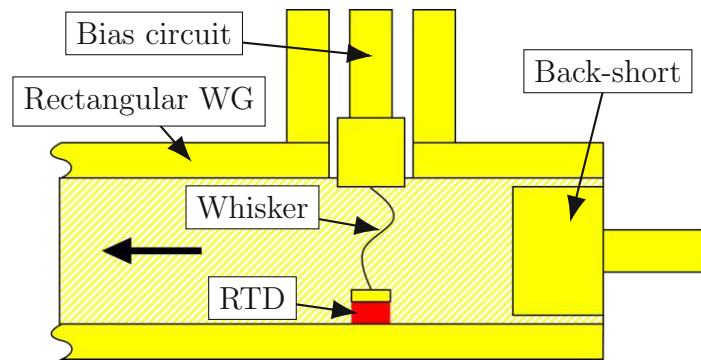


Figure 2.5: A principal sketch of the RTD oscillator with resonator formed by a cavity from a rectangular waveguide. The rectangular waveguide guides the generated waves. The biasing circuit is in the sketch simplified.

in the InAs roughly five times higher than in GaAs, and due to the staggered type band alignment between InAs and AlSb, the transmission coefficient rose in contrast with the GaAs RTD. These materials made the RTD faster which allowed for the high oscillation frequency. For this RTD the barrier thickness was 1.5 nm, the well width 6.4 nm, and the doping was $5 \times 10^{18} \text{ cm}^{-3}$. The peak current density of the RTD was $2.8 \text{ mA}/\mu\text{m}^2$, and the PVCr was 3.4 (-). The oscillator was again built in a rectangular waveguide with a tunable back-short, see Fig. 2.5.

$\text{In}_{0.53}\text{Ga}_{0.47}\text{As}$ and the first monolithic RTD oscillator

Another investigated material used for the RTDs was $\text{In}_{0.53}\text{Ga}_{0.47}\text{As}$ lattice matched to InP substrate, which replaced the GaAs layers, see [96]. The material of barriers was AlAs. These materials are still used in today's state-of-the-art RTD oscillators. The benefits of these materials are the relatively large barrier height of the AlAs for InGaAs (1.2 eV), high electron mobility due to the relatively small band gap (0.74 eV), and large saturation velocity of the electrons. However, the lattice constant of AlAs differs from the lattice constant of $\text{In}_{0.53}\text{Ga}_{0.47}\text{As}$. This creates strain in the AlAs layers, which complicates the growth and limits the barriers' maximal thickness.

A monolithic RTD oscillator that radiated the generated waves into the free space and in which the RTD was made from the materials mentioned above was reported by the University of California [97]. The used RTD in this work had the following parameters; the RTD barrier thickness was 1.4 nm; the well width was 4.1 nm; and the emitter doping was $1 \times 10^{18} \text{ cm}^{-3}$. On the collector side of the RTD, there was a 35 nm long spacer that was directly contacted by a metallic contact, which formed a Schottky contact. The RTD peak current density was $5 \text{ mA}/\mu\text{m}^2$, and the PVCr was 1.7 (-). This oscillator was built using a slot antenna that served as the radiator and resonator. The reported oscillation frequency was 650 GHz, although the output power for this frequency was not measured. For an oscillation frequency of 290 GHz, the output power was $28 \mu\text{W}$. The slot antenna RTD oscillators were operated in an array configuration, where for the highest frequency, an array of 64 devices was used, and for the 290 GHz device,

an array of 16 elements was used. The slot antennas were produced on a sample together with the definitions of the RTDs by micro-manufacturing processes, thus creating a monolithic RTD oscillator. However, because the oscillator's substrate was InP, which has a high dielectric constant, most of the radiated energy went through the substrate. Therefore, the waves were decoupled from the substrate to the free space by a silicon hemispherical lens.

This design also solved low-frequency instability problems of the oscillator that the RTD oscillator with the cavity had. This problem arises because the RTD can form an oscillator together with a parasitic LC created by the biasing circuit. These oscillations are parasitic and ordinary lays in the low-frequency range having the oscillation frequency typically ones of GHz. These oscillations need to be suppressed, which can be done by a shunting resistor that attenuates the parasitic oscillating mode but does not influence the active wanted mode. In this work, the shunt resistors were composed of Schottky diodes grown together with the RTD layers that were fabricated during the micro-manufacturing processes on the slot antennas' ends.

In the forward listed works, we use InGaAs to designate $\text{In}_{0.53}\text{Ga}_{0.47}\text{As}$ lattice matched to InP if not explicitly stated otherwise.

Hemispherical lens

The hemispherical or hyper-hemispherical also lenses prevent the reflection of waves from the bottom side of the InP substrate, as the dielectric constant of the silicon is relatively close to the dielectric constant of the InP. The silicon is nearly transparent to the THz waves. The shape of the lens then prevents refraction and total reflection. However, due to the dielectric constant mismatch of the silicon and the free space, the lens still introduces internal reflection and hence is not entirely transparent for the THz radiation. The Fresnel law can be used to compute the transparency of the lens. For the dielectric constant of the silicon, the transparency is approximately 72 % for the normal direction of the incidence. The hyper-hemispherical lenses can partially collimate the beam of the out-coupled radiation due to intentional refraction on the lenses' surface.

Slot antenna RTD oscillator radiating above the semiconductor substrate

A research group at the Tokyo Institute of Technology (Tokyo Tech) further used and modified the slot antenna RTD oscillator principle. In their particular design, the hemispherical lens was not necessary for operations of the oscillators, see [98], because the waves were radiated above the semiconductor substrate. The RTD materials of the conductive layers and the barrier were InGaAs/AlInAs, respectively. The barrier thickness of the RTDs was 2.3 nm, the well width was 5 nm, and the doping level of the emitter was $1 \times 10^{17} \text{ cm}^{-3}$. The RTDs had a peak current density of $1.4 \text{ mA}/\mu\text{m}^2$ with a PVCR of 2.67 (-). In the presented topology of the oscillator, a secondary radiator (another slot antenna) was coupled to the RTD oscillator with the slot. The secondary radiator was primarily radiating to the free space above the substrate without the

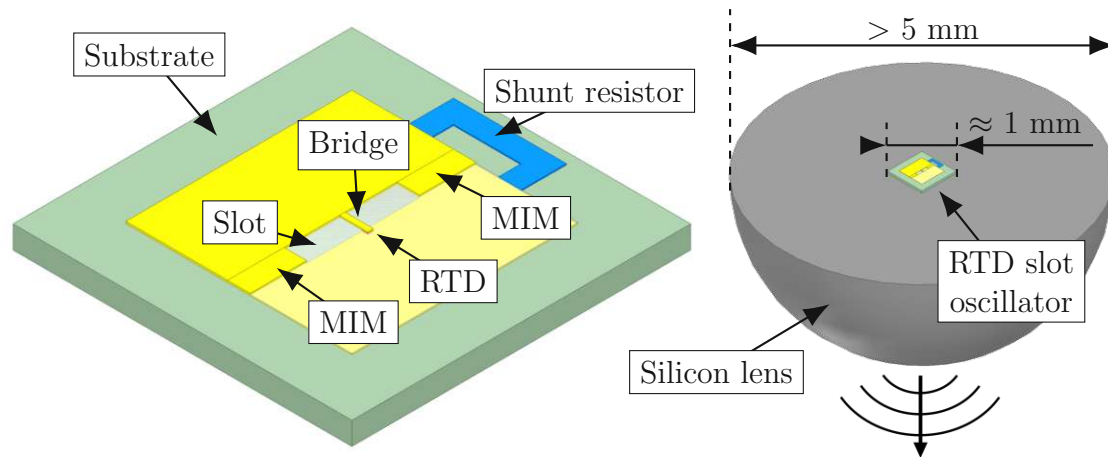


Figure 2.6: Principal sketch of the RTD oscillators with slot antennas. The oscillator requires the usage of the hemispherical silicon lens. The sketch on the right-hand side shows the oscillator on a scale with the lens.

necessity of the silicon lens. The achieved oscillation frequency was 254 GHz. However, the output power was not measured.

In this work, the shunting of the RTD for the parasitic oscillations was done by an ex-post fabricated shunting resistor from a conductive material (Bismut) that was in parallel with the slot. Variants of this type of stabilization are common in the state-of-the-art RTD oscillator. However, it greatly reduces the oscillators' wall-plug efficiency, and thus DC decoupling of the shunt is being used, as will be described in further sections

Tapered slot RTD oscillator

The RTD oscillators with slot antennas were further advanced. In one of the further works, see [88], the researchers from Tokyo Tech used only one slot as both the antenna and the resonator. However, they opened one side of the slot by tapering it, which caused the slot to emit radiation in the horizontal direction along the tapering, similarly as would a Vivaldi antenna radiate. This allowed to not to use of the silicon lens. See Fig. 2.8 for a sketch of a similar design. The tapered slot rested on a structured semiconductor substrate. The RTD was made from InGaAs/AlAs, and the AlAs barriers had a thickness of 1.2 nm. The QW well had a thickness of 4.5 nm. The doping level of the barriers surrounding layers was $1 \times 10^{18} \text{ cm}^{-3}$. The current density of the RTD was $7 \text{ mA}/\mu\text{m}^2$, and the PVCR was 1.9 (-). The output power of $60 \mu\text{W}$ at the oscillation frequency of 405 GHz was reported in this work.

The first THz RTD oscillator

An RTD oscillator working at the fundamental harmonic with oscillating frequency over 1 THz, was constructed by Tokyo Tech, see [99]. The output power was $7 \mu\text{W}$. In this case, a simple slot antenna was used, acting both as the resonator and radiator.

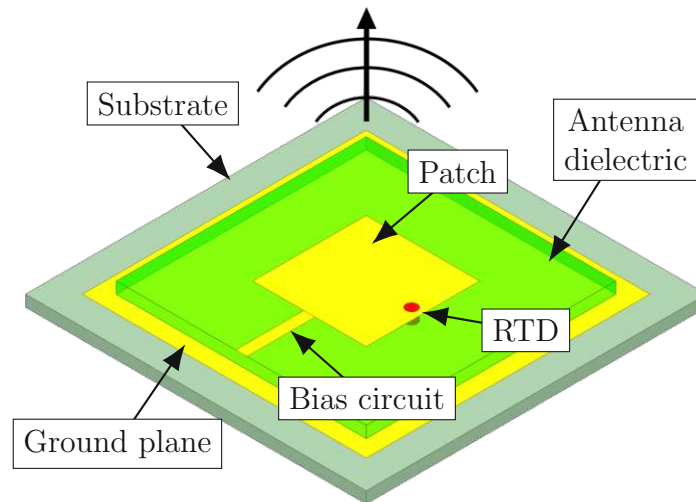


Figure 2.7: Principal sketch of the RTD oscillator with a directly connected patch antenna. We do not display here the details of the biasing circuit.

The slot incorporates two electrodes connected through an RTD by an air bridge in the center of the slot's longer side. On the far edges of the slot, the electrodes are shorted for the AC oscillations and decoupled for DC bias voltage by a metal insulator metal (MIM) capacitor. Due to its simplicity, this topology turned out to be convenient for RTD oscillator development, although it still requires the silicon lens. For further details about the design, consult [100].

In the work that reached 1 THz, InGaAs/AlAs RTDs were used with a barrier thickness of 1.2 nm. The RTD well with a thickness of 4.5 nm was made indium-rich $\text{In}_{0.7}\text{Ga}_{0.3}\text{As}$, which decreases the peak voltage due to its low band gap. The doping level of the emitter was $3 \times 10^{18} \text{ cm}^{-3}$. The emitter was additionally graded in this work, with three InGaAs layers differing in the indium content situated in the emitter next to the barrier. The graded emitter further lowers the peak voltage. This was necessary because RTDs with high peak current densities, which was, in this case, $24 \text{ mA}/\mu\text{m}^2$, might suffer from thermal overheating, and thus, it is necessary to decrease both their area and the operating bias voltage. The PVCR of the RTD was 2.2 (-).

Patch antenna RTD oscillator

Another concept of the RTD oscillator developed by Canon was the usage of a patch antenna as the resonator/radiator, see [82] and the sketch in Fig. 2.7. In this case, an RTD is directly connected between the patch electrode and a ground plane. The oscillator radiates above the substrate, releasing us from using the silicon lens. In this work, a triple barrier diode was used. For the details about the RTD layers, see the reference. The peak of the RTD current density was $2.8 \text{ mA}/\mu\text{m}^2$, and its PVCR was 3 (-). The design achieved a maximum oscillation frequency of 517 GHz with an output power of $1 \mu\text{W}$.

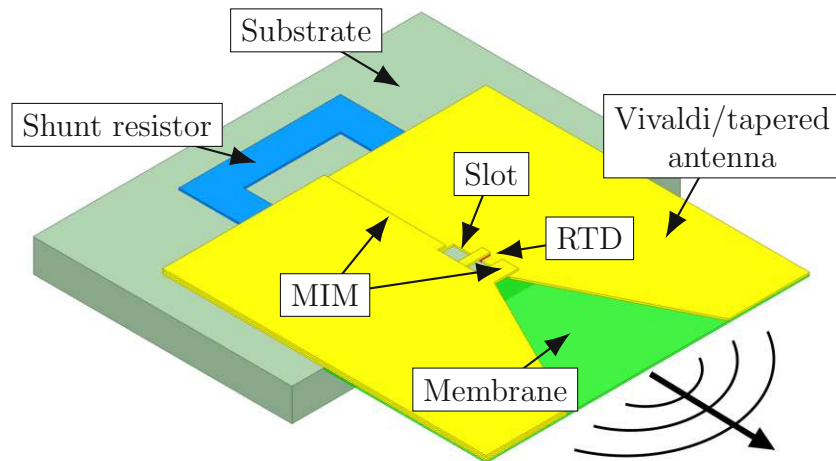


Figure 2.8: Principal sketch of an RTD oscillator with a Vivaldi/tapered antenna as the radiator. The resonator of the RTD is predominantly composed of a slot antenna. The sketch shows the Vivaldi antenna resting on a silicon membrane. In the tapered slot case, the antenna resides on a structured semiconductor substrate instead of on a membrane.

Vivaldi antenna RTD oscillator operating at 1.1 THz

RTD oscillator operating on 1.1 THz was thereafter reported by the University of Darmstadt, where the slot was used as the resonator, and a Vivaldi antenna as the radiator, see [90]. A silicon membrane was used to support the antenna. The resonator and radiator were coupled by leakage through the MIM. For a simplified sketch of the design, see 2.8. The oscillator does not require the use of a silicon lens. The RTD was made of InGaAs/AlAs with a barrier thickness of 1.2 nm. The QW was a composite, where an InAs mini-well with the thickness of 1.2 nm was sandwiched by two $\text{In}_{0.53}\text{Ga}_{0.47}\text{As}$ layers both with the thickness of 1.2 nm. Such a designed QW lowers the energy of the ground subband because it has the maximum of the corresponding wave function in the center of the well, where the InAs layer lowers the potential profile. At the same time, the first excited state is barely influenced because it has the node at the center of the QW well. This increases the separation of the ground and the first excited state, which leads to a decrease in the valley current due to the conduction through the second resonant state. Adjusting the partial thicknesses of the composite QW adds an additional degree of freedom to the RTD design. The adjacent layers to the barriers of the used RTD had doping level $1.5 \times 10^{18} \text{ cm}^{-3}$. The RTD had a peak current density of $14 \text{ mA}/\mu\text{m}^2$, and the PVC was 3.5 (-). The oscillator's output power at the highest achieved oscillation frequency was $0.1 \mu\text{W}$. To lower the contact resistance of the RTD, a highly doped cap layer facing the top contact was implemented.

Thinning the RTD barriers for higher oscillation frequencies

The magnitude of RTDs' NDC can be increased by thinning the barriers. Using the simple slot antenna and thinning the barriers down to 1 nm led to the oscillation frequency of 1.31 THz with the output power of $10 \mu\text{W}$, see [86]. The RTD was composed of InGaAs/AlAs, with

indium-enriched QW $\text{In}_{0.7}\text{Ga}_{0.3}\text{As}$ having a thickness of 3.9 nm. The emitter was graded in three steps, with layers containing varying indium content. The peak current density of the RTD and the PVCR was not stated. However, the current difference between the peak and the valley was $8.5 \text{ mA}/\mu\text{m}^2$.

High-power slot antenna RTD oscillator

High-power RTD oscillators with the output power of $420 \mu\text{W}$ using an asymmetric slot antenna oscillating at 548 GHz were reported by Tokyo Tech, see [87]. The same type of RTD as in the above-described work was used. However, this time the peak current was only $12 \text{ mA}/\mu\text{m}^2$ (the exact layer structure is not stated in this work). The high output power was achieved by the increase of radiation conductance of the slot, which was accomplished by shifting the bridge closer to one of the MIM capacitors, making the slot asymmetrical. The short side of the slot acted inductively, which is necessary to fulfill the oscillation conditions (see Chapter 3), while the prolonged side increased the radiation conductance. The oscillators were combined into an array of oscillators resulting in the output power of $610 \mu\text{W}$ at 620 GHz. The DC-to-RF efficiency of the oscillator, without the shunting resistor, was 1.45 %.

Decrease of the RTD capacitance and increase the high-frequency performance

Increasing the collector spacer thickness of RTDs can decrease the RTD capacitance and thus reduce the RTD RC time constant. The spacer optimization was performed in [101]. In this work, the simple slot antenna was used, and InGaAs/AlAs RTDs with a spacer length of 12 nm. The reduction of the RTD capacitance led to oscillations at the frequency of 1.42 THz with the output power of $1 \mu\text{W}$. The peak current density of the RTD was $19 \text{ mA}/\mu\text{m}^2$, and PVCR was 1.9 (-). The emitter of the RTD was enriched with aluminum in ratios of $\text{In}_{0.53}\text{Al}_{0.1}\text{Ga}_{0.37}\text{As}$, which has a larger band gap than $\text{In}_{0.53}\text{Ga}_{0.37}\text{As}$ (of $\approx 0.1 \text{ eV}$). This results in a similar effect as the graded emitter described above, i.e. decreasing the peak voltage, which was, in this case, 0.4 V.

In contrast to the effect described in the previous paragraph, by reducing the collector spacer thickness of the RTD, one can increase RTD's high-frequency magnitude of the NDC, see [102]–[105]. We have dedicated Section 2.4.2 and Chapter 5 for the details about this effect. RTDs with the reduced collector spacer to 6 nm used in simple slot antenna oscillators were able to sustain oscillations at a frequency of 1.46 THz with the output power of $0.36 \mu\text{W}$, see [84]. Additionally, output powers of $\approx 10 \mu\text{W}$ in the sub-THz range were achieved by varying the RTD area. These RTDs were made of InGaAs/AlAs with 0.9 nm thick barriers. The QW was made from indium rich $\text{In}_{0.9}\text{Ga}_{0.1}\text{As}$, and had width of 3 nm. The material of the emitter contained additional aluminum content in the ratios of $\text{In}_{0.53}\text{Al}_{0.1}\text{Ga}_{0.37}\text{As}$. The doping level of both the emitter and collector was $3 \times 10^{18} \text{ cm}^{-3}$. This resulted in the RTD having a peak current density of $24 \text{ mA}/\mu\text{m}^2$ and a PVCR of 1.8 (-). The voltage of the peak current was 0.27 V.

These results show a counter-intuitive effect for the collector spacer. Prolonging/shortening the spacer lowers/raises the capacitance but also lowers/raises the high-frequency magnitude of the NDC. Additionally, prolonging the spacer can lower the time constant of the RTD given by the electron transit time in the spacer, see [106]. From these results, it seems that the exact RTD type should be adjusted to the (optimized with) radiator/resonator and the values of the parasitics.

Slot antenna optimization

Using the RTD with the 12 nm long spacer, the oscillation frequency was increased by slot antenna optimization. In [107], the slot antenna was shortened to 16 μm (in contrast with the previous length of 20 μm), which resulted in the oscillation frequency of 1.55 THz with the output power of 15 μW . The RTD equivalent parameters are not known for this work.

In the next work of Tokyo Tech, see [85], a lossy conductive InGaAs layer underneath the bridge connecting the RTD was etched out, and the bridge width was increased. This reduced the loss of the slot, which made the oscillator capable of oscillating at 1.92 THz with the output power of 0.4 μW . The antenna length was reduced to 12 μm . The same RTD was used as in the previous work with the optimized RTD capacitance. In this work, the RTD peak current was 50 $\text{mA}/\mu\text{m}^2$, and the PVCR was 1.7 (-).

Eventually, a 1.98 THz RTD oscillator was constructed in [30]. The metal forming the slot antenna was thickened from ≈ 100 nm to 2 μm . The antenna length was further reduced to 9 μm . The same RTD was used as described above, except that the barriers were thinned to 0.9 nm. The RTD peak current density was 31 $\text{mA}/\mu\text{m}^2$, and the PVCR was 1.81 (-). In this work, the output power was not reported. However, it was indirectly reported in [19] to have the output power of 0.1 μW . The reported spectrum of the oscillator's spectral line shows by its width that the oscillator was barely oscillating.

On-Chip RTD oscillator

At the University of Glasgow, a high-power on-chip oscillator with the output power of 1 mW at the oscillation frequency of 260 GHz was constructed, see [33]. The oscillator was not emitting into the free space, but the generated waves were transmitted along a coplanar waveguide (CPW). The resonator was composed of a terminated stub of a CPW or a microstrip line, see Fig. 2.9. The used RTDs were of the InGaAs/AlAs type, with a barrier width of 1.4 nm and with a relatively low doping level of $2 \times 10^{16} \text{ cm}^{-3}$ in 25 nm long layers sandwiching the barriers. These layers are further contacted by layers with a doping level of $2 \times 10^{18} \text{ cm}^{-3}$. The peak current density was 3 $\text{mA}/\mu\text{m}^2$, and the PVCR was 3 (-). The efficiency of the oscillator without the shunting resistor was 2.5 %.

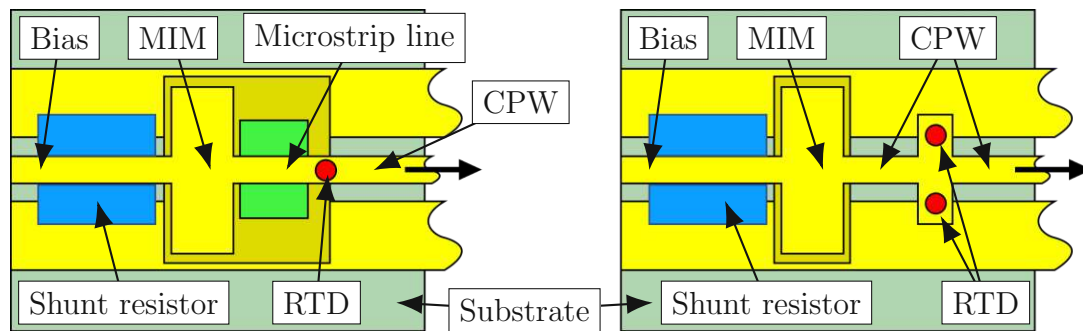


Figure 2.9: Top views of the high-power on-chip oscillators' principal sketches. The sketch on the left-hand side shows an RTD oscillator with a microstrip line resonator. The sketch on the right-hand side shows an RTD oscillator with a CPW resonator. The oscillator with the CPW resonator operates with two symmetrically connected RTDs. The parts of the transmission lines forming the resonators are terminated by a MIM capacitor representing a short AC signal. The produced oscillators are, in both cases, guided by CPWs to a detector.

2.3.2 Chip-sized RTD oscillators

For practical applications, the usage of oscillators that require the silicon lens can be problematic due to their final dimensions. The side length size of monolithic RTD oscillators is without the silicon lens in a scale of hundreds of μm . However, the silicon lens raises the final dimension to $\approx 5\text{ mm}$. This also adds to the costs of the RTD oscillators.

Paradoxically, most of the RTD oscillators already contain an antenna, and thus the need for the use of the silicon lens is just a parasitic property of the slot antenna. Therefore, designing RTD oscillators that do not require the lens is advantageous.

The above summary already described oscillators with the Vivaldi antenna that radiates horizontally along the InP substrate and does thus not require the lens. Also, a patch antenna RTD oscillator was presented that radiates the waves upwards from the substrate. This happens for the patch because the substrate is covered by a metallic ground plane which decouples it from the oscillator.

Secondary radiator

An alternative approach to radiate the waves in the upward direction from the substrate is to use an additional radiator coupled to the slot antenna RTD oscillator. In this case, the slot antenna act mainly as the resonator, and the secondary antenna as the radiator.

This principle was employed in [107], where the slot was inductively coupled to an above-laying patch antenna. The patch antenna was lying on a BCB polymer. See the sketch in Fig. 2.10, where a similar design concept is shown, with a Yagi-Uda antenna instead of the patch. The oscillator operated at 1 THz with the output power of $15\ \mu\text{W}$. Three oscillators were used in an array, which resulted in the output power of $55\ \mu\text{W}$. However, as the patch antenna is a resonant antenna, the resonance of the patch antenna and the oscillating frequency of the slot need to be matched. This requires a very high control of the system parameters, thus making this system

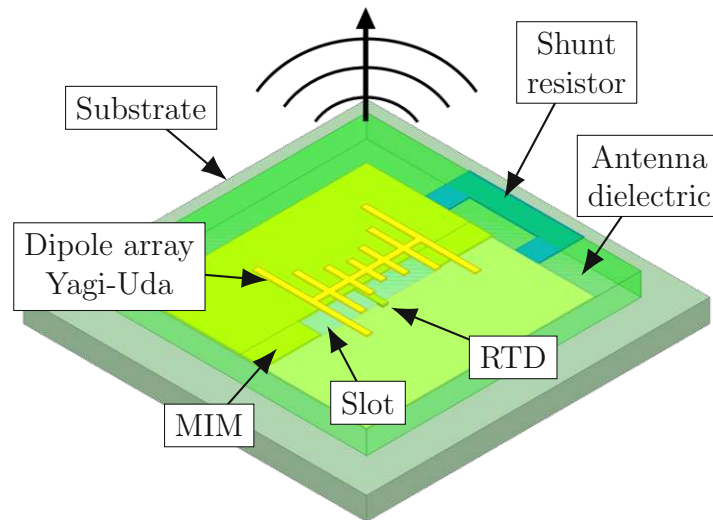


Figure 2.10: Sketch of the chip-size RTD oscillator with a secondary antenna. The oscillators use a slot antenna as a resonator and a dipole array (Yagi-Uda) as the secondary radiator, which radiates the generated oscillations.

difficult to fabricate reliably. The used RTD was InGaAs/AlAs type with the peak current density of $15 \text{ mA}/\mu\text{m}^2$ and with PVCR of 2 (-).

This problem was addressed in [31], where an array of dipole antennas with varying lengths was used instead of the patch. The various length of the dipoles made the radiator broadband. See the sketch of the design in Fig. 2.10. This topology is similar to Yagi-Uda antennas. This design achieved the output power of $21 \mu\text{W}$ at the oscillation frequency of 1.04 THz. The DC-to-RF efficiency of the oscillator was 0.4 %. Instead of the BCB polymer, the COC polymer was used for the dipole array, which was reported to have lower losses. Further employing of this oscillator into an array of 83 locked oscillators resulted in an output power of 0.73 mW.

Another inquisitive approach was to conduct the waves produced by the oscillating slot antenna into guided waves trapped in a waveguide made from the InP substrate, see [108]. The substrate's front and back sides were metalized, creating the radial waveguide in which the waves could have propagated. An array of secondary slot antennas subsequently radiated the guided waves. The slots of this array were fabricated together with the metalization of the front side. This oscillator generated circularly polarized electromagnetic waves and was used to demonstrate a communication link with a data transmission speed of 1 Gbps. The oscillation frequency of this design was 507 GHz, with an output power of $40 \mu\text{W}$. The RTD was InGaAs/AlAs type, with a 0.9 nm barrier. The properties of the RTD were not stated in the report.

Instead of the slot as the resonator, a CPW can be used as was shown in [91]. The radiator was, in that case, a patch antenna that radiated above the substrate and was coupled to the resonator by a microstrip line. The achieved oscillation frequency, in this case, was 692 GHz, and the output power was $9.3 \mu\text{W}$. The RTD was InGaAs/AlAs type, with a barrier thickness of 1.2 nm, and the well was a composite sandwich of InGaAs/InAs/InGaAs with partial thicknesses of 1.1 nm. This design also used DC decoupling of the shunt resistor by a serial capacitance with

the shunt. This increases the total DC-to-RF efficiency, see [56], however, the RTD is still only conditional stable, and the bias source needs not support very low-frequency oscillations.

To increase the output power of the oscillators with the secondary antennas, one can replace the primary slot antenna with a structure that allows one to use a large area of the RTD. Such a structure can be a two-dimensional rectangular cavity with the RTD situated in the middle, forming a double-barrel-like geometry. The cavity is theoretically scaleable in the third dimension together with the RTD area, without much influence on the oscillation frequency. A large RTD area can increase the output power, as we will show in Chap. 3. Nowadays, this concept is underneath intensive research promising close to an mW output power of a single oscillator at 1 THz, see e.g. [109]. The antenna then takes various forms of the shape and of the coupling methods to the resonator, see e.g. [110].

Double-resonant-tunneling-diode patch-antenna

The fabrication of the chip-size RTD oscillators is dramatically simplified if the secondary radiator can be omitted. The patch antenna RTD oscillators in which the RTD is directly connected to the patch are examples of such simple devices. This design was described in the subsection: Patch antenna RTD oscillator, and in Ref. [82]. However, this configuration has a conceptual problem because the bias circuit and the oscillator are strongly coupled. This results in parasitic oscillations, which can lead to unpredictable behavior of the oscillator and to the possibility of misinterpreting the results.

The problem of parasitic oscillation with the biasing line can be solved by including an additional RTD to the oscillator, thus a Double-RTD oscillator, which mirrors the first RTD. This induces a symmetry in the structure that allows the bias line to be completely decoupled.

The double-RTD principle was reported in [80], where the oscillators could cover the sub-THz up to 525 GHz, with output power ranging from 70 to 10 μ W, and in [89], where oscillators operating above 1 THz, were reported. This thesis partially deals with these designs; thus, for details, see Chapter 4.

Building on this principle, Canon optimized such oscillator, see [32], by impedance matching of the patch antenna to the RTD. The impedance matching was done by shifting the double-RTD pair from the edges of the patch closer to its center, which is a very similar concept that was shown in [87]. The oscillation frequency of the oscillator was 450 GHz, and the output was 320 μ W. An exceptional result was achieved, using the Double-RTD principle, when 36 devices were used in a locked array of oscillators. The output power of the array was over 10 mW. The RTD used in this work is poorly documented, and thus the work might be hard to reproduce by the scientific community. This work also used the AC decoupling of the shunt resistor, which increased its wall-plug efficiency.

Traveling-wave oscillator

Recently, an RTD oscillator working in Laser like mode was predicted in [111], [112] and experimentally observed in [113]. In this configuration, the RTD is in the form of a long microstrip line that is on one side terminated by an open circuit and on the other side coupled to an antenna. The RTD stripe, together with its terminators, behaves as a resonator, and due to the gain of the RTD, the system can oscillate. Various types of antennas can be connected to the traveling-wave oscillator, and thus it allows to build of chip-size oscillators. A possible benefit of this configuration can, for example, be a high tunable frequency range of the oscillators.

2.3.3 Design considerations for the RTD oscillators

From the above-listed brief history of the RTD oscillators, we can conclude for the RTDs the followings:

- For the RTDs, the InGaAs and AlAs are well-established materials.
- To achieve high frequencies, one needs to:
 - Increase the ratio $\Delta I/\Delta U$, i.e., the magnitude of the NDC, which can be done by thinning the barriers, optimizing the emitter's doping level, and optimizing the composition of the well and its thickness.
 - Lower the parasitic time constants of the RTD. This can be done by thinning the barrier (increasing the magnitude of the NDC) and increasing/decrease of the collector spacer, which lowers the capacitance/increases the high-frequency NDC (see the discussion about this effect above in the corresponding subsection). Moreover, by increasing the quality of the RTD contacts, i.e., lowering the contact resistance.
- To achieve high output power, one needs:
 - Increase ΔU , ΔI , and reduce the thermal heating of the RTD by lowering the peak voltage. The thermal stability of RTDs can also be improved by an introduction of a material with a higher thermal conductivity than the InGaAs has, close to the actual RTD layers, see [114].
 - Decrease the time constants (as discussed in the point dealing with high-frequencies) if high powers at high frequencies are required.
- For the high efficiency of the oscillators, the peak voltage needs to be reduced, which is influenced by the emitter and the well design.

For the resonators/radiators, we can conclude that:

- High oscillation frequencies can be achieved with the slot antennas.

| | | | | | | |
|--|--|--|--|-------------|----------------|--|
| Ref. | [93]* | [68] | [94] | [95] | [92] | [97] |
| Year | 1984 | 1985 | 1988 | 1989 | 1991 | 1997 |
| Freq. (GHz) | 8.2 | 0.08 | 200 | 420 | 712 | 650 |
| Power (μ W) | 5 | 20 | 20 | 0.2 | 0.3 | - |
| Cond. Mat. | GaAs | GaAs | GaAs | GaAs | InAs | InGaAs |
| Barr. T. (nm) | 5 | 5 | 1.7 | 1.1 | 1.5 | 1.4 |
| Well W. (nm) | 5 | 5 | 4.5 | 4.5 | 6.4 | 4.1 |
| Barr. Mat. | Al _{0.3} Ga _{0.7} As | Al _{0.3} Ga _{0.7} As | AlAs | AlAs | AlSb | AlAs |
| Well Mat. | GaAs | GaAs | GaAs | GaAs | InAs | InGaAs |
| Dop. (10^{18} cm ⁻³) | 1 | 0.05 | 0.2 | 2 | 5 | 1 |
| Emi. Spac. (nm) | - | - | - | - | - | 5 |
| Col. Spac. (nm) | - | - | - | - | - | 35 |
| j_p (mA/ μ m ²) | 0.06 | 0.016 | 0.4 | 1.5 | 2.8 | 5 |
| PVCR (-) | 2.8 | 1.5 | 3.5 | 1.5 | 3.4 | 1.7 |
| ΔU (V) | 0.1 | 0.05 | 0.7 | 0.3 | 0.3 | - |
| ΔI (mA/ μ m ²) | 0.039 | 0.005 | 0.286 | 0.500 | 1.976 | 2.059 |
| Peak U (V) | 0.31 | 0.6 | 0.75 | 0.6 | 1.5 | 0.95 |
| Type | Coax. | Coax. | WG cavi. | WG cavi. | WG cavi. | Slot |
| Emitter | - | - | - | GD | - | - |
| Remark | - | - | - | - | - | FS, SL, A |
| DC-RF Eff. (%) | 2.4 | - | - | 0.001 | 0.005 | - |
| Inst. | Lin. Lab. | Lin. Lab. | Lin. Lab. | Lin. Lab. | Lin. Lab. | Uni. Cal. |
| Ref. | [98] | [88] | [99] | [82] | [90] | [87] |
| Year | 2004 | 2009 | 2010 | 2010 | 2011 | 2012 |
| Freq. (THz) | 0.25 | 0.4 | 1.04 | 517 | 1.1 | 0.55 |
| Power (μ W) | - | 60 | 7 | 1 | 0.1 | 420 |
| Cond. Mat. | InGaAs | InGaAs | InGaAs | InGaAs | InGaAs | InGaAs |
| Barr. T. (nm) | 2.3 | 1.2 | 1.2 | 1.3/2.6 | 1.2 | 1.2 |
| Well W. (nm) | 5 | 4.5 | 4.5 | 7.6/5.6 | 3 \times 1.2 | 4.5 |
| Barr. Mat. | AlInAs | AlAs | AlAs | AlAs+InAlAs | AlAs | AlAs |
| Well Mat. | InGaAs | InGaAs | In _{0.7} Ga _{0.3} As | InGaAs | InGaAs/InAs | In _{0.7} Ga _{0.3} As |
| Dop. (10^{18} cm ⁻³) | 0.1 | 1 | 3 | 2 | 1.5 | 3 |
| Emi. Spac. (nm) | 2.6 | 5 | - | 5 | 1 | - |
| Col. Spac. (nm) | 2.6 | 5 | 25 | 5 | 1 | 25 |
| j_p (mA/ μ m ²) | 1.4 | 7 | 24 | 2.8 | 14 | 12 |
| PVCR (-) | 2.7 | 1.9 | 2.2 | 3 | 3.5 | 2 |
| ΔU (V) | 0.4 | 0.26 | 0.35 | 0.3 | 0.5 | 0.26 |
| ΔI (mA/ μ m ²) | 0.88 | 3.68 | 13.09 | 1.87 | 10 | 6 |
| Peak U (V) | 0.7 | - | 0.8 | 0.65 | 0.65 | - |
| Type | Slot+Slot | Slot + Vival. | Slot | Patch | Slot + Vival. | Asym. Slot |
| Emitter | - | - | In-Graded | - | - | In-Graded |
| Remark | FS | FS, Cap | FS, SL, Cap | FS | FS | FS, SL |
| DC-RF Eff. (%) | - | - | 0.1 | 0.02 | 0.004 | 1.45 |
| Inst. | Tok. Tech | Tok. Tech | Tok. Tech | Canon | Uni. Darm. | Tok. Tech |

Table 2.1: The first part of the RTD oscillators summary. Used abbreviations: * marks a not room temperature device, GD marks a graded doping in the emitter, FS marks an oscillator emitting into the free space, Cap marks an optimized layer for lowering of the contact resistance, SL marks the necessity of the silicon lens, and InGaAs corresponds to the lattice matched layers to the InP.

2. RESONANT-TUNNELING-DIODE OSCILLATORS

| | | | | | | |
|--|--|--|--|--|------------|--|
| Ref. | [86] | [101] | [84] | [85] | [107] | [83] |
| Year | 2012 | 2014 | 2014 | 2014 | 2015 | 2016 |
| Freq. (THz) | 1.31 | 1.42 | 1.46 | 1.55 | 1 | 1.92 |
| Power (μW) | 10 | 1 | 0.36 | 0.4 | 15 | 0.4 |
| Cond. Mat. | InGaAs | InGaAs | InGaAs | InGaAs | InGaAs | InGaAs |
| Barr. T. (nm) | 1 | 1 | 0.9 | 1 | - | 1 |
| Well W. (nm) | 3.9 | 3 | 3 | 3 | - | 2.5 |
| Barr. Mat. | AlAs | AlAs | AlAs | AlAs | AlAs | AlAs |
| Well Mat. | In _{0.8} Ga _{0.2} As | In _{0.9} Ga _{0.1} As | In _{0.9} Ga _{0.1} As | In _{0.9} Ga _{0.1} As | - | In _{0.9} Ga _{0.1} As |
| Dop. (10^{18} cm^{-3}) | 3 | 3 | 3 | 3 | - | 3 |
| Emi. Spac. (nm) | 2 | 2 | 2 | 2 | - | 2 |
| Col. Spac. (nm) | 25 | 12 | 6 | 12 | - | 12 |
| j_p ($\text{mA}/\mu\text{m}^2$) | - | 19 | 24 | - | 35 | 50 |
| PVCR (-) | - | 1.9 | 1.8 | - | 2 | 1.7 |
| ΔU (V) | 0.23 | 0.35 | 0.28 | - | - | 0.4 |
| ΔI ($\text{mA}/\mu\text{m}^2$) | 8.5 | 9 | 10.7 | - | 17.5 | 20.6 |
| Peak U (V) | - | 0.4 | 0.12 | - | - | 0.4 |
| Type | Slot | Slot | Slot | Slot | Slot+Patch | Slot |
| Emitter | In-Graded | 10% Al | 10% Al | 10% Al | - | 18% Al |
| Remark | FS, SL, Cap | FS, SL, Cap | FS, SL | FS, SL, Cap | FS | FS, SL, Cap |
| DC-RF Eff. (%) | - | 0.06 | 0.05 | - | - | 0.03 |
| Inst. | Tok. Tech | Tok. Tech | Tok. Tech | Tok. Tech | Tok. Tech | Tok. Tech |

| | | | | | | |
|--|--|--|--------------------------|--------------|----------------|---------------|
| Ref. | [30] | [31] | [33] | [91] | [89] | [32] |
| Year | 2017 | 2019 | 2019 | 2021 | 2022 | 2022 |
| Freq. (THz) | 1.98 | 1.04 | 0.26 | 0.69 | 1.09 | 0.45 |
| Power (μW) | - | 21 | 1000 | 9.3 | 9 | 320 |
| Cond. Mat. | InGaAs | InGaAs | InGaAs | InGaAs | InGaAs | InGaAs |
| Barr. T. (nm) | 0.9 | 1 | 1.4 | 1.2 | 1 | - |
| Well W. (nm) | 2.5 | 2.5 | 4.5 | 3×1 | 3×1.1 | - |
| Barr. Mat. | AlAs | AlAs | AlAs | AlAs | AlAs | InAlAs |
| Well Mat. | In _{0.9} Ga _{0.1} As | In _{0.9} Ga _{0.1} As | InGaAs | InGaAs/InAs | InGaAs/InAs | - |
| Dop. (10^{18} cm^{-3}) | 3 | 3 | $0.02^{25} \text{ nm}/2$ | - | 3 | - |
| Emi. Spac. (nm) | 2 | 2 | $1.5+25$ | 1 | 1.2 | - |
| Col. Spac. (nm) | 12 | 12 | $1.5+25$ | 1 | 12 | - |
| j_p ($\text{mA}/\mu\text{m}^2$) | 31 | 30 | 3 | 6.6 | 23.6 | - |
| PVCR (-) | 1.81 | 2 | 3 | 1.3 | 3.7 | 2.5 |
| ΔU (V) | 0.51 | 0.35 | 0.7 | 0.3 | 0.33 | 0.55 |
| ΔI ($\text{mA}/\mu\text{m}^2$) | 13.9 | 15 | 2 | 1.5 | 17.2 | 14 |
| Peak U (V) | - | 0.5 | 1 | 0.65 | 0.5 | 0.55 |
| Type | Slot | Slot+Yagi-Uda | CPW/MS | CPW+Patch | Patch | Patch |
| Emitter | 18% Al | 18% Al | - | - | 10% Al | - |
| Remark | FS, SL, Cap | FS, Cap | On-Chip, GD | FS, NS | FS, 2-RTD, Cap | FS, 2-RTD, NS |
| DC-RF Eff. (%) | - | 0.4 | 2.5 | 0.27 | 0.25 | 1 |
| Inst. | Tok. Tech | Tok. Tech | Uni. Glas. | NNFC | TU Wien | Canon |

Table 2.2: The second part of the RTD oscillators summary. Used abbreviations: GD marks graded doping in the emitter, FS marks an oscillator emitting into the free space, Cap marks an optimized layer for lowering of the contact resistance, SL marks the necessity of the silicon lens, InGaAs corresponds to the lattice matched layers to the InP, NS marks the DC decoupling of the shunt resistor, CPW marks the coplanar waveguide, MS marks the microstrip line, and 2-RTD marks use of two RTDs in one oscillator.

- For high-frequency oscillators, one needs to decrease the losses of the resonator/radiator.
- For high-power and high-efficiency single oscillators, one needs:
 - Add an additional degree of freedom for the control of the resonator/radiator parameters for the impedance matching.
 - Increase the radiation conductance of the radiator, for details see Chapter 3. This is ordinarily accomplished by an increase in the radiator’s electrical dimensions.
 - Lower the parasitic losses of the resonator/radiator.
- High power of the devices can then be increased by employing multiple oscillators in a locked array.

2.4 Frequency limitation of RTD oscillators

In this section, we investigate the fundamental mechanism limiting the highest oscillation frequency of RTD oscillators. We can distinguish three different contributions to the frequency limitation:

- Influence of the contact’s parasitics
- RTD dynamics
- Resonator losses and dispersion

Due to the nature of the RTD oscillators, these effects are coupled, and therefore separate investigating of the contributions gives prediction only for the cases where the given parameter dominates. All of these contributions are application-specific and depend on the oscillator’s parameters, such as the used RTD, resonator, and materials. However, similarly to transistor oscillators, we can determine the maximum frequency of an RTD, on which it cannot satisfy the oscillation conditions (derived in the next chapter) anymore, thus leaving the resonator type out of the discussion.

For further discussions about the resonator influence in the high-frequency oscillators, see, e.g., [30], [115], [116].

2.4.1 Contact parasitics

The RTD is connected to the oscillator’s circuit through semiconductor-metal contacts. Figure (2.11) schematically shows a cross-section of the physical layers of contacted RTD in a standard topology and the corresponding small-signal equivalent circuit. The inner RTD layers are connected to the circuit through semiconductor layers, which are then contacted with deposited metallic layers. The semiconductor-metal interface induces contact resistance. In

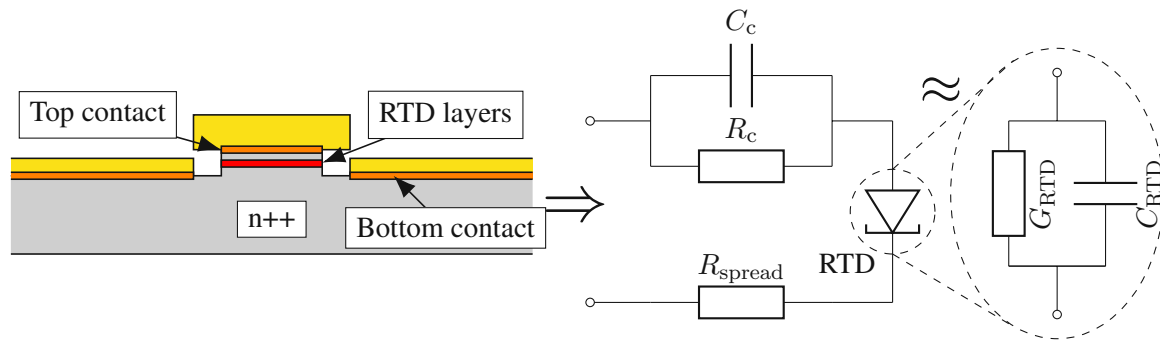


Figure 2.11: Cross-section of the physical RTD connection to the circuit and the corresponding small-signal equivalent circuit.

the depicted schematic, the contact resistance of the top contact is denoted as R_c . Because the current is homogeneous along the top contact, the contact resistance of the top contact is inversely proportional to the contact area. A charge accumulation can be induced on the contacts' interfaces. This results in contact capacitance C_c that is in parallel with the contact resistance and is also proportional to the contact area.

The current that flows through the top contact and the RTD then spreads underneath the RTD in the $n++$ layer (heavily doped semiconductor) and to the metallic bottom contact. In this case, the current does not flow homogeneously through the bottom contact, and thus the dependence of the bottom equivalent contact resistance on the RTD area is more complex than at the top contact case. The resistance due to the spread of the current and the distributed bottom contact resistance is represented in the equivalent circuit by R_{spread} . The contact capacitance of the bottom contact is also present. However, for the simplicity of the circuit, it was omitted from the schematic. If needed, we can transform the resistance R_{spread} to an impedance and include the capacitance as such. Physically, there also exists a parasitic inductance for the current paths. However, this inductance ordinary has a negligible effect due to the sub-micrometer scale of the RTD and its contacts, see [100].

The contact parasitics are connected in the oscillator in series between the RTD and the resonator. As is typical in electrical circuits, an RC time constant originating from the contact parasitics is considered to limit the frequency operational region. To determine the maximal operation frequency of an RTD, we replace it with the equivalent small-signal equivalent circuit, which is a parallel connection of the RTD capacitance C_{RTD} and conductance G_{RTD} , see [71], [100].

Simplified parasitics

At first, we simplify the problem and neglect the spreading resistance and investigate the maximum oscillation frequency. We return to the effect of the spreading resistance further in the

section. For this case, at the outer port RTD, we can write the input small signal admittance as:

$$Y = A \frac{1}{\frac{R_c}{1+j\omega C_c R_c} + \frac{1}{G+j\omega C}}, \quad (2.1)$$

where A is the active area of the RTD. We search for the frequency at which the real part of the admittance is zero, as this marks the frequency where the system shows no NDC for the resonator. For this case, we can write:

$$\omega_0^2 = -G_{\text{RTD}} \frac{1 + R_c G_{\text{RTD}}}{G_{\text{RTD}} C_c^2 R_c^2 + R_c C_{\text{RTD}}^2}. \quad (2.2)$$

Let us assume an RTD with the conductance of $-50 \text{ mS}/\mu\text{m}^2$ and the capacitance of $12 \text{ fF}/\mu\text{m}^2$, and the contact parasitics with the resistance value of $2 \Omega\mu\text{m}^2$ and the capacitance value of $20 \text{ fF}/\mu\text{m}^2$. In that case, the maximum frequency is approximately 2.3 THz. Although this is a crude approximation, it is quite close to the highest achieved oscillation frequency of the RTD oscillators of 1.98 THz, see [30], which was achieved with an RTD with similar parameters.

Often in RTD oscillators a condition $R_c G_{\text{RTD}} \ll 1$ is satisfied (because typically $R_c \approx 1$ to $10 \Omega\mu\text{m}^2$ and $G_{\text{RTD}} \approx -1$ to $-100 \text{ mS}/\mu\text{m}^2$), and $C_{\text{RTD}}^2/C_c^2 \approx 1$ and thus we can write a simplified formula:

$$\omega_0^2 \approx -\frac{G_{\text{RTD}}}{R_c C_{\text{RTD}}^2}, \quad (2.3)$$

which gives, for our example RTD the maximum frequency of 2.1 THz. This formula clearly shows the influence of the RTD parasitics, C_{RTD} and R_c , on the maximum frequency. The RTD RC time constant due to the parasitics is, in the simplified case, equal to the geometrical mean of the partial RC time constants; $R_c C_{\text{RTD}}$ and $-\frac{C_{\text{RTD}}}{G_{\text{RTD}}}$.

Typical values of the contact parasitics

In the above analysis, we have used specific values for the parasitic elements. The value of the contact resistance is for the real devices difficult to estimate as this depends on the quality of the metal-semiconductor interface, which also depends on the processing steps. Therefore, one ordinary has to rely on measured values. It seems that the best results are achieved for the InGaAs RTDs if the strained cap layer for the top contact is used. The strained cap is enriched of Indium, see [117]. Typically the composition for the enriching is $\text{In}_{0.7}\text{Ga}_{0.3}\text{As}$. If the contacts are then stripped from oxides before the metal deposition, and Ti/Pd/Au metallic layers are deposited, then the contact resistance can be as low as $2\text{-}3 \Omega\mu\text{m}^2$, see, e.g., [80], [118].

The estimation of the contact capacitance can be performed as outlined in [73] (Sections (2-9) and (2-10)), which is based on the Schottky barrier height. However, due to the Fermi level pinning (from the interface states), the barrier height needs to be also determined from a measurement in this material system, see e.g. [119], [120]. Estimation for the doping level of $5 \times 10^{19} \text{ cm}^{-3}$ and $\text{In}_{0.7}\text{Ga}_{0.3}\text{As}$ (barrier height $\approx 100 \text{ meV}$) gives the contact capacitance in the range of $18\text{-}25 \text{ fF}/\mu\text{m}^2$, which lines up with values obtainable from the literature, see [71], [121].

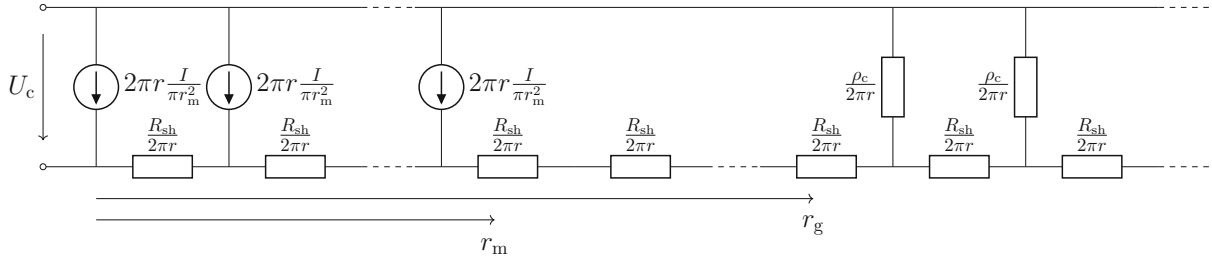


Figure 2.12: Equivalent circuit for describing the spreading resistance for an axially symmetric RTD.

Spreading resistance

Next, we address the estimation of the spreading resistance and its effect. This contribution arises from the currents spreading through the underlying semiconductor conducting layer and spilling over a portion of the bottom electrode.

For axially symmetric RTDs (cylindrical geometry of the mesa, usually used), we can derive an expression for the spreading resistance from the transmission line theory, see [122]–[124]. The transmission line method is only applicable if the transfer length, which is the effective length of the contact (the length over which the current is being absorbed to the contact), is much larger than the thickness of the conductive layer because then one can assume uniform current distribution in the semiconductor layer. In RTDs, the spreading depth is generally limited by the depth of the doped layer underneath the RTD layers, which is usually in the range of 0.5–1 μm .

For the equivalent circuit describing the spreading resistance, see Fig. 2.12. Here r is the radial coordinate, I is the current flowing through the RTD, r_m is the mesa radius, R_{sh} is the sheet resistance of the conductive layer beneath the mesa, r_g is the radius to the outer bottom contact, and ρ_c is the contact resistance of the bottom contact. We assume a uniform distribution of the current in the RTD mesa, represented by the current sources in the mesa part.

For the equivalent circuit of the spreading resistance, we can write the following differential equation:

$$\frac{d^2U(r)}{dr^2} + \frac{1}{r} \frac{dU(r)}{dr} + \frac{R_{sh}}{2\pi r} I'_p(r) = 0, \quad (2.4)$$

where I'_p is the current flowing in the parallel branches of the circuit to the channel, for which we can write:

$$I'_p(r) = \begin{cases} I_0 \frac{2\pi r}{\pi r_m^2}, & \text{if } r \leq r_m \\ 0, & \text{if } r_m < r \leq r_g \\ -U(r) \frac{\rho_c}{2\pi r}, & \text{if } r > r_g. \end{cases} \quad (2.5)$$

From the solution of the differential equation, we obtain the following solutions for the three

regions:

$$\begin{cases} R_{\text{spread},1} = \frac{R_{\text{sh}}}{4\pi}, & \text{if } r \leq r_m, \\ R_{\text{spread},2} = \frac{R_{\text{sh}}}{2\pi} \ln \frac{r_g}{r_m}, & \text{if } r_m < r \leq r_g \\ R_{\text{spread},3} = \sqrt{\frac{\rho_{c,b}}{R_{\text{sh}}}} \frac{R_{\text{sh}}}{2\pi r_g} \frac{K_0\left(\sqrt{\frac{R_{\text{sh}}}{\rho_{c,b}}} r_g\right)}{K_1\left(\sqrt{\frac{R_{\text{sh}}}{\rho_{c,b}}} r_g\right)}, & \text{if } r > r_g. \end{cases} \quad (2.6)$$

where K_0 and K_1 are the zeroth and first-order modified Bessel kind of the second kind, respectively. The spreading resistance is then:

$$R_{\text{spread}} = R_{\text{spread},1} + R_{\text{spread},2} + R_{\text{spread},3}. \quad (2.7)$$

The mesa column itself has a resistance that we still need to include in our assessment. This resistance is equal to the following:

$$R_{\text{mesa}} = R_{\text{sh}} t \frac{h}{\pi r_m^2}, \quad (2.8)$$

where t is the thickness of the n++ channel, and h is the height of the mesa.

The dependencies of the contributions of the contact parasitics for cylindrical rotation symmetrical geometry on the mesa area are shown in Fig. 2.13. The figure shows plots for the resistances of the top contact, spreading resistance, mesa resistance, and total parasitic resistance for the following parameters of the model: $\rho_{c,t} = 2 \Omega\mu\text{m}^2$, $\rho_{c,b} = 10 \Omega\mu\text{m}^2$, $R_{\text{sh}} = 4.4 \Omega$, $h = 0.15 \mu\text{m}$, and $t = 0.45 \mu\text{m}$, which are realistic parameters of the state-of-the-art RTDs used in RTD oscillators. The pole of the impedance function of the bottom contact resistance and contact capacitance (assuming $20\text{fF}\mu\text{m}^2$) is at $\approx 0.8 \text{ THz}$, and thus we can assume that this contact is for the high-frequencies (HF) (around 2 THz) shorted, making $R_{\text{spread},3} = 0$. In Fig. 2.13, we show the DC and HF cases for the bottom contact. The pole of the impedance function of the top contact is for the example parameters at $\approx 4 \text{ THz}$, and thus we neglect the influence of the contact capacitance of the top contact.

From Fig. 2.13, we can see that the spreading resistance has minimal effect for the small RTD areas. The high-frequency RTD oscillators have RTD areas in the range of 0.2 to $0.5 \mu\text{m}^2$. For these areas, the resistance of the top contact dominates, and thus our estimation of the maximum frequency from the top contact's influence was relatively precise. The spread resistance influence dominates for large RTD areas.

2.4.2 Frequency dependence of the RTD conductance

The circuit parameters of the RTDs differ at DC and high frequencies. Generally, the magnitude of the NDC decreases with increasing frequency. Two known effects play a role in the high-frequency response:

- Relaxation time of the electrons in the QW
- Transport time of the electrons in the depletion layer

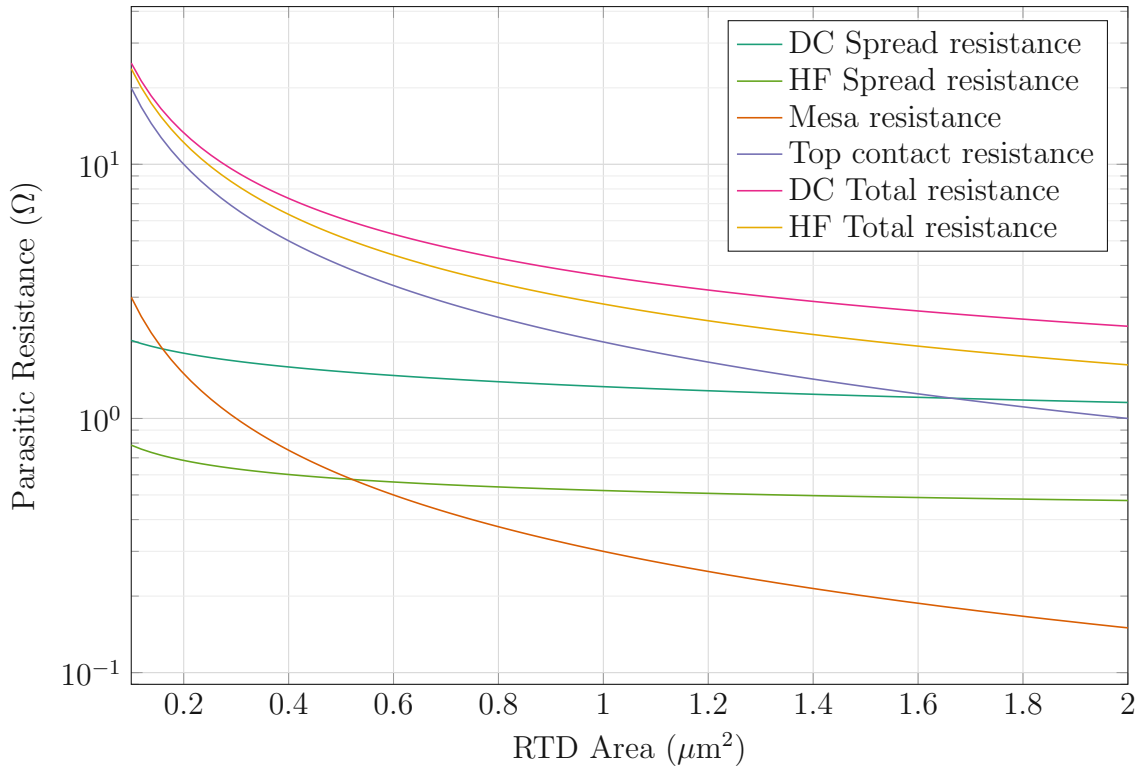


Figure 2.13: Comparison of the contributions of the parasitic resistances. The DC case corresponds to the case where the bottom contact resistance is in effect, and the HF case corresponds to the shorted bottom contact resistance by the contact capacitance.

RTD Relaxation time

For details about the description of the following effect, see [71], [102]–[104], [125]. Here we deal mainly only with an intuitive understanding of the effect.

In the sequential tunneling picture of the RTD, see [126], it is assumed that the electrons transport through the RTD by, at first, their tunneling to the QW, where their phase is broken, and thus they are localized there, and by their following tunneling out of the QW. During this process, the electrons dwell in the QW for a certain time before tunneling out. Predictions from the sequential tunneling picture are the same predictions as the predictions from the coherent tunneling picture, see [70]. We will speak here only about electron transport through the ground subband. As the electrons tunnel in and out of the QW, a certain average number of electrons occupy the QW. The number of electrons dwelling in the QW depends in the stationary case on the applied bias voltage. If the bias voltage is rapidly perturbed to a new bias, then the number of electrons in the QW is not equal to the stationary number of electrons corresponding to the new bias. It takes a certain time before the QW relaxes into the new steady state. This time for small perturbation of the bias is the dwell time which is given as:

$$\tau_{\text{dwell}} = \frac{1}{\nu_e + \nu_c}, \quad (2.9)$$

where ν_e and ν_c are the tunnel rates of the electrons from the QW to the emitter and collector, respectively. The tunnel rates depend on the barrier thickness, QW width, and the position of the

QW ground state in the band diagram relative to the contacts (emitter/collector).

However, because the electrons carry the electric charge, there are Columb interactions between the electrons in the QW. Adding a new electron to the already charged QW increases the energy necessary to add another one. Therefore, with the increasing electron density in the QW, while keeping the bias constant, the QW shifts towards higher potentials. In the DC case, the current density flowing through the RTD is proportional to the electron density in the QW, which means that the electron density is maximal at the peak current. This effect influences the idealized I-V curves of RTDs we have described in the section about the principle of RTDs, such that the voltage of the peak current is shifted towards larger voltages, while the voltage of the valley current is almost not influenced. This shift of the current peak voltage amplifies the magnitude of NDC (the NDC region becomes steeper).

If we consider the Columb interactions for the perturbation of the bias voltage, the relaxation time for the QW now can be longer or shorter than the dwell time. The relaxation time is then given as follows:

$$\frac{1}{\tau_{\text{rel}}} \approx \frac{1}{\tau_{\text{dwell}}} + \beta \left(\nu_e - \frac{N_e - N_{2D}}{\rho_{2D}} \nu'_e (V_{\text{we}}) + \frac{N_{2D}}{\rho_{2D}} \nu'_c (V_{\text{wc}}) \right), \quad (2.10)$$

where $\beta = e^2 \rho_{2D} / C$, in which C is the QW capacitance, ρ_{2D} is the density of states of the electrons in the QW, N_e is the electron injection concentration for the ground subband from the emitter, $\nu'_e (V_{\text{we}})$ and $\nu'_c (V_{\text{wc}})$ are the first derivations of the tunnel rates, for the emitter and collector respectively, with the change of the corresponding well-emitter V_{we} and well-collector V_{wc} energy variations, see [102].

If the RTD is biased in the NDC region ν_e gets small, $\nu'_e (V_{\text{we}}) > 0$, and for small perturbations of the bias inequality $N_e > N_{2D}$ is always valid. Then τ_{rel} is longer than τ_{dwell} . The effect is reversed for the positive differential conductance region, and τ_{rel} is shorter than τ_{dwell} .

If periodic variations of the bias take less time than is τ_{rel} , the charge density in the QW cannot keep up with the changes, and for very fast variations, the charge density limits to a constant. Although the charge in the QW is nearly constant for the very fast periodic variations of the bias, the current through the RTD still changes. However, the constant charge density disables the effect on the I-V that the Columb interactions have, and thus the amplification of the NDC is not active. We can conclude that the magnitude of NDC decreases with the frequency and converges to a certain high-frequency value.

The external RTD current is proportional to a weighted average of the QW-emitter and collector-QW currents. The weight for the QW-emitter current is $d/(d+l)$, where d is the equivalent length of the emitter, and l is the equivalent length of the collector. The weight for the collector-QW current is $l/(d+l)$. The equivalent lengths contain half the width of the well, the corresponding barrier thickness, and the corresponding space charge regions, composed of the screening length for the emitter and the depletion layer for the collector. These weighting coefficients originate from the current continuity equations for the emitter, collector, and QW. For the periodic bias variations, the partial current densities are not equal. The collector current

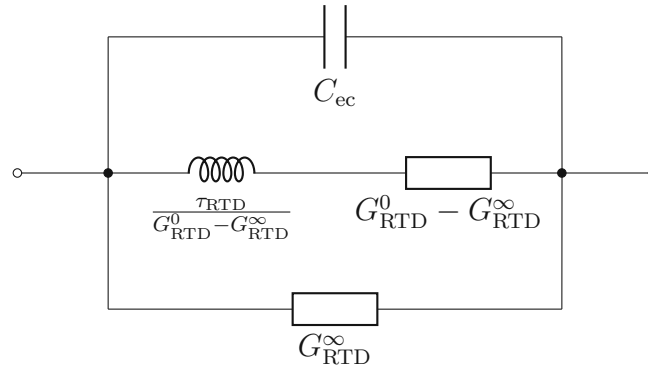


Figure 2.14: Small-signal equivalent circuit of an RTD resulting from the Columb interaction dynamics. The circuit consists of two resistors, inductance, and capacitance, thus we call the circuit RLRC.

depends on the QW's static charge density and the barrier's transparency. The emitter current, except for those, also depends on the available number of electrons in the emitter fulfilling the resonant condition of the QW. In the NDC region, the collector current has a PDC character for the very fast periodic bias variation because of the change in the transparency of the barrier. The emitter current has an NDC character because of the change in the number of electrons available for the tunneling. Therefore, the RTD can still show NDC at high frequencies if the ratios $d/(d+l)$ and $l/(d+l)$ do not lower the magnitude of the NDC contribution from the emitter current below the PDC contribution of collector current.

It can be shown that the frequency dependence of the RTD admittance is:

$$y_{\text{RTD}} = j\omega c_{\text{ec}} + g_{\text{RTD}}^{\infty} + \frac{g_{\text{RTD}}^0 - g_{\text{RTD}}^{\infty}}{1 + j\omega\tau_{\text{rel}}}, \quad (2.11)$$

where c_{ec} is the emitter-collector capacitance, g_{RTD}^0 is the DC conductance, and g_{RTD}^{∞} is the HF conductance that we have described above. The above-listed RTD parameters are in the units per unit area. This dependence can be represented by the RLRC equivalent shown in Fig. 2.14.

Let us apply the above-presented model to an example RTD, with 1.0 nm barriers, that was experimentally studied in [89]. The frequency dependence plots of conductance (real part of admittance of the RLRC model) and the capacitance (imaginary part of admittance of the RLRC model scaled by the $1/\omega$) at the point of the largest NDC of the RTD are shown in Fig. 2.15. From the plots, we can observe the drop in the conductance magnitude with frequency. Together with the conductance, the capacitance also lowers. The figure also graphically shows the influence of τ_{rel} , which was, in this case, ≈ 97 fs and corresponded to the roll-off frequency of ≈ 1.65 THz. We have used the here presented method to estimate the parameters for the RTD for which we have performed maximum frequency analysis due to the contact resistance in Section 2.4.1.

The above-presented principle is valid only if the bias voltage perturbation is small. Chapter 5 of this thesis, and references [105], [127], are then dedicated to the description of this effect for the large bias perturbations.

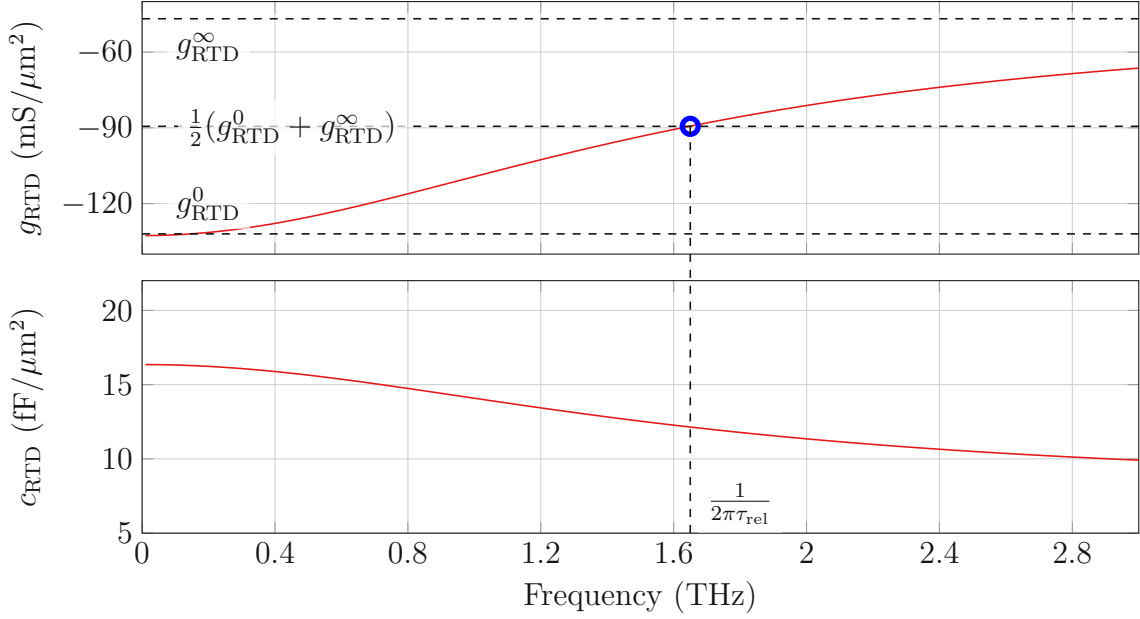


Figure 2.15: Frequency dependence of the conductance and the capacitance of an RTD, with 1.0 nm barriers, that was experimentally studied in [89].

Electron transport time

Except for the QW relaxation time, the electron transport time in the carrier-free region of the collector limits the RTD performance. The carrier-free region consists of the spacer and the depletion region of the collector and has the length of d_{dep} . The electrons injected from the QW into this region must travel through it to the electron reservoir in the collector, which takes a certain time. Typically these electrons are quickly accelerated to the saturation velocity due to the strong electric field. The maximum velocity arises from the interaction of the traveling electron with the semiconductor lattice by the coupling to acoustic and optical phonons, see [43]. Thus it takes time $\tau_{\text{dep}} = d_{\text{dep}}/v_{\text{sat}}$ for the electrons to reach the collector. For the $\text{In}_{0.53}\text{Ga}_{0.47}\text{As}$ alloy the saturation velocity is 3×10^5 m/s, see [100].

From the Shockley-Ramo theorem, see [128], [129], the external RTD current is constituted from the average of the traveling current. It can be shown that RTD shows no gain if the depletion layer causes π phase difference between the driving voltage and the current reaching the collector, see [121].

Then, the maximum achievable frequency due to the electron transport time is:

$$f_{\text{max,transport}} = \frac{1}{2\tau_{\text{dep}}}. \quad (2.12)$$

For an RTD with a spacer length of 12 nm, the depletion transport time is $\tau_{\text{dep}} = 40$ fs, and the corresponding maximum frequency is $f_{\text{max,transport}} = 12.5$ THz. This maximum frequency is much higher than the maximum frequency caused by the RTD parasitics (contact resistance and the RTD capacitance), which was ≈ 2.3 THz, and the roll-off frequency (corresponding to the relaxation time), which was, for the example RTD ≈ 1.65 THz. Considering the effect of the

electron transport time on the RTD conductance solely, then at 2 THz, the gain drops only to $\approx 96\%$ when compared to the DC conductance. Thus the electron transport time in the collector is not the dominant effect lowering the performance of RTDs with short spacers.

Chapter 3

Analysis of RTD oscillators

This chapter consists of two parts. The first part describes the well-known analysis of autonomous nonlinear circuits that we have reduced and translated for the RTD oscillators. We offer methods for designing RTD oscillators that are easy to take over. The second part contains original scientific contributions, that were published in a peer-reviewed journal, see [130]. In this part, we establish the fundamental power limitation of the RTD oscillators, which marks the upper bound in the output power. We show that the maximum power does not depend on the peak current density of the RTD but rather on the voltage separation of the peak and the valley current and the value of the output conductance (e.g., for antennas, the radiation conductance). The RTDs' peak-to-valley current difference and capacitance determine how close we can approach the upper bound.

More specifically, the first part of this chapter describes the small-signal and large-signal analysis of RTD oscillators. We start with the small signal analysis of the oscillator, where we introduce a small signal equivalent circuit and the oscillation conditions, which gives us a tool for whether the oscillator can oscillate and on which frequency. Using the small-signal approximation, we describe the mechanism of the start of the oscillations. Next, we show the connection between the small signal and the large-signal analysis. Further, we present the large-signal analysis of the oscillators in the quasistatic regime, which allows us to determine the output power of the RTD oscillators. Next, we describe the large-signal effects of oscillations on the RTDs' I-V curves. The methodology developed in this chapter is not exclusive to RTDs and can be used in analyzing all oscillators using an active part with the NDC.

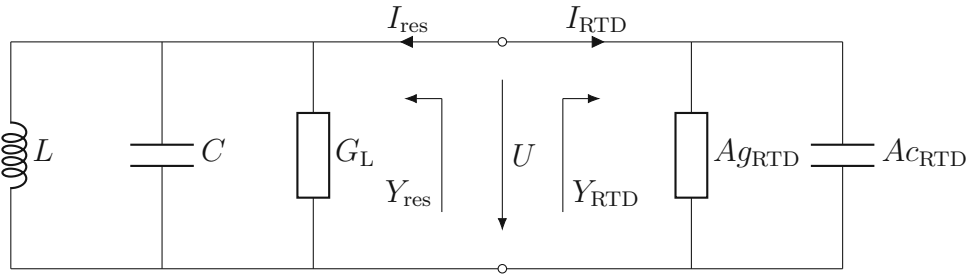


Figure 3.1: Linear equivalent circuit of an oscillator with NDC element with its parasitic capacitance considered. The RTD capacitance and conductance are being scaled with the active area A .

3.1 Small-signal analysis of an oscillator with NDC

In this section, we assume that all the devices and parts used for the description behave linearly, which means that for every component, the magnitude of the response is directly proportional to the magnitude of the excitation and the superposition principle applies. The small-signal analysis is used to determine whether the system can oscillate and the frequency of the oscillation.

Because of the linearity, we can perform the analysis in the domain of the Fourier images, i.e., with admittances/impedances of the elements. For the equivalent circuit of the resonator, we use a parallel resonant circuit formed of inductance L , capacitance C , and conductance G_{loss} . The conductance G_{loss} represents the resonator's losses. The RTD in its simplest form can be approximated as a parallel combination of its differential conductance g_{RTD} per unit area and the equivalent differential capacitance c_{RTD} per unit area, which comes from the intuitive geometrical topology of RTDs. In the previous chapter, we introduced the RLRC model for the RTD, which we can transform into the parallel connection of g_{RTD} and c_{RTD} , and take these values to be frequency dependent fitting the admittance of the RLRC model. The equivalent parameters of the RTD are then scaled with the actual active area of the RTD A . In the previous chapter, we described the effect of the contact parasitics that limited the performance of the oscillators. For the small-signal analysis, we can simplify the circuit and include these in the admittance of the resonator.

Figure 3.1 shows the equivalent circuit of the RTD oscillator. Y_{res} is defined as:

$$Y_{\text{res}} = G_L + j\omega C + \frac{1}{j\omega L}, \quad (3.1)$$

where ω is the angular frequency. Y_{RTD} is defined as:

$$Y_{\text{RTD}} = A (g_{\text{RTD}} + j\omega c_{\text{RTD}}). \quad (3.2)$$

We use the slightly more abstract mathematical language of eigenvalues to describe the circuit, as we can then easily generalize the analysis for oscillators with multiple RTDs. For the current flowing into the resonator, we can write:

$$I_{\text{res}} = Y_{\text{res}} U, \quad (3.3)$$

and for the current flowing into the RTD:

$$I_{\text{RTD}} = Y_{\text{RTD}}U. \quad (3.4)$$

Then, if we connect the circuits as shown in Fig. 3.1, where from the definition of the directions of the currents $I_{\text{RTD}} = -I_{\text{res}}$, we can write:

$$0 = (Y_{\text{res}} + Y_{\text{RTD}})U. \quad (3.5)$$

This equation is an eigenvalue equation. To avoid a trivial solution of $U = 0$ (resulting in no oscillations), the determinant of this equation needs to be zero. In our case, the linear system is one-dimensional, and thus the eigenvalue is simply:

$$0 = Y_{\text{res}} + Y_{\text{RTD}}. \quad (3.6)$$

Equation (3.6) is the oscillation condition. If we substitute in the oscillation condition the admittances for the resonator and the RTD and split the equation for the real and imaginary parts, we can write:

$$0 = G_{\text{loss}} + Ag_{\text{RTD}}, \quad (3.7)$$

$$0 = \omega C - \frac{1}{\omega L} + \omega A c_{\text{RTD}}, \quad (3.8)$$

From Eq. (3.8) we can write for the frequency:

$$f = \frac{1}{2\pi\sqrt{L(C + Ac_{\text{RTD}})}}. \quad (3.9)$$

Equations (3.7) and (3.9) tell us that the losses of the resonator need to be compensated by the gain (negative losses, the NDC) of the RTD and that the oscillation frequency is equal to the resonant frequency of the combinations of the reactive parts of the resonator and the RTD by the Thompson formula. Although these equations give us an intuitive description of the system in practice, one typically uses Eq. (3.6) (split into its real and imaginary parts) because the values of the admittances are usually known only numerically, and are frequency dependent.

With Eq. (3.6), our small-signal analysis can end. However, it is worth a while to understand the processes of how the oscillations start. This discussion also should explain why we sometimes discuss the NDC as a gain. We consider the simplest circuit possible, in which we combine the capacitances and conductances of the RTD and the resonator into new parts C_c and G_c , respectively, in whose the RTD contributions are already scaled by the active area. This results in an equivalent circuit shown in Fig. 3.2. Then we can write for the common node:

$$i_{G_c} + i_{C_c} - i_L = 0, \quad (3.10)$$

which, if differentiated with respect to time, corresponds to the following homogeneous differential equation:

$$\frac{d^2}{dt^2}u(t) + \frac{G_c}{C_c} \frac{d}{dt}u(t) + \frac{1}{LC_c}u(t) = 0. \quad (3.11)$$

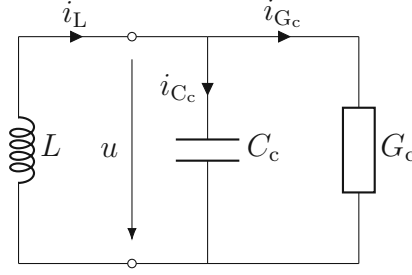


Figure 3.2: Simplified linear equivalent circuit of an RTD oscillator.

In the time domain, the general solution of this differential equation is:

$$u(t) = \exp\left(-\frac{\omega_0}{2Q}t\right) (U_1 \cos(\omega_1 t) + U_2 \sin(\omega_1 t)) , \quad (3.12)$$

where $\omega_1 = \omega_0 \sqrt{1 - \frac{1}{4Q^2}}$ which is the oscillation frequency, $\omega_0 = \frac{1}{\sqrt{LC_c}}$ which is the eigen frequency of the system, and $Q = \frac{1}{G_c} \sqrt{\frac{C_c}{L}}$ which is the quality factor of the system. If we then arbitrarily specify initial conditions, e.g. as $u(0) = 0$ and $i_L(0) = I_0$, then we can write:

$$u(t) = \frac{I_0}{\omega_1 C_c} \exp\left(-\frac{\omega_0}{2Q}t\right) \sin(\omega_1 t) . \quad (3.13)$$

Then, if $G_c < 0$, then $Q < 0$, and we get sinusoidal oscillations with the frequency of ω_1 whose amplitude is exponentially raising with time. The magnitude of the amplification is indirectly proportional to the circuit Q-factor. In the linear analysis, the amplitude is not limited and rises to infinity. We address the problem of the amplitude limitation in the large-signal analysis. The circuit amplifies its own response due to the negative value of G_c . Therefore, we can call the negative value of G_c the gain. In this thesis, we used the terms gain and negative conductance equivalently, as the context will require.

Note that the oscillation frequency ω_1 can also be purely imaginary for small values of $|Q|$. For these cases, $u(t)$ does not have oscillatory character anymore but only exponentially raises/drops (based on the sign of G_c).

Alternatively, we can write a set of two equations for the above-mentioned equivalent circuit as:

$$\frac{du}{dt} = \frac{1}{C} (i_L - i_{G_c}) = \frac{1}{C} (i_L - G_c u) , \quad (3.14)$$

$$\frac{di_L}{dt} = -\frac{1}{L} u . \quad (3.15)$$

We can visualize the solution of this set in a phase diagram of the state variables u and i , where we evaluate for them the time derivatives. An example of the oscillator's phase space is shown in Fig. 3.3. The figure also shows the negative differential resistance and an example trajectory of the rising oscillations. The adjoined plots then show the rise of the current and of the voltage. For this specific example, we have chosen artificial parameters of an oscillator, where $C = 1$ fF, $L = 0.1$ pH, and $G_c = -0.5$ mS. The initial conditions were $i_L = 1 \mu\text{A}$ and $u = 0$ V.

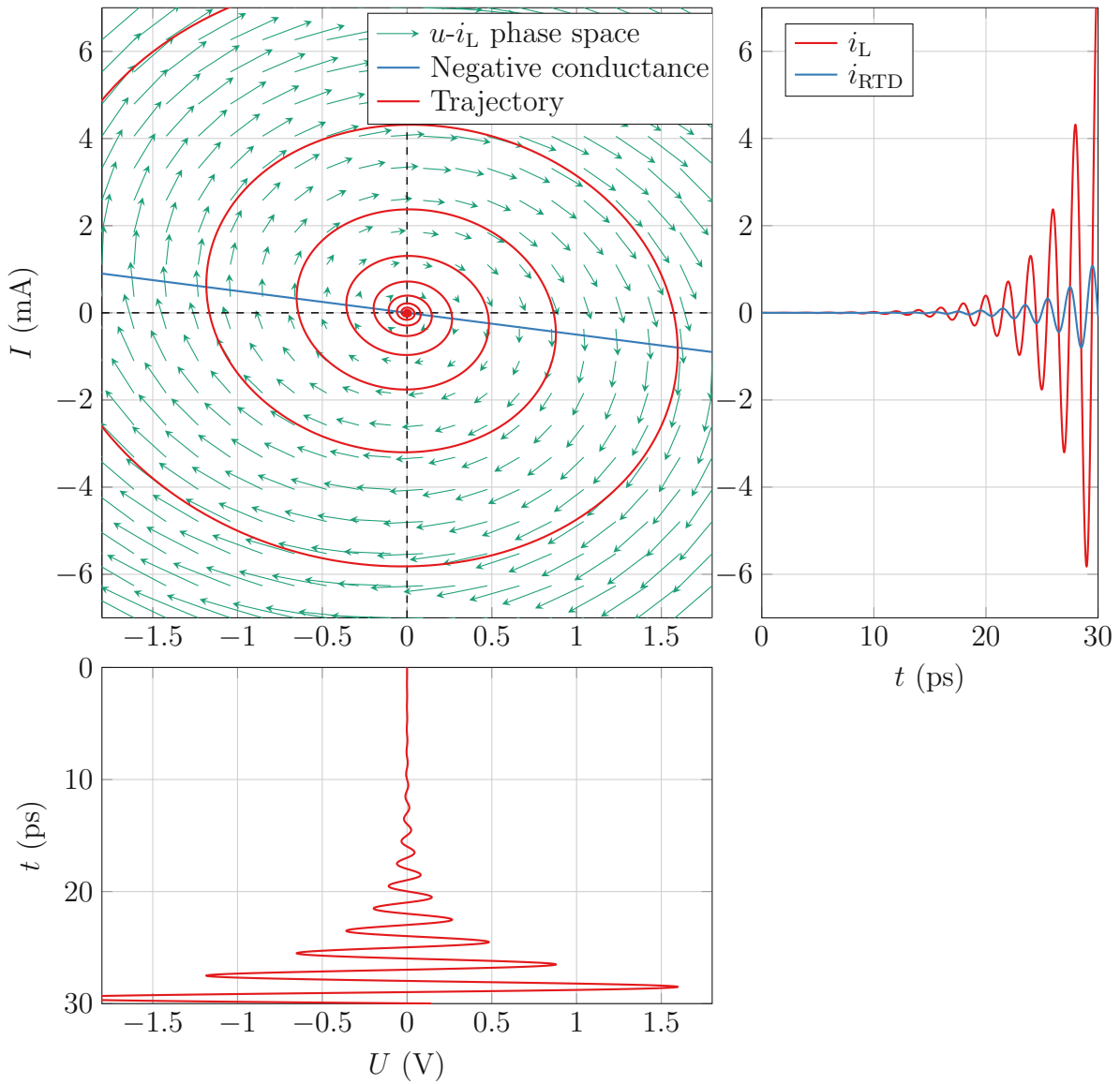


Figure 3.3: Phase space of the oscillator with parameters $C = 1$ fF, $L = 0.1$ pH, and $G_c = -0.5$ mS. The straight blue line corresponds to the NDC, and the red spiral represents a dynamic raise u and i_L . The initial conditions were $i_1 = 1 \mu\text{A}$ and $u = 0$ V. The adjacent plots then show the trajectory in the time domain for the corresponding quantity.

We have assumed the initial disturbance, which resulted in the initial conditions. How did it happen that there was stored energy (current flowing through it) in the inductor and no energy stored in the capacitor (voltage on it) in the beginning? Whether we chose the inductor, the capacitor, or both to store the energy at time zero is arbitrary, as we are changing only the initial phase and amplitude of the oscillations. In the analogy of the mechanical clock, this would correspond to a situation in which we would displace the pendulum from the equilibrium position (potential energy) and release it or to a situation where we would give it an initial impulse force resulting in kinetic energy. In both cases, the outside world is needed to take action to start the oscillations.

The same principle is valid also for our electronic oscillator. There are two evident sources of such an action. One is the thermal noise, and the other one is a transient effect, appearing when we change the bias at the RTD to the NDC region. The thermal noise comes, for example, from the Johnson–Nyquist noise (resistor noise), as the RTD generally acts as a resistor. The Johnson–Nyquist noise is a white noise and can temporarily induce a current through the RTD with a frequency equal to the oscillation frequency, and thus start the oscillations.

Alternatively, as the RTD needs to be biased, there is a transient voltage change in the circuit during the biasing. This transient has a broad spectrum that also contains the frequency of the oscillations and thus can also start the oscillations. Exact quantifications of the starting mechanism are not crucial for the oscillators operated in the harmonical steady state because Eq. (3.13) shows the starting amplitude only shifts the oscillations in time. Due to the finite quality factor of the system, the oscillator is started by a broader frequency range than the exact oscillation frequency can start the oscillations. The knowledge of the exact mechanism of the start-up might be important in certain applications, for example, in high-speed communications with on-off keying. We should add that decreasing the values of the Q-factor increases the magnitude of the phase noise, see, e.g., [131].

As the oscillation amplitude increases, the energy periodically stored in the inductor and the capacitor also increases. In the above differential equation, this rise in energy is covered by the NDC of the RTD. However, a passive device exhibiting NDC at zero bias does not exist. The RTD with the NDC is a passive part, meaning that its current-voltage (I-V) curve occupies only the first and the third quadrant of the corresponding characteristic, i.e., the current sign is the same as the sign of the applied voltage. Thus, an external biasing source, which provides the energy, is necessary for the oscillators. See Sec. 3.4 for details about the energy in the system.

We have used the here-derived oscillation condition Eq. (3.7) in the previous chapter, where we dealt with the maximum oscillation frequency of the RTD oscillators.

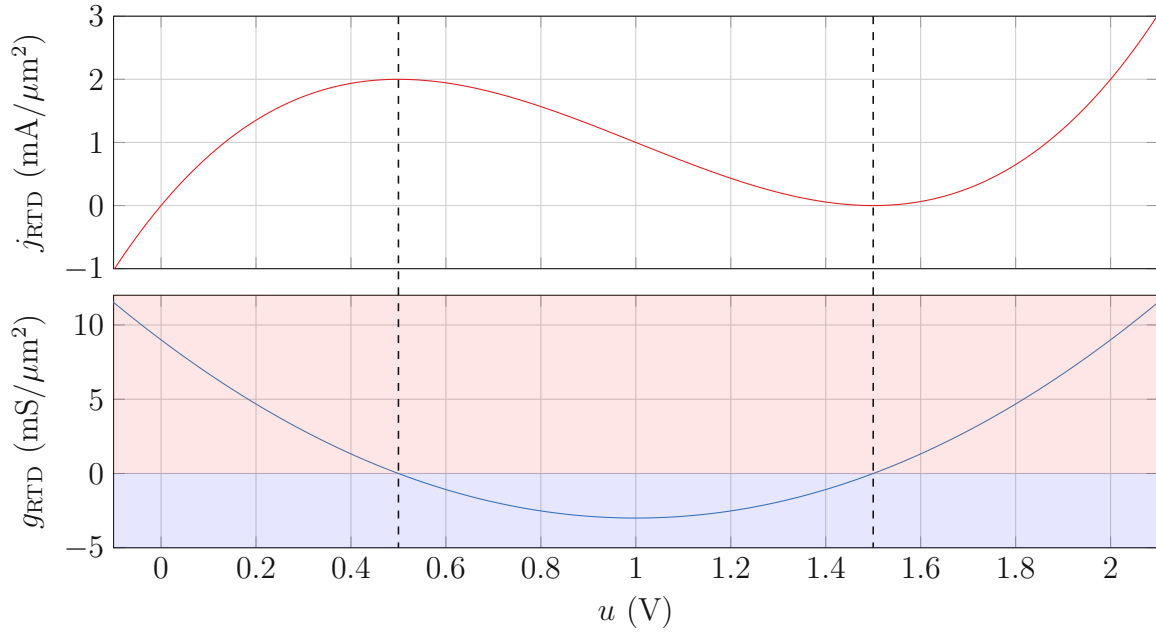


Figure 3.4: An example of a current-voltage (I-V) curve and its first derivative (g_{RTD}) of a device exhibiting NDC. The used curve is a polynomial of the third order. The blue shading marks the NDC region where g_{RTD} is negative, and the red shading marks the positive g_{RTD} region.

3.2 Relation between the large-signal and small-signal analysis

For an example of a physical, although still idealized, I-V curve which show the NDC, see Fig. 3.4. The I-V curve is, in this case, constructed from a polynomial of the third order:

$$j_{\text{RTD}} = g(u - U_0) + b(u - U_0)^3 + J_0, \quad (3.16)$$

where g , b , u_0 , and i_0 are the polynomial parameters, u is the voltage on the RTD, and j_{RTD} is the current density per unit area flowing through the RTD. Notice that the I-V curve resides only in the first and third quadrants of the diagram. This description of the NDC devices for oscillators was done in [132].

With the introduction of the polynomial of the third order, we cannot use the linear analysis any further, and we need to proceed to the non-linear large-signal analysis. To be able to use the real I-V curve for the small-signal analysis, we have to rewrite Eq. (3.11), assuming linearity of the resonator and scaling the RTD with the active area, as:

$$C \frac{d^2 u}{dt^2} + \frac{d^2 A \sigma_{\text{RTD}}}{dt^2} + G_L \frac{du}{dt} + \frac{dA j_{\text{RTD}}}{dt} + \frac{1}{L} u = 0, \quad (3.17)$$

where σ_{RTD} is the charge per unit area stored in RTD's capacitance. Using the chain rule, we can write:

$$C \frac{d^2 u}{dt^2} + \frac{\partial A \sigma_{\text{RTD}}}{\partial u} \frac{d^2 u}{dt^2} + \frac{\partial^2 A \sigma_{\text{RTD}}}{\partial u^2} \left(\frac{du}{dt} \right)^2 + G_L \frac{du}{dt} + \frac{\partial A j_{\text{RTD}}}{\partial u} \frac{du}{dt} + \frac{1}{L} u = 0. \quad (3.18)$$

Assume that we still analyze the circuit for small amplitudes, then we can neglect the second-order varactor term and write:

$$(C + A_{c_{\text{RTD}}}) \frac{d^2}{dt^2} u + (G_L + A_{g_{\text{RTD}}}) \frac{d}{dt} u + \frac{1}{L} u = 0, \quad (3.19)$$

where:

$$g_{\text{RTD}} = \left. \frac{\partial j_{\text{RTD}}}{\partial u} \right|_{u=U_{\text{bias}}}, \quad (3.20)$$

$$c_{\text{RTD}} = \left. \frac{\partial \sigma_{\text{RTD}}}{\partial u} \right|_{u=U_{\text{bias}}}, \quad (3.21)$$

are the differential conductance and capacitance of the circuit. The resulting equation is identical to Eq. (3.11) in its form, and therefore it has the same solution, although limited only to small voltages in this case. We can use it to determine whether the system with a custom I-V can fulfill the small-signal oscillation conditions, which would tell us whether the system is capable of oscillations.

Figure 3.4 also depicts the first derivative of the I-V curve, which corresponds to its small signal conductance at the given bias voltage calculated from Eq. (3.20). The plot of G_{diff} shows that there is a minimum of G_{diff} and that G_{diff} is negative only in certain parts of the I-V curve (blue region). This is the NDC region of the I-V curve.

3.3 Large-signal analysis

3.3.1 General method

To determine the oscillation frequency, we needed only the small-signal RTD response. However, in such an analysis, we have assumed the oscillating voltage to be infinitely small. Being able to predict the oscillating amplitude is crucial because it determines the oscillator's output power. For the output power generated by an RTD oscillator on a load directly connected to it, we can write:

$$P = G_{\text{load}} \frac{1}{T} \int_0^T u_{\text{RTD}}^2(t) dt \quad (3.22)$$

where G_{load} is the loading conductance on which the power is dissipated, u_{RTD} is the oscillating voltage, and T is the period of the oscillations. Infinitely small voltage amplitude then results in limiting to zero output power. However, for practical applications, the output power needs to be non-zero. Therefore, our analysis needs to include the large signal response of the RTD. This section describes a method for u_{RTD} estimation.

As the RTD is a non-linear element with memory, its external output current is, in general, a functional of the applied voltage and its history:

$$j_{\text{RTD}}(t) = j(u_{\text{RTD}}(t)). \quad (3.23)$$

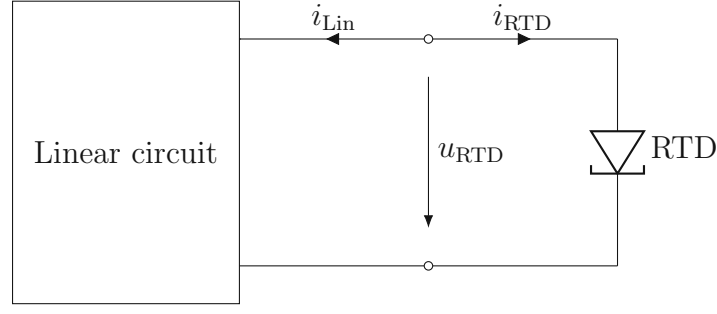


Figure 3.5: Non-linear circuit corresponding to the RTD oscillator. We can separate the circuit into the linear part containing all the linear elements and the part containing the non-linear RTD. For the lack of a better symbol, we designated the RTD by the symbol for tunnel diodes.

Our task is to find u_{RTD} that non-trivially solves this equation. The equation can be multi-valued; thus, to find the physical solution, we should find every solution and analyze its origins, i.e., track the dynamic behavior of their start-up. We will demonstrate the tracking of the solutions in the following subsection.

Further, we assume that the oscillator already operates in the steady harmonic state, i.e., its response is periodic and can be described by a Fourier series. For the periodic oscillations, we can expand u_{RTD} and the RTD current density j_{RTD} by the Fourier series as:

$$j_{\text{RTD}}(t) = \text{Re} \left\{ \sum_{n=0}^{\infty} J_{\text{RTD}}^{(n)} \exp(jn\omega_0 t) \right\}, \quad (3.24)$$

$$u_{\text{RTD}}(t) = \text{Re} \left\{ \sum_{n=0}^{\infty} U_{\text{RTD}}^{(n)} \exp(jn\omega_0 t) \right\}, \quad (3.25)$$

where n is the harmonic number, ω_0 corresponds to the angular oscillation frequency and $J_{\text{RTD}}^{(n)}$ and $U_{\text{RTD}}^{(n)}$ to the amplitudes of the corresponding current/voltage harmonics.

The equivalent circuit for the RTD oscillator, where the RTD is assumed to have a non-linear response, is shown in Fig. 3.5. We separated the circuit into the purely linear part, which includes the resonator and the parasitics, and the non-linear part, which corresponds to the RTD. For the lack of a better symbol for the RTD, we use the schematic symbol for a tunnel diode.

From our definition of the current directions and Kirchhoff's current law, the current flowing into the linear circuit i_{lin} needs to be equal to the negative value of the RTD current scaled by the RTD active area Aj_{RTD} :

$$i_{\text{Lin}} = -i_{\text{RTD}} = -Aj_{\text{RTD}}, \quad (3.26)$$

where i_{Lin} can be expanded similarly as j_{RTD} by the Fourier series, into $I_{\text{Lin}}^{(n)}$ coefficients. Exploiting the orthogonality property of the Fourier expansion, we can then write:

$$I_{\text{Lin}}^{(n)} = -AJ_{\text{RTD}}^{(n)}. \quad (3.27)$$

For the relation between the current and voltage in the linear circuit, we use its impedances at the corresponding frequencies of the harmonics, which allows us to write:

$$0 = U_{\text{RTD}}^{(n)} + Z_{\text{Lin}}^{(n)} AJ_{\text{RTD}}^{(n)}. \quad (3.28)$$

We note that $J_{\text{RTD}}^{(n)}$ for a specific harmonic depends on all of the harmonics of U_{RTD} through Eqs. (3.23), (3.24), and (3.25). To obtain the oscillating voltage, we need to solve the system of equations for all harmonics composed from Eq. (3.28). In other words, we need to balance it by adjusting the harmonic coefficients $U_{\text{RTD}}^{(n)}$. This is why this method is called the method of harmonic balance.

In a complete general case, the set of equations is infinite and thus is for little use if we do not truncate the solution only for a limited number of harmonics. The truncation is justifiable, as the oscillation voltage needs to have finite power, and thus its bandwidth should be limited. In practice, one can truncate the harmonics based on the nonlinearity strength (meaning amplitude of the generated higher harmonics in reference to the first harmonic) and the corresponding values of $Z_{\text{Lin}}^{(n)}$. However, the truncation is based on empirical knowledge, and its validity should be consistently checked.

To simplify the solution, we consider for the linear circuit the simple equivalent resonant circuit from Fig. 3.1. Then the impedance of it for the higher harmonics is approximately represented only by the capacitance. Because the capacitor impedance decreases with the frequency, we can assume that this capacitance is shorting the higher harmonics of the RTD current in Eq. (3.28). Based on this argument, we can assume that the harmonics play only a minor role in the analysis. Of course, this argument may fail for strong nonlinearity and small values of the capacitor. However, we stick to it at this point because it allows us to derive an analytical formula for the oscillator voltage. If we truncate the harmonics as:

$$Z_{\text{Lin}}^{(n)} = \begin{cases} Z_{\text{Lin}}^{(1)} & n = 1 \\ 0 & \text{else} \end{cases},$$

we can write a single equation for the voltage amplitude:

$$0 = U_{\text{RTD}}^{(1)} + Z_{\text{Lin}}^{(1)} A J_{\text{RTD}}^{(1)}. \quad (3.29)$$

Next, we apply a bias voltage U_{B} through the linear circuit, biasing the RTD into the center of the NDR region, and thus we can write the voltage on the RTD:

$$u_{\text{RTD}} = U_{\text{B}} + U_{\text{RTD}}^{(1)} \cos(\omega_0 t). \quad (3.30)$$

We have fixed the phase of the oscillating voltage to cosine because there is phase freedom due to the circuit being time-invariant in the harmonic steady state. Generally, we can do this only for one of the harmonics and in a case with multiple non-linear elements only at one circuit node. Then from the RTD response given by Eq. (3.23) to u_{RTD} we can get the first harmonic of the RTD current as:

$$j_{\text{RTD}}^{(1)} = 2 \frac{\omega}{2\pi} \int_0^{\frac{2\pi}{\omega}} j(u_{\text{RTD}}(t)) \exp(-j\omega_0 t) dt, \quad (3.31)$$

where the real part of the result corresponds to the current that is in phase with the driving voltage (active current), and the imaginary current part corresponds to the current that has a $\pi/2$

phase shift (reactive current). Multiplying with the factor of two, we add the contribution of the projection of the current to the negative frequency of the first harmonic.

From the projection of the current, we can define a large signal (LS) admittance of the RTD:

$$Y_{\text{RTD}}^{(1)} = A \frac{j_{\text{RTD}}^{(1)}}{U_{\text{RTD}}^{(1)}}, \quad (3.32)$$

which is scaled by the RTD active area. In a more detailed way, we can rewrite the admittance as and define the large signal conductance G_{RTD} and susceptance B_{RTD} :

$$Y_{\text{RTD}}^{(1)} = A (g_{\text{RTD}} + jb_{\text{RTD}}) = A \left(\text{Re} \left\{ \frac{j_{\text{RTD}}^{(1)} (U_0, U_{\text{RTD}}^{(1)})}{U_{\text{RTD}}^{(1)}} \right\} + j \text{Im} \left\{ \frac{j_{\text{RTD}}^{(1)} (U_0, U_{\text{RTD}}^{(1)})}{U_{\text{RTD}}^{(1)}} \right\} \right). \quad (3.33)$$

From Eq. (3.33), we can see that the LS admittance depends both on the bias voltage U_0 and the amplitude of the first harmonic of the oscillating voltage $U_{\text{RTD}}^{(1)}$. If we substitute Eq. (3.32) to Eq. (3.29), and use $Y_{\text{Lin}}^{(1)} = 1/Z_{\text{Lin}}^{(1)}$ we can write:

$$0 = Y_{\text{RTD}}^{(1)} + Y_{\text{Lin}}^{(1)}. \quad (3.34)$$

This equation represents the oscillation conditions for the large-signal case (if the truncation to the first harmonic is justified). In its form, the equation is equivalent to the small-signal oscillation condition given by Eq. (3.6). The large-signal condition defines the oscillation voltage amplitude and the oscillation frequency, which can differ from the small-signal case if the RTD capacitance is non-linear.

The power generated on the conductance of the linear circuit $G_{\text{Lin}}^{(1)}$ (real part of $Y_{\text{Lin}}^{(1)}$) by the first harmonic of the voltage is then from Eq. (3.22) given as:

$$P^{(1)} = \frac{1}{2} G_{\text{Lin}}^{(1)} \left(U_{\text{RTD}}^{(1)} \right)^2. \quad (3.35)$$

3.3.2 Third-order I-V curve approximation

Next, we show the results of the above-described method for an idealized example I-V curve. For simplicity, we assume that the RTD capacitance is linear. We thus replace the RTD with a parallel connection of its linear capacitance, which we can immediately add to the linear circuit, and a third-order polynomial I-V curve, of which example we have shown in Fig. 3.4 and described it with Eq. (3.16). If we apply in Eq. (3.16) the equation for the voltage sweep given by Eq. (3.30), then the projection of the current to the first harmonic computed from Eq. (3.31) is:

$$I_{\text{RTD}}^{(1)} = A \left(g U_{\text{RTD}}^{(1)} + \frac{3b}{4} \left(U_{\text{RTD}}^{(1)} \right)^3 \right). \quad (3.36)$$

From Eq. (3.32), this results in the conductance of the RTD to be:

$$G_{\text{RTD}}^{(1)} = A \left(g + \frac{3b}{4} \left(U_{\text{RTD}}^{(1)} \right)^2 \right). \quad (3.37)$$

Using the large-signal oscillation condition given by Eq. (3.34) and evaluating its real part, we can determine the oscillation amplitude as:

$$U_{\text{RTD}}^{(1)} = \sqrt{\frac{4}{3b} \left(-\frac{G_{\text{Lin}}^{(1)}}{A} - g \right)}. \quad (3.38)$$

Note that the parameter g is negative when the RTD is biased in the NDC region. The derived voltage is used in Eq. (3.22) to determine the output power. Also note that G_{Lin} does not need to be equal to G_{load} . This corresponds to cases where G_{Lin} is composed of G_{load} and an additional parasitic conductance representing parasitic losses. For details about this phenomenon, see Section 3.5.

We can estimate the parameters g and b , so the polynomial approximately fits an I-V curve of a real RTD, by matching the stationary points of the I-V curves, as:

$$g = -\frac{3}{2} \frac{\Delta J}{\Delta U}, \quad (3.39)$$

and

$$b = 2 \frac{\Delta J}{\Delta U^3} = -\frac{4}{3} \frac{g}{\Delta U^2}, \quad (3.40)$$

where ΔJ is the current density difference between the valley and the peak of the I-V curve, and ΔU is the voltage difference between the peak and the valley-current densities.

Using these expressions, we can write for the oscillating amplitude:

$$U_{\text{RTD}}^{(1)} = \Delta U \sqrt{1 + \frac{G_{\text{Lin}}^{(1)}}{Ag}}. \quad (3.41)$$

Remembering that g is negative as Eq. (3.39) shows, Eq.(3.41) tells us that $A|g| \geq G_{\text{Lin}}$ for the system to oscillate. The oscillation amplitude raises with decreasing G_{Lin} (or increasing $A|g|$) and saturates to ΔU . Because all the reactive elements were assumed to be linear, the oscillation frequency does not depend on the voltage and is the same as in the small-signal case.

There might be a question of whether the used bias point in the center of the NDR is the best choice. If we choose a bias point with shifted with voltage U_d from the center of the NDC to either side, we can again write for the first harmonic of the oscillating voltage as:

$$U_{\text{RTD}}^{(1)} = \Delta U \sqrt{1 - 4 \frac{U_d^2}{\Delta U^2} + \frac{G_{\text{Lin}}^{(1)}}{Ag}}, \quad (3.42)$$

The equations show that if the bias deviates from the NDC center, we get a consistently smaller amplitude of the oscillation than in the center. So the oscillation voltage achieves maximum at the center of the NDC. However, this principle is not general and is only strictly valid for the third-order polynomial and not for the general I-V curve, as we will show in the further section.

If we substitute the real part of Eq. (3.34) back into Eq. (3.42) we can calculate the dependence of $g_{\text{RTD}}^{(1)}$ on $U_{\text{RTD}}^{(1)}$. Fitting the parameters g , b , I_0 , and U_0 from an example I-V curve shown in Fig. 3.7 results in gain plots shown in Fig. 3.6 for a pick of U_d . The figure also shows a solution for Eq. (3.42) in an example case where the area of RTD is $1 \mu\text{m}^2$ and $G_{\text{Lin}}^{(1)} = 5 \text{ mS}$. The inset shows the dependency of $U_{\text{RTD}}^{(1)}$ on the bias voltage U_b for the specified load and area..

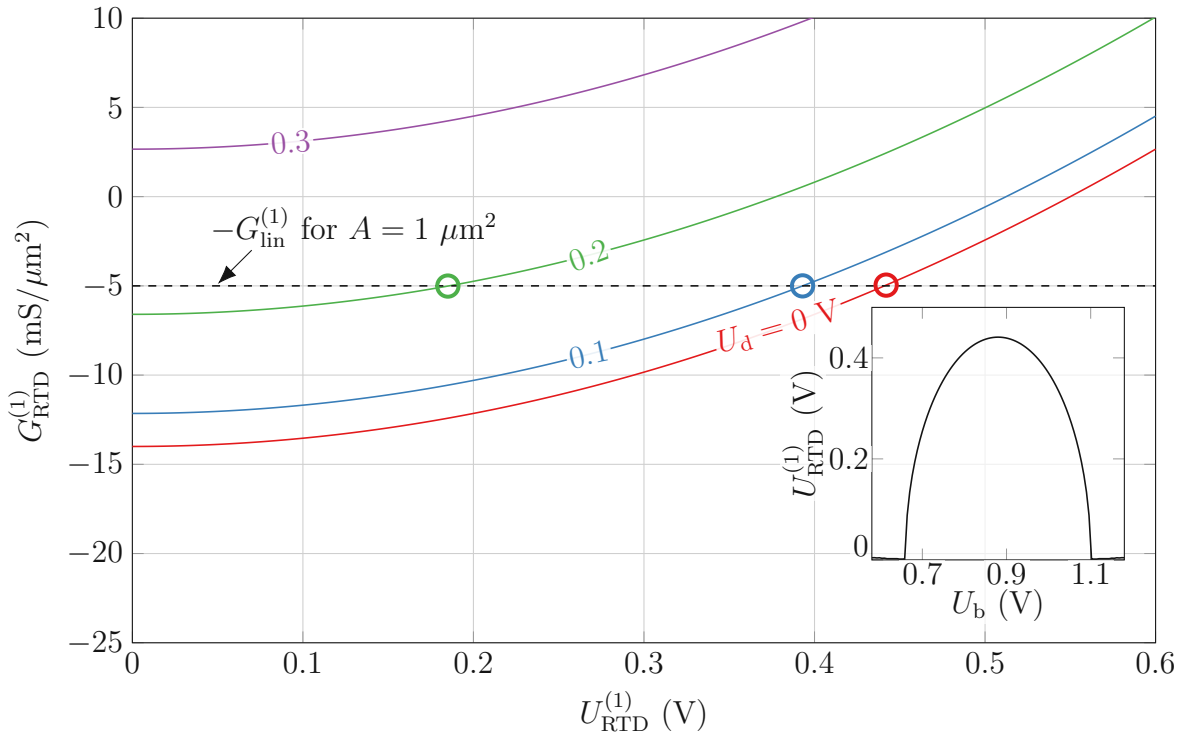


Figure 3.6: Large-signal conductance of an I-V curve of an example RTD (see Fig. 3.7 for details) approximated by the third-order order polynomial. The large-signal conductance is a function of the first harmonic amplitude of the oscillating voltage, and plots of various deviations of the bias point from the point of the maximal gain are shown. The dashed line corresponds to the negative value of $G_{Lin}^{(1)}$, for which we choose a value of 5 mS. The highlighted points correspond to the solution of Eq. (3.42) for RTD area equal to $1 \mu\text{m}^2$. The inset shows the oscillation amplitude voltage dependence on the bias voltage for the specified load and area.

3.3.3 Real I-V curve

The third-order polynomial can serve as a good tool for fast estimation of the RTD voltage if its parameters g , b , I_0 , and U_0 are well fitted to an I-V curve of a real RTD. However, its simplicity hides important features and brings an error in the power predictions when designing the oscillator.

Here we show the use of the same procedure for calculating $g_{RTD}^{(1)}$ as in the previous subsection, but in this case, we utilize an I-V curve of a real RTD. To be more specific, we use the I-V shown in Fig. (3.7) of an RTD that was experimentally studied in [80]. Similarly, as in the third-order approximation case, the large signal conductance $g_{RTD}^{(1)}$ depends both on the amplitude of the first harmonic and on the bias point.

Applying the I-V curve in Eqs. (3.30), (3.31), and (3.32) we compute $g_{RTD}^{(1)}$ for the sweeps of amplitudes and of various biases. From this, we obtain plots shown in Fig. 3.8. In the figure, we also show an envelope function, which represents the minimums of $g_{RTD}^{(1)}$ for all of the bias voltages at the specific $U_{RTD}^{(1)}$. The envelope function shows the maximum attainable gain for the corresponding voltage amplitude that the RTD can show. We can use this function to calculate the maximum power, as shown in the next section.

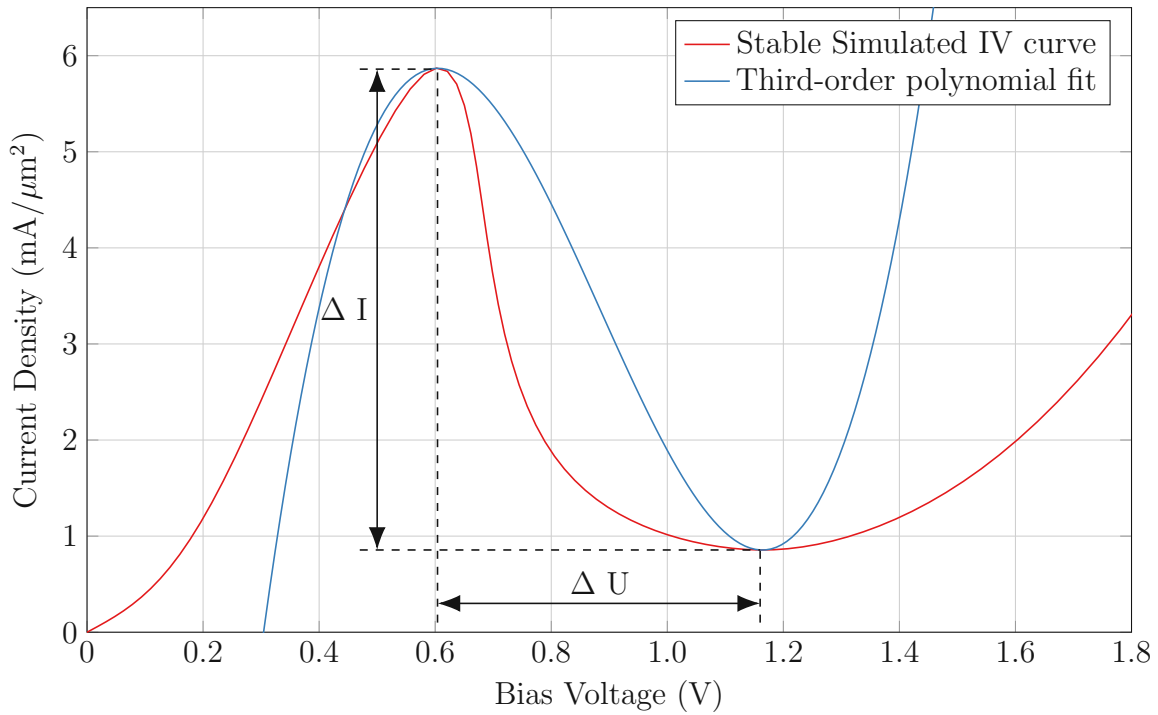


Figure 3.7: I-V curve of an example RTD with 1.6 nm barriers that was detailed studied in [80], and the corresponding third-order polynomial fit. The peak current density was approximately $6 \text{ mA}/\mu\text{m}^2$.

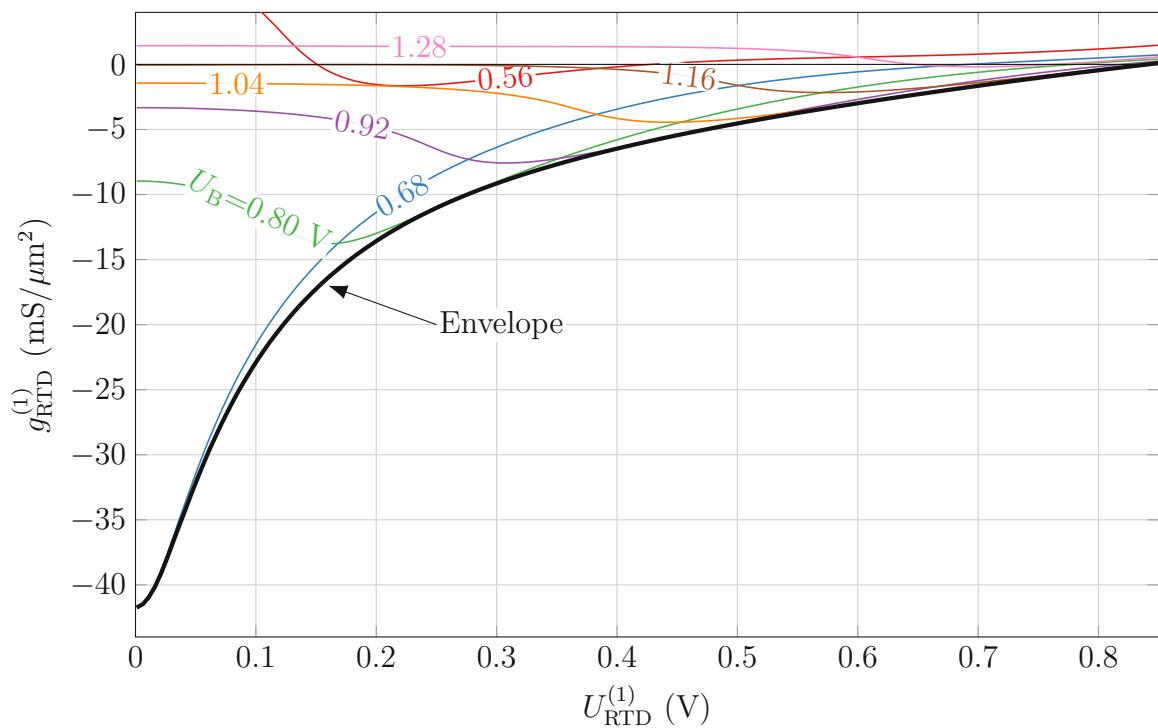


Figure 3.8: Large-signal conductance $g_{\text{RTD}}^{(1)}$ plots for the example RTD for several biases. The envelope function shows the maximal attainable gain.

In general, plots of $g_{\text{RTD}}^{(1)}$ (and $b_{\text{RTD}}^{(1)}$ if the RTD capacitance is non-linear) are not monotonous functions of $U_{\text{RTD}}^{(1)}$. From the solution of differential equation (3.11), we can conclude that for the system to be in a stable harmonical steady-state together with the fulfillment of the large-signal oscillation conditions, we need:

$$\frac{\partial}{\partial U_{\text{RTD}}^{(1)}} \left(G_{\text{RTD}}^{(1)} + G_{\text{lin}}^{(1)} \right) > 0. \quad (3.43)$$

This condition tells us that the stable harmonic-steady-state happens for such $U_{\text{RTD}}^{(1)}$, where a slight increase of $U_{\text{RTD}}^{(1)}$ would decrease the gain in the system and thus as a result, $U_{\text{RTD}}^{(1)}$ would decrease. If the inequality in the condition is reversed, then the increase of $U_{\text{RTD}}^{(1)}$ is increasing the gain, and thus $U_{\text{RTD}}^{(1)}$ would further increase, which would result in an unstable solution. In doing this analysis, one has to remember that with $U_{\text{RTD}}^{(1)}$, $g_{\text{lin}}^{(1)}$ generally varies with frequency, as the oscillation frequency (the frequency corresponding to the admittance of the linear circuit), due to the $b_{\text{RTD}}^{(1)}$ dependence on $U_{\text{RTD}}^{(1)}$, can be changing.

Next, we describe the process of how the oscillation voltage $U_{\text{RTD}}^{(1)}$ changes with the direction of the bias voltage sweep, for an example oscillator, i.e. the solution tracking. Figure 3.9 shows the mechanism of the oscillation amplitude dependence in the large-signal conductance vs. $U_{\text{RTD}}^{(1)}$ plot when the bias voltage is quasi-statically swept in the forward direction. The dashed line shows an example of a loading conductance (its negative value) for the RTD area of $1 \mu\text{m}^2$. For low biases, the oscillation conditions are not satisfied, and thus the circuit does not oscillate. As the bias is increased, we get to a point (the green line) where the oscillation conditions can be satisfied only for relatively large $U_{\text{RTD}}^{(1)}$. The oscillation could start in this regime only if there would be a large perturbation that would produce large enough voltage amplitude to start the oscillations. However, if we rely only on the small perturbation from the noise or from the slow sweep, then the gain needs to be larger than the losses, even for the small amplitudes. As we increase the bias further, the RTD gain surpasses the losses also for the small amplitude. However, note that for our example RTD, this point is unstable as the derivative of the gain's slope is positive (the orange line). Therefore, the amplitude rises, and it follows the curve until it reaches a point where the gain and losses are equal and also the point is stable (the slope is positive). We mark this transient with purple points and arrows. After this transient, the system reaches the first red point (the orange line). If the bias is then increased further, the oscillation amplitudes increase, and in the plot, it follows the red arrows (the purple and pink lines). The amplitude reaches the envelope function (black line), representing the maximal achievable voltage for the example load. The envelope point is a turning point, and with a further increase of the bias, the oscillation amplitude drops, which is represented by the blue arrow and point (the olive line), until the oscillation conditions are again violated (the brown line), at which point the oscillations stop. We have chosen G_{lin} of 11.8 mS and the active area of the RTD of $1 \mu\text{m}^2$, arbitrarily, as this allows us to show the mechanism more clearly. However, these values are not far from the values of used practical resonators.

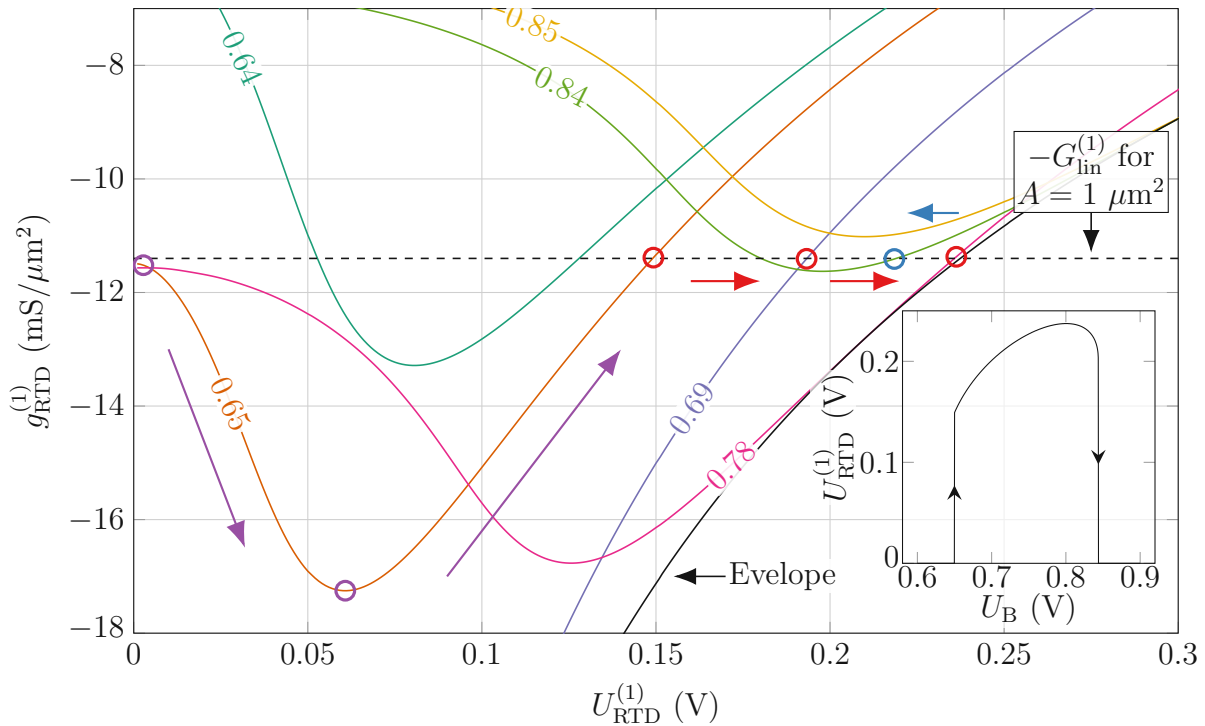


Figure 3.9: Mechanism of the dependence of the oscillating amplitude $U_{RTD}^{(1)}$ on the bias voltage for the forward bias sweep for the real RTD IV curve. The colored solid lines correspond to the dependence of the LS conductance on $U_{RTD}^{(1)}$. The dashed line shows an example of a negative value of the loading conductance, which was, in this case, $G_{lin} = 11.8$ mS. The purple points and arrows show a transient effect when the oscillations start. The red point corresponds to the forward bias sweep, where $U_{RTD}^{(1)}$ is increasing. The blue points and arrows also correspond to the forward sweep. However, now the voltage is decreasing. The inset shows the corresponding dependence $U_{RTD}^{(1)}$ on U_0 for the forward voltage sweep. The solutions marked by the points and arrows are done for the example RTD with an active area of $1 \mu\text{m}^2$.

Figure 3.10 then shows the same mechanism of the oscillation amplitude dependence on the bias, but for the reverse voltage sweep, i.e., from higher to lower voltages. The concept is exactly the same as for the forwardly swept bias, however, the starting and the ending point differ, which results in a hysteresis between the sweeps.

Figure 3.11 puts into perspective the hysteresis in the sweeps as it joins the insets of Figs. 3.9 and 3.10. In the figure, we also show the squared value of $U_{RTD}^{(1)}$, which is according to Eq. 3.35 directly proportional to the output power of the oscillator. This behavior of the output power with the bias voltage is confirmed in the sections dealing with experimental results of Chap. 2.

At the beginning of this section, we stated that the third-order approximation brings an error in the estimation of the output power. The magnitude of the error differs between the various I-V curve and thus is rather specific, depending on the exact shape of the real I-V curve. In Fig. 3.12 we plot the comparison between the output power, given from Eq. (3.35), between the approximation and the result from the real I-V curve as a function of the loading conductance, in which the RTD area was $A = 1 \mu\text{m}^2$. Although the maximum output power for both cases is approximately the same, it happens for differing loading conductances. Further, the third-order

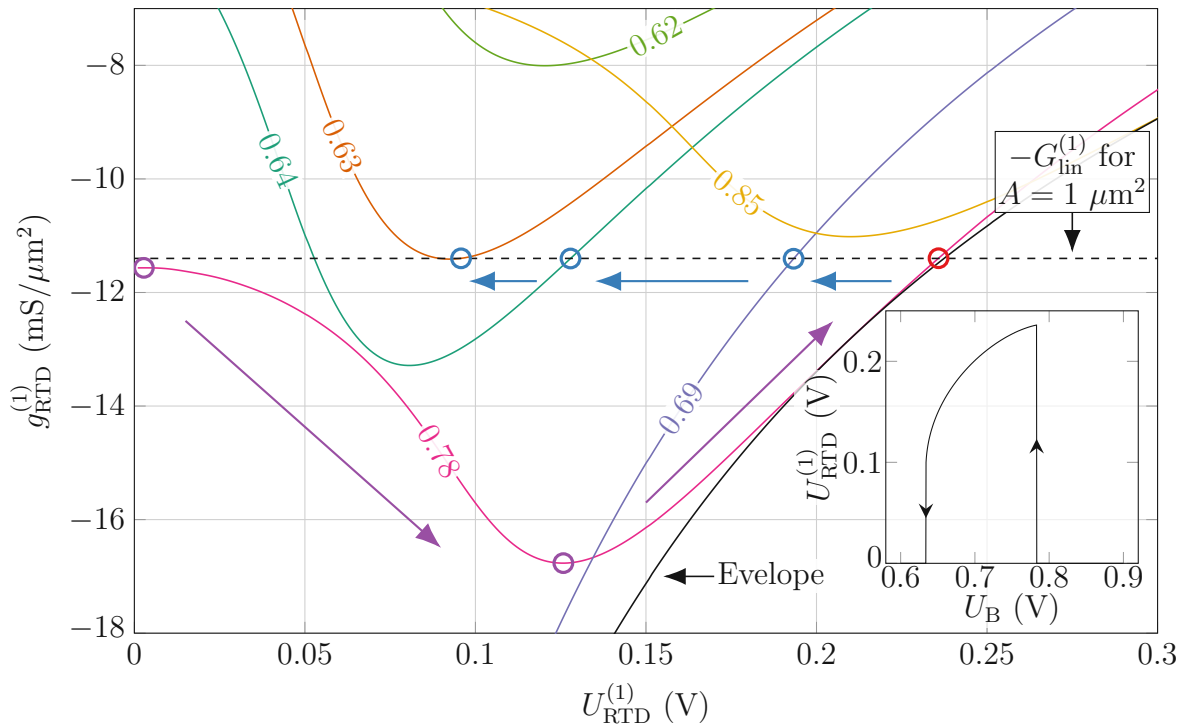


Figure 3.10: The mechanism of the dependence of the oscillating amplitude $U_{\text{RTD}}^{(1)}$ on the bias voltage for the reverse bias sweep for the real RTD IV curve. The parameters of the oscillator are the same as in Fig. 3.9.

approximation fails in predicting the large values of the loading conductance. Nevertheless, in our case, the error near the peak power is approximately 5 to 10 %.

Rigorousness of the analysis

In the above discussion, we treated the problem only from the point of the real part of the RTD admittance. In the rigorous analysis, one also needs to consider the imaginary part and satisfy Eq. (3.28) for all harmonics. As has been stated, the RTD capacitance is also non-linear. Therefore, the oscillation frequency depends on both the bias voltage and the amplitude of the oscillating voltage. The problem can be solved with the method of harmonic balance, assuming that the charge-voltage (Q-V) dependence of the RTD is known. Contrary to the I-V curve, the Q-V dependence for the large-signal response is practically not directly measurable. Moreover, both the RTD large-signal I-V dependence and the Q-V dependence are additionally frequency-dependent. For more details about estimating the frequency-dependent large-signal parameters of RTDs, consult Chapter 5.

3.3.4 Effect of the oscillations on the I-V curve

The nonlinearity of the RTD I-V curve can generate not only the higher harmonics of the current but also a rectified DC current that changes the I-V curve that one measure. We can understand this as the RTD self-rectification of the oscillation voltage. We can show this effect analytically

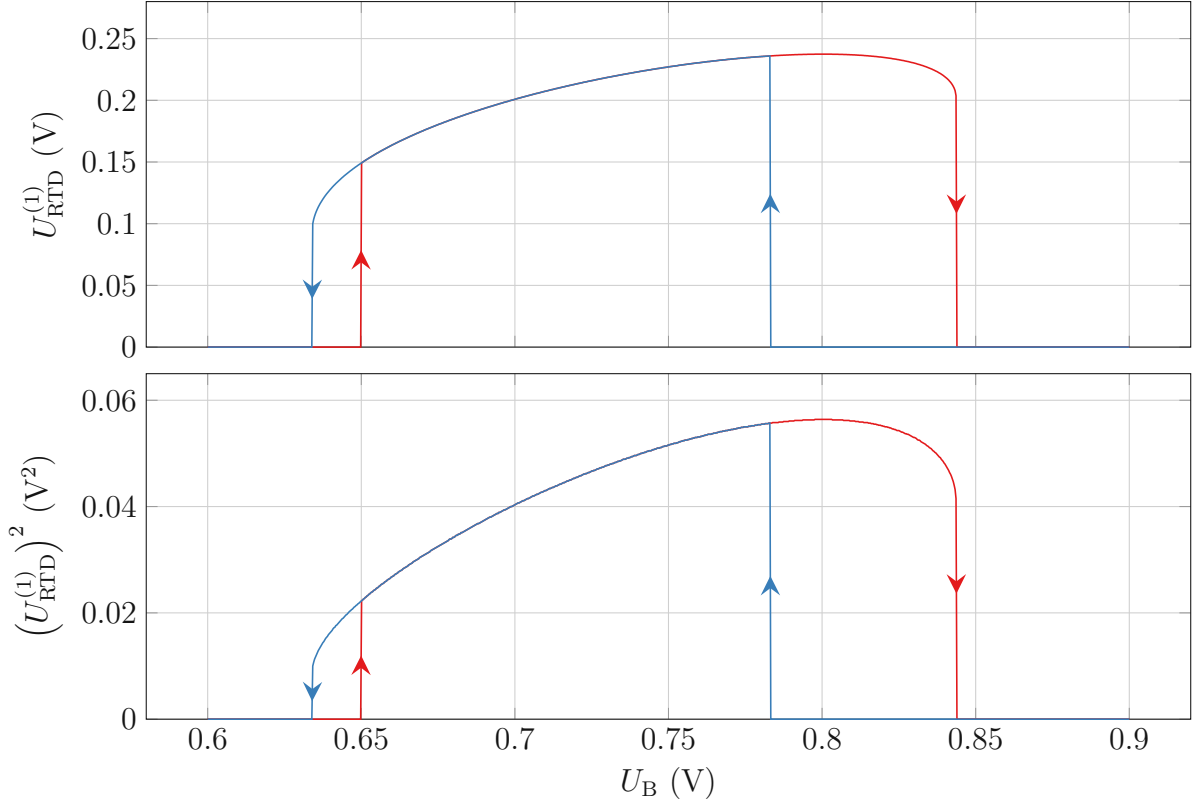


Figure 3.11: The oscillation voltage $U_{\text{RTD}}^{(1)}$ dependence on the bias voltage U_b for the exemplified RTD and the loading conductance. The top plot shows the magnitude of the voltage, and the bottom shows the square magnitude, which is proportional to the output power. The color of the lines then correspond to the forward and backward voltage sweeps. The plots show the hysteresis typical for the RTDs. Also, notice that the oscillations' start and end points do not start with infinite small amplitudes but with already large amplitudes.

with the third-order approximation. If we again apply the voltage Eq. (3.30) to the third order current approximation given by Eq. (3.16) we can write:

$$j = J_0 + g(U_B - U_0) + b(U_B - U_0)^3 + \frac{3}{2}h(U_{\text{RTD}}^{(1)})^2(U_B - U_0) + \left(1 - \frac{(U_{\text{RTD}}^{(1)})^2}{\Delta U^2} - 4\frac{(U_B - U_0)^2}{\Delta U^2}\right)gU_{\text{RTD}}^{(1)}\cos(\omega t) + \text{higher harmonics.} \quad (3.44)$$

The first three terms correspond to the DC current density of a stabilized RTD. The fifth term corresponds to the current of the first harmonic used in the large-signal analysis. The fourth term is an additional DC current representing the rectified oscillating current. If we use the same solution for the amplitude of the oscillation voltage as in Fig. 3.6, we get the I-V curve of the oscillating device shown in Fig. 3.13 (a). The I-V curve for the oscillating system is altered by the self-rectified current, where in its central part, its slope is lower than for the stable system. Next, we show the result of the effect when applied to the I-V curve of the real RTD. Same as for the third-order approximation, we use a constant conductance of the linear circuit with the value of 5 mS. The area of the RTD is also $1 \mu\text{m}^2$. The resulting I-V curve of the oscillating device is

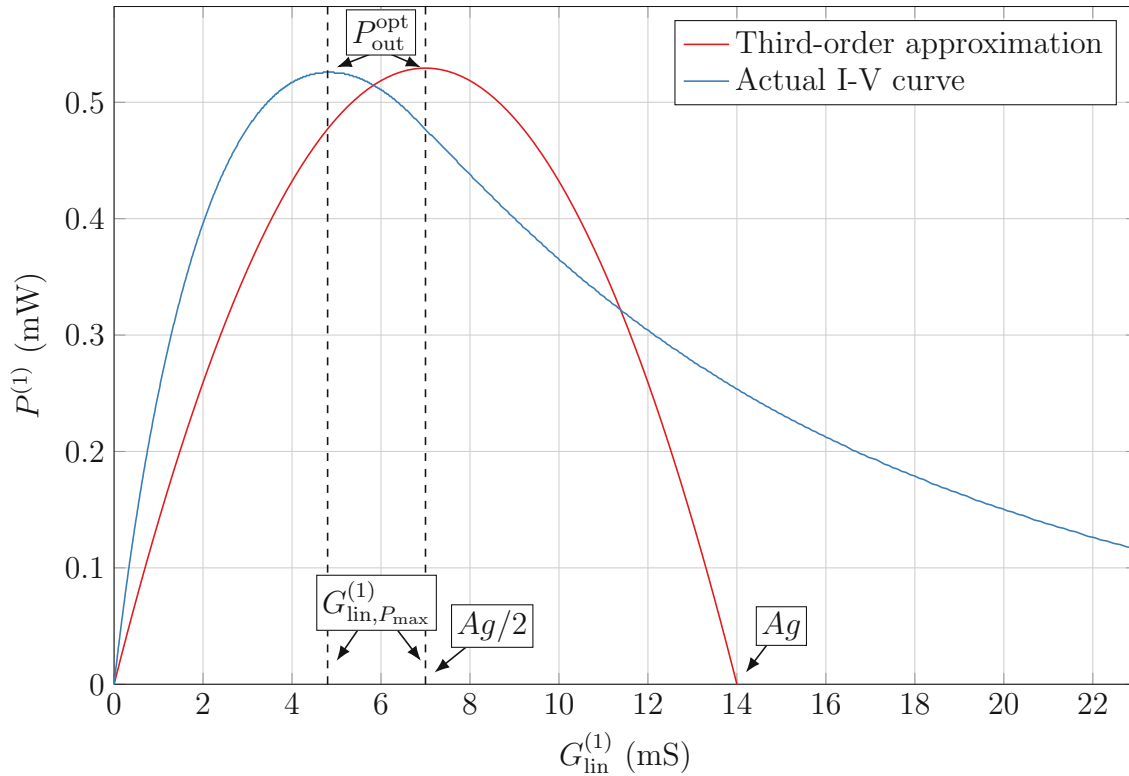


Figure 3.12: Comparison of the output power dependence on the loading conductance $G_{\text{lin}}^{(1)}$ between the estimation from real I-V curve and its third-order fit. The RTD area was in these calculations equal to $1 \mu\text{m}^2$.

shown in Fig. 3.13 (b). The I-V curve is altered in the oscillating region and has a plateau-like character. Additionally, as a consequence of the hysteresis in the oscillating voltage in the bias voltage sweeps, the I-V curve of the real oscillating RTD also shows the hysteresis. Notice that in both cases, exists a point where the I-V is not changed. At this point, the rectified current is zero because the shape of the curve balances it.

3.3.5 Limiting cycle

Similarly, as in the linear case, we can reduce the equivalent circuit of the non-linear oscillator to its simplest form composed of an inductor, capacitor, RTD, and voltage source, as shown in Fig. 3.14. For the third-order polynomial approximation of the RTD I-V curve, we can write the following set of differential equations for the voltage on the capacitor and current the current (already scaled by the RTD area) on the inductors:

$$\frac{du}{dt} = \frac{1}{C_c} (i_L - i_{\text{RTD}}) = \frac{1}{C_c} (i_L - g(u - U_0) - h(u - U_0)^3 - I_0) \quad (3.45)$$

$$\frac{di_L}{dt} = \frac{1}{L} (U_0 - u) \quad (3.46)$$

We can then plot the time derivatives of u and i_{RTD} in their phase space $u-i_{\text{RTD}}$ as is shown in Fig. 3.15, where we choose example circuit parameters to be $L = 0.1 \text{ pH}$, $C = 10 \text{ fF}$, and

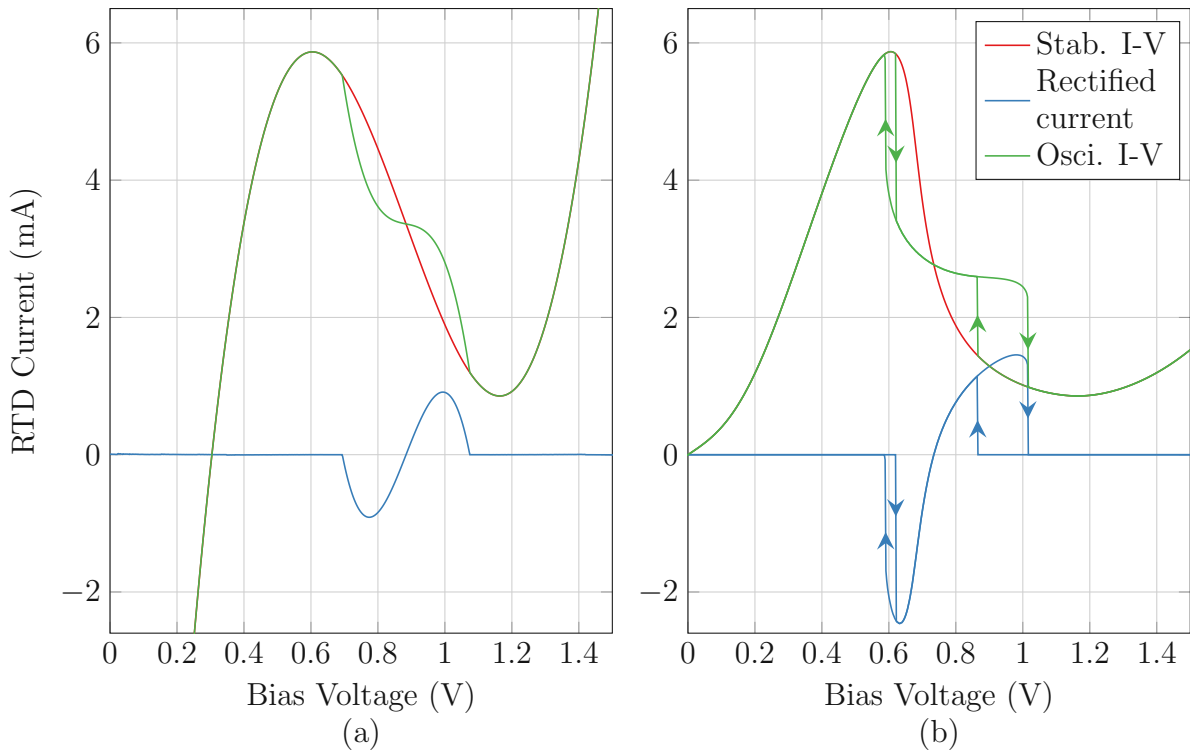


Figure 3.13: Example of the self-rectification of the third-order fit of an RTD I-V curve. The RTD area in the calculations was $1 \mu\text{m}^2$, and the load conductance was 5 mS.

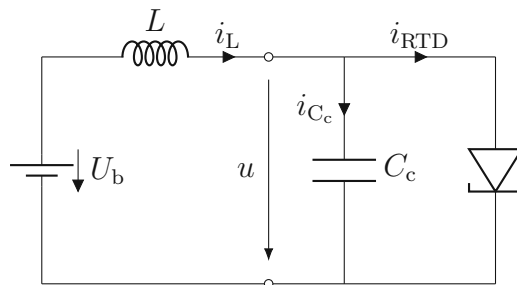


Figure 3.14: Simple equivalent circuit of an RTD oscillator with the DC bias source.

the I-V curve is the third order fit of our example RTD. We put $G_{\text{lin}}^{(1)} = 0 \text{ mS}$ for clarity. The figure shows the trajectory of rising oscillations and the limiting cycle to which the oscillations converge. The initial conditions were, in this case, $u = U_0$ and $i = I_0 + 0.001 \text{ mA}$. The adjoined plots then show the current and voltages in the time domain. The parameters we have chosen are close to those of the real RTD oscillators. The time domain plots show that although the RTD current is highly influenced by its higher harmonics, the voltage in the circuit is nearly higher harmonics free. Because the oscillator is not loaded by the conductance, the oscillations voltage amplitude are reaching the maximal voltage of $\approx 0.55 \text{ V}$.

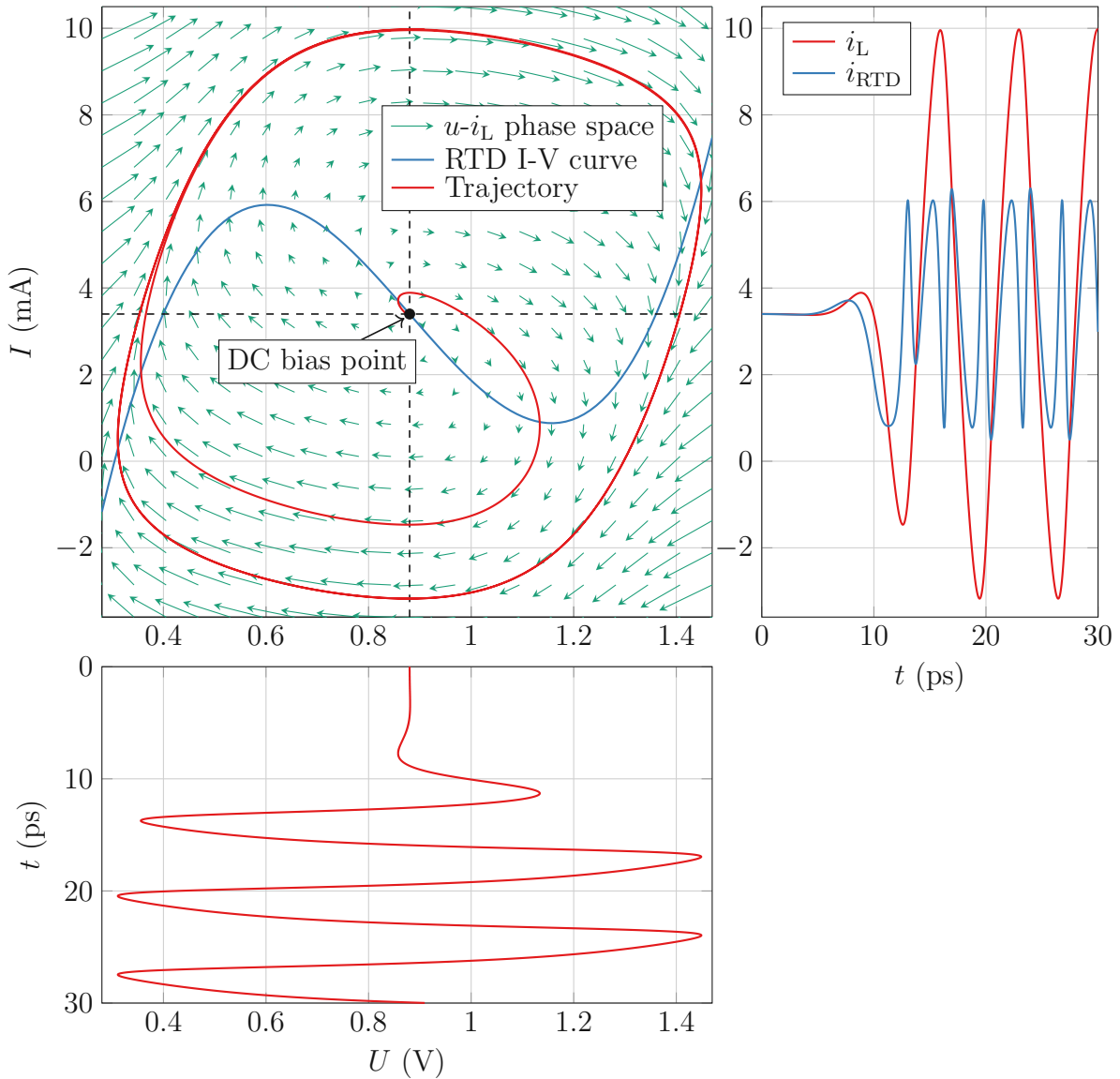


Figure 3.15: Phase space of a non-linear RTD oscillator. The parameters of the oscillator were $L = 0.1$ pH, $C = 10$ fF, and the I-V curve is the third-order fit of our example RTD. The bias voltage was set up to the center of the NDC region. The red spiral line is a trajectory of the rise of the oscillations for initial conditions $u = U_0$ and $i = I_0 + 0.001$ mA. The oscillations are reaching the limiting cycle. The adjunct plots show the oscillations of the corresponding quantities in the time domain.

3.4 Power generation mechanism

In Fig. 3.13, we have shown how oscillations alter the I-V. In that case, the oscillator was loaded by a conductance on which power was dissipated due to the oscillation voltage. However, from the I-V curve, we can observe that the DC current can be the same for the oscillating and stable RTD. Therefore, the oscillating system consumes the same DC power from the external bias source as the stable system, yet there is the power dissipated on the load in the oscillating case. At first glance, this might indicate that the energy conservation law is violated. In this section, we explain the origin of the power dissipated on the load and show that the power is conserved.

We can determine the power dissipated on the RTD from:

$$P_{\text{RTD}} = A \frac{1}{T} \int_0^T u_{\text{RTD}} j_{\text{RTD}} dt. \quad (3.47)$$

The oscillator operates in the harmonic steady-state mode and thus we can distinguish the power of the corresponding harmonics as:

$$P_{\text{RTD}} = P_{\text{RTD}}^{(0)} + P_{\text{RTD}}^{(1)} + \text{higher harmonics}, \quad (3.48)$$

where $P_{\text{RTD}}^{(0)}$ is the DC power dissipated on the RTD and $P_{\text{RTD}}^{(1)}$ is the dissipated power from the first harmonic. If we apply the approximated voltage (neglecting higher harmonics) given by Eq. (3.30) and use the current from the third-order approximation by Eq. (3.44) we can write for the DC power:

$$P_{\text{RTD}}^{(0)} = U_{\text{B}} \left(J_0 + g(U_{\text{B}} - U_0) + b(U_{\text{B}} - U_0)^3 + \frac{3}{2} h \left(U_{\text{RTD}}^{(1)} \right)^2 (U_{\text{B}} - U_0) \right), \quad (3.49)$$

and for the power of the first harmonic:

$$P_{\text{RTD}}^{(1)} = \frac{1}{2} \left(U_{\text{RTD}}^{(1)} \right)^2 \left(1 - \frac{\left(U_{\text{RTD}}^{(1)} \right)^2}{\Delta U^2} - 4 \frac{(U_{\text{B}} - U_0)^2}{\Delta U^2} \right) g. \quad (3.50)$$

Setting the bias to the center of the NDC region ($U_{\text{B}} = U_0$) and remembering that g is negative, results in the power $P_{\text{RTD}}^{(1)}$ being negative for $U_{\text{RTD}}^{(1)} < \Delta U$; in this case $P_{\text{RTD}} < P_{\text{RTD}}^{(0)}$. The excess of the power, $P_{\text{RTD}} - P_{\text{RTD}}^{(0)}$, is equal to the power delivered to the load $P^{(1)}$ defined in Eq. 3.35 and thus $P^{(1)} = -P_{\text{RTD}}^{(1)}$. This is where the heart of power generation lies: **when the voltage on the RTD is oscillating the RTD consumes less power than is delivered from the external power source; the excess of the power ($-P_{\text{RTD}}^{(1)}$) is then delivered to the load.** For details see Fig. 3.16 which shows this principle for two cases of the bias voltage for our example RTD. Notice that when the bias is at the center of the NDC, $P_{\text{RTD}}^{(0)}$ is strictly equal to a power that is dissipated when the RTD is stable ($P_{\text{RTD}}^{(0)}$ is constant). This means that in the oscillating case, the oscillator (the system) still consumes the same power as in the stable case, yet $P_{\text{RTD}} < P_{\text{RTD}}^{(0)}$, so the RTD consumes less. This property is a direct consequence of the NDC (negative g).

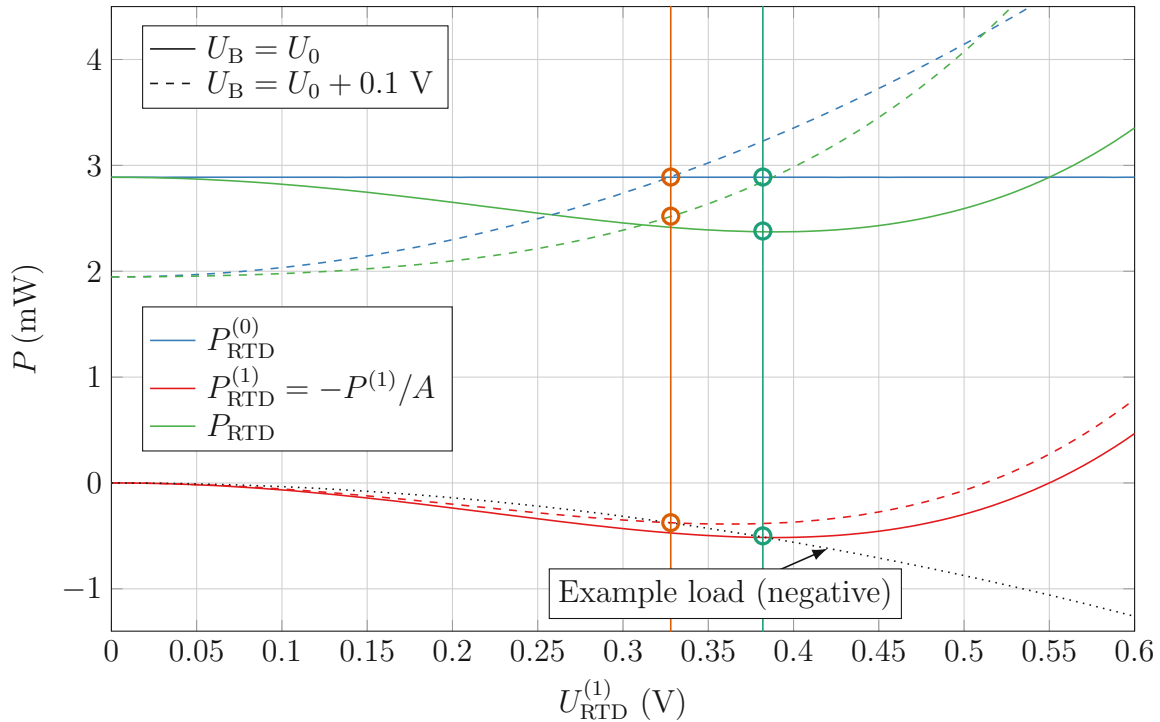


Figure 3.16: Power dissipation on the example RTD with the active area of $1 \mu\text{m}^2$ for the bias at the center of the NDC and if deviated from it by positive 0.1 V. The dotted line shows a negative value of power dissipated on an external load (7 mS for $1 \mu\text{m}^2$ RTD). The vertical lines and the corresponding points mark the solutions of the large-signal oscillation conditions for the external load.

If we change the bias, then $P_{RTD}^{(0)}$ can be higher or lower than would be for the stable system. Nevertheless, $P_{RTD}^{(1)}$ is still negative in this case for stable oscillations ($P_{RTD} < P_{RTD}^{(0)}$) and this excess is delivered to the load. For details, see Fig. 3.16, which shows this principle for two cases of the bias voltage for our example RTD.

A simplified example comparing devices with NDC and with PDC is shown in Fig. 3.17. The figure shows that the device with NDC consumes less energy when the voltage on it oscillates than at the stable bias point over the same time. Meanwhile, the device with PDC consumes more for the oscillating voltage. We have chosen linear versions of PDC and NDC here as they clearly show the principle. For nonlinear devices, we also need to consider self-rectification and, thus, the change of their bias DC current.

We were discussing this topic in the harmonic steady-state where the large-signal oscillation conditions are satisfied. When the oscillations are starting, the harmonic steady-state analysis is not rigorously applicable anymore. However, we can still say that when the oscillations are starting, there would be an additional excess of power (the powers are not balanced in the steady-state, see the difference between the dotted line and the red line in Fig. 3.16 before the solution points), which would be charging the LC resonant circuit until the large-signal oscillation conditions would be satisfied.

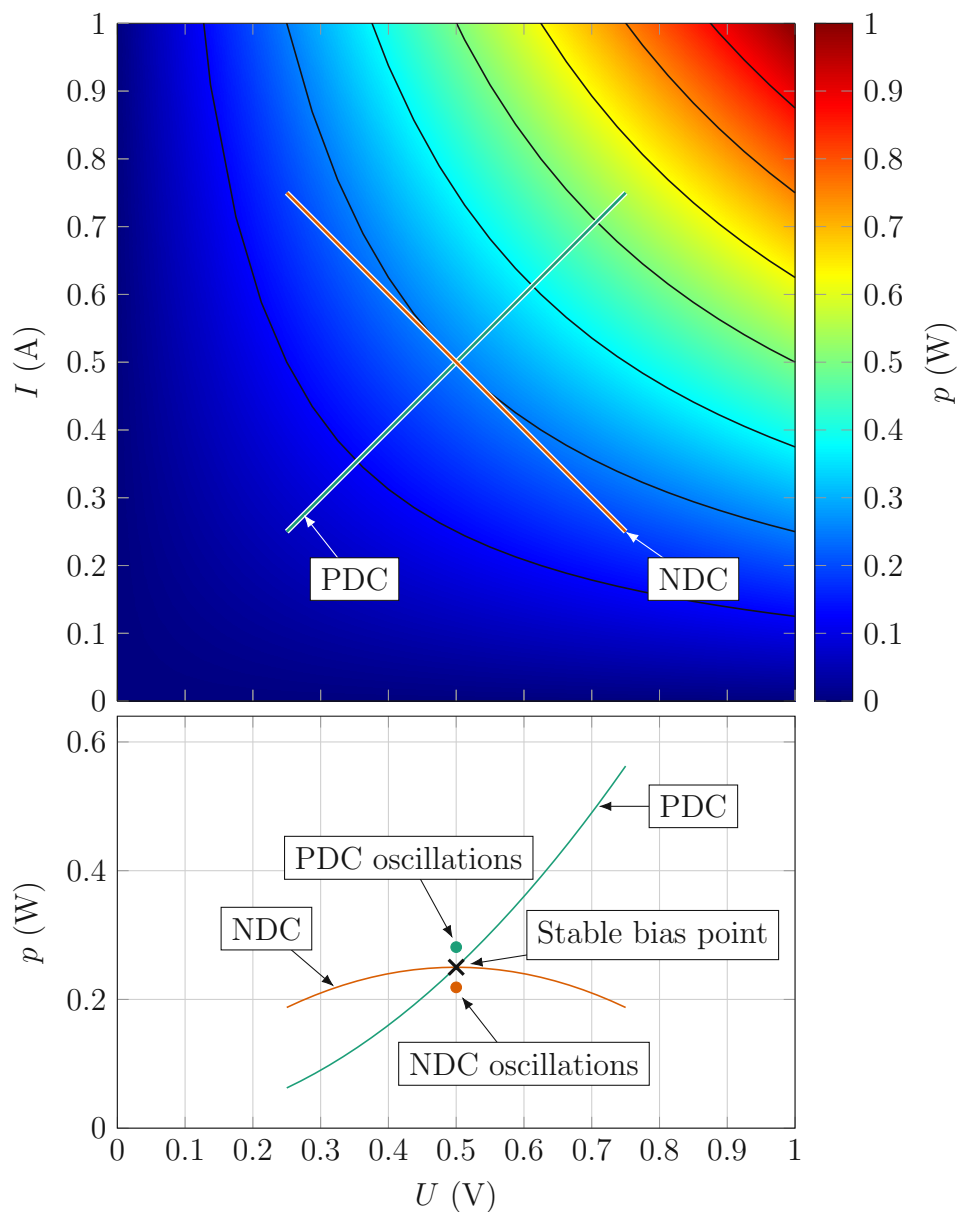


Figure 3.17: Idealized example visualization of the power relations for devices with PDC and NDC. The top plot shows voltage sweeps with an amplitude of 0.5 V and bias voltage also of 0.5 V on I-V curves of the PDC and NDC devices and a corresponding map of the instantaneous power $p = ui$. The bottom plot shows the instantaneous powers for both of the devices. The total power consumed by the device with the NDC when the voltage oscillates is lower than over the same time when the voltage is stationary at the bias point. However, due to the linearity, the DC power consumed from the source is equal to the power at the stable bias point. The excess power is delivered to the load. Meanwhile, the device with PDC consumes more when the voltage is oscillating, which would need to be supplied to the oscillator for stable oscillations.

3.5 Output power and its limitation

In this section, we establish the upper bound on the output power of the RTD oscillators. This shows results that were partly published in the peer-reviewed journal article C. Spudat, P. Ourednik, G. Picco, *et al.*, “Limitations of output power and efficiency of simple resonant-tunneling-diode oscillators,” *IEEE Transactions on Terahertz Science and Technology*, vol. 13, no. 1, pp. 82–92, 2023. DOI: 10.1109/TTHZ.2022.3228069.

The output power of the oscillator that is delivered to a load conductance $G_{\text{load}}^{(1)}$ can be reformulated from Eq. (3.35) as:

$$P_{\text{out}} = \frac{1}{2} \eta G_{\text{lin}}^{(1)} \left(U_{\text{RTD}}^{(1)} \right)^2, \quad (3.51)$$

where η is the system efficiency which we define as $\eta = G_{\text{load}}^{(1)} / G_{\text{lin}}^{(1)}$, in which $G_{\text{lin}}^{(1)}$ is (in the simplest case) the parallel combination of $G_{\text{load}}^{(1)}$ and of a conductance $G_{\text{loss}}^{(1)}$. $G_{\text{loss}}^{(1)}$ represents the parasitic conductance (losses) of the system. $U_{\text{RTD}}^{(1)}$ is still understood to be function of $G_{\text{lin}}^{(1)}$ and of the RTD properties.

Having defined $P_{\text{RTD}}^{(0)}$ from the previous sections and P_{out} we can directly define the DC-to-RF effectivity as:

$$\eta_{\text{DC-to-RF}} = \frac{P_{\text{out}}}{P_{\text{RTD}}^{(0)}}. \quad (3.52)$$

Its value depends on the exact I-V curve.

In practical systems, $G_{\text{load}}^{(1)}$ is usually limited to a certain value. For example, suppose we want to radiate the generated power by an antenna directly connected to the RTD. In that case, $G_{\text{load}}^{(1)}$ is the radiation conductance of the antenna, which is confined to a value that depends on the antenna geometry and the oscillation frequency. We can then ask a question: what is the maximum power that RTD can generate for the specific load? If we keep $\eta G_{\text{lin}}^{(1)}$ in Eq. (3.51) constant, the output power is maximized, when $U_{\text{RTD}}^{(1)}$ is maximized. In practical applications, one is also limited by the RTD design of the RTD wafer, which determines the I-V curve of the RTD, i.e., the peak current density, peak-to-valley ratio, and ΔU . Thus, to find the maximum power for the specific output conductance, we have restricted ourselves only to the change in the RTD area.

We use the third-order approximation of the I-V curve to simplify the analysis. Further, we set the bias point to the center of the NDC region where we have shown the output power is maximal. In this case $U_{\text{RTD}}^{(1)}$ is given from Eq. (3.41), and if we let $A \rightarrow \infty$ we obtain the maximum power:

$$P_{\text{out}}^{A \rightarrow \infty} = \frac{1}{2} \eta G_{\text{lin}}^{(1)} \Delta U^2. \quad (3.53)$$

Therefore, the maximum output power depends only on the conductance of the load, and on the voltage difference between the peak and valley current. We have to note that this power represents the unattainable upper bound. It is because in practical oscillators, the oscillation conditions need to be satisfied, and to compensate for the large capacitance of the RTD due to

the large area, we need to compensate with the resonator geometry. However, this compensation ordinary leads to a decrease of η . The peak current density of the RTD does not play a role in Eq. (3.53), and thus it is only ΔU^2 that determines the maximum power. The peak-to-valley current difference, and the capacitance per unit area of the RTD then only determine how close one can get to the maximum power. Increasing the current difference increases the magnitude of g which allows using of smaller areas to achieve the same output voltage (Eq. (3.41)). For a detailed discussion about the output power limitation, see [130].

Similarly, we can write for the DC-to-RF efficiency for the third-order approximation as:

$$\eta_{\text{DC-to-RF}} = \frac{\eta G_{\text{lin}}^{(1)} \Delta U^2}{2AU_0 J_0} \left(1 + \frac{G_{\text{lin}}^{(1)}}{Ag} \right). \quad (3.54)$$

which shows that for $A \rightarrow \infty$ the efficiency $\eta_{\text{DC-to-RF}}^{A \rightarrow \infty} \rightarrow 0$.

The above-presented principle of the maximal output power can be quite easily graphically illustrated on the dependence of the RTD conductance on the squared amplitude of the oscillation voltage. In Fig. 3.18, the highlighted areas are proportional to the partial powers in the system. The generated power is the power generated by the RTD; the potential output power is the power that would be delivered to $G_{\text{load}}^{(1)}$ if not for parasitic; and output power is the actual power delivered to $G_{\text{load}}^{(1)}$. The output power corresponds to the intersection between the generated and potential output power. With increasing area (or with increasing g by change of the RTD), the slope of the RTD conductance is increased, which increases the output power until the line is entirely vertical, which marks the maximal attainable power. The plot also shows that the simple parasitic losses (parallel connection of the parasitic loss conductance with the active load) always decrease the output power. Notice that with the increasing area, the effect of the losses on the output power decreases. In practical systems $G_{\text{load}}^{(1)}$ decreases with A .

The above-described principle is valid not only for the third-order approximation but also for real RTDs. The envelope function of the gain plot in Fig. 3.8 is a monotonous function of the voltage, and thus increasing the active area of the RTD leads to the same behavior of power limitation as was shown in Fig. 3.18. For our example real RTD the maximum squared voltage is $\approx 0.72 \text{ V}^2$. However, because of the concave shape of the envelope function, the power limits to is maximum slower with the area (for antenna conductances \lesssim the maximal RTD conductance) than for the third-order approximation.

The slot antenna on a semiconductor substrate is a standardly used antenna for the RTD oscillators and its maximal radiation conductance is $\approx 7 \text{ mS}$ at the $\lambda/2$ resonance, see [130]. This conductance results in the upper bound of the output power for our example RTD in $\approx 2.5 \text{ mW}$ if we use the actual I-V and $\approx 1.1 \text{ mW}$ for the third order approximation. However, as we stated above, this bound is not achievable, because in practical RTD oscillators if $A \rightarrow \infty$ then due to the capacitive loading of the antenna $G_{\text{load}}^{(1)} \rightarrow 0$, and thus the output power $\rightarrow 0$. Therefore, there exist an achievable maximum of the output power for finite areas of the RTD, that depends on the radiation conductance, parasitic losses, the susceptance of the antenna,

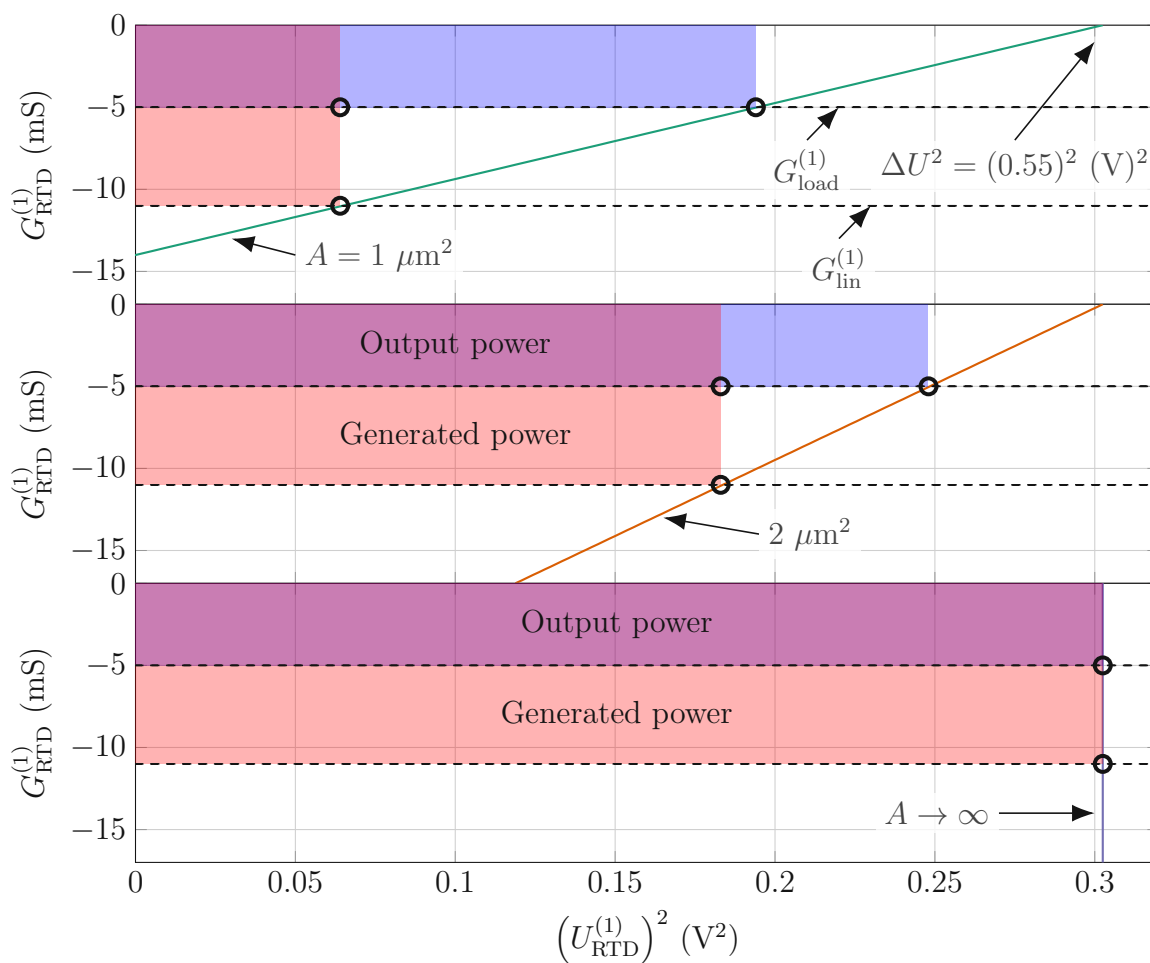


Figure 3.18: Graphical illustration of the output power dependency on the RTD area. The full line is the conductance dependence on the squared amplitude of the oscillation voltage. The dashed lines correspond to $G_{\text{load}}^{(1)}$ and $G_{\text{lin}}^{(1)}$. The circles mark the solutions for the voltage amplitudes. The powers in the system are proportional to the highlighted areas. The red shading corresponds to the power delivered into the total load $G_{\text{lin}}^{(1)}$. The purple shading corresponds to the output power if the oscillator would have $\eta = 1$. The area from the intersection of these then corresponds to the actual output power delivered to $G_{\text{load}}^{(1)}$.

and on the RTD parasitics. This maximum can be found by optimization of the RTD area using the large-signal analysis described in this chapter. We show the theoretical prediction and experimentally confirmation of this maximum in Chapter 4.

What we have so far described is valid if the load and the loss conductances are connected directly in parallel to the RTD. In practical systems, there can exist various parasitic separating the load and the RTD (for example, the contact impedance of the RTD or an impedance transformer) that transforms the value of the RTD oscillation voltage to a voltage at the load conductance. Eq. (3.51) is still valid also in these cases, however, the definition of η needs to take into account this transformation effect, and $G_{\text{lin}}^{(1)}$ needs to include the additional circuitry, see [100].

We should add that the above-described approach is in contrast to an optimization of the power by change of the loading conductance $G_{\text{load}}^{(1)}$ while keeping the RTD parameters and its

area constant as was done in Refs. [100], [130], [132]. For the third order approximation of I-V curves, we can derive this optimum using Eq. (3.41) and Eq. (3.39) in Eq. (3.50) and searching for its inflection point for $G_{\text{lin}}^{(1)}$ we get:

$$P_{\text{out}}^{\text{opt}} = \frac{3}{16} \eta A \Delta U \Delta J, \quad (3.55)$$

for

$$G_{\text{lin}, P_{\text{max}}}^{(1)} = -\frac{Ag}{2}. \quad (3.56)$$

The maximum output powers for the RTD area of $1 \mu\text{m}^2$, for the actual I-V curve and its third-order polynomial approximation, are shown in Fig 3.12. For the conductance $G_{\text{lin}, P_{\text{max}}}^{(1)}$, the DC-to-RF efficiency is also the highest, and we can express it as:

$$\eta_{\text{DC-to-RF}}^{\text{max}} = \frac{3}{16} \eta \frac{\Delta U \Delta J}{U_0 J_0}. \quad (3.57)$$

For typical values of state-of-the-art RTD oscillators $\eta \approx 0.05$, $\Delta U \approx 0.5 \text{ V}$, $\Delta J \approx 10 \text{ mA}/\mu\text{m}^2$, $U_0 \approx 0.5 \text{ V}$, and $J_0 \approx 10 \text{ mA}/\mu\text{m}^2$, we get that the maximum DC-to-RF efficiency is $\approx 1 \%$.

The fact that the $P_{\text{out}}^{\text{opt}}$ and $\eta_{\text{DC-to-RF}}^{\text{opt}}$ happens for the same $G_{\text{lin}}^{(1)}$ is valid only for the third-order approximation and is generally invalid for I-V curves of real RTDs, see [130]. Also, the optimum power and the maximum efficiency values differ for the real RTD from the values derived here. However, the tools derived in this chapter can be easily used to obtain these.

3.6 Conclusions

In this chapter, we have presented the well-known analysis of the RTD oscillators. We have derived the small-signal oscillation conditions for RTD oscillators, and we have shown their operation principle of the amplitude rise in the time domain. Next, we have presented a method for determining the oscillation amplitude and the output power. Based on this, we have derived large-signal oscillation conditions. Next, we have explained the nature of the hysteresis, the plateau-like character of I-V curves, and the dependence of the oscillating voltage on the bias voltage. We have described the mechanism of power generation and shown why the system can generate power.

Besides the well-established analysis, we have derived here the fundamental power limitation of RTD oscillators delivered to a load with specific load conductance, which is proportional to the squared voltage difference between the peak current and the valley current. We have also shown that parasitic losses can only decrease the output power in a system without contact parasitic. This part represents an original scientific contribution that was published in a peer-reviewed journal, see [130].

Chapter 4

Double-RTD Oscillator

In this chapter, we describe the concept of double-RTD patch antenna oscillators, which allows us to build the true chip-size sub-THz and THz oscillators. The concept offers the advantages of simplicity, compactness, high isolation of the oscillator from the external biasing circuitry, and substantial output powers comparable with the output powers of more complex chip-sized oscillators. Using this concept and operating 1.6 nm RTDs resulted in output power of 10 μW at the fundamental frequency of 525 GHz and 70 μW at 330 GHz. The relatively thick barrier RTD allowed us to use solely optical lithography processes. The presented oscillators represented an order-of-magnitude increase in the output power compared to previous reports on patch-antenna RTD oscillators.

Next, we present an optimized design of the double-RTD patch antenna oscillators, in which to achieve operating frequencies over 1 THz, we have reduced the influence of the system's parasitics. The patch antenna's parasitics were reduced by replacing the slanted bridges connecting the RTDs with conical vias, which decreased the parasitic inductance of the antenna. Further, instead of 1.6 nm barrier RTDs we implemented 1.0 nm barrier RTDs. These changes resulted in the oscillator operating with an output power of 9 μW at the fundamental frequency of 1.09 THz, 15 μW at 0.98 THz, and up to 27 μW at the lower frequencies of 620-660 GHz.

In the further part of the chapter, we show examples of potential real-life applications of RTD oscillators. The fabricated oscillators were used as sources for sub-THz FMCW radar and optical coherent tomography. For these applications, an RTD oscillator operating at 680 GHz, with a bandwidth of 38 GHz, and output power of 23 μW provided a spatial resolution of 4 mm. We have used frequency tuning of the RTD by the sweep of its bias, which course needed to be corrected to achieve reliable operations.

In the final part of the chapter, we describe well-known measurement methods used to characterize the presented oscillators.

4.1 Sub-THz chip-size double-RTD oscillator with patch antenna

Results shown in this section were partly published in the peer-reviewed journal article P. **Ourednik**, T. Hackl, C. Spudat, *et al.*, “Double-resonant-tunneling-diode patch-antenna oscillators,” *Applied Physics Letters*, vol. 119, no. 26, 263509, 2021. DOI: 10.1063/5.0068114.

4.1.1 Operation principle

The most direct and simple way to build a chip-size RTD oscillator is to use a single resonant patch antenna that acts simultaneously as a resonator and a radiator. The RTD is, in this case, directly connected to the antenna. The RTD oscillator in this configuration emits upwards from the chip. This approach demonstrated the fundamental oscillation frequency of 517 GHz with the output power in the 1 μ W range; at \approx 330 GHz, the output power was in the 10 μ W range, see [82]. In this section, we describe a design that solves issues of this approach of the simple patch oscillators and demonstrate an order of magnitude higher output power at similar and slightly higher frequencies than previously reported.

In the simplest configuration, as was done in [82], an RTD patch-antenna oscillator contains only a single RTD. However, a symmetric double-RTD (DRTD) configuration we study in this chapter, which schematic is shown in Fig. 4.1, has several advantages. First, a DRTD oscillator can potentially generate higher output power, and we demonstrate that. However, the radiation efficiency of an antenna drops with larger RTD areas due to a larger capacitive load, see Fig. 4.8. This behavior determines an optimum relation between the patch-antenna dimensions and RTD area. Second, we design the oscillator to operate in an asymmetric mode, i.e., there is a phase difference of π between the AC voltages on the RTDs. That guarantees that the RTD oscillator is strictly decoupled from the external circuitry at its fundamental oscillation frequency since the bias line is connected at the node of the electric field distribution in the patch antenna, see Fig. 4.1.

The symmetry of the oscillator does not fully solve the decoupling issue because the RTDs can also operate in a symmetrical mode (AC voltages are in phase at both RTDs). The patch antenna in this mode is typically strongly coupled to the bias line (see Fig. 4.1) and the external, with respect to the patch, parts of the oscillator. This mode needs to be suppressed. Otherwise, it might become the fundamental oscillation mode. The characteristics of this mode are determined by the parameters of the patch antenna with RTDs, bias line, metal-insulator-metal (MIM) capacitor, and a shunt resistor. The parameters of these elements are chosen so that the mode is shifted to low frequencies and attenuated (the oscillation conditions for the must not be fulfilled mode). To increase the damping, we choose to make the bias line fabricated on a thin dielectric (\approx 160 nm Si_3N_4) and make the line relatively long, with a length of 250 μm . The shunt resistor also contributes to the damping of the symmetrical mode. However, to maximize the

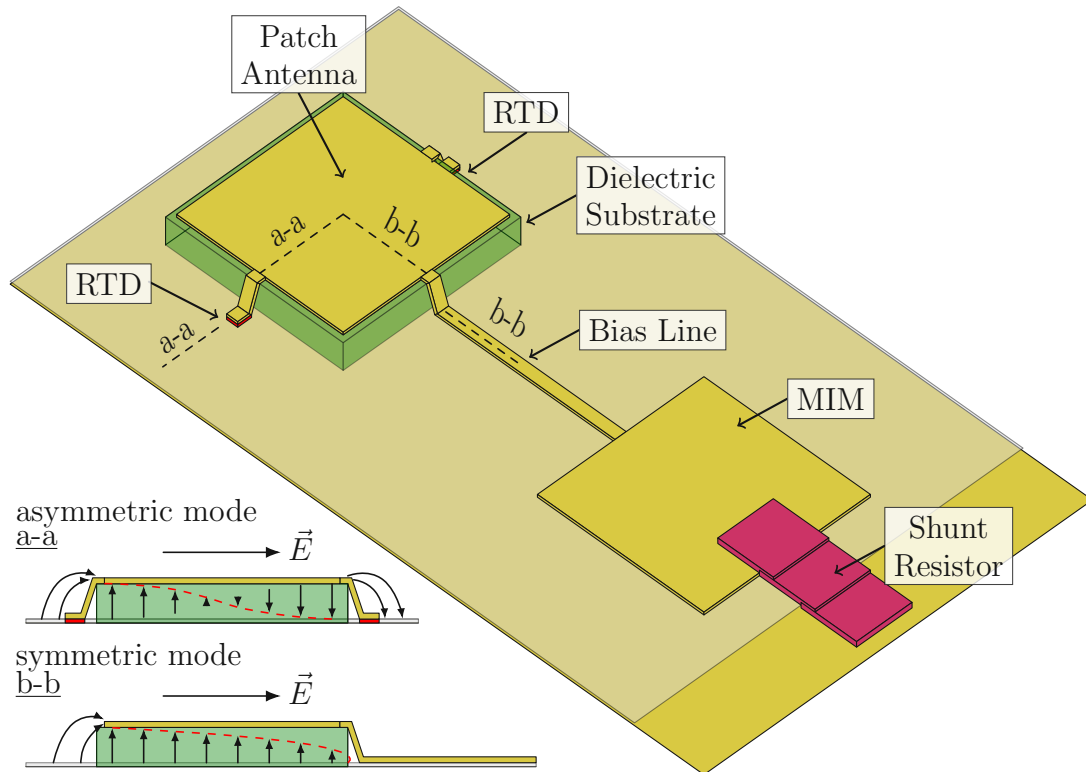


Figure 4.1: Sketch of the proposed design. The RTDs are symmetrically connected to the patch antenna. They are biased through the bias line, which is terminated by a MIM capacitor and a shunt resistor to suppress low-frequency parasitic oscillations. The insets show the sketches of the electric field distribution in the patch antenna in the cross-section planes “a-a,” and “b-b” perpendicular to the ground plane for asymmetric and symmetric modes, the polarization of the emitted radiation is also indicated. See also the distribution of the electric field at the surface of the ground plane in Fig. 4.2.

attenuation contribution from the shunt resistor, its resistance should match the impedance of the parallel plate waveguide formed by the MIM, which is difficult to achieve due to the MIM’s low impedance. In addition, the shunt provides isolation of RTD’s NDC from the biasing circuit. When the sum of the RTD conductance and that of the shunt is positive, the shunted RTD is unconditionally stable from the point of view of the external biasing circuitry.

Electric field distribution

Figure 4.2 shows the plots for the electric-field component normal to the ground plane of the oscillator for asymmetric and symmetric oscillation modes, illustrating the origin of the emitted polarization and the operating principle of the oscillators. For the example shown in Fig. 4.2 we choose a $150 \mu\text{m}$ patch antenna with $6 \mu\text{m}^2$ (double) RTD area.

The electric-field polarization of the oscillating asymmetrical mode, shown in Fig. 4.2(a), is in the y-direction, i.e., along a line connecting two RTDs. The node of the mode is in the middle of the patch between two RTDs. On the other hand, the polarization of the lowest-order symmetrical mode, see Fig. 4.2(b), is in the perpendicular direction, and its node is near the

connection point between the microstrip bias line and the MIM capacitor.

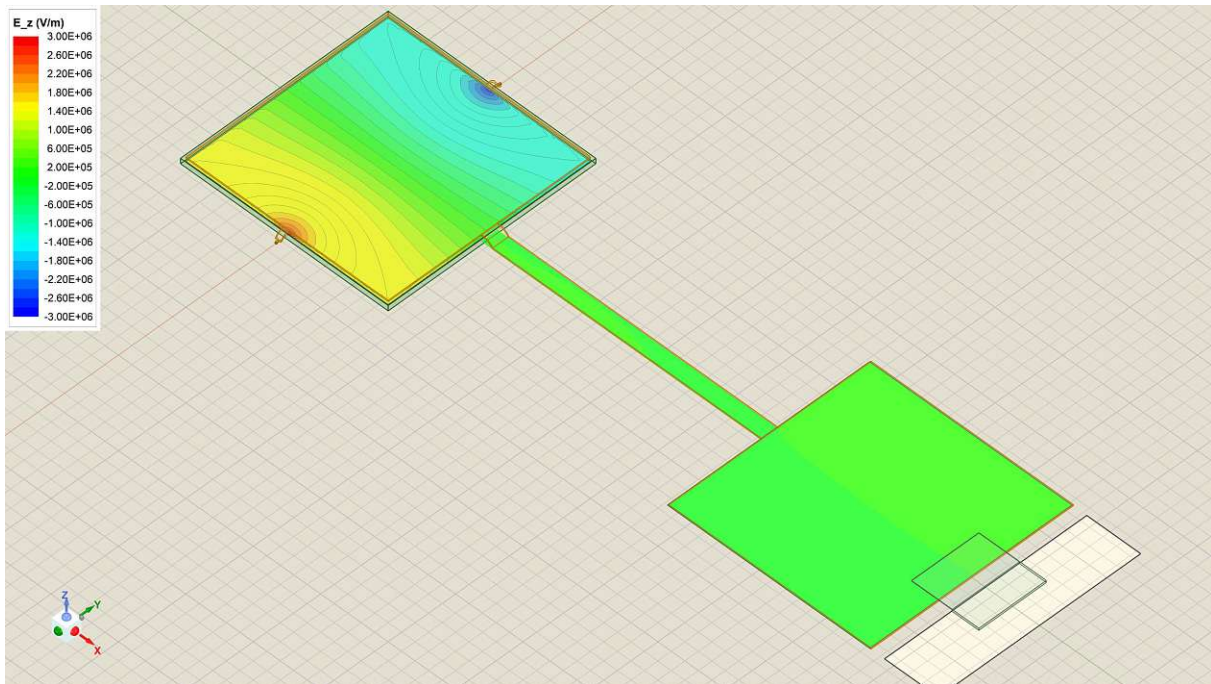
4.1.2 1.6 nm RTD

The essential parts of the oscillator are the RTDs, which have to provide sufficiently high NDC to compensate for the ohmic and radiation losses, as was shown in Chapter 3. In this case, we intentionally choose an RTD design with relatively thick barriers of 1.6 nm and rather low current density ($<10 \text{ mA}/\mu\text{m}^2$) when compared with the state-of-the-art RTD oscillators, see Chapter 2 or Refs. [71], [106]. Although that inevitably leads to frequency and power limitations of our oscillators, that has allowed us to use rather large-area RTDs in the oscillators and to rely only on the optical lithography for the fabrication of the devices.

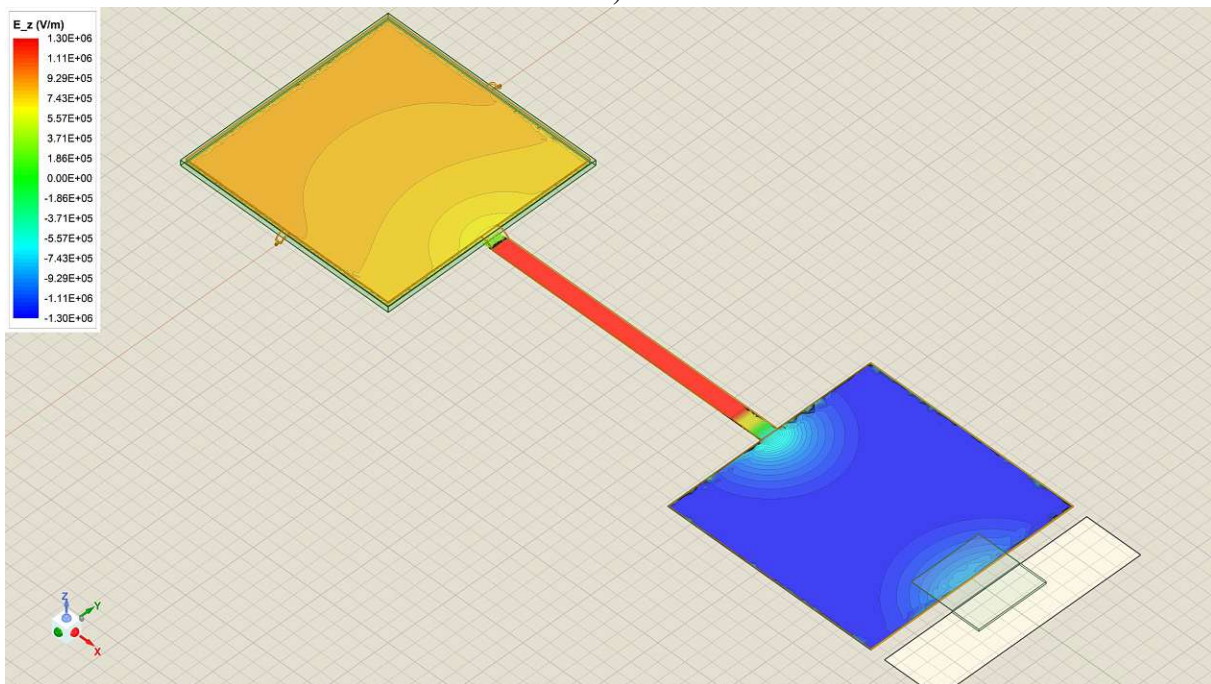
In this work, we have been using InGaAs/AlAs RTDs grown on an InP substrate with the design of the layers similar to the one used in the RTD oscillators (with diverse RTD-barrier thicknesses) in the past, see [90], [105], [133], [134]. Our RTDs had 1.6 nm AlAs barriers sandwiching a composite $\text{In}_{0.53}\text{Ga}_{0.47}\text{As}/\text{InAs}/\text{In}_{0.53}\text{Ga}_{0.47}\text{As}$ quantum well (QW) with the nominal thickness of each sublayer of 1.2 nm. The barriers are surrounded by $\text{In}_{0.53}\text{Ga}_{0.47}\text{As}$ layers, which are n-doped at the level of $1.5 \times 10^{18} \text{ cm}^{-3}$ except for 1.2 nm undoped spacers immediately next to the barriers. The more distant n++ $\text{In}_{0.53}\text{Ga}_{0.47}\text{As}$ layers were doped at the level of nominally $5 \times 10^{19} \text{ cm}^{-3}$. The RTDs' measured and simulated I-V curves are shown in Fig. 4.3. The peak current density of the RTDs is $5.8 \text{ mA}/\mu\text{m}^2$ with a peak-to-valley current ratio of 8.9 as measured on test RTDs on the same wafer. The measured I-V curve of an oscillating RTD in Fig. 4.3 was obtained by subtracting the shunt current, ensuring that the peak-to-valley current ratio corresponds to that of the test RTDs. The roll-off of the RTD conductance (G_{RTD}) and also capacitance (C_{RTD}) with frequency is determined by the RTD charge-relaxation time (τ_{rel}), which is defined both by the electron tunnel lifetime in the QW and also essentially by the Coulomb-interaction effects, see Chapter 2 and [102]–[104], [125]. At the frequencies around 500 GHz, our RTDs are working in the regime, where $\omega\tau_{\text{rel}} \sim 1$, therefore the conductance roll-off effects are becoming significant for the frequency limitation of our RTD oscillators.

4.1.3 Analysis of the oscillators

Figure 4.4 shows an equivalent circuit used in the theoretical analysis of the oscillation frequencies of RTD oscillators. Y_{ant} represents the admittance of a bare (without RTDs) patch antenna, as seen from the port 1-1' connected at the positions of RTDs. The part $\text{Im}(Y_{\text{ant}})$ describes the antenna susceptance, the part $\text{Re}(Y_{\text{ant}})$ contains the antenna losses, including its radiation conductance, ohmic losses in the metal layers, and the dielectric losses (in SU-8). For the asymmetric and symmetric modes, we calculate the admittance of the antenna (with the rest of the oscillator circuitry, including the bias line, MIM, etc.), assuming the corresponding symmetry of the electromagnetic fields. Y_{ant} can be obtained from the two-port admittance matrix (Y_{ij}), which is calculated by the electromagnetic simulator, U_i denotes the RTD voltages, the indexes 1



a)



b)

Figure 4.2: The figures show the distribution of the normal to the ground plane (z -axis) component of the electric field at the surface of the ground plane in the resonance for the (a) asymmetric and (b) symmetric modes. The structure parameters are chosen so that the symmetric mode is damped (attenuating). Due to the symmetry of the structure with respect to the x - z plane, the electric field in the emitted radiation should be polarized along the y -axis for the asymmetric and along the x -axis for the symmetric modes.

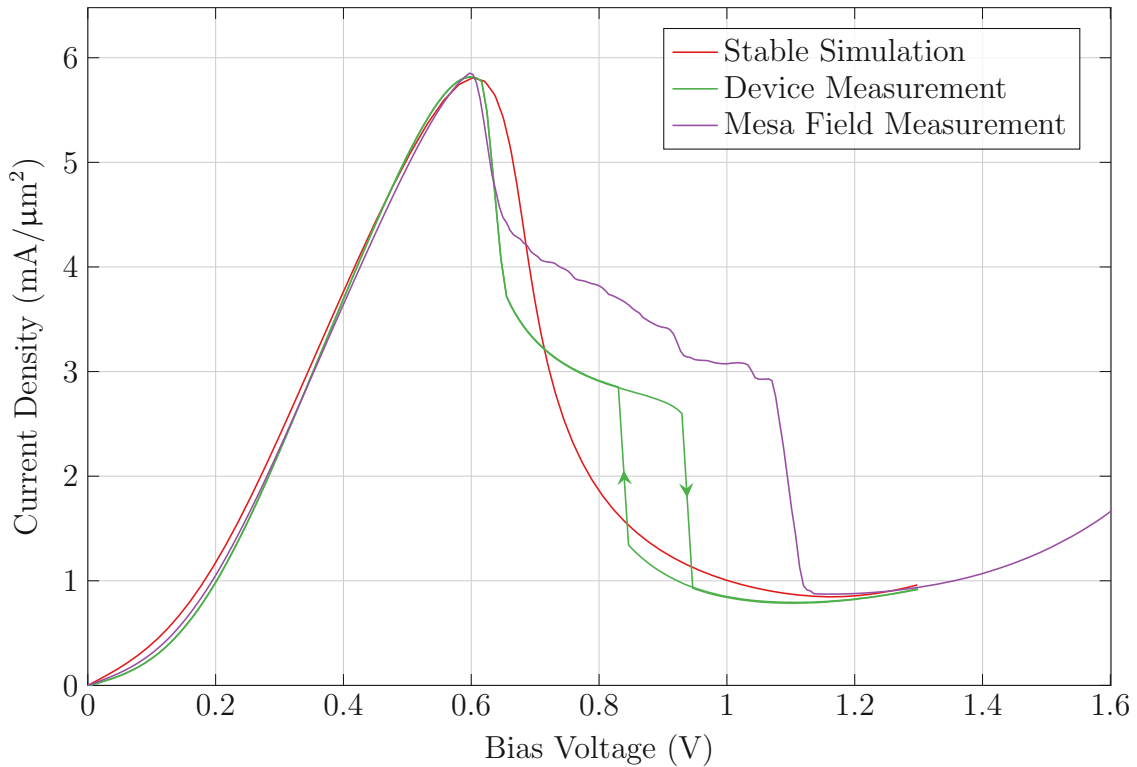


Figure 4.3: Measured (green) and calculated (blue and orange) I-V curves of an RTD, which was integrated with a square patch antenna with the length of $50 \mu\text{m}$; the nominal DRTD area was $4 \mu\text{m}^2$, the oscillator was working at 525 GHz. A stable (no oscillations) DC I-V curve is also shown in blue for comparisons. The I-V curve exhibit hysteresis regions, which were predicted in Chapter 3. Arrows indicate the bias-sweep directions.

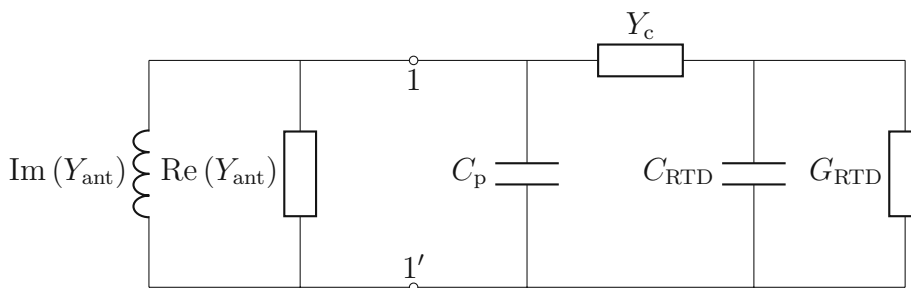


Figure 4.4: Small-signal model of the oscillator.

and 2 correspond to two RTDs in the oscillator; because of the structure symmetry: $Y_{11} = Y_{22}$, $Y_{12} = Y_{21}$) as shown in the following derivation:

$$\begin{bmatrix} Y_{11} & Y_{12} \\ Y_{21} & Y_{22} \end{bmatrix} \begin{bmatrix} U_1 \\ U_2 \end{bmatrix} = \begin{bmatrix} Y_{\text{ant}} & 0 \\ 0 & Y_{\text{ant}} \end{bmatrix} \begin{bmatrix} U_1 \\ U_2 \end{bmatrix} \quad (4.1)$$

$$\begin{bmatrix} Y_{11} - Y_{\text{ant}} & Y_{12} \\ Y_{12} & Y_{11} - Y_{\text{ant}} \end{bmatrix} \begin{bmatrix} U_1 \\ U_2 \end{bmatrix} = \mathbf{0} \quad (4.2)$$

$$(Y_{11} - Y_{\text{ant}})^2 - Y_{12}^2 = 0 \quad (4.3)$$

$$Y_{\text{ant}} = Y_{11} \pm Y_{12} \quad (4.4)$$

where the positive and negative signs correspond to symmetric and asymmetric modes, respectively. Eq. (4.2) is an eigenequation similar to Eq. (3.5) from Chapter 3, except now the system is two-dimensional.

The right part of the equivalent circuit from the port 1-1' represents the RTDs with the frequency-dependent capacitance $C_{\text{RTD}}(\omega)$ and conductance $G_{\text{RTD}}(\omega)$, calculated based on the model described in Refs. [102]–[104], [125]. C_p is a stray parasitic capacitance, and Y_c represents the contact admittance of the RTDs, which includes the contact resistance (also the spreading one) and capacitance of the top and bottom ohmic RTD contacts.

Figure 4.5 shows the simulated susceptances at the port 1-1'. The crossing point with the zero axis of the curve $\text{Im}(Y_{\text{ant}})$ shows the eigenfrequency of a bare patch antenna without RTDs. When RTDs load the antenna, the crossing (resonance) points shift to the lower frequencies due to the RTD capacitance, which is proportional to the RTD area. That is a significant effect. The oscillators operate at frequencies significantly below the eigenfrequency of the bare patch antenna; the patch has predominantly inductive behavior at these oscillation frequencies.

For the large-signal analysis, we perform the same analysis outlined in Section 3.3 for the first harmonic. To include the higher harmonic effect in the DRTD case, we would need to consider harmonics for both RTDs, which doubles the rank of the equation system. If we truncate the system only for the fundamental harmonic, then the solutions from the linear analysis for the symmetric and asymmetric modes are still valid. In this case, we can simply use the conductance given from Eq. (4.4) and combine it with the contact parasitics, which results in Y_{lin} . This conductance is then used in the large-signal analysis to determine the oscillation amplitude and the output power for the asymmetrical and symmetrical modes. Note that one can fix phase only on one of the RTDs and for a single harmonic.

4.1.4 Fabrication of the devices

Figure 4.6 shows a scanning-electron-microscope (SEM) image of a patch-antenna RTD oscillator. The patch antennas were squares with the side length varying between 50 and 200 μm with a 50 μm step. For the fabrication, a 1 \times 1 cm cleaved sample was used.

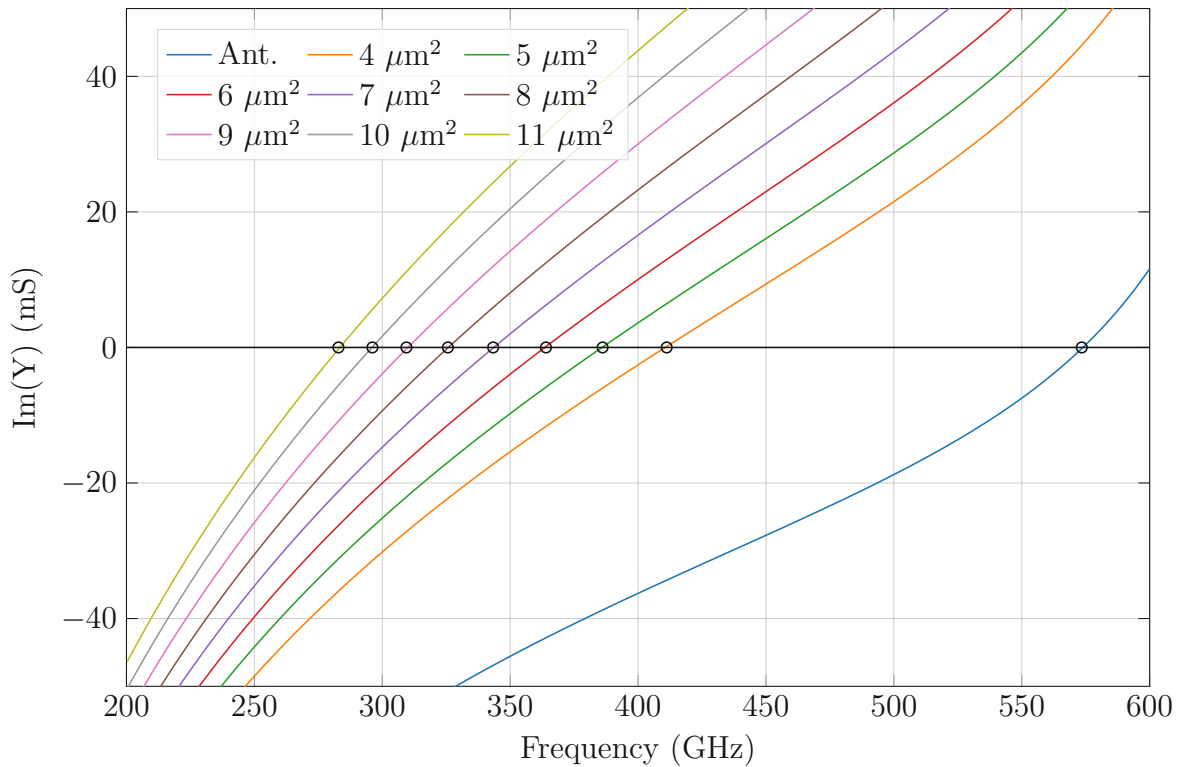


Figure 4.5: Susceptance plots for 150 μm large bare antenna without RTDs and for antennas loaded by RTDs with different areas (indicated in the figure). The crossing points with zero axis mark the oscillation frequencies.

Top RTD contact

The fabrication process starts with the deposition of Ti/Pd/Au as a top RTD contact with the (single) mesa areas ranging between 2 and 5.5 μm^2 . The layers were deposited by an E-beam evaporator, and the corresponding thicknesses of its sublayers thickness were 15/15/170 nm. The titanium layer serves as an adhesion layer, and the palladium layer acts as a diffusion barrier for the gold. This relatively large thickness improves the heat transport from the RTD layers during operation. For the patterning, we used a bi-layer photoresist process, in which PMGI (lift-off resist (LOR)) and AZ-5214e (patterning resist) were used. The patterning AZ-5214e photoresist is photosensitive to UV light (i-line) and can be used for both positive and negative photo-lithography. Although it shows an undercut when used in the negative tone, the undercut slope is still insufficient for lift-offs of relatively thick metal layers. The LOR can be developed without any exposure. If covered from the top by the patterned resist, the developer slowly and controllably develops the LOR from the open side underneath the patterned resist. The underdevelopment increases the undercut of the resists system. The patterning resist was then, in our case, used in the positive tone because it increases the maximal resolution.

We performed two sequential spin-coatings and soft-bakes, first for the LOR and then for the patterning resist. The spin-coated thickness of the LOR was 300 nm. We diluted 1:1 the patterning AZ-5214e resist with its solvent (EBR) to decrease the spin-coated thickness also to

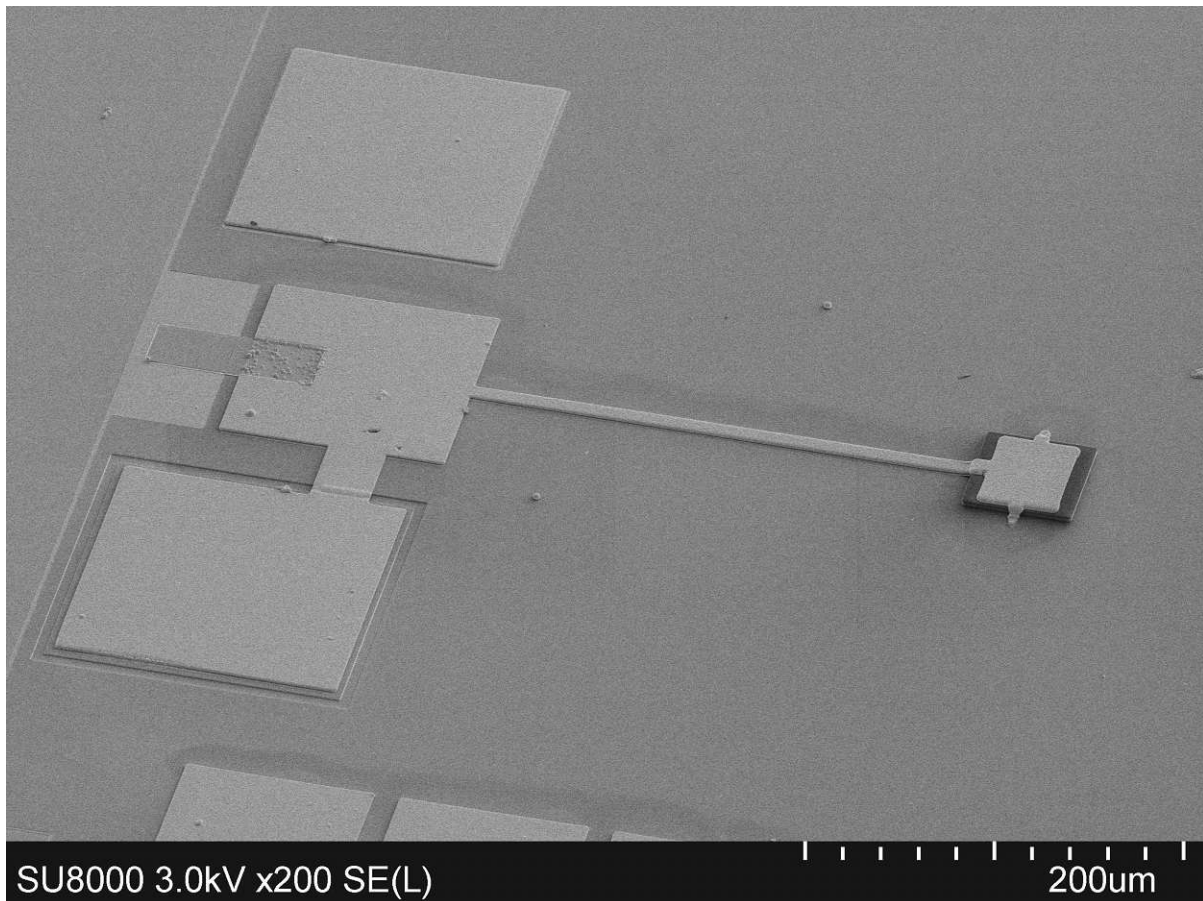


Figure 4.6: SEM image of a DRTD oscillator with 50 μm patch antenna.

300 nm, which helps to increase the lithography resolution. The mask was aligned to the sample with an MJB4 mask aligner, and 365 nm UV light was used to expose the photoresist. Both the patterning resist and the LOR were developed in the same step, using AZ MIF 726 developer. After the development, a short O₂ plasma etch was done to ash the residual photoresist. Right before the evaporation, the sample was etched with a 20 % HCl acid to etch the native oxide of the InGaAs layer. The metal stack was evaporated in an electron beam evaporator, and the lift-off of the unwanted metal was done in a DMSO stripper at 80 °C.

Together with the RTD top contact, we have fabricated auxiliary 2D arrays of mesas for characterization purposes (including a big contact pad for the second contact) and alignment markers used to align the sub-sequential layers.

We have estimated the specific contact resistance of the top contacts fabricated with the above-described procedure to be in the range $\approx 2\text{-}3 \Omega \mu\text{m}^2$ according to the measurements on test samples. The contact resistance was measured by the transmission line method.

RTD Mesa definition

The RTD mesas were defined by a wet etching process, where the evaporated top contact served as a mask during the etching. For the etching, we have used a diluted Piranha solution

$\text{H}_2\text{SO}_4/\text{H}_2\text{O}_2/\text{H}_2\text{O}$, with a molecular weight ratio of 1:1:80. The etching solution was cooled down in an ice-bath close to 0 °C. The etch rate was then approximately 1.4 nm/sec. The etch rate and the etch depth were measured with a Dektak profilometer. The RTD wafer was wet-chemically etched down to the bottom n++ layer. For our RTD, we have etched 180 nm deep. After the etching, the sample was left for two hours in a deionized water bath, which was heated up to 80 °C, to dissolve an arsenic oxide contamination from the etching.

The auxiliary arrays introduced in the previous section differed by design in the area of the RTD mesas. After the etching step defined the mesas, we could have contacted them with a gold whisker (bonding wire with 25 μm in diameter) and measured their I-V curves.

Lower contact for the RTD and passivation

Next, we deposited a second contact metallic contact layer on the sample's entire surface (except small auxiliary trenches lying far from the active region of the future antennas). The patterning process for the trenches was done the same way as for the top contact. The metallic layers composed of Ti/Pd/Au with thicknesses of 15/15/60 nm were evaporated with the electron beam evaporator. These layers formed the RTDs' lower electrode and the patch antenna's ground plane. We have estimated the contact resistance of the lower electrode to be $\approx 10 \Omega \mu\text{m}^2$, from TLM measurements on a test sample.

The top RTD contacts were under-etched during the wet etching process defining the RTDs' active area. This under-etching resulted in an undercut, which we used during the deposition of the lower contact as an auto-masking feature. The auto-masking guaranteed an electrical separation between the top and the lower electrode, allowing the lower electrode to be as close as possible to the mesa's stalk. This process helps to decrease the spreading resistance.

Further, we have dry-etched the trenches by a reactive ion etching with inductively coupled plasma (RIE-ICP). The trenches serve as an electrical separation of the contact pad in case of errors in the passivation. The gas used for the etching was Ar/Cl, and we used a soft mask from the PMGI resist patterned by the patterning resist. The patterning resist was before the etching stripped off. The depth of the trenches was approximately 700 nm, reaching the semi-insulating InP substrate. They can be seen in Fig. 4.6 around the contact pad at the bottom of the picture.

The sample surface was then covered by 160 nm Si_3N_4 passivating layer. We deposited the Si_3N_4 layer by the plasma-enhanced chemical vapor deposition. The passivation layer was opened at the top of the RTD mesas, exposing the top RTD contacts. The human-controlled alignment was too difficult as the design required precision greater than 200 nm over the whole sample. The mesas represent an irregularity in an otherwise plane sample at this step. Therefore, we used the method of planarization to open the RTDs selectively. A thick layer of 1 μm PMGI resist was spin-coated and consequentially baked, above its glass transition temperature, at 220 °C. The spin-coating and resist reflow evened out the sample's surface into a single plane. Next, we dry-etch the resist with an O_2 plasma to a thickness ≈ 200 nm. At this thickness, the tops of the RTD mesas were uncovered, while the rest of the sample was still covered by

the resist. The passivation layer was then dry etched by the RIE, using CHF_3 and O_2 gasses. Before this, we covered the sensitive parts of the design that were not intended to be opened by an additional resist, which protected these parts during the planarization.

Next, we used a soft mask made of patterned AZ-5214e, with which we opened the contact pads for the lower electrode and the shunt resistor contacts to the lower electrode in the passivation layer, with the same dry etching process as for the mesa openings. The resulting patterned SiN layer forms the MIM capacitor insulator and the antenna bias line.

Antenna dielectric, bridges, the antennas, and the shunt resistor

For the dielectric of the patch antenna, SU-8 negative tone photoresist was used. SU-8 is a permanent resist when cross-linked. $4\ \mu\text{m}$ thick blocks from SU-8 were then formed as the patch-antenna dielectric between the RTD pairs. The SU-8 was spin-coated, soft-baked, exposed with a negative mask, cross-linked by an additional illumination and by a hard-bake, developed in acetone and isopropyl alcohol, and cured at $200\ ^\circ\text{C}$. The dielectric constant of SU-8 was assumed to be 2.8, and its $\tan \delta$ was assumed to be equal to 0.03 in the working frequency range of the oscillators, see [135].

Because the SU-8 is a negative tone photoresist, its side walls naturally have a negative slope (slight undercut). However, we need a metallic connection between the RTDs lying on the base and the antennas on top of the blocks. Tilt the samples during the metal deposition was not available for us. As the blocks are much higher than the thickness of the metal we could deposit, we needed to introduce a smooth transition between the mesas and the top of the block. For this, we have patterned adjacent blocks and partially overlapping of PMGI resists to the SU-8 blocks with a thickness of $\approx 800\ \text{nm}$ and width of $3\ \mu\text{m}$. Next, we have reflowed the blocks with the same procedure as for the planarizing. This process formed the blocks into smooth barrel-like shapes.

Further, we used the same bi-layer process we used for the top contact to create the antennas, bridges to the top RTD contacts, bias line, and the top metallization of the MIM capacitor. However, this time we used the non-diluted patterning resist with a thickness of $1.4\ \mu\text{m}$ to cover the SU-8 blocks better. Of course, the bridges from PMGI were slightly developed during the development. However, its resistance against development rises with the baking temperature and time, which were high during the previous reflow step. Subsequently, a metal stack Ti/Au with the corresponding thicknesses of 15/185 nm was deposited by evaporation. To increase the thickness of the antenna layer metal and fix occasional cracks in the bridges, we electroplated an additional $0.8\ \mu\text{m}$ thick gold layer, where the plating was constrained only in the vertical direction by an extra lithography step.

As the last step, a shunt resistor was fabricated. The same bi-layer process was used with the non-diluted patterning resist. The shunt resistor was made out of indium-tin-oxide, which has conductivity approximately $1 \times 10^5\ \text{S}/\mu\text{m}$. The deposition was done by an RF sputtering. The deposited thickness of the shunt was 200 nm.

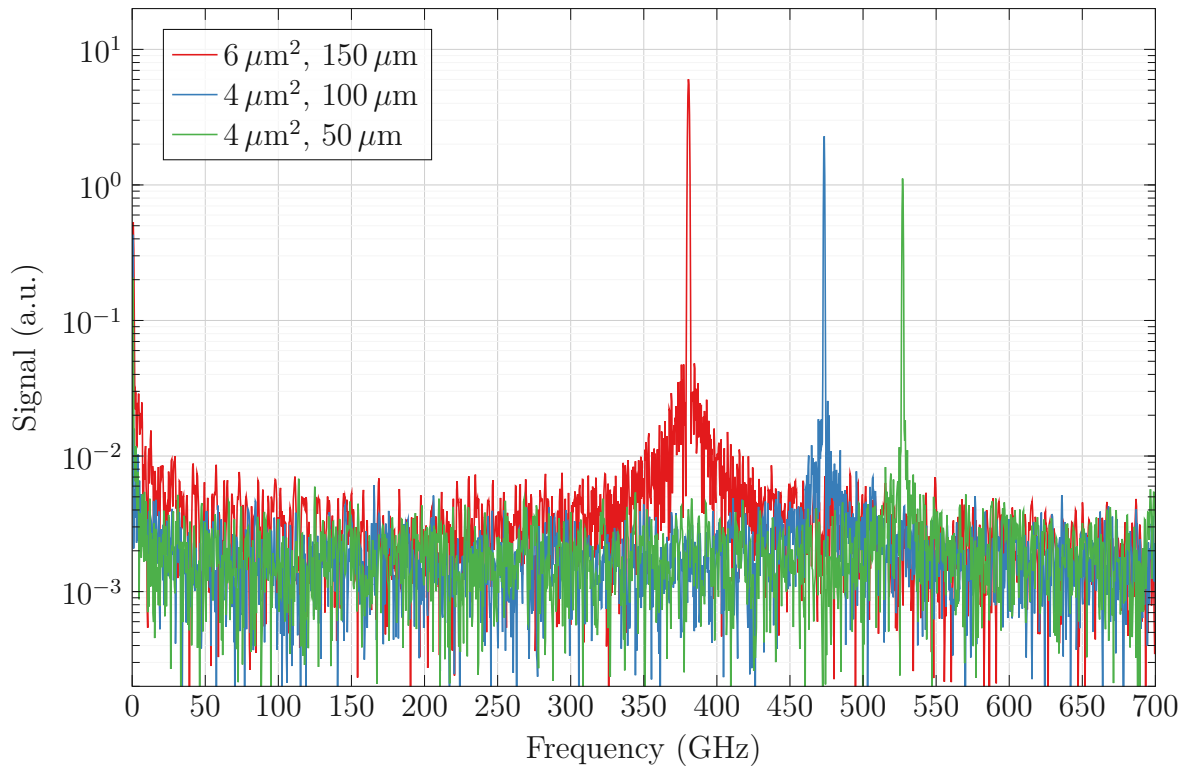


Figure 4.7: Measured frequency spectra for three oscillators with the patch-antenna lengths of 150, 100, and 50 μm , and the combined areas of two RTDs of 6 and 4 μm^2 .

4.1.5 Oscillators' performances

Oscillation frequency

Figure 4.7 shows several representative spectra of the RTD oscillators. For the given set of patch antennas dimensions and combined areas of two RTDs in the range 4-6 μm^2 , the oscillation frequencies were in the range from 300 GHz up to the highest frequency of 525 GHz. The spectra confirm that the oscillators were working at their fundamental frequencies; no indications for the subharmonics have been measured below the fundamental frequency lines, see Fig. 4.7. The spectra measurements have been done with a Fourier-transform interferometer in the Martin-Puplett configuration. For details about the Martin-Puplett interferometer principle, see subsection 4.4. The low-frequency limit of the interferometer is roughly 50 GHz, its frequency resolution is around 1 GHz, and a Golay cell has been used as a radiation detector in the interferometer.

Output power

The output power of the oscillators was measured by a calibrated pyroelectric detector, see Sec. 4.4, and corrected for the overlap of the antenna radiation patterns with the opening window of the detector. Figure 4.8 shows the output power and the fundamental frequencies of a set of patch-antenna oscillators. The maximum power of 70 μW was achieved at 330 GHz for the

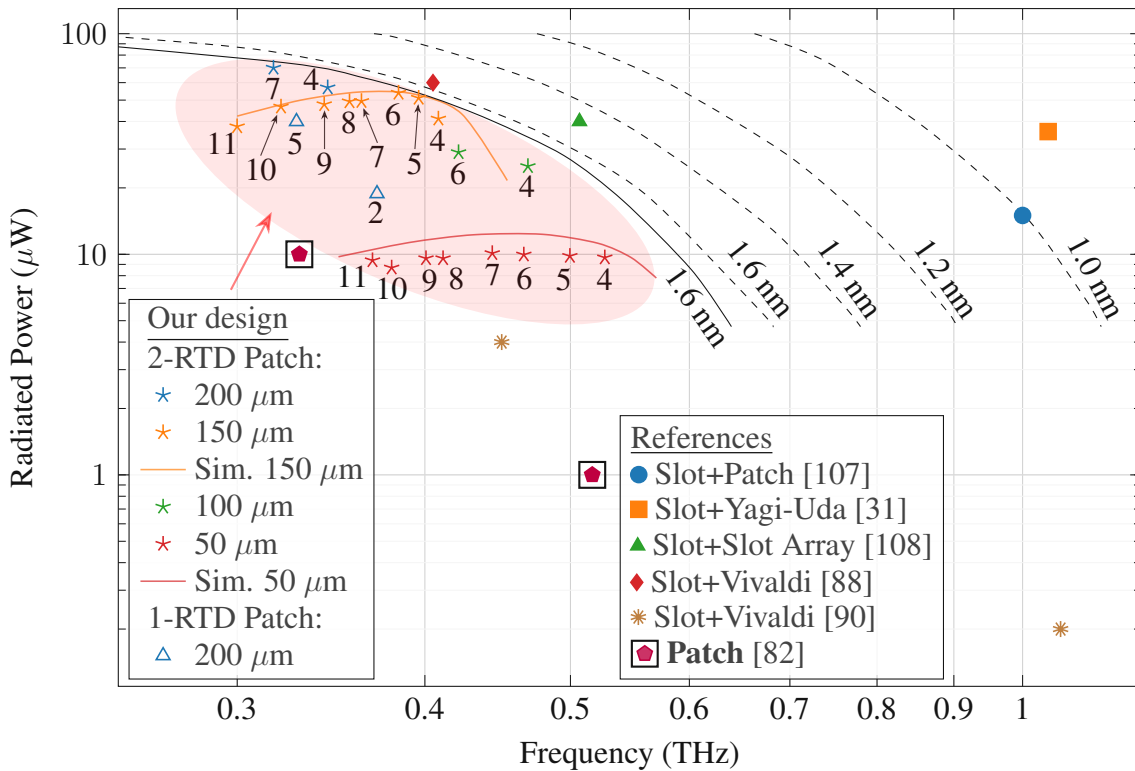


Figure 4.8: Output power vs. fundamental frequency for our patch-antenna RTD oscillators with different antenna and RTD dimensions. Numbers next to the symbols give DRTD areas in μm^2 , red and orange lines show simulated output power for the 50 and 150 μm patch antennas with different RTD areas; the solid black line indicates the maxima of such lines for different patch dimensions. The dashed lines show simulated output-power maxima for further optimized designs with reduced parasitics and thinner RTD barriers (1.6-1.0 nm, with the same “ ΔU ” as the measured I-V for 1.6 nm). The plot also shows the data on other reported on-chip (no Si lens) RTD oscillators operating at the fundamental frequency at the time of the presented oscillators’ development. The only previous report on fundamental-frequency single-patch-antenna RTD oscillators was Ref. [82].

antenna length of 200 μm with the DRTD area of 4 μm^2 . At the maximum achieved frequency of 525 GHz (50 μm antenna with the DRTD area of 4 μm^2), the output power was 10 μW .

Figure 4.9 shows the measured dependence of the output power vs. bias in the NDC region of RTDs, where one can see the typical (see Chapter 2 or, e.g., [105]) hysteresis behavior, depending on the direction of the bias sweep. The origin of the hysteresis and the plateau-like profile in the NDC region was explained in the previous Chapter. The theoretical dependence of the output power vs. bias is in good agreement with the measurement data, see Fig. 4.9, including the hysteresis behavior and the current step in the I-V curve. For the model of the RTD in the large-signal analysis, we used the DC large-signal conductance of the fundamental harmonic of the RTD. We have scaled the DC large-signal conductance at the operation frequency by the frequency dependence of the small-signal conductance from the model derived in Refs. [102]–[104].

The same procedure has been used for the calculation of the output power of the oscillators

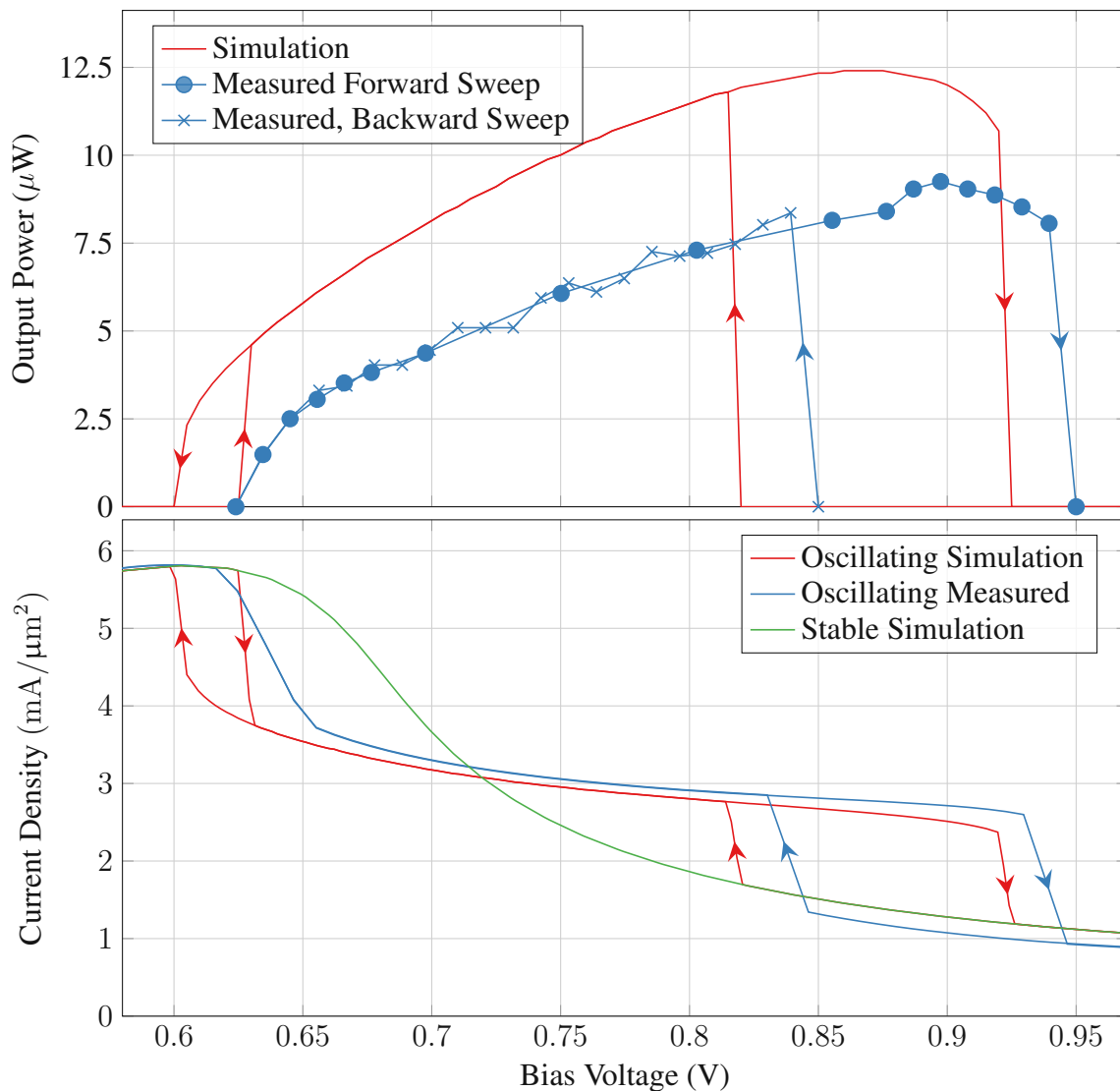


Figure 4.9: Theoretical and measured dependence of the oscillator oscillating at 525 GHz output power on the bias voltage and corresponding sections of the measured and simulated I-V curve. Both I-V curves and power characteristics exhibit hysteresis regions. Arrows indicate the bias-sweep directions.

for antennas with different dimensions and different RTD areas, see Fig. 4.8. The calculation results are in good agreement with the measurement data. The output power and operating frequency of DRTD patch-antenna oscillators could be further increased, see Fig. 4.8, if one would use RTDs with thinner barriers and higher current density (that would require smaller-size RTDs and the use of e-beam lithography) and if one would reduce the parasitics in the oscillators, e.g., by making shorter vertical RTD air bridges with smaller parasitic inductance (the contribution of the horizontal part of the air bridges to the total antenna inductance is proportional to the horizontal length times a relatively large scale factor, which is the ratio of the patch and the air-bridge widths). The output power of $\gtrsim 10 \mu\text{W}$ at 1 THz should be achieved with such optimized oscillators with 1 nm barrier RTDs. Staying with low-current-density 1.6 nm barrier RTDs, as in this design, one can, e.g., increase the thickness of the patch dielectric up to $6 \mu\text{m}$

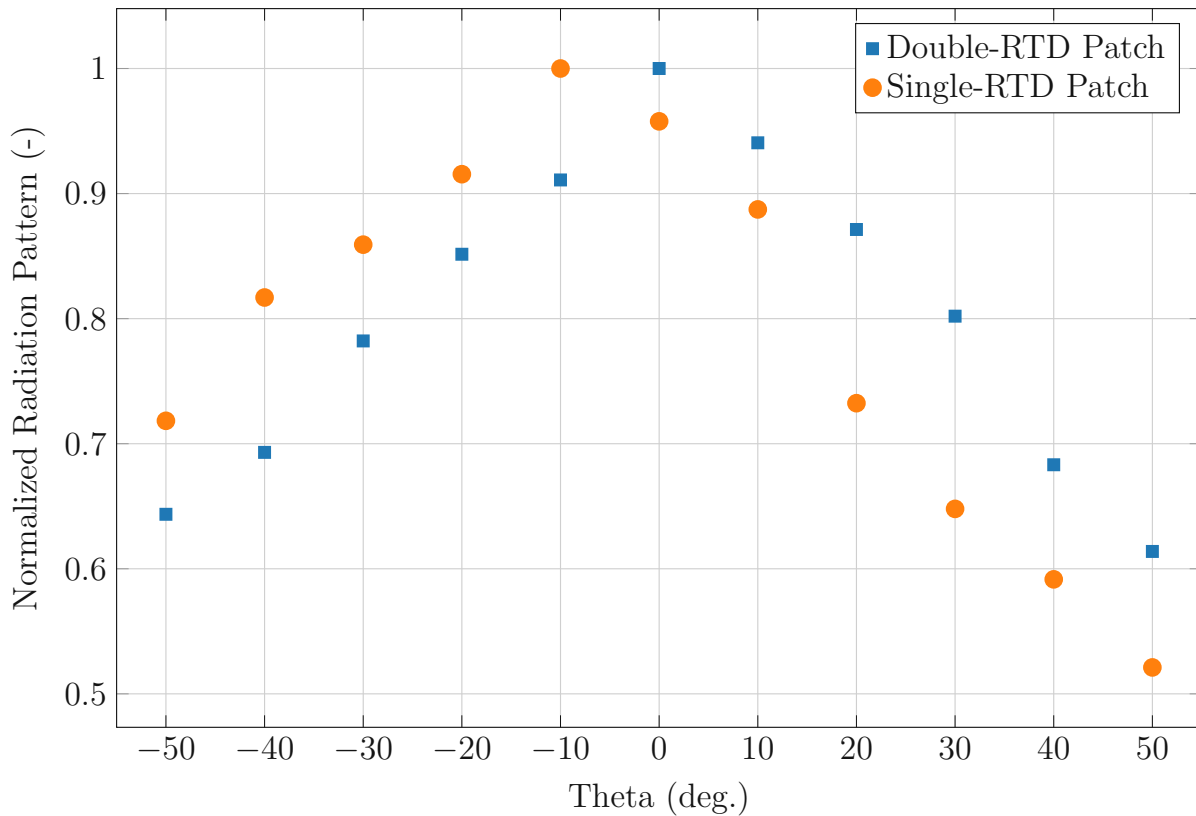


Figure 4.10: The radiation patterns of the oscillators measured in the plane perpendicular to the ground plane and connecting the RTDs for an oscillator with two RTDs and a single RTD. The radiation patterns are of single- and double-RTD, but otherwise identical, oscillators with $150 \mu\text{m}$ patch antennas and $4 \mu\text{m}^2$ single-RTD areas.

keeping the same antenna dimensions, which would extend the oscillator frequency to 670 GHz with the output power of $\approx 1 \mu\text{W}$.

Active mode

Our oscillators were designed to be operating in the lowest-order asymmetric mode. To verify that, we have measured the radiation pattern and the polarization of the output radiation. The asymmetric mode has the electric field polarization along the axis of the two patch-antenna RTDs (the signal level for the cross-polarization was below the noise floor, not measurable). On the contrary, the polarization of the symmetric mode is in the orthogonal direction. The lowest-order asymmetric mode should also have a symmetrical single-lobe radiation pattern with the maximum perpendicular to the substrate. However, the next higher-order asymmetric mode should have a two-lobe radiation pattern with the maxima close to the plane of the substrate. The measurements of the radiation pattern, see Fig. 4.10, and of the polarization, as well as the good agreement of the measured and calculated operating frequencies and output powers, confirm that all our DRTD oscillators were operating in the lowest-order asymmetrical mode at the fundamental frequency. The symmetrical oscillation modes were suppressed in all these oscillators.

The radiation pattern measurements shown in Fig. 4.10 were not highly precise due to disturbance of the radiation pattern by the contact needles, reflections from the detector, and the environment, which is seen in a slight asymmetry of the radiation pattern of a DRTD oscillator. For comparison, we have measured the radiation pattern of a single-RTD, but otherwise identical, patch-antenna oscillator. As expected, the radiation pattern is tilted in the direction of the RTD: the RTD creates a capacitive load to the patch antenna, which tips its radiation lobe. We note that our single-RTD oscillators had approximately half the output power of their DRTD counterparts. Specifically, for the antenna length of $200\ \mu\text{m}$ the maximum DRTD oscillator radiated power was $70\ \mu\text{W}$ at 330 GHz, although the single-RTD counterpart was operating at 329 GHz and radiating $40\ \mu\text{W}$.

4.1.6 Patch antenna loss assessment

The dielectric losses in SU-8 (although significant) do not play a dominant role in our oscillators at their operating frequencies. Their contribution to the total losses in the patch antennas is approximately three to four times less than the contribution from the metal losses, see Fig. 4.11. The patch antennas in our oscillators are operated at frequencies significantly below their self-resonant frequency (no RTDs). Therefore, the energy stored in the antennas is dominantly magnetic, and the corresponding magnetic field causes surface currents and losses in the metals. The energy stored in the electric field of the patch increases with the increase of the operating frequencies of the patch antennas towards their self-resonance. Therefore, the contribution of the dielectric (SU-8) losses is also getting higher.

4.1.7 Summary for the sub-THz patch antenna oscillators with bridges

In summary, the concept of a DRTD patch-antenna oscillator offers a series of advantages compared to other types of RTD oscillators. First, it emits the radiation upwards from the substrate and does not require a Si-lens, which gives an advantage of compactness compared to typical slot-antenna RTD oscillators with Si lenses. Second, the patch antenna operates simultaneously as a resonator and a radiator. Therefore such oscillators are simpler than the other types of on-chip oscillators with coupled resonator-radiator designs. Third, compared to single-RTD patch-antenna oscillators, the DRTD design can provide potentially higher output power, and its asymmetric mode of operation inherently guarantees the decoupling of the oscillator from the external bias circuitry at the fundamental oscillation frequency. We demonstrate an order of magnitude higher output power experimentally at slightly higher frequencies compared to previously reported patch-antenna RTD oscillators. We have demonstrated $\approx 10\ \mu\text{W}$ output power at the fundamental frequency of 525 GHz and $70\ \mu\text{W}$ at 330 GHz using RTDs with relatively thick barriers of 1.6 nm and relatively low peak current density of $5.8\ \text{mA}/\mu\text{m}^2$. Only optical lithography has been used in the fabrication process. We also show that significantly

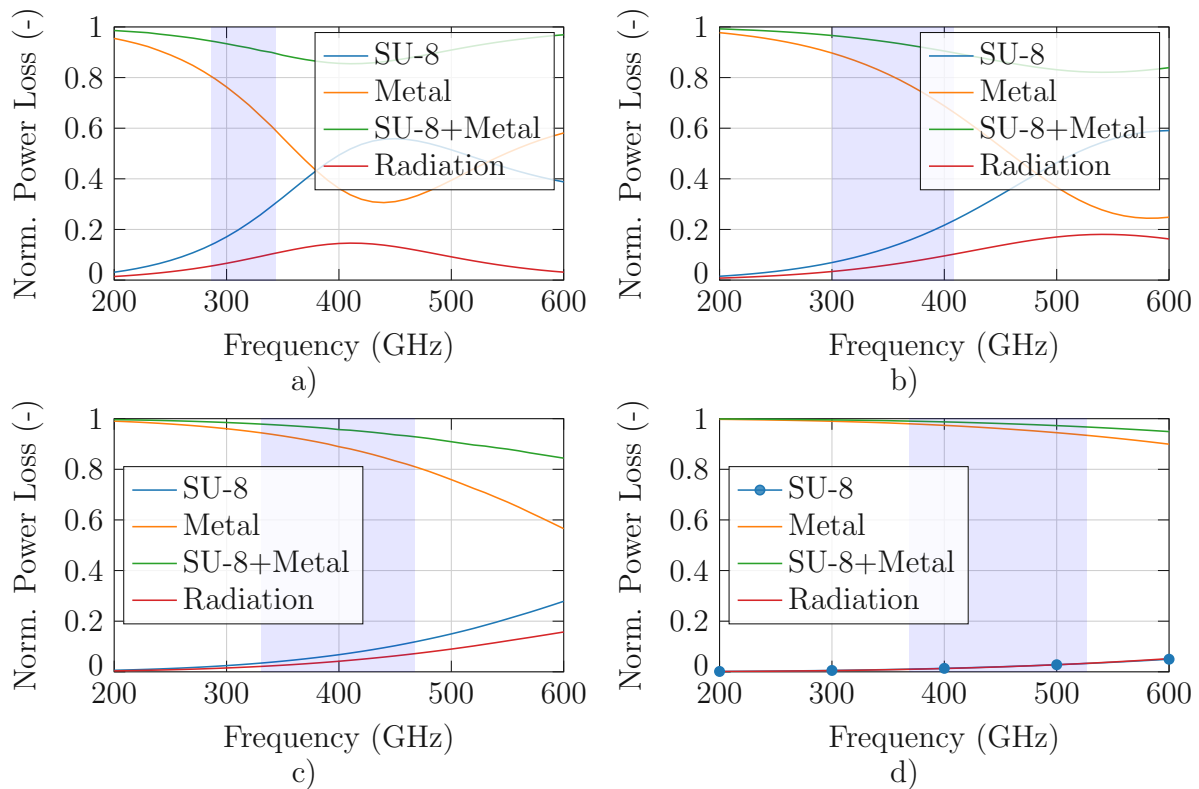


Figure 4.11: Power losses normalized to accepted power for: a) 200 μm , b) 150 μm , c) 100 μm and d) 50 μm patch antennas. The shaded blue regions mark ranges of the operational frequencies for the presented antennas.

higher operating frequencies and output powers are achievable with further optimization of the patch antenna and RTD parameters.

4.2 Bridge-less double-RTD oscillator beyond 1 THz

Results shown in this section were partly published in the peer-reviewed journal article P. **Ourednik** and M. Feiginov, “Double-resonant-tunneling-diode bridge-less patch-antenna oscillators operating up to 1.09 thz,” *Applied Physics Letters*, vol. 120, no. 18, 183501, 2022. DOI: 10.1063/5.0090519.

The above-described design was limited in its performance by the parasitics of the DRTD oscillator. In this section, we demonstrate that these parasitics can be substantially reduced. Additionally, we use thinner-barrier (1 nm) RTDs. These modifications allowed us to extend the fundamental operating frequencies of these oscillators above 1 THz and demonstrate the output power in the range of ten(s) of μW , which is close to the state-of-the-art level of chip-size oscillators.

A schematic of the DRTD patch-antenna oscillator is shown in Fig. 4.12. The oscillators share many features with the above-described design. The patch, as in the previous design, lays on a dielectric layer above the metalized ground plane of the chip. Metal bridges/vias

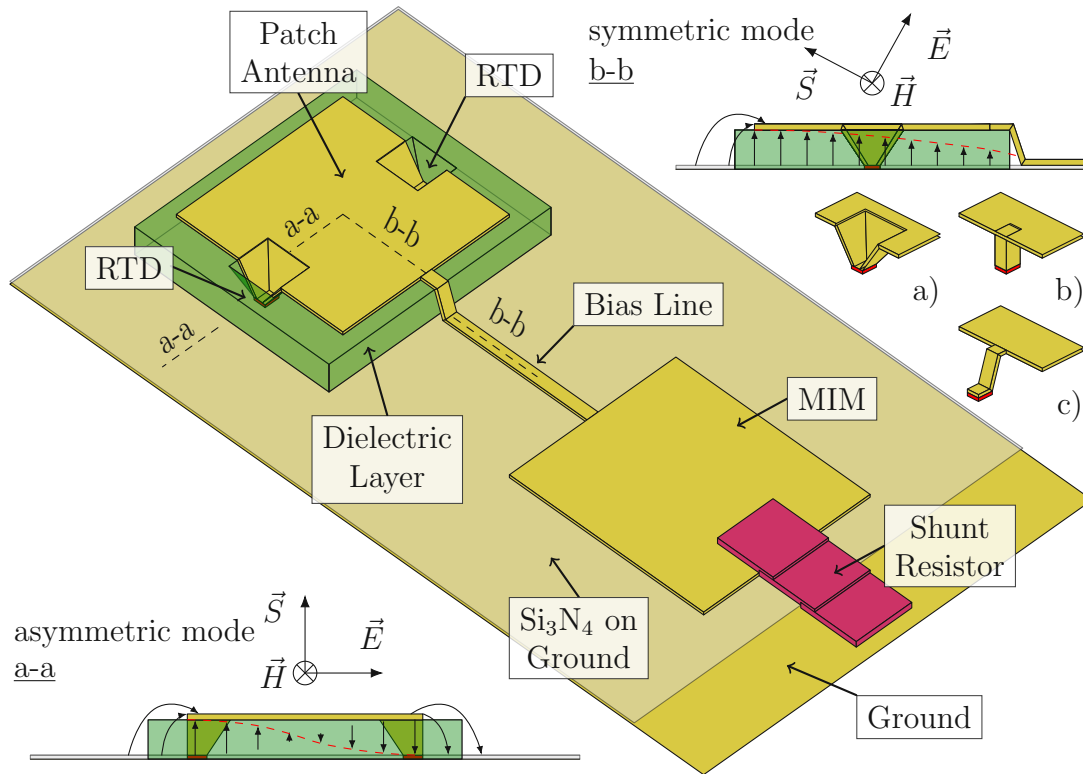


Figure 4.12: A sketch of a DRTD patch-antenna oscillator with conical vias. The DC bias is applied between the upper MIM metal layer and the ground-plane metallization. The shunt resistor prevents low-frequency parasitic oscillations. The “a-a” and “b-b” cross sections show the distribution of the electric field and the radiation polarization for the asymmetrical and symmetrical modes, respectively. The other insets show conical (a) and vertical (b) vias and a slanted bridge (c) for connection between the RTDs and the patch.

symmetrically connect the patch on both sides to two nominally-identical RTDs. The oscillator supports the two modes, the asymmetric and the symmetric, from which the asymmetric is the wanted one, and the symmetric needs to be suppressed. We optimized the bridges connecting the RTD and the patch in this design, along with the optimization of the RTDs themselves.

4.2.1 Conical vias

The patch antennas in RTD oscillators typically operate below their $\lambda/2$ Eigen (no RTDs) frequency since the RTD capacitance is rather high. In this regime, the patch impedance is predominately inductive. To increase the operating frequency of the oscillator, one needs to reduce the inductance and (inductive) parasitics of the patch, especially those related to the bridges connecting the patch to the RTDs. The reduction of parasitics is one of the crucial traits of the oscillators that allowed us to increase the oscillation frequency.

In the previous design, the bridges were narrow slanted metal stripes, as in Fig. 4.12 c). The inductance due to the horizontal (parallel to the ground plane) length of the stripe could be estimated as that of a piece of a microstrip: $\mu_0 l_{st} h_{st} / w_{st}$, where μ_0 is the free-space permeability, l_{st} , h_{st} and w_{st} are the length, height, and width of the microstrip, respectively. The width of

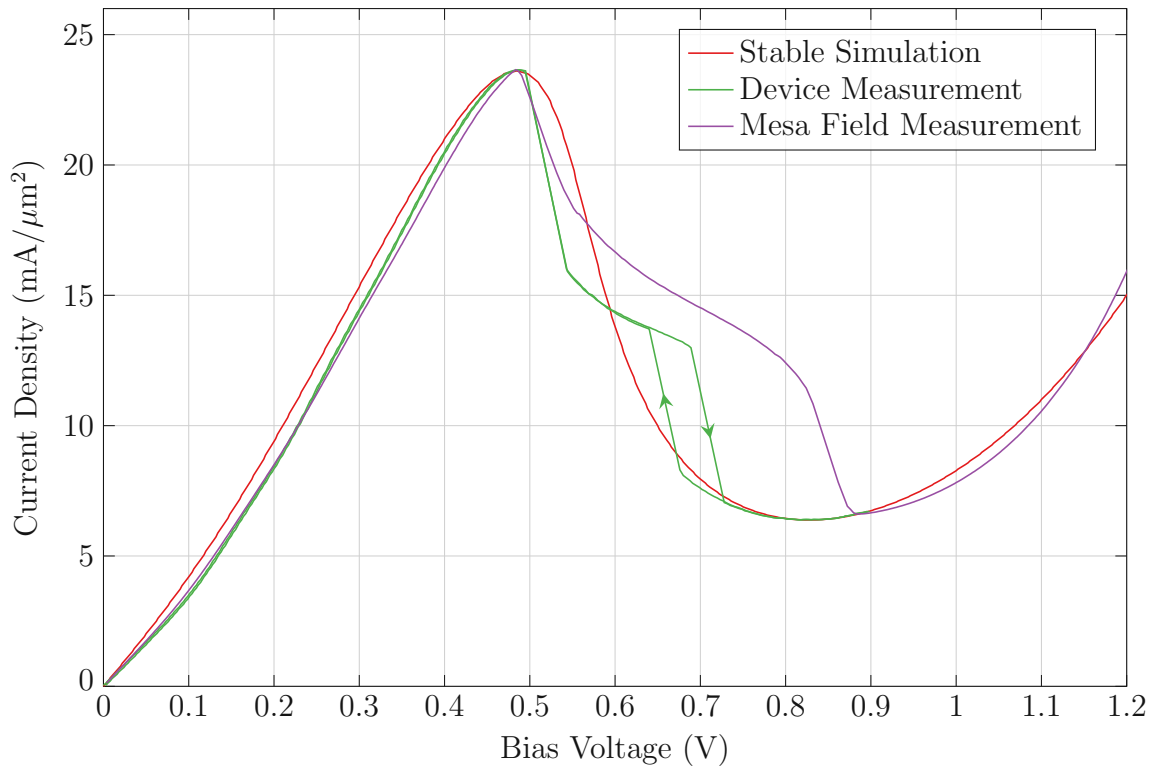


Figure 4.13: Measured (green and purple) and simulated (red) RTD I-V curves. The green curves correspond to an oscillating $0.67 \mu\text{m}^2$ DRTDs integrated with $40 \mu\text{m}$ patch antenna. The purple curve corresponds to a mesa-field measurement. The red curve is for a stable RTD.

the stripe bridge is much smaller than the width of the patch. Thus its parasitic inductance is large (compared to the same-length section of the patch). The vertical portion of the stripe (vertical via) could be roughly regarded as a coaxial structure with the inductance proportional to $\log(l_p/2w_{st})$, where l_p is the patch length between RTDs. From both perspectives, increasing the bridge width should reduce its parasitic inductance.

Specifically, in the previous design, we have used slanted stripe bridges, as in Fig. 4.12 c), with $3 \mu\text{m}$ width, $7 \mu\text{m}$ length, and $4 \mu\text{m}$ thick patch dielectric. In this investigation, we keep the same thickness of the patch dielectric but replace the stripe bridge with a conical via, as in Fig. 4.12 a), with the upper diameter of $10 \mu\text{m}$; this leads to the reduction of the bridge parasitic inductance by 3.8 pH , which corresponds to a large value compared to the inductance of 3.2 pH of a square $40 \mu\text{m}$ patch. For smaller patches, the relative reduction of inductance is even more dramatic. Additionally, the conical via has a lower ohmic resistance due to its larger surface: for the above parameters of the bridges, the conical via gives the reduction of the skin-effect ohmic resistance by 1Ω at 1 THz . For comparison, the replacement of the slanted stripe bridge with the above parameters by a vertical column via with square cross-section, see Fig. 4.12 b), with the sides equal to the stripe width would give a reduction of the parasitic inductance by 3.1 pH and of the ohmic resistance by 0.5Ω (at 1 THz).

4.2.2 1.0 nm RTD

Another crucial trait of the presented oscillators is using RTDs with thin (1 nm) barriers. The RTDs were grown on semi-insulating InP substrate and had nominally 1.0 nm AlAs barriers sandwiching a composite $\text{In}_{0.53}\text{Ga}_{0.47}\text{As}/\text{InAs}/\text{In}_{0.53}\text{Ga}_{0.47}\text{As}$ quantum well with the nominal thickness of each sublayer of 1.1 nm. On the emitter side of RTDs, we incorporate a 25 nm long $\text{In}_{0.53}\text{Ga}_{0.37}\text{Al}_{0.1}\text{As}$ step emitter, see [99], with the n-doping of $3 \times 10^{18} \text{ cm}^{-3}$, the collector side contained a 12 nm undoped $\text{In}_{0.53}\text{Ga}_{0.47}\text{As}$ spacer. The other layers surrounding the above barrier region on both sides were $\text{In}_{0.53}\text{Ga}_{0.47}\text{As}$ layers with the n++ doping of $5 \times 10^{19} \text{ cm}^{-3}$. The I-V curve of the RTDs is shown in Fig. 4.13. The peak current density is $23.6 \text{ mA}/\mu\text{m}^2$ with a peak-to-valley current ratio of 3.7. For RTDs with a current density around $20 \text{ mA}/\mu\text{m}^2$ and above, it is the highest reported peak-to-valley current ratio to date, see, e.g., [30], [101]. The characteristic inverse-relaxation-time frequency ($1/2\pi\tau_{rel}$) for these RTDs in the NDC region is $\approx 1.6 \text{ THz}$. Hence, at the frequencies around 1 THz, which is our focus in this design, we assume that the RTDs are working in the quasi-static regime ($\omega\tau_{rel} \ll 1$). The theoretical I-V curve (which is in good agreement with the experimental one, see Fig. 4.13) and the relaxation time were calculated following the procedure described in the previous section.

4.2.3 Fabrication of the optimized devices

We needed to decrease the RTD capacitance and the inductance of the patch antennas to achieve high frequencies. Both of these parameters are influenced by the sizes of the corresponding parts. To achieve oscillation frequencies over 1 THz, the RTD area of the oscillators needed to be smaller than $1 \mu\text{m}^2$. Although theoretically possible, reproducible fabrication of the devices on this scale is challenging in practice with conventional lithography with direct contact with the mask and the sample. Especially the alignment that would comfort the error margins at these scales was beyond our capabilities. Therefore we changed our technology to electron beam lithography (EBL), where a well-controlled flow of electrons does the exposure (electron energy is in the range of tens of keV). The EBL system is simultaneously an SEM, which allowed us to perform the required high-precision alignment. However, here described fabrication should be possible using industrial-grade optical lithography.

Because of the use of the EBL, we needed to change the used photoresists to those sensitive to the electron beam. For the lift-off processes, we kept using the LOR as the layer for the undercut and replaced the patterning resist with PMMA AR-P 679.04. We followed the instructions in its datasheet for the fabrication steps. We have been stripping this combination of the resists in the DMSO and the acetone.

The fabrication process started with the fabrication of the RTD mesas. The patterned top electrode made of Ti/Pd/Au with thicknesses 10/10/180 nm was deposited onto the RTD sample's surface. The wet-chemical etching formed the mesas by the Piranha solution described in the previous section, with which we etched $\approx 180 \text{ nm}$ deep, reaching the bottom contact layer of the

RTD. The combined areas of double RTDs were in the range of 0.4-1.4 μm^2 (single RTDs with the areas $\gtrsim 1 \mu\text{m}^2$ were prone to thermal breakdown).

Following the mesa forming, the second metallization layer was evaporated, which formed the bottom electrode for the RTDs and the ground plane for the patch antennas. The “self-aligning” process was again used here. The second metalization was also Ti/Pd/Au, with corresponding thicknesses 10/10/60 nm.

The whole surface was then covered by 180 nm Si_3N_4 , which formed a dielectric layer under the bias line and of the MIM capacitor. The SiN layer was opened at the top of the mesas and in the areas of the contact pads to the ground plane. The opening was done in this case by the EBL, not by the planarization. Although the planarization does not require high precision alignment, it is prone to open the passivation on unwanted places where contamination particles are present, which can lower the yield of the working devices.

After the opening, the sample was covered by a 4 μm thick negative photoresist (AR-N 7720.30), which formed a dielectric layer under the patch antenna. This fabrication step was critical because the design required a smooth photoresist surface in the regions of the conical vias. For this purpose, the 4 μm thick resist was spin-coated in four (0.2, 0.8, 1.5, and 1.5 μm thick) layers. Each layer was exposed by the electron beam and developed, forming open larger-diameter circles subsequently around the RTD mesas. Each layer of the resist has been thermally re-flowed to form a smoothed dielectric under-layer of the conical via with an upper diameter of around 10 μm . Additionally, the re-flowed photoresist created a smooth slanted external edge, which was used to connect the patch and the bias line. Figure 4.14 shows an SEM micrograph of a fabricated oscillator with conical vias.

Further, a structured Ti/Au layer with a thickness of 10/350 nm was then deposited by RF sputtering. This layer formed the patch antenna, bias line, upper metal of MIM, and the metallization of the conical vias to RTDs at the edges of the patch antennas, see Fig. 4.14. The sputtering helped better to cover the slanted edges of the dielectric layer. The patch antennas had a square geometry with side lengths in the range of 40-80 μm . Finally, a shunt resistor (Indium-Tin-Oxide) was deposited by the RF sputtering between the upper MIM metal layer and the ground plane.

In the implementation, we have omitted the usage of the trenches, as the deposited Si_3N_4 as the quality and thickness of the layer allowed us not to. However, these trenches should be introduced again for devices where a wire bonding for the biasing would be utilized.

4.2.4 Performance of the optimized design

Oscillation frequency

As in the previous case, the spectra of fabricated DRTD patch-antenna oscillators were measured with the Martin–Puplett interferometer with the Golay cell as a detector. A set of representative

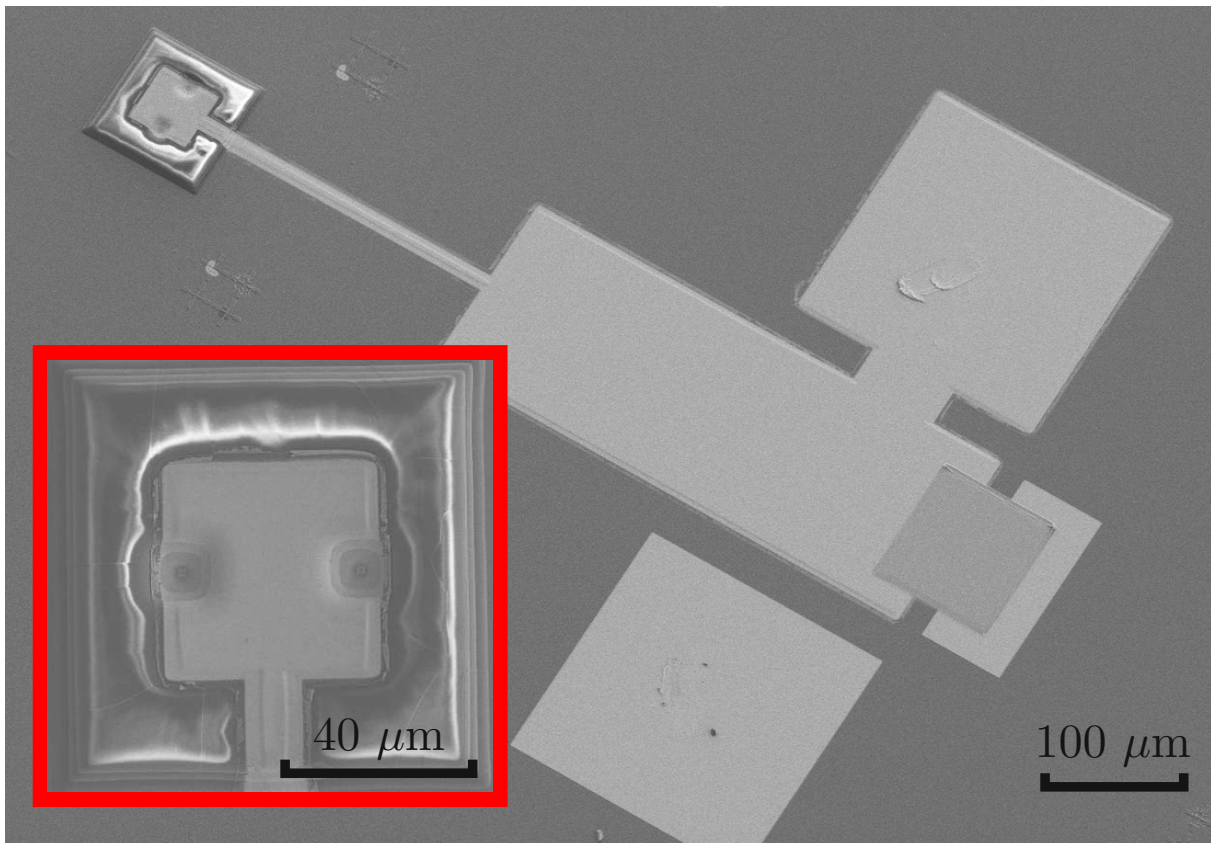


Figure 4.14: SEM micrograph of a 1.09 THz oscillator with 40 μm patch antenna. The dark gray substrate is the gold ground plane covered by the Si_3N_4 . The light-gray lower and upper squares are the contact pads to the ground plane and the upper MIM layer (top RTD electrode). The inset shows details of the patch. The illusion of the antenna being melted into the dielectric under-layer is due to the electrostatic charging inside SEM.

spectra is shown in Fig. 4.15. The spectra contained no indications of subharmonics or additional spurious frequency lines.

Additionally, we have proven that the emitted radiation has electric-field polarization along the line connecting the double RTDs in the patch antennas: the Martin–Puplett interferometer contains a linear polarizer at its input. When the sample was rotated by 90° , no radiated signal was measurable for the cross-polarization. The orientation of the emitted radiation (see Fig. 4.12) and the clean measured spectra prove that the oscillators at the measured frequencies were working at the fundamental asymmetric modes.

Output power

The emitted power was measured in a separate double-parabolic-mirror setup with a pyroelectric detector, see Sec. 4.4. The measured power was corrected for the solid angle of the collection mirror by considering the patch antenna's radiation patterns. Figure 4.16 shows the measured output powers and the operating frequencies of several sets of DRTD patch oscillators with different patch dimensions and different DRTD areas. The highest achieved frequency was

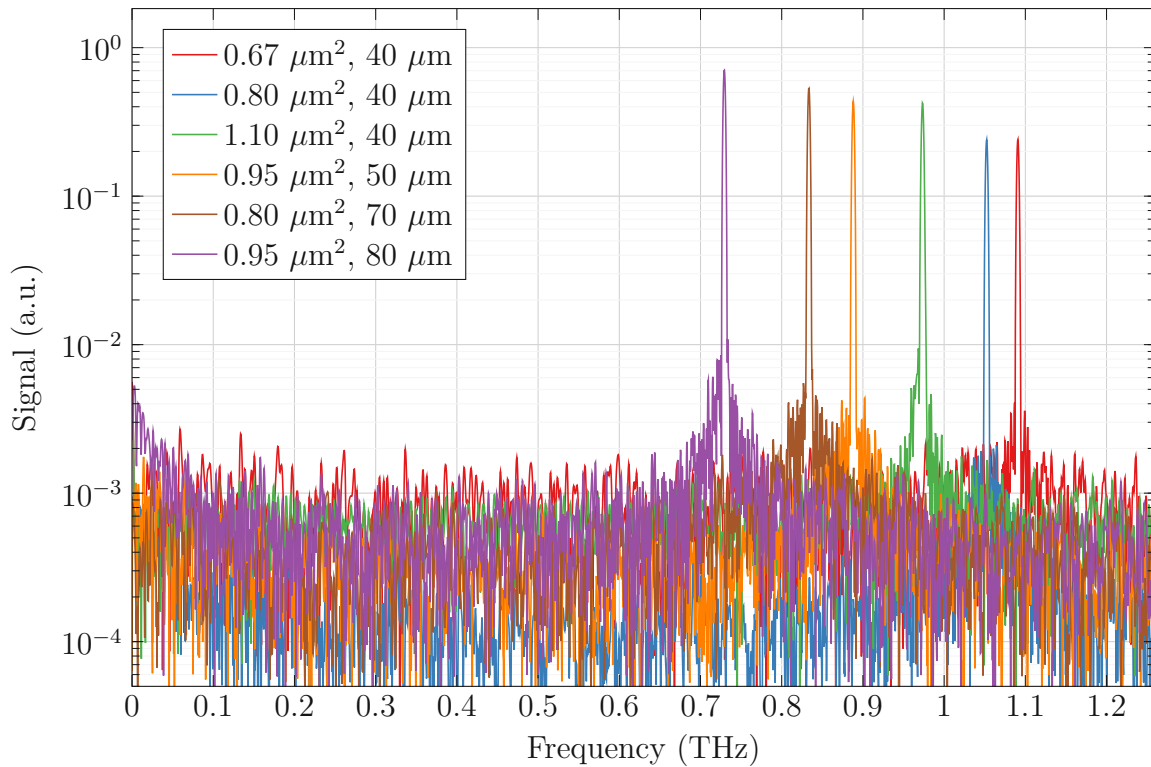


Figure 4.15: Representative measured spectra of DRTD bridge-less patch-antenna oscillators.

1.09 THz, where we have measured $9 \mu\text{W}$ with an oscillator with $40 \mu\text{m}$ patch and $0.67 \mu\text{m}^2$ double RTDs, $15 \mu\text{W}$ have been reached at 0.98 THz . At lower frequencies, around $620\text{-}660 \text{ GHz}$, we could measure the output power of $27 \mu\text{W}$. The measured data points show an intuitively expected behavior: the larger patch antennas operate at lower frequencies; the smaller the RTD areas, the higher the operating frequency, but the output power is getting lower.

As an illustration, Fig. 4.17 shows the simulated output power vs. bias for the device oscillating at the frequency of 1.09 THz . The figure also shows the corresponding section of the simulated and measured I-V curve for an oscillating RTD; it has a characteristic step and hysteresis in the NDC region due to the self-rectification effect, both for the output power and I-V curves. The simulations are in good agreement with the measurement results. The simulation procedure for the oscillator output power, including the self-rectification effects, has been described for the above-described sub-THz design with the bridges.

4.2.5 Comparison with the chip-sized RTD oscillators

The above parameters demonstrate an essential improvement compared to our previous design of the DRTD patch-antenna oscillators, where the operating frequencies were limited to $330\text{-}525 \text{ GHz}$. The data also represents a significant improvement compared to other reported fundamental-frequency patch-antenna single-RTD oscillators, which had power in the range $1\text{-}10 \mu\text{W}$ at $330\text{-}517 \text{ GHz}$, see [82]. In general, the parameters of our oscillators are better or close to the other types of on-chip RTD oscillators without Si lens; however, those oscillators

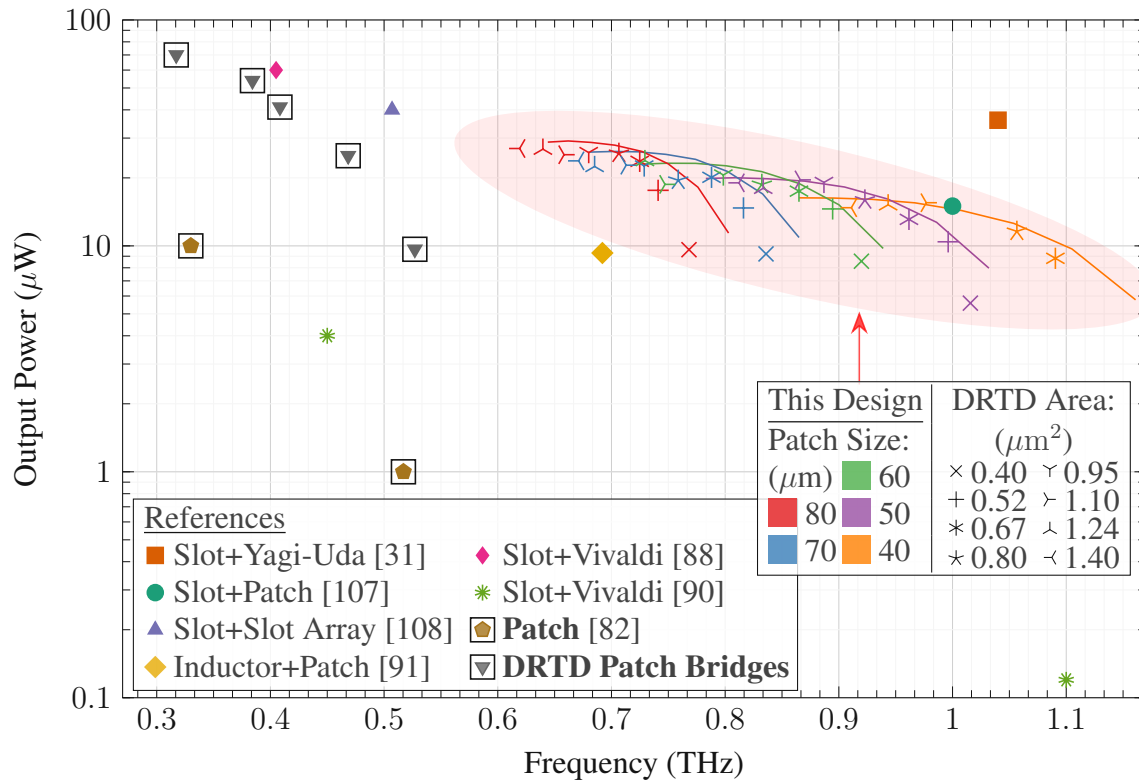


Figure 4.16: Radiated power vs. frequency for a set of samples with different patch-antenna sizes and DRTD areas. The previously reported literature data for RTD oscillators without Si lenses are also shown for comparison in the plot at the time of the presented oscillators' development. The box around the symbol highlights the simple patch-antenna oscillators.

have significantly more complex multi-antenna designs, where the RTD slot resonators are coupled either with other emitting slots or additional patch/Yagi-Uda/Vivaldi radiators, see [31], [88], [90], [91], [107], [108]. The highest power for all types of RTD oscillators above 1 THz was reported with the slot RTD resonators coupled to Yagi-Uda radiators ($36 \mu\text{W}$ at 1.04 THz), see [31]; the data we report for the DRTD patch-antenna oscillators are getting close to this level. Comparing the here presented devices to common (bulky) slot-antenna fundamental RTD oscillators with Si-lens that can operate at higher frequencies and that have reached the output power of $30 \mu\text{W}$ at 1.25 THz, see [101], we conclude that our (compact) DRTD patch-antenna oscillators are already not far away from them.

Figure 4.16 also shows the simulated dependencies of the output power vs. frequency for different patch antennas and varying RTD areas. The simulation and measurement results are in very good agreement with each other, and simulations are well in agreement with the qualitative behavior of the oscillators described above.

4.2.6 Losses in the dielectric

Apart from the radiation losses, the main loss mechanisms in the patch antennas are due to the ohmic (metal) and dielectric resonator losses. The ohmic metal-surface resistance is increasing

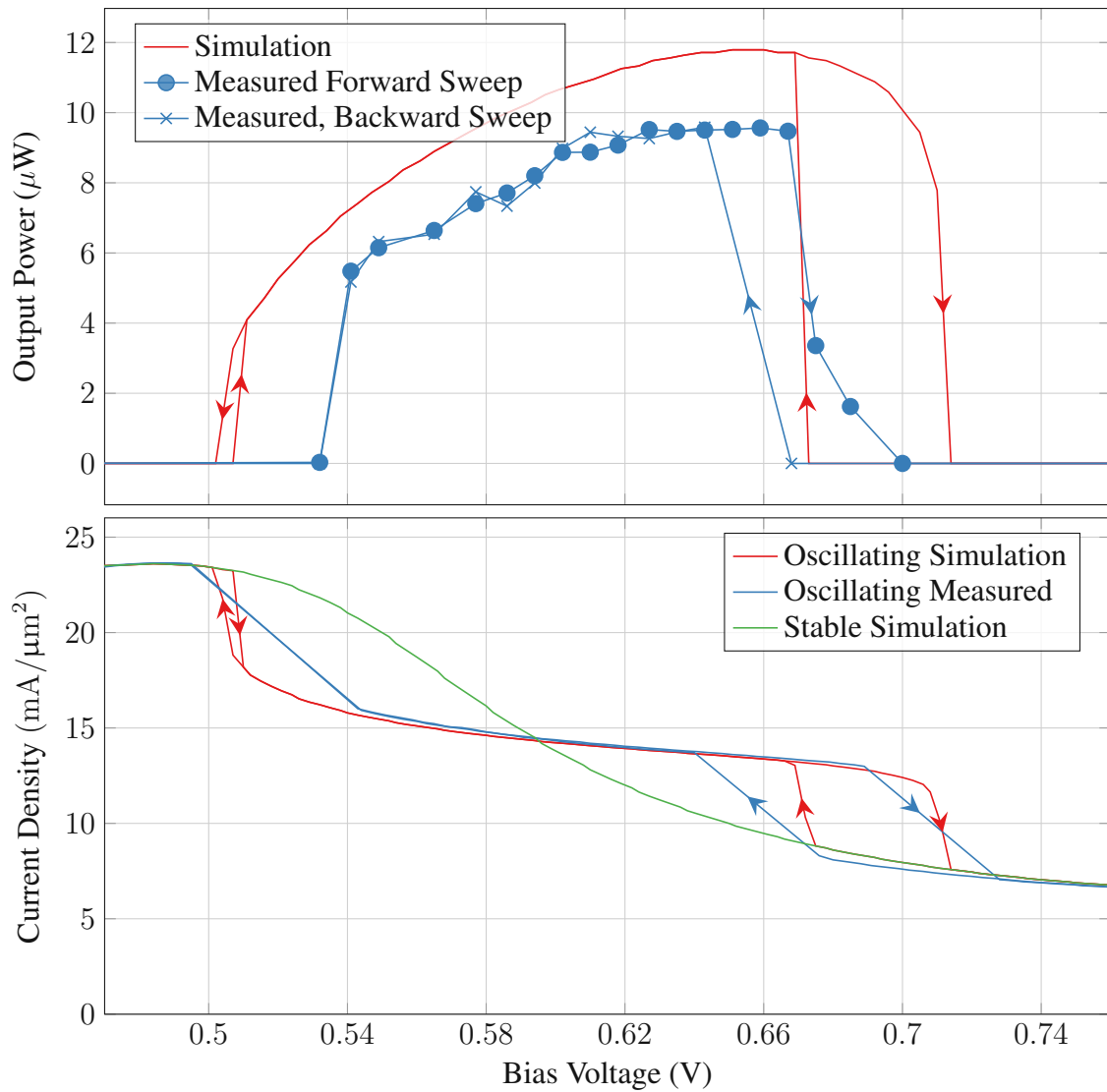


Figure 4.17: Measured and simulated output power vs. RTD bias and the corresponding section of an oscillating device's measured and simulated I-V curves. The shown data are for the device oscillating at the frequency of 1.09 THz.

with frequency due to the skin effect. The losses in the dielectric materials are usually also increasing with the frequency in the THz range, although that depends on the specific properties of the dielectrics. However, the level of particular losses depends on the resonant mode's electromagnetic properties in the patch antenna. The amounts of the electric and magnetic energy periodically stored in a patch antenna are equal at the antenna eigen-resonance (without RTDs) frequency. For our patch antennas, the dielectric losses overweight by far the metal (ohmic) losses in this regime, see, e.g., the normalized losses for 40 μm patch antennas in Fig. 4.18. However, when the antenna is capacitively loaded by RTD(s) and its resonance frequency is reduced, the electric energy is getting localized in the RTD capacitance for the most part, and only (predominantly) magnetic energy remains periodically stored in the patch. Consequently, the fraction of the dielectric losses in the patch compared to the metal ones is dropping very rapidly with the reduction of frequency (with the increase of the RTD area); in the operating

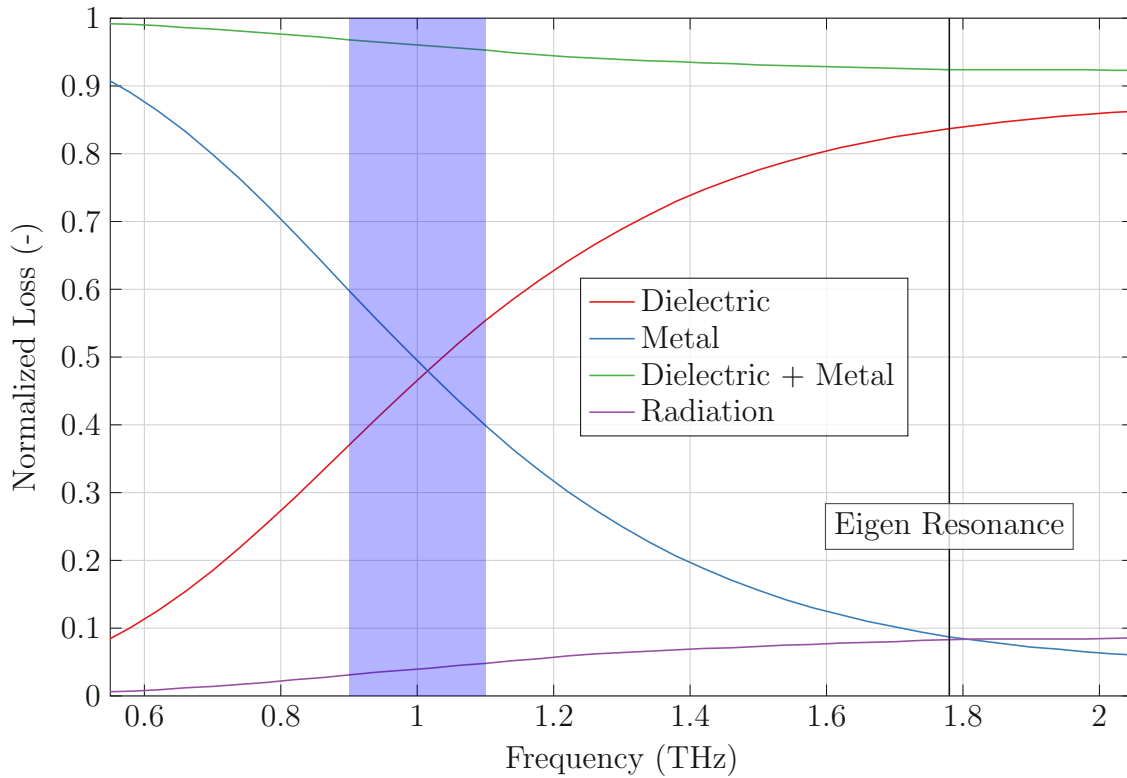


Figure 4.18: Dielectric, metal, and radiation losses normalized to the accepted power of the antenna of size $40 \mu\text{m}$. The blue region corresponds to the operating frequencies of our $40 \mu\text{m}$ oscillators.

frequency range of our oscillators, both types of resonator losses are approximately at the same level. In other words, the metal resonator losses do increase at higher operating frequencies. However, the dielectric losses are increasing much faster due to the rapid build-up of the electric energy in the patch when the operating frequency is getting close to the eigenfrequency of the patch resonator.

The dielectric properties of the photoresist AR-N 7720.30 we used in our patch antennas are not documented at THz frequencies. Thus, we have assumed them to be close to the properties of SU-8, considering that both the photoresist and SU-8 are based on Novolac resin. The reported SU-8 dielectric constant in the working range of our oscillators is 2.7, and the reported $\tan \delta$ varies from 0.05 to 0.14 at 1 THz, see [135], [136]. In our electromagnetic simulations of the patch antennas, we used the worst-case value of 0.14 for $\tan \delta$. The resulting calculated output power level of our oscillators is well in agreement with the experimental values, see Fig. 4.16. We note that our previous estimate of the expected output-power level, in the previous section, below ~ 1 THz with 1-nm barrier RTDs was more optimistic since we assumed $\tan \delta = 0.03$ previously and “ δU ” of ≈ 0.55 V instead of ≈ 0.35 V, which have the RTD used in this work. We write “ δU ” in quotation marks because we used the actual I-V curve for the output power estimations and not the third-order approximation.

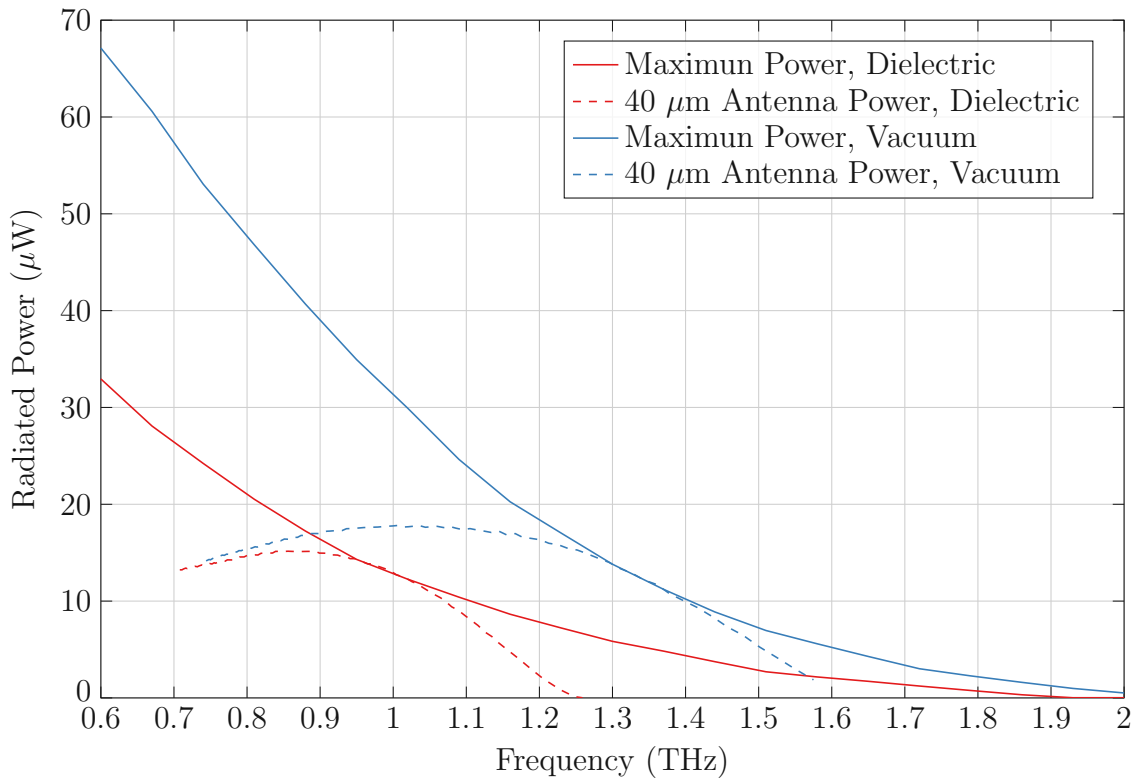


Figure 4.19: Simulated radiated power for patches with AR-N 7720.30 as a dielectric and for empty patches. The solid lines show envelopes created from sweeps of the antenna sizes and DRTD areas, and the dashed lines show radiated power for 40 μm antenna where the DRTD areas were swept.

4.2.7 Summary for the THz patch-antenna DRTD oscillators

The above discussion indicates that the dielectric losses are crucial to achieving higher output power and higher operating frequency of the patch-antenna RTD oscillators. Figure 4.19 shows the expected output power of our oscillators for a sweep of antennas sizes and DRTD areas and, specifically, for the 40 μm patch antenna with the photoresist as a dielectric and if the dielectric would be removed. One should be able to achieve a significantly higher output power in the latter case. We have attempted to remove the photoresist by the O_2 ashing process but were not yet successful since the thermal expansion of the photoresist during the process was destroying the contacts to RTDs. To achieve higher oscillation frequencies, we also reduced the dimensions of patch antennas. Optimization of the DRTD patch-antenna oscillators along these lines should improve their performance beyond the level achieved by the RTD oscillators so far in the frequency range above 1 THz.

In this part, we demonstrated double-resonant-tunneling-diode patch-antenna oscillators having output powers of 9 μW at the fundamental frequency of 1.09 THz, 15 μW at 0.98 THz, and up to 27 μW at the lower frequencies of 620-660 GHz. These parameters are substantially superior to those previously reported for patch-antenna RTD oscillators, and they are close to the state-of-the-art level for all other types of RTD oscillators at around 1 THz.

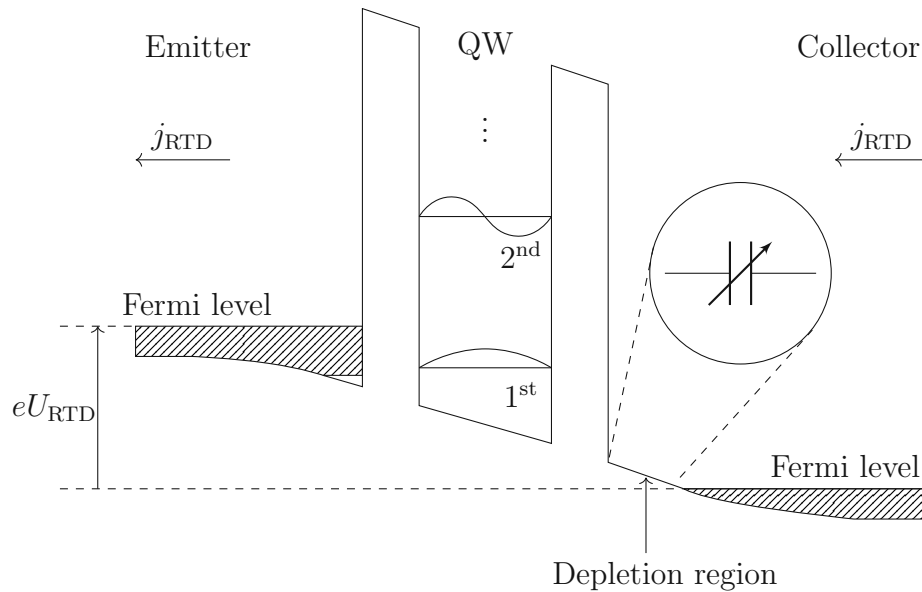


Figure 4.20: Band diagram of an RTD with the explicit depiction of the depletion region. The depletion region separates the accumulation of the charge in the emitter and the collector, creating a capacitor. The length of the depletion region is voltage-dependent. Thus the RTD capacitance is also voltage-dependent. The RTD acts as a varactor.

4.3 FMCW and OCT application of RTD oscillators

Results shown in this section were partly presented at the scientific conference and published in its proceedings P. Ourednik, G. Picco, and M. Feiginov, “Chip-size resonant-tunneling-diode oscillator as a fmcw and oct source,” in *2022 47th International Conference on Infrared, Millimeter and Terahertz Waves (IRMMW-THz)*, 2022, pp. 1–2. DOI: 10.1109/IRMMW-THz50927.2022.9896064.

In this section, we show the behavior of resonant-tunneling-diode (RTD) oscillators regarding their frequency tuning and investigate the possibility of employing the RTD oscillators in THz frequency-modulated continuous wave (FMCW) radars and optical coherent tomography (OCT) applications. The frequency tunability of RTD oscillators was addressed, e.g., in [137]. However, the behavior of fast linear frequency chirps was never shown. In this part, we use the above-described double-RTD oscillator with a nominal barrier thickness of 1 nm.

4.3.1 RTD oscillator frequency tunability

The oscillation frequency of an RTD oscillator depends on the bias applied to the RTD since the RTD depletion region and quantum-well capacitances are bias-dependent. In Fig. 4.20, we show the depletion layer in the band diagram of the RTD. Therefore, the RTD oscillator can be used as a voltage-controlled oscillator with bias control. However, the frequency response of the oscillator is not linear with a linear bias voltage sweep. FMCW radars require the source to generate linear frequency chirps in time to determine the target’s distance and speed reliably.

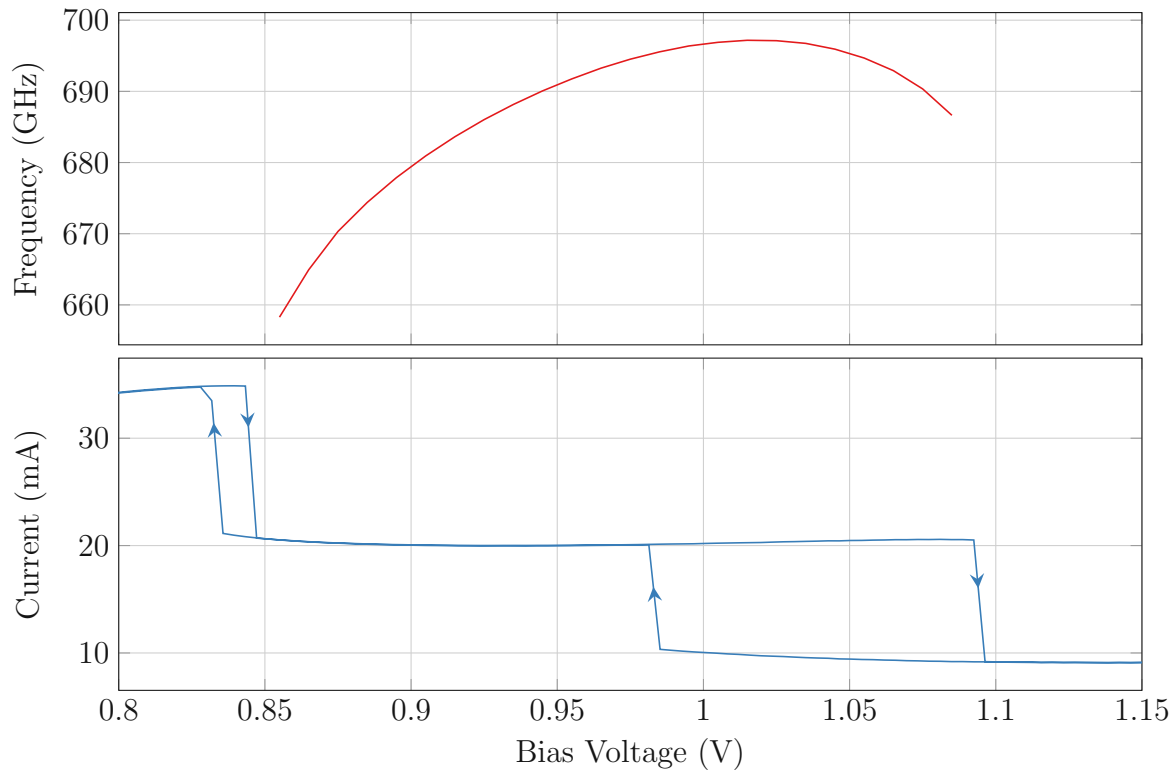


Figure 4.21: The dependence of the oscillator operation frequency on the bias voltage and the relevant part of the I-V curve (shunt subtracted). The frequency tuning shows the non-linear inflection character. The arrows indicate the backward and forward sweeps of the relevant part of the I-V curve in the oscillation range.

For this study, we have used the concept of the oscillators described in the previous section. However, to enhance the tune-ability, we have fabricated a device with $60 \mu\text{m}$ antenna and $1.5 \mu\text{m}^2$ DRTD area.

The measured frequency response as a function of the bias voltage of our RTD oscillator is shown in Fig. 4.22. The bottom plot shows details of the I-V curve zoomed in the oscillation region. The I-V curve is striped of the shunt resistor contribution, which is needed to suppress the low-frequency parasitic oscillations. The oscillation region is between the two hysteresis regions. The data shows two regions of possible operation, before and after the maximum. The first part gives a higher tunability range, which was 38 GHz in our case. The second part gives a lower tunability but an almost constant output power (for our device, see, e.g., Fig. 4.17). We use the first part with a wider frequency range in this example. As the measurement has shown, the shape of the frequency vs. bias voltage curve is not linear. The non-linear frequency sweep would cause a not constant FMCW-detection frequency, hugely decreasing the final resolution.

4.3.2 Frequency response linearization

To linearize the frequency response in time, one must create a non-linear voltage sweep to compensate for the frequency non-linearity. An arbitrary waveform generator generated the

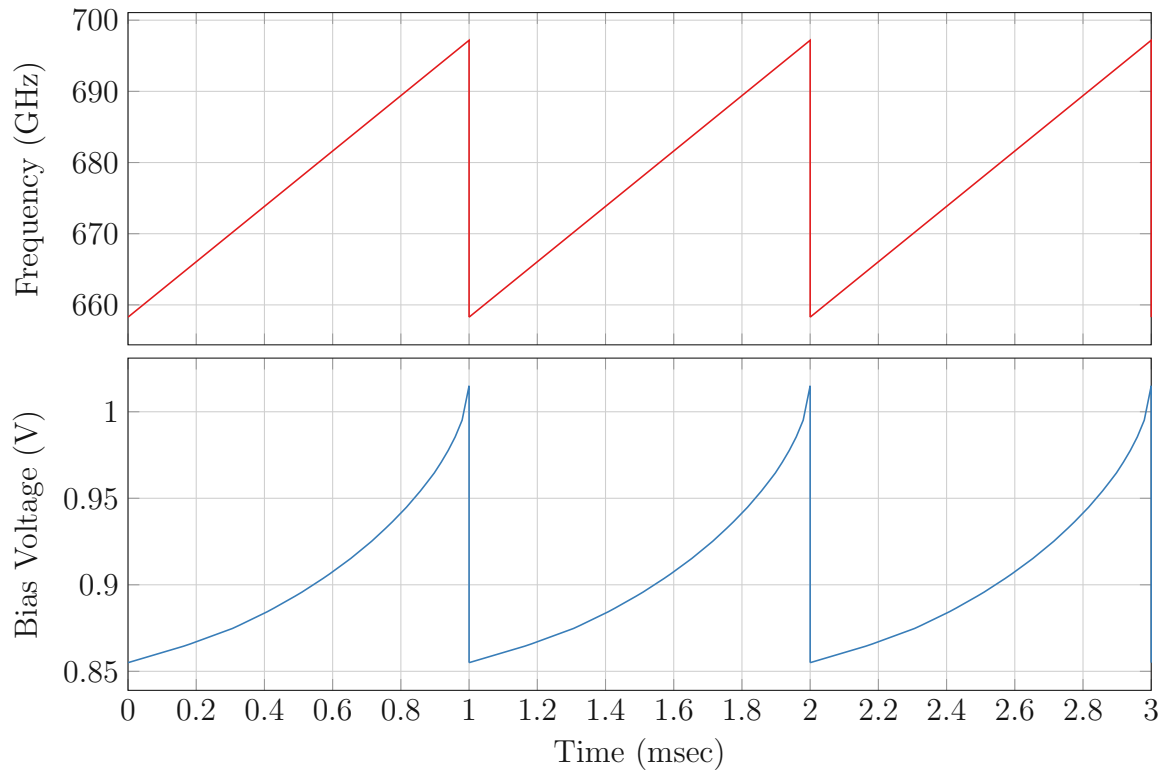


Figure 4.22: Sequence of the linearized chirps for the first section of the first frequency region and the corresponding sequence of the bias voltage sweeps that are linearizing the response.

properly shaped voltage sweep with a duration of 1 ms. It consisted of 50 segments with a duration of $20 \mu\text{s}$ each. The resulting linearized frequency sweep with the span of 38 GHz is shown in Fig. 4.22). The frequency-sweep rate is limited by the control equipment, the external parasitics of the oscillator, and by the RTD-resonator properties. The internal (inverse) time constants of RTD itself are in the THz range; thus, they do not impose any relevant limitations. Much faster sweep rates are possible.

A control voltage was applied to the RTD oscillator, which corresponds to a continuous train of saw-tooth linearized frequency sweeps. The modulated RTD oscillator generates a nearly rectangular spectrum with a bandwidth of 38 GHz, which is shown in Fig. 4.23). A slight deviation of the spectrum from an ideal rectangular shape is due to the bias dependence of the RTD oscillators' output power, as shown in the previous sections. The calibrated pyroelectric detector measured the output power of $23 \mu\text{W}$. The spectrum was measured with an interferometer in the Martin-Puplett configuration, see 4.4, and a Golay cell as the detector. The interferometer basically corresponds to a typical OCT measurement configuration; given a linear frequency sweep with a rectangular spectrum, the interferogram in Fig. 4.24 has a $\sin(x)/x$ shape, as expected. The peak of the interferogram corresponds to the configuration when both interferometer mirrors have an equal offset from the wire-grid interferometer polarizer. The peak width shows a 4 mm OCT resolution, corresponding to the 38 GHz bandwidth of the oscillator frequency sweeps.

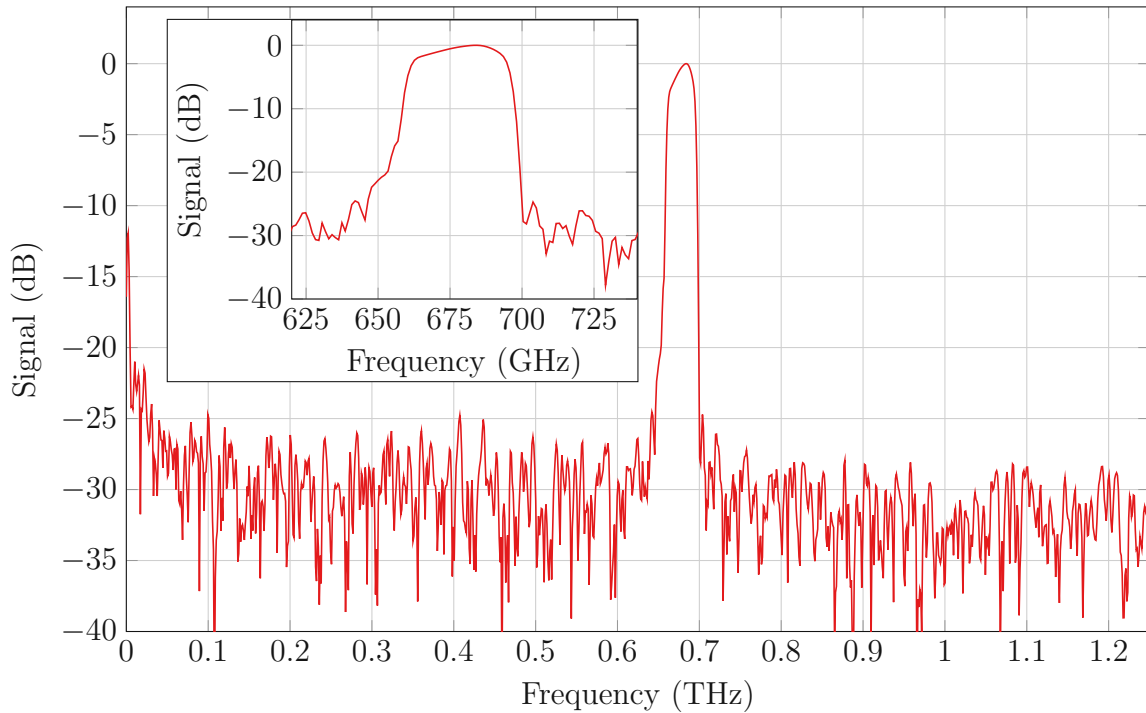


Figure 4.23: Measured frequency spectrum of the RTD oscillator with applied linearized frequency modulation. The inset shows zoomed part of the spectrum near the operation frequency.

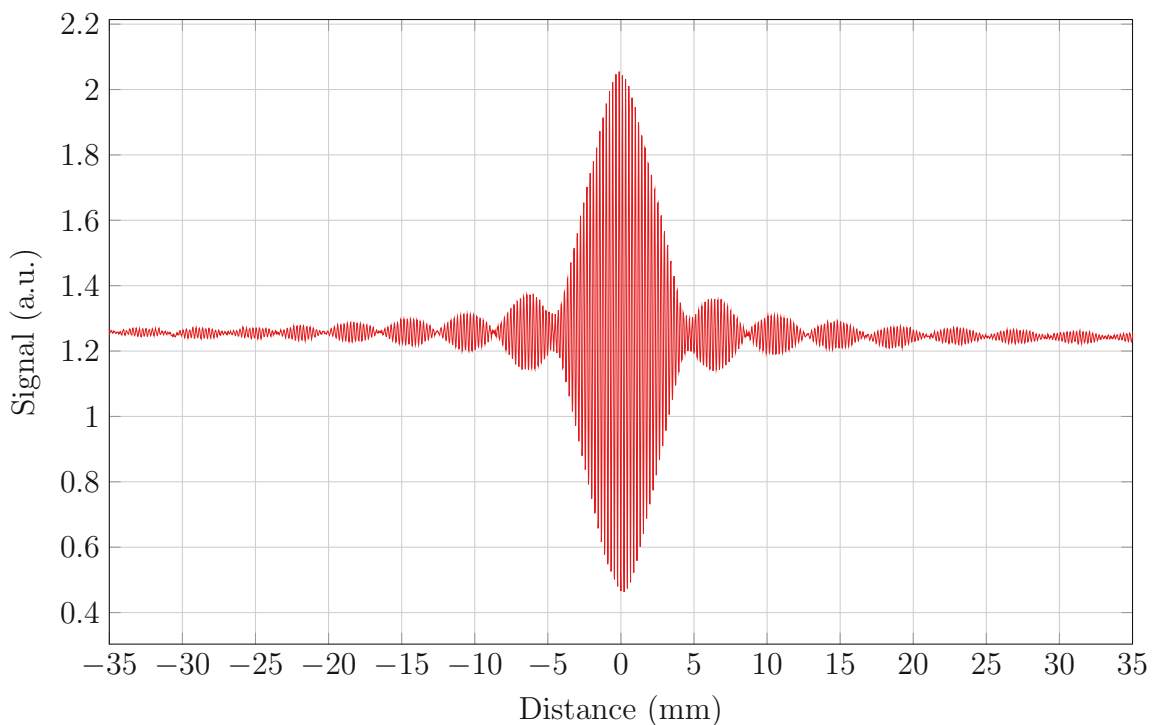


Figure 4.24: Measured interferogram of the output oscillator signal with the applied linearized frequency modulation. The period of the $\sin(x)/x$ function (OCT resolution) corresponds to half of the reciprocal bandwidth.

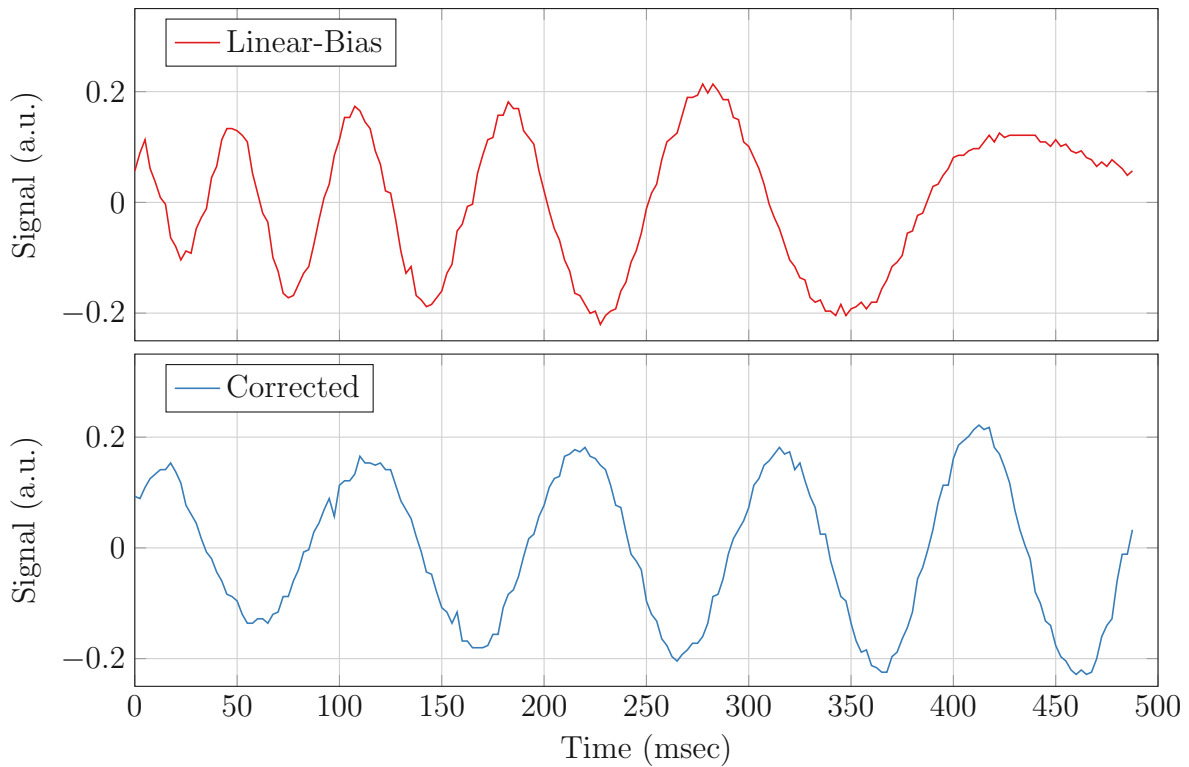


Figure 4.25: Detected FMCW-radar signals for the linear bias chirp and the corrected frequency chirp for a target at a distance of 23 mm in the time domain.

4.3.3 FMCW Radar

To confirm the functionality of the source, we tried to build an FMCW radar. The mutual shift of the mirrors in the interferometer allows one to create two paths with different times of flight. The power detector then mixes the delayed responses due to the square-law detection. The output frequency is then equal to the difference between the input frequencies. The Golay cell's response time is 30 ms; therefore, for the expected range of the detected frequency, we used a chirp with a duration of 490 ms. Fig. 4.25 compares the detected time domain signals for a simple linear bias chirp and a corrected chirp linearizing the frequency sweep. The target (static mirror in the moving arm of the interferometer) was at 23 mm. The linear chirp shows a frequency modulation in time. In contrast, the corrected chirps show a sinusoidal signal with a constant frequency. Fig. 4.26 then shows the corresponding range plots. The shape of the curve corresponding to the linear chirp shows a noticeable broadening of the peak, effectively decreasing the resolution and the signal strength. The corrected linearized chirp shows a clear peak corresponding to the target's distance.

4.3.4 Summary for the FMCW and OCT RTD oscillator source

We have presented one possible real-life application of the RTD oscillators: the functionality of RTD oscillators as sources for sub-THz and THz FMCW radars and OCT applications. The presented source provided a spatial resolution of 4 mm with an output power of $23 \mu\text{W}$ with an

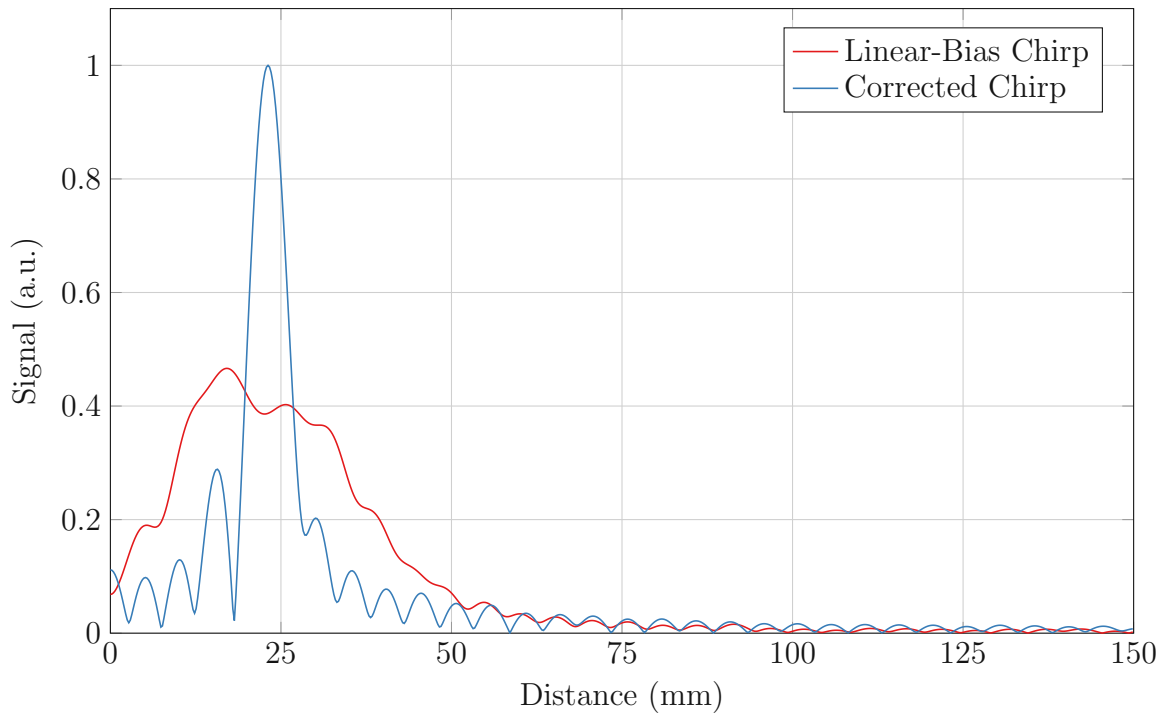


Figure 4.26: Detected FMCW-radar signals for the linear bias chirp and the corrected frequency chirp for a target at a distance of 23 mm in the range plot.

average operation frequency of 680 GHz and 38 GHz (5.5 %) bandwidth. This is an FMCW radar operating at the highest frequency so far. However, the RTD oscillators are like all other oscillators, prone to locking to a signal with a similar frequency as their oscillation frequency if such a signal impinges on the oscillator, see, e.g., [138]. In the FMCW radar, the returning echo from the target towards the oscillator can cause the oscillator to lock to it (injection locking). This would distort the frequency tuning, which would then rather be insteps than in a continuous manner. Thus, the echoing signal needs to be suppressed by either putting the source of the axis or by an isolator. In our case, signal isolation is one of the key properties of the Martin-Pupplet interferometer, see section 4.4 for more details. Another solution can be employing another modulation schema, such as subcarrier modulation of the RTD, see [57]. In this scheme, the amplitude of the RTD oscillations is modulated with a linear frequency modulation signal. Then, although the oscillation frequency is locked, the amplitude can still be adjusted, and thus the modulation can be performed. The subcarrier modulation concept requires high bandwidth of the modulation signal, the same bandwidth as the detection bandwidth. In the direct modulation, as described in this section, a large bandwidth is generated by the RTD; thus, the requirements on the driving circuitry are much more moderate.

4.4 Measurement system

In this section, we briefly describe the measurement system used to measure the oscillation frequency of the oscillators and for the FMCW radar. Here presented measurement methods

are well-known. However, it is important to describe them to put the obtained results into the right perspective. The core of the frequency measurement apparatus is the Martin-Pupplet interferometer.

Martin-Pupplet interferometer

We used an interferometric approach to measure the oscillation frequency of the oscillators. In this method, the incoming signal, in the form of a collimated beam, is divided into two arms of the interferometer with a beam splitter. The length (and thus its delay) of one of the arms can be changed. The split signals are merged again, and their interference is detected with a power meter. For the sinusoidal input signal, if the merged signals are in the phase, we detect maximum power and minimum if they are out of phase. Changing the delay of the arm, we get a periodical maximum and minimums of the detected signal (interferogram), which period corresponds to the frequency of the input signal as:

$$f = \frac{c_0}{2}d, \quad (4.5)$$

where c_0 is the speed of light and d is the spatial distance corresponding to the detected signal's period. In case the input signal is composed of many frequencies, we perform a Fourier transform of the detected signal over the full span of the delay that the interferometer can deliver. This gives us the input signal spectrum, where the formula mentioned above transforms the spatial dimension into the frequency dimension. The frequency resolution of the interferometer corresponds to the maximal delay of the variable arm over which we can detect at least one period of the detected signal. In our case, the interferometer arm length was 30 cm, and thus the maximum resolution of the system was 1 GHz. The resolution limit also limits the minimum measurable frequency. However, additionally by the detector's frequency sensitivity, alignment of the interferometer, and the divergence of the collimated beam. For our system, the minimal frequency was due to the beam divergence of approximately 50 GHz. The beamsplitter's operation range, detector sensitivity, and alignment give the maximum frequency.

Semi-transparent mirrors can be used for the beamsplitter, e.g., a silicon plate for the THz frequencies. However, due to the certain thickness of the mirrors, the beamsplitters act as Fabry-Perot resonators, which limits their frequency band, see [139].

The Martin-Pupplet interferometer works similarly to standard interferometers, except that it manipulates the polarizations of the beams, see the principal schematic in Fig.4.27. It polarizes the input beam by a wire grid to have only, in our case, vertical polarization. Then it splits it by wire grid polarizer (beam splitter) into two beams having both vertical and horizontal polarizations. The wire grid of the beamsplitter is rotated to split the signal with a ratio of 1:1. In our case, for splitting the beam under the angle of 45° , the angle between the wire grid and the horizontal plane should be 36.26° . The split beams are reflected back to the beam splitter by rooftop mirrors that flip only the horizontal polarization (depending on the orientation of the mirror), making the beam that propagated through the beamsplitter during the splitting

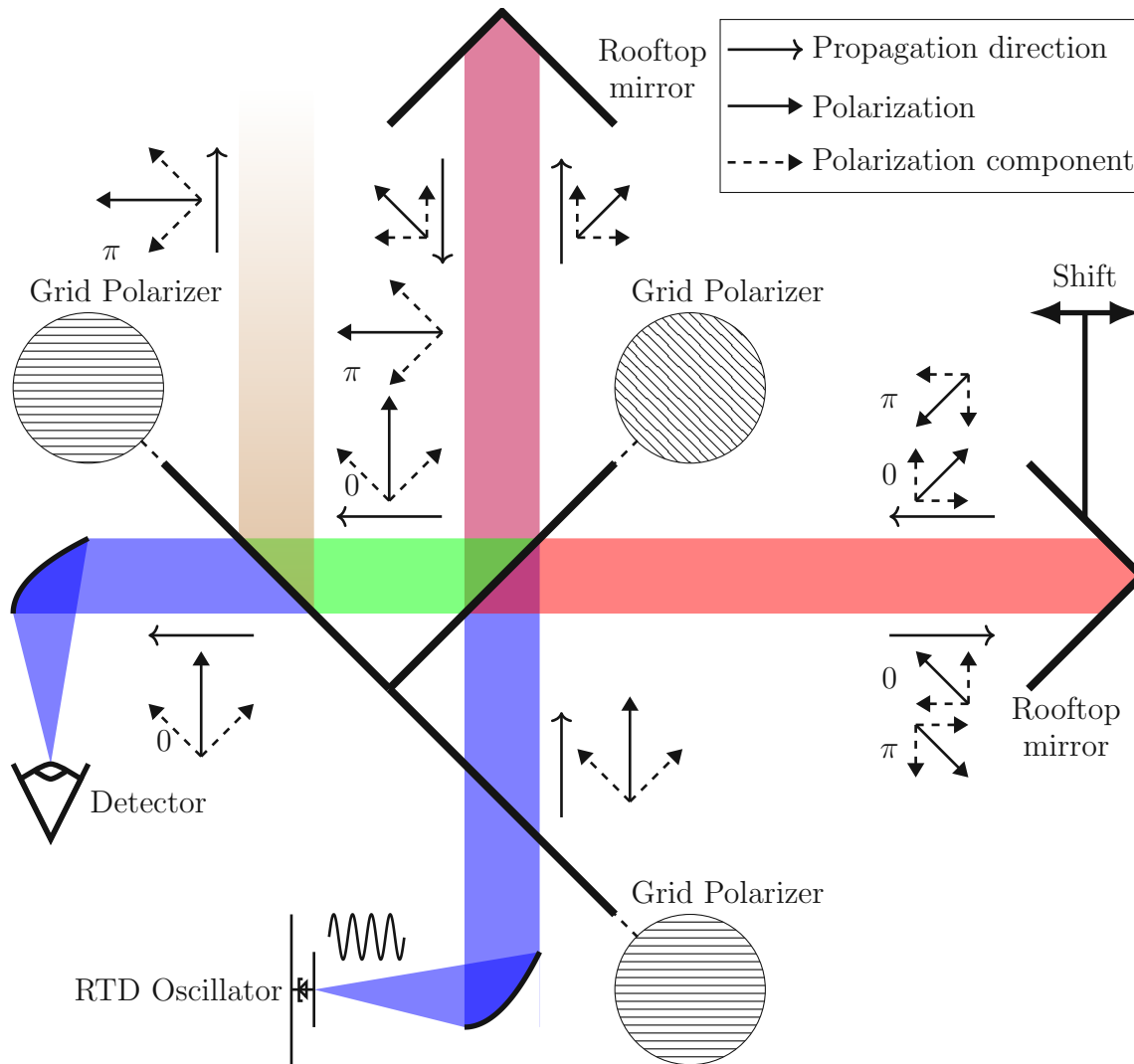


Figure 4.27: Principal schematic of Martin-Puplet interferometer. The polarization is of the electric field and is shown in the view of the propagation. The beam splitter is, in this case, a grid polarizer. The mirrors in the interferometer are rooftop mirrors that flip only the horizontal polarization. The interferometer has two inputs and two outputs. The secondary input (that would be reflected from the first grid polarizer) is not marked, and the output for horizontal polarization (shown in the brown fading color) was not used.

is reflected from the splitter, and the beam that was reflected during the splitting propagates through the splitter. The output signal's polarization changes with the shiftable arm's delay. If we filter out one of the polarization, we obtain the interferogram. The wire grid polarizer does not introduce the Fabri-Perot resonator and thus can be used in the interferometer to measure large frequency bands. The maximum operating frequency of wire grid polarizers is limited by the wire separation length, which must be smaller than is than half of the wavelength.

Because of the flips of the polarizations by the rooftop mirrors, there are no back-reflected waves toward the signal source. This feature allowed us to build the FMCW radar without locking the oscillator. However, this left the radar to be usable in this configuration only for targets flipping one of the polarizations.

Detectors and the Lock-in amplification

As the detector for the frequency measurement, we used GC-1P Golay cell. The Golay cell is a sensitive detector with noise equivalent power of $\approx 1.5 \times 10^{-10} \text{ W/Hz}^{1/2}$. However, it is not well-suited for precise power measurements because of the difficulties in reliably calibrating it.

For the output power measurement, we used a pyroelectric sensor, SLT THz 20 HS. The pyroelectric sensor has much lower detectivity than the Golay cell and suffers from acoustic distortion. According to the manufacturer, the minimum measurable power is $\approx 10 \mu\text{W}$. However, it can be reliably calibrated by a metrology authority. The used pyroelectric was calibrated by PTB. During the power measurement, we tried to accurately recreate the same measurement setup used during the calibration with a double parabolic mirror setup, in which we focused the output signal from the RTD onto the detector.

Due to the thermal noise in the system, the noise generated from the amplifiers of the detectors, $1/f$ noise, and the limited output power of the RTD oscillators, we need to employ lock-in amplification of the signal. The input signal is modulated by amplitude modulation (on-off keying) for the lock-in amplification. The detected signal is then multiplied by the modulation signal and integrated by a low-pass filter, which is equivalent to a homodyne detection scheme. Because of the filtering, we suppress the broadband noise. The modulation additionally shifts the detected signal from DC to the modulation frequency, which reduces the $1/f$ noise and allows us to use amplifiers with high gain without drift compensation.

The modulation can be done by a chopper, a fan that periodically blocks the beam path. However, the used detectors are sensitive to the turbulent air in their vicinity, and thus we can also modulate the bias of the RTD with the on-off keying to achieve the same result. The used detectors are relatively slow; thus, the modulation frequency is in the range of tens of Hz.

Chapter 5

Large signal RTD dynamics

This chapter shows the dynamical behavior and inner mechanics of RTDs as responses to the dynamical perturbation of the bias voltage. What differentiates the work described in this chapter from the previous works is that, in this case, the perturbation does not need to be small, and thus we call this chapter Large signal RTD dynamics. This chapter shows results that were partly published in the peer-reviewed journal article P. **Ourednik**, G. Picco, D. Tuan Nguyen, *et al.*, “Large-signal dynamics of resonant-tunneling diodes,” *Journal of Applied Physics*, vol. 133, no. 1, p. 014 501, 2023. DOI: 10.1063/5.0134223.

As we have shown in Chap. 2, RTD oscillators are close to satisfying basic requirements for practical applications. However, the design and analysis of RTDs in RTD oscillators is still, to a large extent, based on empirical and phenomenological modeling. That hinders further development of RTD oscillators, thus indicating an urgent need to develop an accurate, sufficiently-general, but also sufficiently-simple, physics-based method for the simulation of the RTD dynamics. The aim of this chapter is to provide such a method.

An RTD oscillator consists of a resonator/radiator and an RTD as an active element; the analysis of such an oscillator can be split into two parts. The resonator/radiator is the linear part, its modeling is straightforward and can be reliably done with commercial electromagnetic simulators. The RTD, on the other hand, is an essentially nonlinear component; its nonlinearity eventually determines the oscillation amplitude and the output power of the RTD oscillators. Therefore, an accurate large-signal (LS) (i.e., nonlinear) dynamical model for RTDs is required.

So far, the dynamical RTD models are available only in the small-signal (SS) approximation, see [102]–[104], [125], [140], [141]. Those models show that the charge-relaxation processes govern the RTD dynamics with a certain bias-dependent SS relaxation time constant τ_{rel} , see [102]–[104], [125]. Until now, LS analysis of RTDs in RTD oscillators has been done in the following ways: (i) quasi-static LS analysis of RTDs; in this case, one relies on the measur-

able static RTD I-V curves; this approach is applicable only at low frequencies ($\omega\tau_{\text{rel}} \ll 1$, ω is the angular frequency); (ii) extrapolation of the nonlinear DC RTD characteristics to higher frequencies, see [80], [100], [142], accuracy and validity of such approaches are questionable; (iii) high-frequency ($\omega\tau_{\text{rel}} \gg 1$) LS model, see [105] in this case, the quantum-well (QW) charge cannot follow the AC oscillations and effectively gets “frozen” (Coulomb interaction of the QW electrons is effectively suppressed in this regime), which greatly simplifies the LS analysis.

None of the above approaches provides an accurate dynamic LS RTD model for the intermediate frequency range ($\omega\tau_{\text{rel}} \sim 1$), which is the most common operating range in state-of-the-art RTD oscillators. This chapter aims to develop such a physics-based model; the model should also cover the low- and high-frequency regimes.

Another problem we address concerns the set of parameters required to construct an accurate dynamical LS model. Among such basic parameters are the tunnel rates through the RTD barriers, the electron concentration in the QW (N_{2D}), and the geometrical RTD capacitances. These parameters could be calculated with the help of commercial simulators for RTDs and quantum structures, e.g., these simulators can fairly well reproduce the RTD peak current density and its bias position. However, those simulators fail to accurately describe the NDC region of the experimental RTD I-V curves since the NDC and the neighboring regions are governed by more subtle parameters, like the broadening of the quantum levels, scattering rates, structural imperfections, etc. Those parameters are not known and hardly measurable in practice. Therefore, our second objective is to formulate an approximate but sufficiently accurate dynamic LS model that relies solely on the measurable DC RTD I-V curve and the basic RTD parameters, which can be easily and reliably calculated or estimated, knowing the nominal parameters of the RTD layers.

The chapter is organized as follows: In Section 5.1, we formulate the static and dynamic RTD models. Section 5.2 explains how the RTD dynamics can be described in a phase space, defined by the RTD bias and QW electron density. In Section 5.3, we demonstrate that an LS RTD admittance can be with good accuracy described by a simple RLRC equivalent circuit. In Section 5.4, we formulate a simplified model for RTD dynamics, which is based on the knowledge of the basic RTD parameters and measured (or measurable) RTD I-V curve. Section 5.5 explains the connection between the LS and SS dynamical RTD parameters. In Section 5.6, the RTD dynamics in the high-frequency limit is discussed. In Section 5.7, we discuss the main approximations of our dynamical models. Section 5.8 gives a qualitative explanation for the variation of the RTD dynamical characteristics with the AC amplitude. We conclude in Section 5.10.

5.1 Static and dynamic RTD models

For illustrative purposes, we applied the theoretical models to an RTD, which we have experimentally studied and used in RTD oscillators up to 0.5 THz that were described in Chap. 4 and

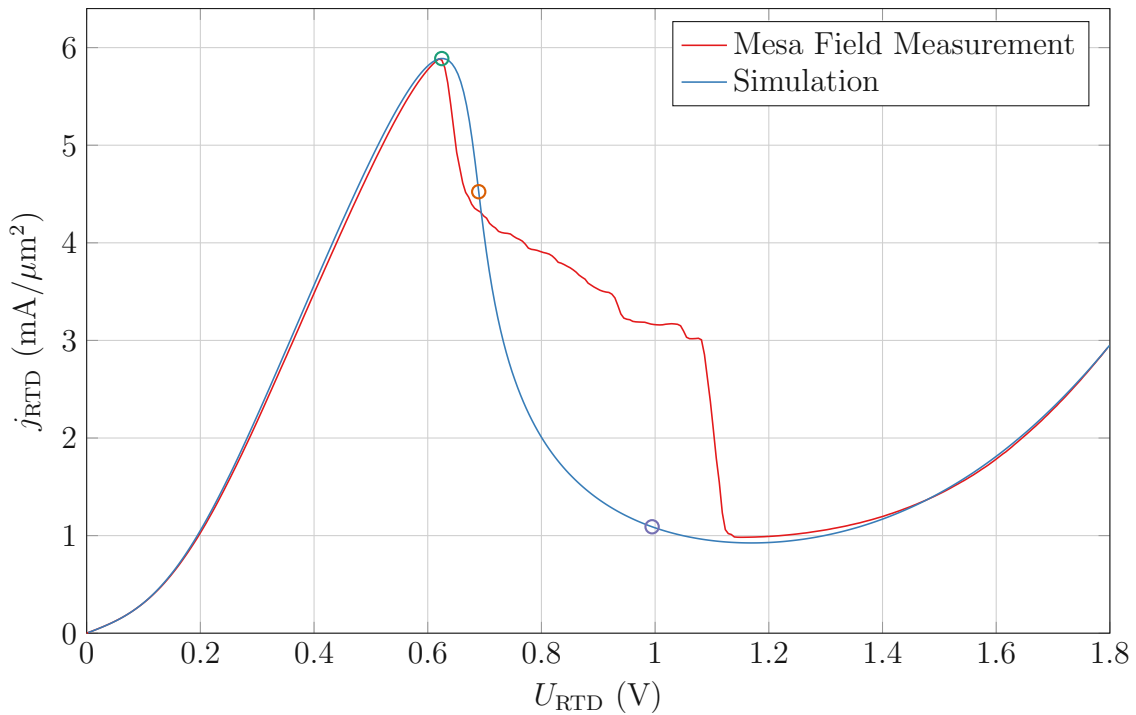


Figure 5.1: Measured and simulated (Hartree approximation) I-V curves of an RTD studied in Ref. [80] and used as an example structure in the present work. The colored circles correspond to several bias points, for which we discuss representative RTD-response characteristics in this chapter.

in Ref. [80]. This is a representative RTD, and it has rather typical characteristics for RTDs used in the state-of-the-art sub-THz and THz RTD oscillators.

5.1.1 Static RTD model

The static (DC) characteristics of an RTD are calculated by a self-consistent solution of the Schrödinger and Poisson equations (Hartree approximation) in the active RTD region between (and slightly within) the highly-doped contact regions on both sides of the barriers. The calculated DC I-V curve of the above RTD is shown in Fig. 5.1, where the RTD nominal parameters were fine-tuned to fit the measured data.

We further used the computed static RTD parameters to calculate the SS dynamic RTD characteristics, see [102]–[104], [125] The maximum of τ_{rel} of this RTD in the NDC region is ≈ 350 fs, which corresponds to the characteristic frequency of ≈ 450 GHz when the condition $\omega\tau_{\text{rel}} \approx 1$ is fulfilled. The results presented in this chapter are also applicable in a straightforward manner to other RTDs with thinner or thicker barriers with accordingly modified τ_{rel} ; the characteristic frequencies are rescaled as $\propto 1/\tau_{\text{rel}}$ in this case.

5.1.2 LS dynamic RTD model

We formulate the dynamic (AC) LS RTD model in the sequential-tunneling approximation, see [126]. Further, we assume that the current density is homogeneous in the emitter- and collector-barrier regions of the RTD. This is a valid approximation if the electron transit time (τ_{dep}) through the collector-depletion region is small ($\omega\tau_{\text{dep}} \ll 1$). This condition is usually satisfied since the typical THz state-of-the-art RTDs have a short depletion region, see, e.g. [84], [101], where $\tau_{\text{dep}} \ll 100$ fs, as we have described in Sec. 2.4.2 of Chap. 2. Also, τ_{dep} is usually $\ll \tau_{\text{rel}}$ in such RTDs; therefore, we neglect τ_{dep} in the subsequent analysis. We also neglect the effect of the plasma oscillations in the contacts, because the plasma oscillation frequency (> 10 THz) is much higher than is the operation frequency of the RTD oscillators.

The alignment between the QW subbands and the emitter and collector regions determines the currents flowing in those regions. These currents also define the time evolution of the QW charge. These internal currents, the QW charge evolution, and the connection of the internal RTD parameters (charges and currents) to the external RTD parameters (U_{RTD} and j_{RTD} , where U_{RTD} is the bias across the RTD and j_{RTD} is the external RTD current density) can be described by the following set of equations:

$$j_e = e \left(\sum_i N_{e,i} \nu_{e,i} - N_{2D} \nu_{e,1} \right), \quad (5.1)$$

$$j_c = e (N_{2D} - N_c) \nu_c, \quad (5.2)$$

$$\Delta j \stackrel{\text{def}}{=} j_e - j_c = e \partial_t N_{2D}, \quad (5.3)$$

$$j_{\text{RTD}} - j_e = -\partial_t Q_e, \quad (5.4)$$

$$F_e = F_e(U_{\text{RTD}}, N_{2D}), \quad (5.5)$$

$$F_e - F_c = -\frac{e N_{2D}}{\varepsilon}, \quad (5.6)$$

$$U_{\text{RTD}} = U_c(F_c) + U_e(F_e), \quad (5.7)$$

where e is the elementary charge; t is the time; ε is the dielectric constant of the RTD layers; j_e and j_c are the current densities in the emitter- and collector-barrier regions, respectively; N_{2D} is the 2D density of electrons in the QW; ν_c is the electron tunneling rate from the ground QW subband to the collector; $\nu_{e,i}$ is the corresponding tunneling rate from an i -th QW subband to the emitter; N_c is the 2D collector injection electron concentration for the ground QW subband (it is equal to N_{2D} if the ground QW subband is kept in equilibrium with the collector); $N_{e,i}$ are the corresponding emitter injection electron concentrations for the respective QW subbands; Q_e is the screening charge in the emitter; F_e and F_c are the electric fields inside the emitter and collector barriers, respectively; U_c and U_e are the potential differences between the collector- and emitter-Fermi levels and the bottom of the first QW subband, respectively.

A sketch of the RTD band diagram corresponding to the set of Eqs. (5.1-5.7) is shown in Fig. 5.2. The model describes forwardly biased RTDs. Equations (5.1) and (5.2) describe the

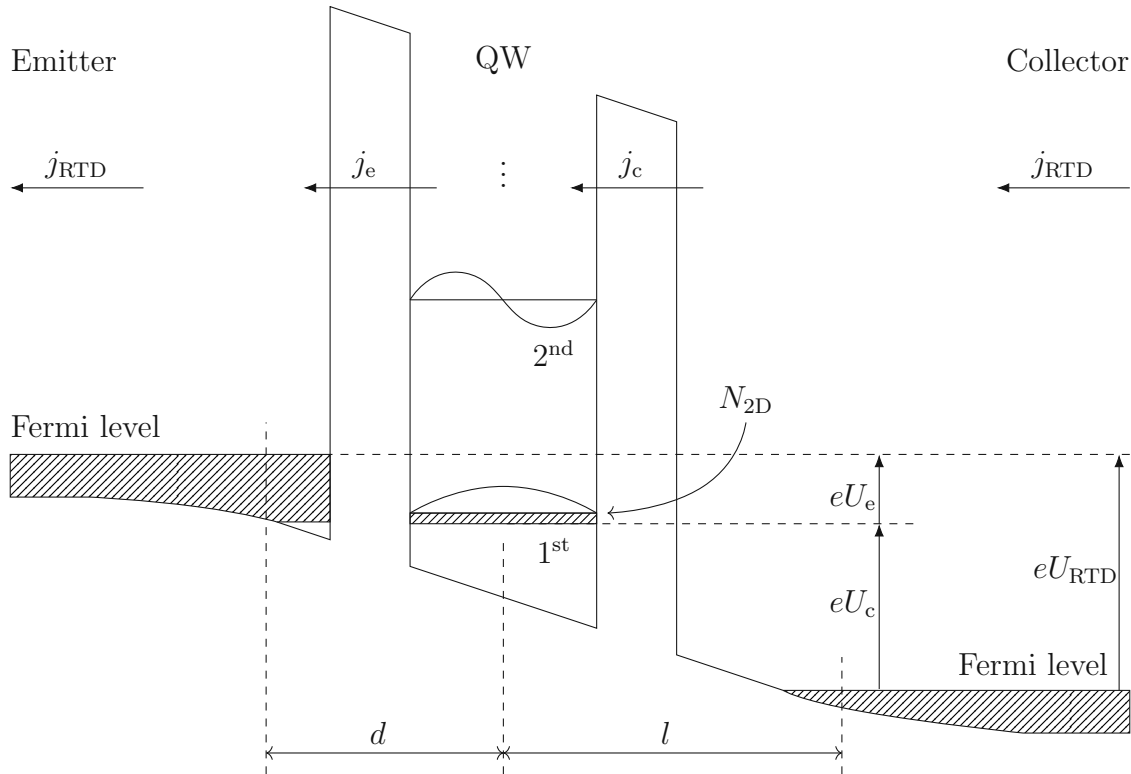


Figure 5.2: The sketch of the Γ -band diagram of a typical RTD. The sketch does not show the detailed band structure of the QW, which can be more complicated due to a mini-well. The number of resonant states is truncated to only two, as typically, only those play the dominant role in electron transport. Note that the currents have the conventional direction.

tunnel currents through the emitter and collector barriers, respectively. The terms with N_{2D} describe the outgoing electron flow from the QW; in these terms, we assume that all electrons in the QW are in the ground subband, i.e., the electrons tunneling into excited subbands are immediately scattered to the ground one. The other terms in (5.1) and (5.2) describe the electron flows into the QW. $\nu_{e,i}$, ν_c , $N_{e,i}$, and N_c are determined by the alignment of the QW subbands with the emitter and collector regions. $\nu_{e,1}$ is strongly dependent on the broadening (scattering, interface roughness, etc.) of the ground QW subband; this broadening eventually defines the RTD characteristics in the NDC region and its vicinity. Equations (5.3) and (5.4) are the continuity equations for the QW and emitter charges, respectively. Equations (5.5), (5.6), and (5.7) describe the voltage drops across the RTD. One can represent U_c and U_e as unique functions of F_c and F_e , respectively; the sum of U_c and U_e is equal to the total RTD bias, as stated by (5.7). The fields F_c and F_e are connected to each other and N_{2D} by the Poisson equation, that leads to Eq. (5.6). We can also note that the field F_e is uniquely defined by the RTD bias and N_{2D} ; we denote this by Eq. (5.5).

A simplified version of the model described by Eqs. (5.1-5.7) has been used in the past for the analysis of LS high-frequency ($\omega\tau_{rel} \gg 1$) RTD characteristics in Ref. [105] and a linearized version of the model has been used for the analysis of the SS RTD characteristics in Refs. [102]–[104], [125]. However, the model has not been applied to the analysis of the LS

RTD dynamics in a general case.

With Eqs. (5.1-5.7), one can represent all internal RTD parameters (current densities, tunnel rates, etc.) as functions of just two parameters: N_{2D} and U_{RTD} . In this sense, these two parameters (N_{2D} and U_{RTD}) define the phase space of an RTD. Indeed, N_{2D} and U_{RTD} fully define the potential band profile inside an RTD and, therefore, all its state parameters. These two phase-space parameters also determine the external RTD current density (j_{RTD}). We can make this dependence explicit in the following way. Starting with Eq. (5.4), expressing Q_e via F_e (using the Poisson equation) as:

$$F_e = -\frac{Q_e}{\varepsilon}, \quad (5.8)$$

we get:

$$j_{RTD} = j_e + \varepsilon \partial_t F_e. \quad (5.9)$$

From the chain rule for the time derivative of F_e we get:

$$\partial_t F_e = \frac{\partial F_e}{\partial U_{RTD}} \partial_t U_{RTD} + \frac{\partial F_e}{\partial N_{2D}} \partial_t N_{2D} \quad (5.10)$$

Using Eq. (5.6) we can write for the partial derivatives:

$$\frac{\partial F_e}{\partial U_{RTD}} = \frac{\partial F_c}{\partial U_{RTD}}, \quad (5.11)$$

$$\frac{\partial F_e}{\partial N_{2D}} = \frac{\partial F_c}{\partial N_{2D}} - \frac{e}{\varepsilon}. \quad (5.12)$$

Next, we can write for the partial derivative of the emitter voltage according to U_{RTD} :

$$\frac{\partial U_e}{\partial U_{RTD}} = d \frac{\partial F_e}{\partial U_{RTD}}, \quad (5.13)$$

where $d = \frac{\partial U_e}{\partial F_e}$, and using Eq. (5.7) we can express this partial derivative as:

$$\frac{\partial U_e}{\partial U_{RTD}} = 1 - l \frac{\partial F_c}{\partial U_{RTD}}, \quad (5.14)$$

where $l = \frac{\partial U_c}{\partial F_c}$. In their definition, l and d have the meaning of the effective thicknesses of the collector- and emitter-barrier regions, which include the screening and the depletion lengths, the respective barrier thickness, and half of the QW width, see Fig. 5.2. We can intuitively understand this definition if we rewrite, the definition of l using the Poisson equation as $\delta Q_c = \varepsilon \delta U_c$. The collector charge is changing only at the end of the depletion region because the depletion layer is fully “filled,” and thus the length l corresponds to its entire length. This is in contrast to the position of the center of the “mass” of the collector charge, which is located in the center of the depletion region.

Set of Eqs. (5.13-5.14) can be solved for the partial derivative of F_e using Eq. (5.11) as:

$$\frac{\partial F_e}{\partial U_{RTD}} = \frac{1}{l + d}, \quad (5.15)$$

Analogically, we can write the partial derivatives of the emitter voltage according to N_{2D} and solve them using Eq. (5.12) as:

$$\frac{\partial F_e}{\partial N_{2D}} = -\frac{e}{\varepsilon} \frac{l}{l+d}, \quad (5.16)$$

Using the above-derived expressions for the partial derivatives and Eq. (5.3) allows us to rewrite the equation for j_{RTD} as:

$$j_{\text{RTD}} = j_c + \frac{d}{l+d} e \partial_t N_{2D} + C_{\text{ec}} \partial_t U_{\text{RTD}}, \quad (5.17)$$

where $C_{\text{ec}} = \varepsilon/(l+d)$ is the geometrical RTD capacitance.

In the following analysis, we will use Eq. (5.17) rewritten further in the following form:

$$j_{\text{RTD}} = e N_{2D} \nu_c + \frac{d}{l+d} \Delta j + C_{\text{ec}} \partial_t U_{\text{RTD}}, \quad (5.18)$$

where we used Eq. (5.3) to eliminate the time derivative of N_{2D} and replaced j_c with Eq. (5.2), neglecting the back injection from the collector (the term with N_c). The latter assumption holds true in almost all RTDs used in RTD oscillators, except for some rather exotic structures with very high doping in the collector, see, e.g., [84]. We also note that Eq. (5.17) (if we replace $e \partial_t N_{2D}$ with Δj) and Eq. (5.18) correspond to the Shockley-Ramo theorem, see [128], [129].

5.2 RTD dynamics in phase space, “full model” (FM)

Our next task is to determine the time evolution of the parameters N_{2D} and U_{RTD} . If we know them, then, as stated above, we can determine all internal RTD parameters with Eqs. (5.1-5.7) and also the external RTD current with Eq. (5.17) or (5.18). In other words, we need to find the dynamical RTD trajectories in the N_{2D} - U_{RTD} phase space.

The time evolution of N_{2D} is determined by Eq. (5.3), and Δj can be expressed as a function of the static values of N_{2D} and U_{RTD} . Knowing Δj , we can fully describe the dynamic evolution of N_{2D} for an arbitrary time-dependent RTD bias (U_{RTD}). For the calculation of the RTD trajectories, we only need to know Δj . A map of $\Delta j(U_{\text{RTD}}, N_{2D})$ calculated by a static solution of the Schrödinger and Poisson equations (N_{2D} and U_{RTD} are fixed at each point) is shown in Fig. 5.3.

To make the analysis more intuitive, we note that the current difference $\Delta j(U_{\text{RTD}}, N_{2D})$ can be regarded as a “restoring force” for the deviations of N_{2D} from its equilibrium (DC) values N_{2D}^{DC} . It describes the dynamics of the relaxation of N_{2D} to N_{2D}^{DC} , when N_{2D} is perturbed (the perturbation is not necessarily small) for a fixed U_{RTD} . When U_{RTD} varies in time, Eq. (5.3) describes the trajectories of N_{2D} in the phase space.

Further, we apply a harmonic AC bias with the amplitude of U_{AC} in addition to a DC bias U_{B} :

$$U_{\text{RTD}} = U_{\text{B}} + U_{\text{AC}} \cos(\omega t), \quad (5.19)$$

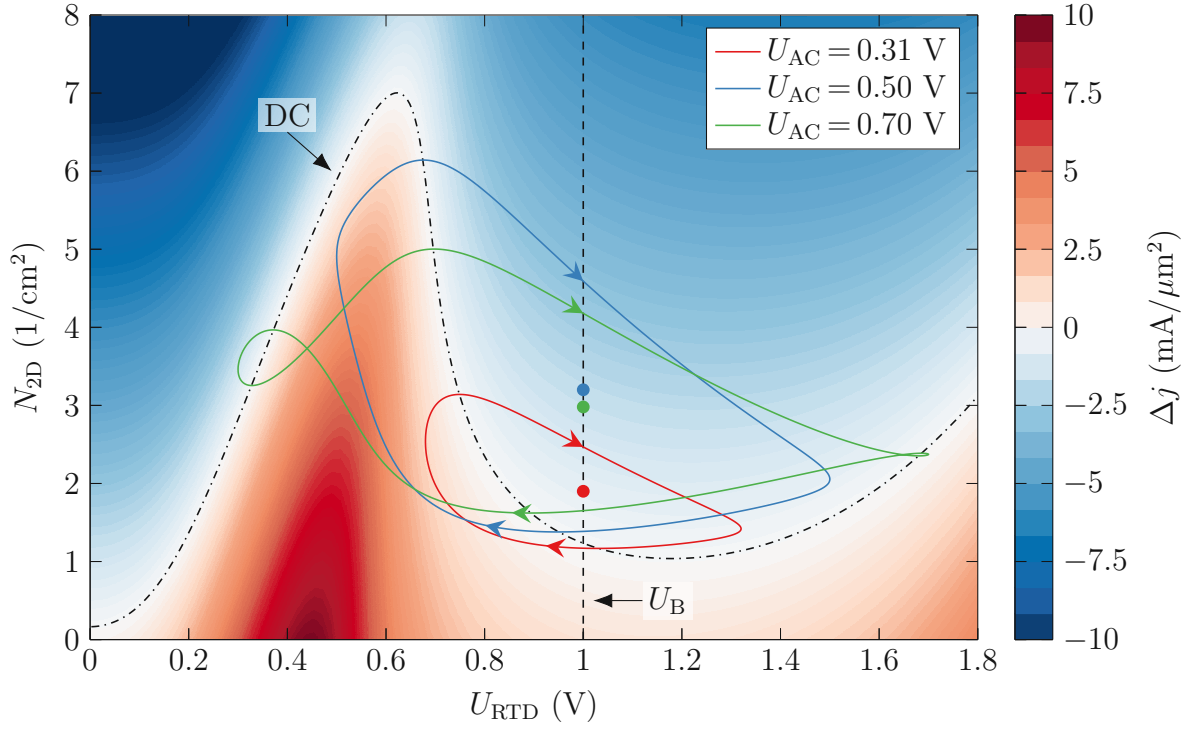


Figure 5.3: Δj in the phase space of U_{RTD} and N_{2D} for the example device. The white contour highlighted by the dash-dotted line corresponds to the equilibrium. The continuous lines show trajectories of N_{2D} at the frequency of 1 THz for various amplitudes at the bias voltage of $U_B = 1$ V. The dots on the bias line correspond to N_{2D} averaged over one period.

and calculate N_{2D} . Several N_{2D} steady-state trajectories for the frequency of 1 THz and various U_{AC} are shown in Fig. 5.3. Knowing the trajectories, we calculate the RTD current density with Eq. (5.18). If the first harmonic of the RTD current is selected, then its real and imaginary components combined define a complex (1st harmonic, marked by the (1) in the superscript) RTD admittance:

$$Y_{LS} = G_{LS} + jB_{LS} = \frac{j_{RTD}^{(1)}}{U_{AC}}. \quad (5.20)$$

The AC amplitude does not need to be small in this analysis; therefore, we denote it as a large-signal (LS) response. G_{LS} is the LS conductance, and B_{LS} is the LS susceptance. The frequency dependence of G_{LS} at different biases and for different AC amplitudes is shown in Fig. 5.4. The variation of G_{LS} with the AC amplitude is relevant for determining oscillators' output powers, see, e.g., [130].

5.3 RTD LS equivalent circuit

The large signal conductance G_{LS} shown by the curves in Fig. 5.4 takes quasi-static values (corresponding to the DC I-V curve) at low frequencies; we denote these values as G_{LS}^0 . On the other hand, they converge asymptotically to specific high-frequency values with an increase in frequency, as was shown in Ref. [105]; we denote them as G_{LS}^∞ . These values correspond to a

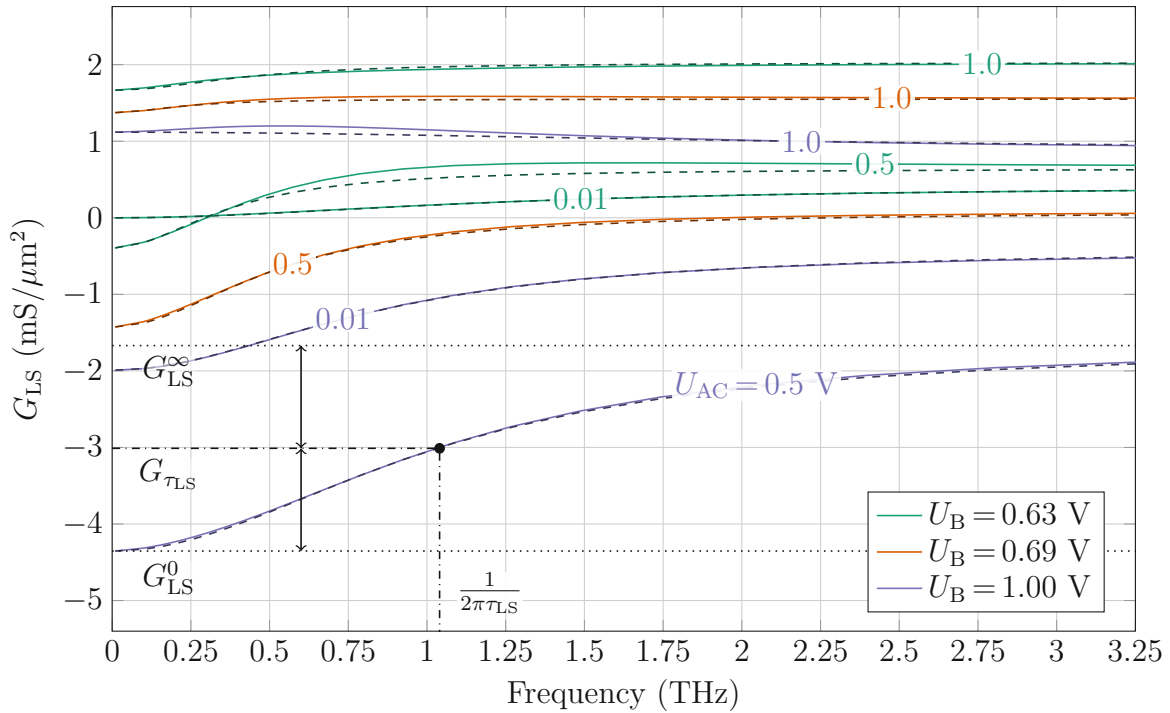


Figure 5.4: G_{LS} for various bias voltages and AC amplitudes. The dashed lines correspond to approximations with the RLRC model. The numbers on the lines correspond to the AC voltage amplitudes. An example of τ_{LS} estimation is shown for the case of $U_{ac} = 0.5$ V and $U_B = 1.00$ V.

situation when the frequency of the applied AC signal is so high that the QW charge cannot follow the bias variations: $N_{2D} \rightarrow \text{constant}$ in this case and the trajectories in Fig. 5.3 become horizontal.

Further, the roll-off of G_{LS} with the frequency we approximate with:

$$G_{LS} = G_{LS}^{\infty} + \frac{G_{LS}^0 - G_{LS}^{\infty}}{1 + (\omega\tau_{LS})^2}, \quad (5.21)$$

giving the correct low- and high-frequency asymptotic values. τ_{LS} is a fitting parameter, defined as $\tau_{LS} = 1/\omega$ at the frequency, when the simulated curve crosses the middle level between the low- and high-frequency asymptotic values, denoted as $G_{\tau_{LS}}$ in Fig. 5.4. τ_{LS} is dependent on U_{AC} and the bias point U_B . The approximate curves are very close to those obtained by full-model simulations, see Fig. 5.4.

Due to the causality of a response function, Eq. (5.21) has to satisfy the Kramers-Kronig relation. With the account of the last term (with C_{ec}) in Eq. (5.18), that leads to the following expression for Y_{LS} :

$$Y_{LS} = j\omega C_{ec} + G_{LS}^{\infty} + \frac{G_{LS}^0 - G_{LS}^{\infty}}{1 + j\omega\tau_{LS}}. \quad (5.22)$$

The expression corresponds to an equivalent RLRC circuit shown in Fig. 5.5. The circuit has the very same structure as the one derived for the small-signal RTD response in Ref. [102] by linearizing Eqs. (5.1-5.7). The only difference is that the small-signal parameters (SS DC conductance G^0 , SS HF conductance G^{∞} , and τ_{rel}) need to be replaced by the LS ones.

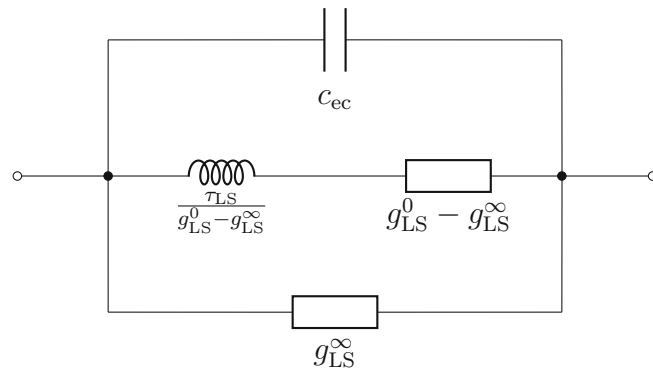


Figure 5.5: RLRC equivalent circuit for the LS response of the RTD. The circuit elements in the model depend on the bias U_B and AC amplitude U_{AC} .

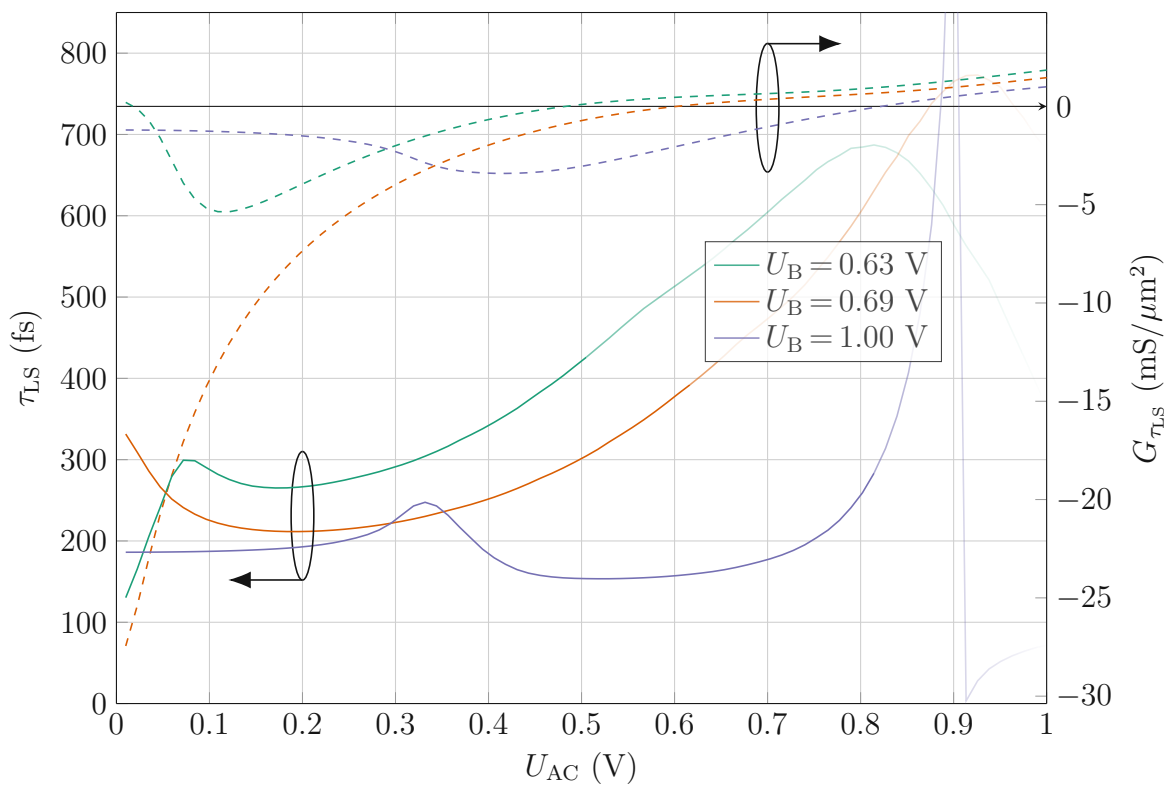


Figure 5.6: Dependence of τ_{LS} on U_{AC} at different bias points. The dashed lines show the LS conductances for frequencies corresponding to $\omega\tau_{LS} = 1$. The τ_{LS} lines are shown in the faded colors in the regimes when the $G_{\tau_{LS}}$ conductance turns positive because τ_{LS} loses its meaning there as $G_{LS}^0 \approx G_{LS}^\infty$.

Fig. 5.6 shows the U_{AC} -dependence of τ_{LS} for different bias points and the dependence of LS conductance for frequencies corresponding to τ_{LS} . At low U_{AC} , τ_{LS} is converging to (SS) τ_{rel} , as it should, but τ_{LS} does show a strong dependence on U_{AC} for larger AC amplitudes. Particularly important is that τ_{LS} can significantly decrease at higher U_{AC} and become significantly smaller than τ_{rel} . That allows RTDs to operate at higher frequencies than anticipated from the SS analysis, e.g., RTD can then provide larger than anticipated output power at intermediate frequencies. The curve at $U_B = 0.69$ V is particularly important in this context since it corresponds to a maximum of NDC, and it is a typical operating point of RTDs in oscillators: τ_{LS} is significantly decreasing with U_{AC} in this case.

τ_{LS} can diverge because the first-order RLRC equivalent circuit is not able to capture the fine details in the frequency dependence of G_{LS} , see plots in Fig. 5.4. If $G_{LS}^0 \approx G_{LS}^\infty$, then those fine details become dominating, and τ_{LS} shows a diverging behavior. However, those divergences do not affect the accuracy of the model since $G_{LS} \approx \text{constant}$ in such cases, and their frequency dependence can be neglected. Additionally, this typically happens for large U_{AC} when G_{LS} becomes positive: such U_{AC} is of no interest to RTD oscillators since G_{LS} must be negative in oscillators. Therefore τ_{LS} is shown with faded colors in Fig. 5.6 in such regimes.

5.4 Reconstruction of the phase map, “simplified model” (SM)

To calculate the phase map as in Fig. 5.3, one needs to start with a self-consistent solution of the Schrödinger and Poisson equations and then calculate the internal parameters of the RTD, like the tunnel rates through the barriers, the positions of the QW subbands, the QW charge, etc. The procedure has been described above, and it relies on a number of assumptions related to the internal RTD parameters, which are not well known and not directly measurable (barrier thicknesses, exact band profile (actual layer compositions), broadening of the subbands, etc.). Therefore, for practical use, it is desirable to simplify the procedure of the reconstruction of the phase map and to make it defined by the parameters, which are either directly measurable or can be more or less reliably estimated, knowing the nominal parameters of the RTD layers.

To this purpose, we define a simplified model based on the following main assumptions: (i) the whole tunnel RTD current is ascribed to the tunneling via the ground QW subband, and back injection from the collector into the QW is neglected; (ii) the parameters d , l , and ν_c are kept constant. Knowing these parameters and the measured RTD I-V curve, we further estimate $\nu_{e,1}$.

We start with assumptions (ii). Keeping d as a constant is justifiable since the screening length in the emitter is only weakly dependent on F_e . The variation of l is larger since the depletion length in the collector is changing with bias. However, for the biases in the NDC region and around it, the variation of l becomes limited: l is changing by about 10 % at most for our example RTD in this bias range, as this RTD has relatively high collector doping. This

scale of variation of l is typical for THz RTDs. We fix l equal to the value it takes in the NDC region. For the RTD analyzed in this work, we estimate d to be 9 nm, taking into account the Thomas-Fermi screening length in the emitter. Considering the collector's depletion length, we estimate l to be 15 nm in the NDC region. In the following, we keep the lengths fixed.

Keeping d and l constant near the NDC region lets us derive a simple equation for U_e from Eqs. (5.6) and (5.7):

$$U_e = U_{e,0} + \frac{d}{l+d} U_{\text{RTD}} - \frac{1}{C} e N_{2\text{D}}, \quad (5.23)$$

where $C = \varepsilon(l+d)/ld$ is the QW capacitance and $U_{e,0}$ is an initial value of U_e . We will need Eq. (5.23) relating U_e to $N_{2\text{D}}$ and U_{RTD} in the subsequent steps. Note that U_e and $N_{2\text{D}}$ are not necessarily zero at zero bias, and l can have a somewhat different value at zero bias than in the NDC region. To define $U_{e,0}$ with good accuracy, one can choose a bias point in the NDC region, keep $N_{2\text{D}} = 0$, and then calculate U_e and define $U_{e,0}$ as a deviation of U_e from $U_{\text{RTD}}d/(l+d)$ at this bias point.

Further, ν_c is bias-dependent. However, contrary to $\nu_{e,1}$, ν_c does not exhibit abrupt changes with bias. It is a monotonous and smooth function of bias (of F_c , to be more precise). In the NDC region and its vicinity, the variation of ν_c typically does not exceed about 5 %. Therefore, we fix ν_c at its level in the NDC region. For our example RTD, we estimate ν_c to be approximately $5.2 \cdot 10^{12} \text{ s}^{-1}$ in the NDC region. We keep it fixed at this level in the following. Those estimates for d , l , ν_c , and $U_{e,0}$ can be done with relatively-simple static calculations or commercial simulators based on the nominal parameters of the RTD layers.

Now we come back to the assumptions (i). We are primarily interested in an accurate description of the RTD characteristics at the biases in and near the NDC region. At such biases, the back injection of electrons from the collector into the QW is typically negligibly small. Therefore, we neglect the term with N_c in Eq. (5.2). Further on, as mentioned above, that also allows us to use the simplified Eq. (5.18) for the calculation of the external RTD current (j_{RTD}). As a next step, knowing ν_c and the measured RTD I-V curve, we reconstruct $N_{2\text{D}}^{\text{DC}}$ from Eq. (5.2), since $j_c = j_{\text{RTD}}^{\text{DC}}$ in the DC case: $N_{2\text{D}}^{\text{DC}} \approx j_{\text{RTD}}^{\text{DC}}/e\nu_c$.

We note that in the DC case, $j_e = j_{\text{RTD}}^{\text{DC}}$ as well. The tunneling rate $\nu_{e,1}$ changes dramatically in the NDC region compared to ν_c , and its derivative actually defines the shape of the NDC region in RTDs. We can estimate $\nu_{e,1}$ in the following way. We can approximate the emitter current, keeping only the contribution of the ground QW subband, as:

$$j_e = e\nu_{e,1} (N_{e,1} - N_{2\text{D}}), \quad (5.24)$$

where $N_{e,1}$, taking into account the Fermi distribution of electrons available to tunnel into the QW, can be written as:

$$N_{e,1} = \rho_{2\text{D}} kT \ln \left(1 + \exp \left(\frac{eU_e}{kT} \right) \right), \quad (5.25)$$

where $\rho_{2\text{D}}$ is the 2D density of states in the QW, k is the Boltzmann constant, and T is the temperature, which is 300 K in our case. Thus, Eq. (5.24) allows us to determine the behavior

of $\nu_{e,1}$. We proceed as follows. We sweep the bias (U_{RTD}) for a measured RTD I-V curve. For each point of U_{RTD} , one calculates $N_{2\text{D}}^{\text{DC}}$ from $j_{\text{RTD}}^{\text{DC}}$, as described above; next, one computes U_e and $N_{e,1}$ with Eqs. (5.23) and (5.25); then one calculates $\nu_{e,1}$ with Eq. (5.24). $\nu_{e,1}$ is physically a function of U_e and this procedure relates $\nu_{e,1}$ to U_e in a wide range of values of U_e . These values cover all the values of U_e , which can occur in the phase space in the vicinity of the NDC region. In such a way, we define $\nu_{e,1}(U_e)$.

In Eq. (5.24), the whole tunnel current injected from the emitter into the QW is ascribed to the direct injection into the ground subband. This picture is physically accurate for the description of the RTD in the current-peak and NDC regions of the I-V curve. However, it becomes inaccurate in the valley region of the I-V curve, and at higher biases. This is because the current growth in the valley region is due to the electron tunneling to the second subband (with subsequent scattering into the ground one). In Eq. (5.24), we basically artificially increase $\nu_{e,1}$ at such biases to mimic the second-subband current by attributing it to the direct tunneling into the ground subband. This is a mathematical trick, which allows us to describe accurately the injection current in the whole range of biases with the tunnel rate $\nu_{e,1}$ only, whereas $\nu_{e,1}$ is modified and not more physical in the valley region. Yet the subsequent comparison of the time constants shows that the resulting error is relatively small because the behavior of the relaxation processes in the valley region of the I-V curve is dominated by ν_c , i.e., by the tunneling to the collector, since ν_c is typically $\gg \nu_{e,1}$ in the region.

In such a way, we determine d , l , ν_c , and $\nu_{e,1}(U_e)$. Then using the equation for the collector current (5.2), the approximation of the emitter current for the ground subband (5.24), and the solution for the emitter voltage drop from (5.5), (5.6), and (5.7), we can approximately reconstruct the phase map for Δj and analyze the RTD dynamics (trajectories), as in the full-model case.

We restrict the operating voltages to the values where the tunneling of electrons from the collector to the QW is negligible since we neglect this mechanism in our model. If necessary, this mechanism can easily be added to the model in the same way as we have done that for the injection current from the emitter in Eqs. (5.24) and (5.25).

5.5 Connection between the LS response and the SS relaxation time constant

To shed more light on the RTD dynamics, we reconstruct the phase map in a different but equivalent way, starting with the parameter τ_{rel} . In the SS approximation, τ_{rel} describes the charge relaxation processes for small deviations (denoted with δ) from the stationary DC states: $\partial_t \delta N_{2\text{D}} = -\delta N_{2\text{D}} / \tau_{\text{rel}}$. By linearizing Eqs. (5.2-5.4), (5.24), and using (5.23), similarly as was shown in Ref. [102], one can derive the following equation for τ_{rel} :

$$\frac{1}{\tau_{\text{rel}}} \approx \frac{1}{\tau_{\text{dwell}}} + \beta \left(\frac{\nu_{e,1}}{1 + \exp\left(-\frac{eU_e}{kT}\right)} + \frac{N_{e,1} - N_{2\text{D}}}{e\rho_{2\text{D}}} \nu'_{e,1}(U_e) + \frac{N_{2\text{D}}}{e\rho_{2\text{D}}} \nu'_c(U_c) \right), \quad (5.26)$$

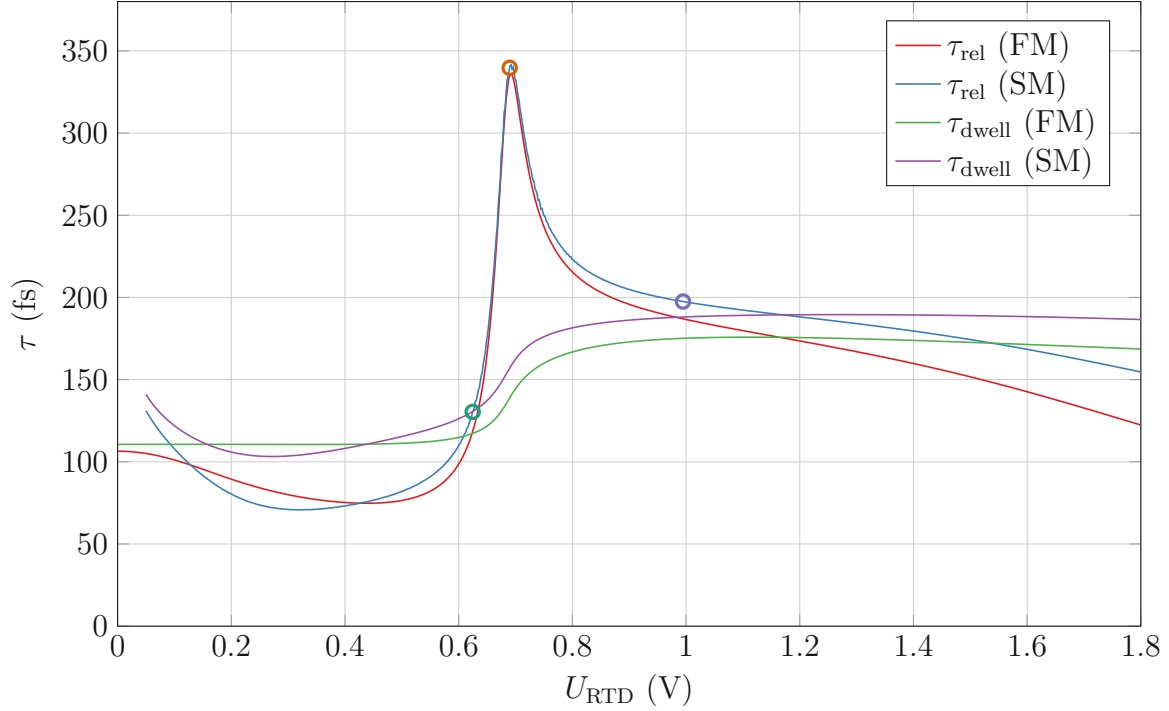


Figure 5.7: τ_{dwell} and τ_{rel} as functions of U_{RTD} for the full model (FM) and the simplified model (SM). For small biases, the SM reconstruction is inaccurate due to neglect of the back injection from the collector. On the other hand, the error for large biases is mostly because ν_c is kept constant in the framework of the SM model.

where $\beta = e^2 \rho_{2\text{D}} / C$ and $\tau_{\text{dwell}} = \nu_c + \nu_{e,1}$ is the electron dwell time for the ground QW subband. In Eq. (5.26), we have neglected the back injection from the collector and tunneling via excited QW subbands, as in the definition of the SM model. In further analysis, we also neglect the last term in Eq. (5.26) with $\nu'_c(U_c)$, to keep the approximations conform with the SM model of Section 5.4, since $\nu_c \approx \text{constant}$. Using the parameters ν_c , $\nu_{e,1}$, $N_{2\text{D}}$, l , and d calculated with the SM model, we can compute the bias dependence of τ_{rel} and τ_{dwell} . Fig. 5.7 shows a comparison of τ_{rel} and τ_{dwell} calculated in such a way with the full-model (FM) simulations.

Next, we can extend τ_{rel} over the whole phase space by using Eq. (5.26), as shown in Fig. 5.8. In Fig. 5.8, we are clipping the low biases values where the back injection from the collector has a noticeable effect, and the reconstruction procedure is inaccurate. One can observe the tilt of the τ_{rel} peak in the phase space, the slope of which is given by Eq. (5.23) when we keep U_e as a constant (τ_{rel} peak occurs at the maximum of NDC at a specific value of U_e). The slope is proportional to the collector capacitance $C_{\text{wc}} = \varepsilon/l$, i.e., $e\delta N_{2\text{D}} = C_{\text{wc}}\delta U_{\text{RTD}}$. The space charge in the QW causes the tilt due to the Coulomb interaction. Additionally, Fig. 5.8 shows the effect of the explicit dependency of τ_{rel} on $N_{2\text{D}}$, which leads to a decrease of τ_{rel} with $N_{2\text{D}}$ in the NDC region. Both of these effects influence the dynamic parameters describing the LS response.

We note then that we can come to the definition of τ_{rel} by linearizing Eq. (5.3):

$$\delta N_{2\text{D}} \frac{\partial \Delta j}{\partial e N_{2\text{D}}} = \partial_t \delta N_{2\text{D}} \implies \frac{\partial \Delta j}{\partial e N_{2\text{D}}} = -\frac{1}{\tau_{\text{rel}}}. \quad (5.27)$$

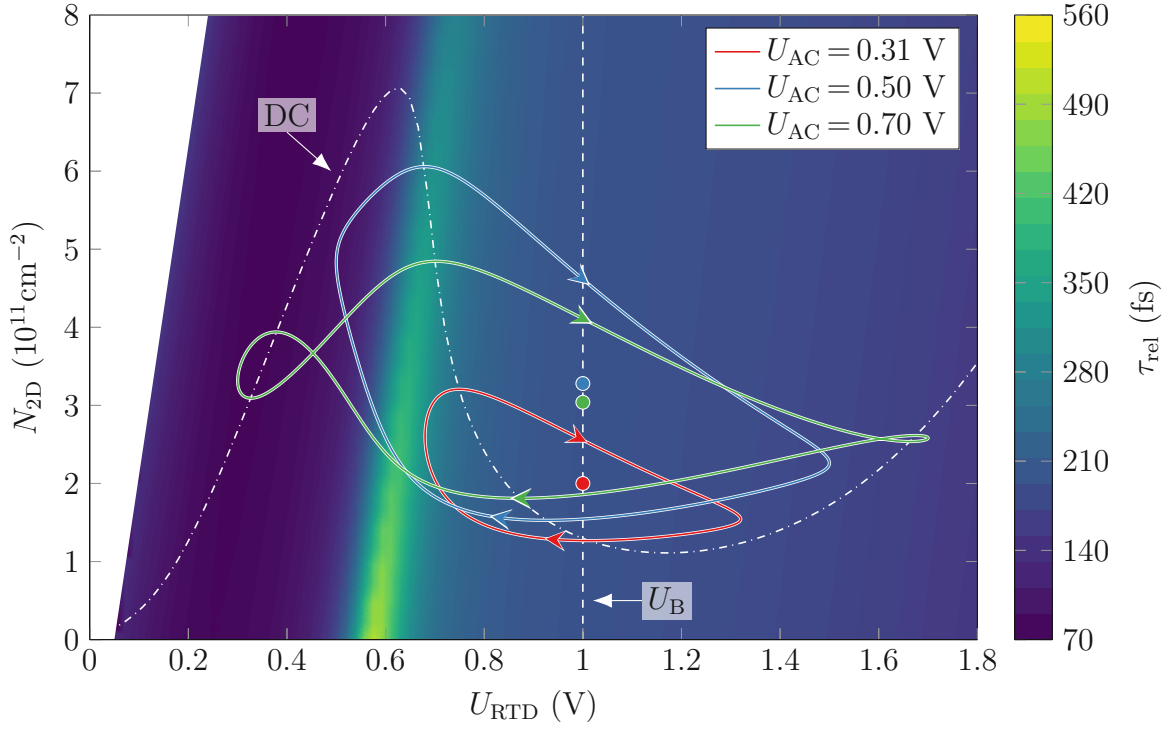


Figure 5.8: Calculation results based on the simplified model, which relies on the measured RTD I-V curve and estimates of RTD parameters. Reconstruction of τ_{rel} in the phase space. The white dashed-dotted line shows $N_{2\text{D}}^{\text{DC}}$, and the full lines show trajectories of $N_{2\text{D}}$ at the frequency of 1 THz for various AC amplitudes at the bias of $U_{\text{B}} = 1$ V. The dots lying on the bias line correspond to $N_{2\text{D}}$ averaged over one period.

The phase map of τ_{rel} represents a map of the derivative of Δj . Then, knowing $1/\tau_{\text{rel}}$ (or rather $\partial\Delta j/\partial eN_{2\text{D}}$), we can reconstruct Δj in the phase space by integrating it as:

$$\Delta j(U_{\text{RTD}}, N_{2\text{D}}) = -e \int_{N_{2\text{D}}^{\text{DC}}}^{N_{2\text{D}}} \frac{dN_{2\text{D}}}{\tau_{\text{rel}}(U_{\text{RTD}}, N_{2\text{D}})}. \quad (5.28)$$

Knowing the map of Δj reconstructed in such a way, we can calculate the LS response, and thus τ_{LS} , in the same way as it was shown in the previous sections. A comparison of τ_{LS} calculated with the approximated procedure with the accurate full simulations of τ_{LS} is shown in Fig. 5.9. The results from the reconstruction procedure of the simplified model, based on the measured data and the limited knowledge of the RTD parameters, are in good agreement with the results produced by the full model.

5.6 High-frequency (HF) response

At very high frequencies, the electron density in the QW asymptotically approaches a constant value $N_{2\text{D}}^{\infty}$. We can find $N_{2\text{D}}^{\infty}$, if we put the averaged (over one cycle) value of Δj equal to zero while keeping $N_{2\text{D}}$ constant:

$$\langle \Delta j(U_{\text{RTD}}, N_{2\text{D}}^{\infty}) \rangle = 0. \quad (5.29)$$

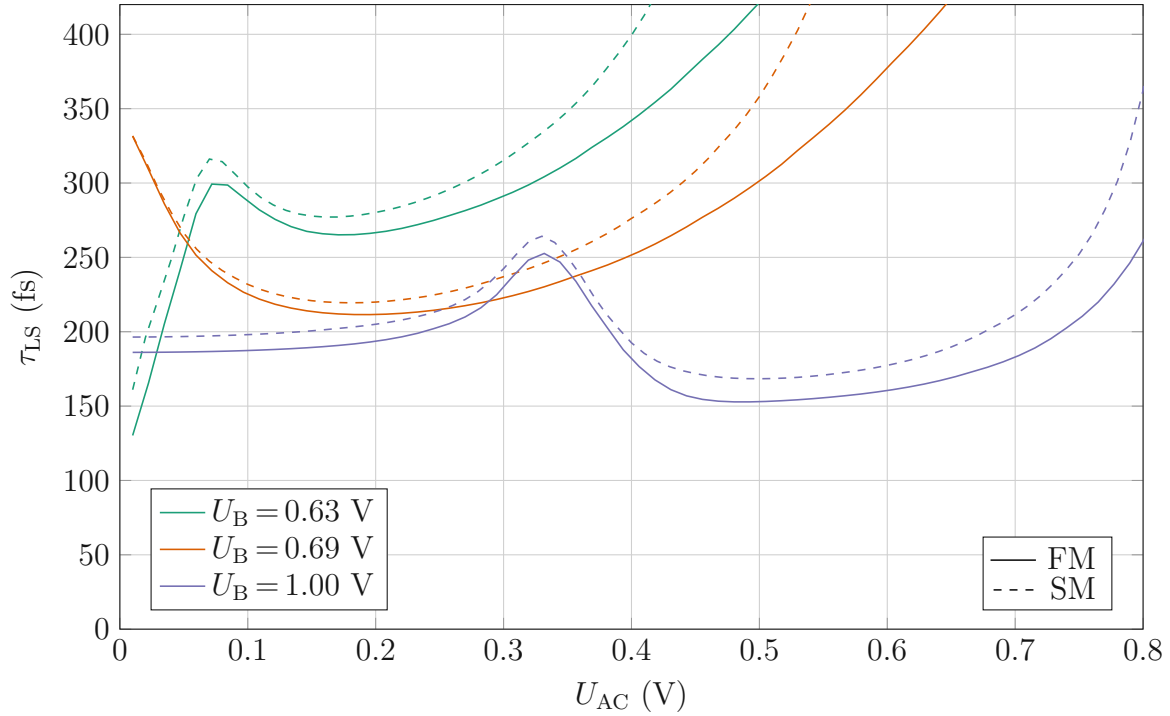


Figure 5.9: Comparison of τ_{LS} given by the full-model solution and the reconstructed solution from the simplified model. The full lines are obtained from the full model, and the dashed lines are from the SM reconstruction.

The procedure implies that there is no net change of the QW charge in a cycle. Although Eq. (5.29) has to be solved numerically to find N_{2D}^∞ , the solution is straightforward and simple.

Knowing N_{2D}^∞ , the time-dependent course of the HF difference current Δj is given by Eq. (5.28), which we can use in Eq. (5.18) to determine the RTD HF external current. A comparison of the HF current calculated from the full model and the reconstructed model with the DC current is shown in Fig. 5.10 for $U_B = 1$ V and $U_{AC} = 0.5$ V. We can observe the shift of the peak current towards lower voltages for both methods. The reconstructed (SM) model shows a slightly lower peak-to-valley ratio than the full model. That is mainly caused by the error in τ_{rel} prediction in the positive differential conductance (PDC) region (neglect of back injection from the collector and $\nu_c = \text{constant}$).

Using the HF RTD current in Eq. (5.20), we can determine G_{LS}^∞ . For example, for the amplitude of 0.5 V, G_{LS}^∞ is 1.7 mS/ μm^2 for the full model and 2.0 mS/ μm^2 for the simplified (reconstruction) model, which are quite close to each other. The above-presented method liberates us from the requirement to know the complete set of RTD parameters to determine G_{LS}^∞ , and it can serve as a complement to the method described in Ref. [105].

5.7 Second-subband current

Throughout the chapter, we have used several assumptions related to the second-subband charge and current.

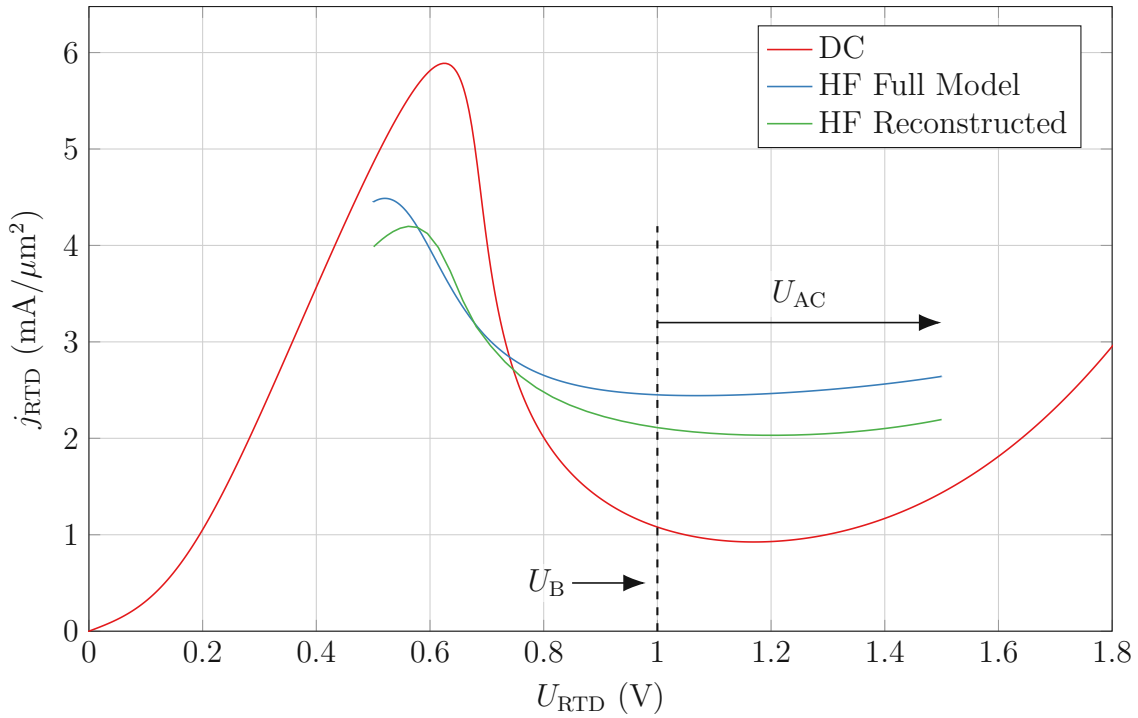


Figure 5.10: Comparison of the real current flowing through the RTD for the DC case, full model (FM) solution, and the SM reconstruction for $U_B = 1$ V and $U_{AC} = 0.5$ V.

First, in the operation regime of RTDs around their peak, NDC, and valley regions, the second-subband electron concentration N_{2D-2} is negligibly small compared to that in the ground subband (N_{2D}), and its influence on the RTD band profile is neglected. This assumption is justified as the second-subband current (which could be dominating in the valley region) does not exceed the peak current (dominated by the ground subband) in the operation regimes of RTDs. Further, those currents are proportional to the electron concentration in each of the subbands multiplied by the respective tunnel rates. However, the tunneling rate is much higher for the second subband than for the ground one, which leads to the strong inequality $N_{2D-2} \ll N_{2D}$, justifying our assumption.

Second, we have assumed that the scattering time from the second to the ground subband ($\tau_{\text{scat}-2}$) is much shorter than the second-subband tunnel lifetime ($\tau_{\text{dwell}-2}$), i.e., $\tau_{\text{dwell}-2} \gg \tau_{\text{scat}-2}$ and the electrons tunneling into the second subband are immediately scattered to the ground one. Together with the first assumption above, this justifies the use of the phase space for the description of the RTD states: the RTD band profile and the QW currents are fully determined by just two parameters, N_{2D} and U_{RTD} . If the second assumption is not fulfilled ($\tau_{\text{dwell}-2} \sim \tau_{\text{scat}-2}$), we need to take into account the second-subband scattering rate, and the self-consistent calculation of the trajectories in the phase space would require accounting for the time evolution of N_{2D-2} . That would require more extensive numerical calculations to describe the RTD dynamics.

However, in the opposite limiting case, when $\tau_{\text{dwell}-2} \ll \tau_{\text{scat}-2}$, a simplified analysis of the RTD dynamics could be again recovered. The calculation procedure for the ground-subband

trajectory (its N_{2D} , τ_{rel} , τ_{LS} , currents, etc.) described here is applicable in this case, the ground subband becomes decoupled from the second one. Knowing the ground-subband trajectory, one calculates afterward the second-subband current, which is essentially a parallel channel to the ground-subband current. The ground- and second-subband currents should then be summed up to get the total RTD current. The only difference to the calculation procedures described here is that the phase-map reconstruction is no longer applicable since the measured current contains the contributions of both subbands.

5.8 Discussion on acceleration of LS response

The simulations we presented in this chapter show that the RTD dynamics and τ_{LS} are dependent on U_{AC} . Particularly, τ_{LS} can become shorter or longer than SS τ_{rel} at certain RTD biases. This behavior can also be explained qualitatively.

At low frequencies, the RTD operates in a quasi-static regime, and its trajectories in the phase space closely follow the DC line. At high frequencies, the trajectories are horizontal: N_{2D} does not change anymore with AC voltage. If we take an intermediate frequency ($\omega \sim 1/\tau_{rel}$) and look at the behavior of the trajectories for different AC amplitudes U_{AC} , then the trajectories will be closer to the DC line when the RTD is fast in this regime (short τ_{LS}), or closer to the horizontal line when the RTD is slow (long τ_{LS}). These considerations are helpful for a qualitative understanding of the RTD dynamics.

One specific bias point we can look at is $U_B = 1$ V. This point is close to the right edge of the NDC region, where RTD oscillators typically provide the highest output power and the RTD AC amplitude takes the largest values. Fig. 5.6 shows that RTD is fast for $U_{AC} \lesssim 0.25$ V, since it is operated in the region with fast relaxation, see Fig. 5.8. Then τ_{LS} starts growing with further increase of U_{AC} and reach a maximum at $U_{AC} = 0.31$ V, see Fig. 5.6. That happens because the AC voltage swing culminates at lower biases in the slow-relaxation region, see the trajectory for $U_{AC} = 0.31$ V in Fig. 5.8; that slows down the RTD response, and the trajectory becomes more horizontal. With further increase of U_{AC} , the sinusoidal AC voltage swings pass through the slow-relaxation region and culminate in the region with fast relaxation, see the trajectory with $U_{AC} = 0.5$ V in Fig. 5.8; the trajectory follows more closely the DC line. The RTD response is accelerated, τ_{LS} drops, see Fig. 5.6. With further increase of U_{AC} , see the trajectory with $U_{AC} = 0.7$ V in Fig. 5.8, the trajectories culminate in the PDC regions, where a fast relaxation to DC N_{2D} values below the peak and above the valley levels occurs. The trajectory becomes more horizontal, and the RTD response somewhat slows down, τ_{LS} grows a bit, see Fig. 5.6.

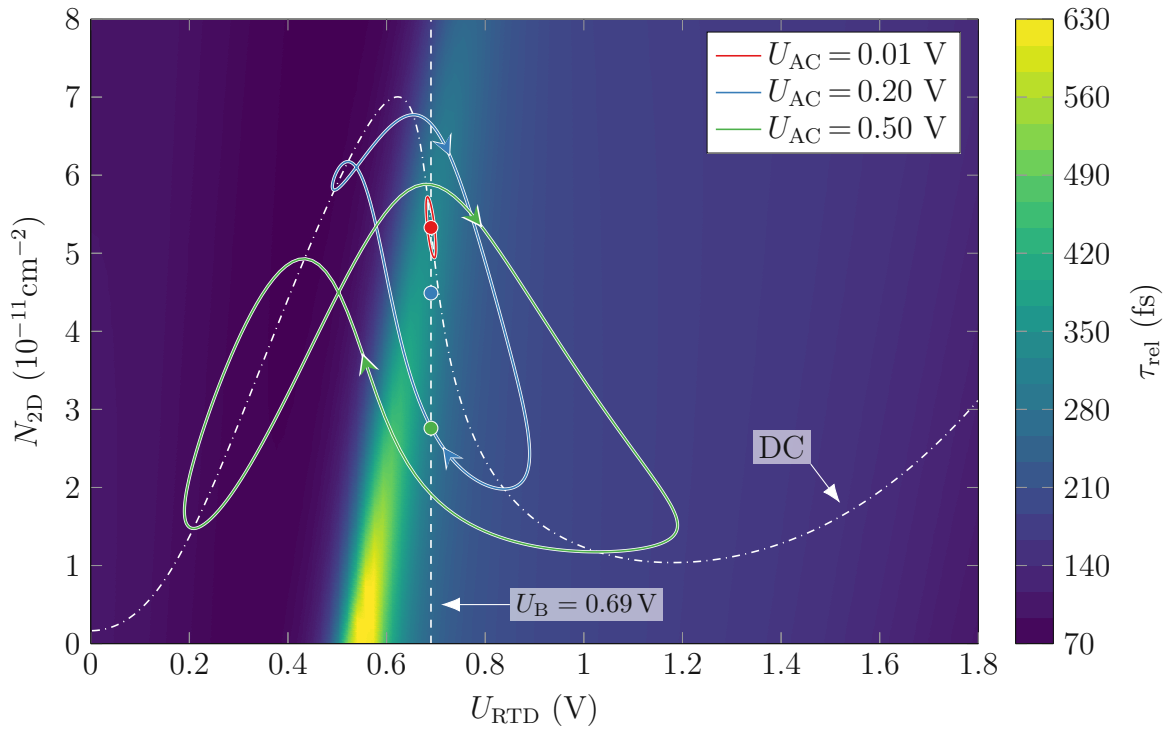


Figure 5.11: Dynamic trajectories in the phase space for τ_{rel} (calculated with the full model) for an RTD biased at the maximum NDC for different AC amplitudes (U_{AC}) at the frequency corresponding to the reciprocal SS relaxation time constant ($1/2\pi\tau_{\text{rel}}$). The colored points represent the average value of $N_{2\text{D}}$ over one cycle for the corresponding amplitude.

5.9 Dynamic response at the bias point of the highest NDC

Another characteristic bias point is $U_{\text{B}} = 0.69 \text{ V}$, where NDC has a maximum, see dynamic trajectories in Fig. 5.11. The SS τ_{rel} has a maximum at this point as well, as one can see in Fig. 5.7, i.e., the SS RTD response is the slowest at this bias. One can see also in the map for τ_{rel} in Fig. 5.11 that τ_{rel} has a maximum (yellow stripe) at this bias point. For a detailed description of the trajectories, see Fig. 5.12. The trajectory with $U_{\text{AC}} = 0.01 \text{ V}$ (Fig. 5.12 a) at the frequency corresponding to the reciprocal SS relaxation time constant ($1/2\pi\tau_{\text{rel}}$, i.e., $\approx 450 \text{ GHz}$) has a noticeable tilt towards the horizontal line when compared to the DC line. With the increase of U_{AC} , the RTD is driven outside the slow-response region (into the blue areas in Fig. 5.11), which leads to the acceleration of the RTD response: τ_{LS} decreases with the increase of U_{AC} , see Fig. 5.6. The trajectory with $U_{\text{AC}} = 0.2 \text{ V}$ follows more closely the DC line, see (Fig. 5.12 b)). This behavior occurs for $U_{\text{AC}} \lesssim 0.2 \text{ V}$, when the AC voltage swings are lying roughly between the peak and valley points. This mechanism of the acceleration of the RTD response is particularly efficient at this bias point since the AC voltage swing is sinusoidal, and the RTD spends disproportionately more time in the phase space at extreme points of the AC voltage swing (culminations), where the RTD response is fast. With further increase of bias, the AC voltage swings culminate in the PDC regions. The fast relaxation at the extreme points then

drives N_{2D} to DC values, which are below the peak and above the valley levels. The trajectory eventually becomes more horizontal (see Fig. 5.12 c) with $U_{AC} \lesssim 0.5$ V), RTDs are getting slower in this regime, τ_{LS} grows with the increase of U_{AC} , when $U_{AC} \gtrsim 0.2$ V, see Fig. 5.6.

For illustrative purposes, the map of τ_{rel} in Fig. 5.11 was calculated with the full model, although Fig. 5.8 shows the τ_{rel} map calculated with the simplified model. Both maps look almost identical, which gives one more indication of good accuracy of the simplified model.

Here, we discuss the RTD dynamics at the bias point of the NDC maximum. To better qualitatively describe the RTD behavior, we introduce a projection of the phase-space trajectory onto the cosinusoidal first harmonic as:

$$N_{2D,R}(t) = \left(\frac{\omega}{\pi} \int_0^{\frac{2\pi}{\omega}} N_{2D}(t) \cos(\omega t) dt \right) \cos(\omega t). \quad (5.30)$$

The slope of the projections in the phase space shows how vertical the dynamic characteristic is. The speed of the response can then be qualitatively described if we compare the slope at the operational frequency with the slope at the low-frequency limit. The projection also partly determines G_{LS} through Eqs. (5.18) and (5.20). At DC and low frequencies, the conductance is given solely by the first term in Eq. (5.18), which corresponds to $N_{2D,R}$. At high frequencies, the projection is zero, and the conductance is given solely by the second term in Eq. (5.18).

Fig. 5.11 shows the responses on the map of τ_{rel} in the phase space at the frequency corresponding to the reciprocal SS relaxation time constant ($1/2\pi\tau_{rel}$). Figure 5.12 shows the dynamic responses on the map of Δj in the phase space when the RTD is biased at the maximum of the NDC. We show plots for very low frequency (LF), very high frequency (HF), and frequency corresponding to the reciprocal SS relaxation time constant ($1/2\pi\tau_{rel}$), which is ≈ 450 GHz in this case. The figure shows responses for U_{AC} of a) 0.01 V, b) 0.20 V, and c) 0.50 V. The colored dashed lines show $N_{2D,R}$ shifted by the averaged value of N_{2D} . The insets then show the projections $N_{2D,R}$ only. The slope of the “relaxation frequency” (blue) lines, when compared to the LF responses (red) lines, show the speed of the response: the more horizontal the line is, the slower the response. The plots show the trend described in Section 5.8 of the response accelerating with the increasing amplitude until a certain point when the response starts to decelerate.

5.10 Conclusion

We have presented a simulation model for the analysis of the large-signal (LS) dynamics of RTDs. The model is based on the analysis of dynamical trajectories in phase space, defined by N_{2D} and U_{RTD} ; the trajectories are governed by the emitter-collector difference current (Δj). We have shown that the map of Δj in the phase space can be reconstructed based on a simplified procedure relying on the measured DC RTD I-V curve and a few relatively simple and rough assessments for the tunnel rates through the RTD barriers. The resulting approximate dynamical

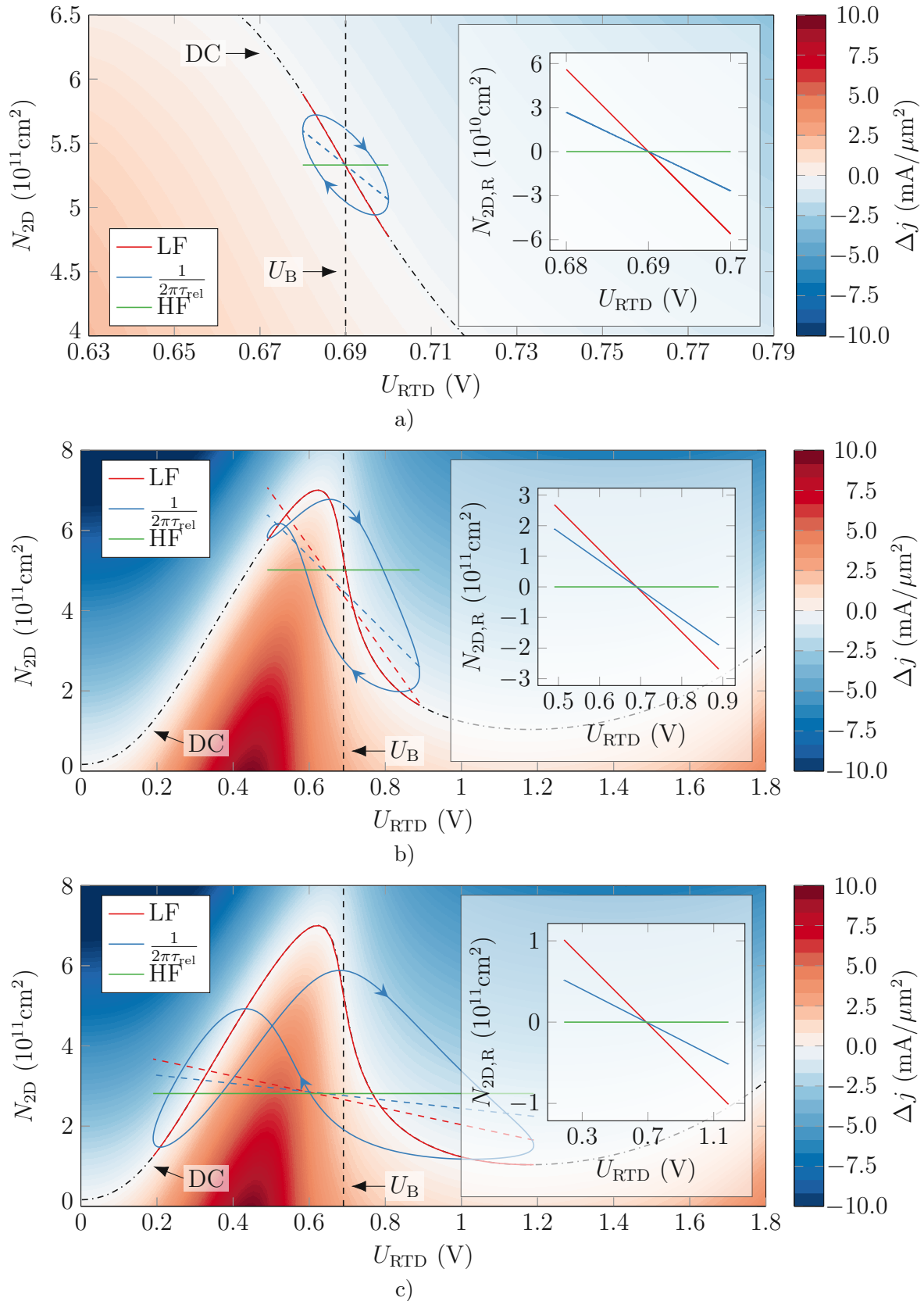


Figure 5.12: Dynamic responses in the phase space for Δj (calculated with the full model) of the RTD biased at the maximum NDC for U_{AC} of a) 0.01 V, b) 0.20 V, and c) 0.50 V. The full-colored lines show the general response of N_{2D} , and the colored dashed lines show the projection $N_{2D,R}$ shifted by the average of N_{2D} . The insets then show $N_{2D,R}$ only.

RTD characteristics are in good agreement with exact calculations. We further demonstrate that the frequency dependence of the LS RTD admittance can be described by a simple RLRC equivalent circuit, which has the same structure as the circuit previously derived for the small-signal (SS, linearized) RTD admittance. The elements of the circuit are: the measurable DC RTD conductance, the high-frequency RTD conductance, the geometrical RTD capacitance, and a relaxation time constant (τ_{LS}), which defines the transition frequency between the quasi-static and high-frequency operation regimes of an RTD. We further show that τ_{LS} is, in general, strongly dependent on the RTD operation bias and also on the amplitude of the AC signal. We show that τ_{LS} can be shorter than SS τ_{rel} , i.e., RTDs can exhibit faster LS dynamics than otherwise predicted by SS analysis.

Chapter 6

Thesis Conclusions

In this thesis, we have dealt with RTD oscillators in the context of sub-THz and THz sources. In the first chapter, we have summarized the problem of the generation of THz waves and their applicability. We have introduced there the THz gap and the electronic and photonic devices that are progressively closing it. However, the operability and output parameters of these devices suffer in the THz from their fundamental limitations. The photonic devices are closing the gap from the side of high frequencies. They operate on the principles of Lasers and face fundamental limitations because the THz photon energy is comparable to and smaller than the thermal energy at room temperature. This limits the photonic devices to operate on temperatures far below zero degrees Centigrade and in a pulsed regime. On the other side, electronic devices are closing the THz gap from the low-frequency side. They operate on principles of electronic oscillators or frequency multipliers and are limited by the RC time constants of their parasitics. This limits electronic devices to very small dimensions. The RTDs are used in the sub-THz and THz electronic oscillators because they show the negative differential conductance in the THz band.

In the second chapter, we have shown a detailed overview of RTD oscillators. We have described the operation principle of the RTDs and showed that their I-V curves show an NDC region. The NDC can compensate for losses in resonant circuits and thus support stable oscillations. Next, we have followed the historical development of the RTDs in the context of the RTD oscillators, from which we have concluded the state-of-the-art of the RTD oscillators. Nowadays, these RTD oscillators are directly radiating the output power to the free space, their operating frequencies are attacking 2 THz (the current record is 1.98 THz), their output power is reaching 1 mW (on chip) for single oscillators and 10 mW for arrays of oscillators in the sub-THz range and tens of μ W when operated around to 1 THz, their DC-to-RF efficiencies are attaining ones of %, and their dimensions are getting closer to the true chip-size devices. Further, we have analyzed the fundamental maximum frequency limitations of the RTD oscillators due to the RTD

parasitics, which are the contact parasitics of the RTD, the RTD capacitance, and the roll-off of the RTD gain with the frequency. The rough analysis of the parasitics' effects showed that the state-of-the-art RTDs' maximal frequency is limited to approximately to 2.3 THz.

The third chapter can be divided into two parts, review and scientific. The first review part describes the well-known methods for the analysis of the RTD oscillators. At first, we described a linearised model of the RTD, which resulted in the small-signal oscillations conditions of the RTD oscillators. These conditions determine the oscillation frequency and also the minimal gain (magnitude of the NDC) that the RTD needs to have for the system to oscillate. Next, we have introduced the large-signal analysis where the non-linearity of the RTD was not disregarded. The analysis based on the harmonic balance method has resulted in large-signal oscillation conditions, which determine the amplitude of the oscillation voltage and the oscillation frequency. The knowledge of the voltage amplitude is essential because the output power of RTD oscillators is proportional to its square. Based on the argument that the capacitance of the RTD is shorting the higher harmonics of the oscillation voltage, we have simplified the analysis by considering only the first harmonic of the voltage. This simplification led us to the derivation of large-signal conductance and susceptance of the RTD, which allowed us to analyze the non-linear RTD oscillator in simple terms. We have introduced a third-order polynomial fit of an I-V curve of a real RTD, using which we could have analytically explained the self-rectification effect of the oscillations that adds the plateau-like character in the RTD I-V curve of an oscillating device. Also, we have shown the essence of power generation, which is based on the fact that for an oscillating voltage, a (linear) device with an NDC consumes less power than is delivered from the external energy source. The second part of the chapter presented novel scientific contributions by deriving the not-achievable upper bound of the RTD oscillators' output power. The upper bound of the output power depends solely on the maximum radiation conductance of the antenna and on the amplitude of the maximum voltage for which the RTD still shows negative conductance. The RTD peak-to-valley current difference and the RTD capacitance influence how close the output power can get to the power optimum. The upper bound can serve as a tool for comparison of the performance of varying antennas and RTDs.

In the fourth chapter, we have described a chip-size simple RTD oscillator design that radiates above the substrate. The oscillator used a patch antenna as both the resonator and the radiator. Although a similar design is known from the past, we have significantly revised it and eliminated its main drawback, which lies in parasitic oscillations with the biasing circuit. Using two RTDs connected to the patch in mirrored configuration and thus making the oscillator symmetric made the oscillator completely decoupled from the bias circuitry for the asymmetrical operation mode. Besides that, the asymmetric mode has a symmetric radiation pattern with the maximum pointing perpendicularly to the substrate. Using the pair of RTDs in one oscillator can also increase the output power. Using RTDs with 1.6 nm thickness of barriers, we have been able to construct oscillators operating at the maximum oscillation frequency of 525 GHz with an output power of $\approx 10 \mu\text{W}$, and with the maximum power of $70 \mu\text{W}$ at 330 GHz. These results represented

an order of magnitude increase in the output power compared to the previous result. The RTDs with the 1.6 nm thickness of the barriers had the peak current density of $\approx 6 \text{ mA}/\mu\text{m}^2$ (with peak to valley current ratio of 8.9), which allowed us for the fabrication of the oscillators to use solely optical lithography processes. The analysis of the limiting factors has shown that to increase the oscillation frequency of our oscillators, we need to reduce the parasitics induced by the slant bridges connecting the RTDs and the patch, the RTD contact parasitics, and the ohmic losses in the antenna. Therefore, we have replaced the bridges with conical vias that reduced their parasitic inductance and resistance. Furthermore, we have used RTDs with 1.0 nm barrier thickness having the peak current density of $\approx 24 \text{ mA}/\mu\text{m}^2$ (with peak to valley current ratio of 3.7), which have been able to cover for the parasitics losses at higher frequencies. Using the conical vias, the optimized RTD, and reducing the size of the antenna and the areas of the RTD (which required the usage of the electron beam lithography), the oscillators have been able to operate up to 1.09 THz with the output power of $\approx 9 \mu\text{W}$ and to cover the sub-THz range from 620 GHz to 1 THz with output powers in the range between 15 to 27 μW . These results are comparable with the state-of-the-art RTD oscillators radiating above the ground plane. However, the here presented design brings substantial simplicity of the design, which leads to simplified fabrication processes and better controllability of the final parameters of the oscillators. We have shown that for the further increase of the oscillation frequency and of the output power, the limiting factor is the losses in the antenna dielectric, which can be reduced by a change of the dielectric material or by the removal of the material (sacrificial layer) after the fabrication. Next, we have used one of these RTD oscillators as a source for FMCW radar and OCT applications in the sub-THz range. The presented source provided a spatial resolution of 4 mm with an output power of 23 μW with an average operation frequency of 680 GHz and 38 GHz (5.5%) bandwidth. The output frequency of the source was tuned by the change of the RTD bias, for which the bias sweep needed to be corrected to achieve optimal performance. We have proved this by the detection of an example target. However, as the RTD oscillators are prone to injection locking, the source needs to be isolated from the reflected waves. In our case, this isolation was provided by the Martin–Puplett interferometer.

In the fifth chapter, we have presented a model for analyzing the dynamic large-signal characteristics of RTDs. The model is based on the analysis of dynamical trajectories in phase space, defined by the RTD bias and electron density in the RTD quantum well. We have demonstrated that a simple equivalent circuit, composed of a capacitor, inductor, and two resistors (RLRC), accurately describes the large-signal admittance of RTDs. The circuit components can be described in geometrical RTD capacitance, relaxation time, and low- and high-frequency resistors. The equivalent circuit has the very same structure as that previously derived for small-signal RTD admittance, although with deviating parameters, which are now dependent on the AC-signal amplitude. We have shown that the large-signal RTD relaxation time can be shorter and longer than the small-signal one. The shorter large-signal relaxation time for the RTD oscillators leads to higher output powers at high frequencies. We have further shown

that an accurate dynamic model can be reformulated approximately, relying only on a directly measurable DC I-V curve and a few other RTD parameters, which could be easily estimated with simple DC calculations. The design and analysis of RTDs in RTD oscillators are still, to a large extent, based on empirical and phenomenological modeling. The presented method in this chapter is accurate, physical-based, and sufficiently uncomplicated, which can remove one of the significant obstacles to the further development of THz RTD oscillators.

Bibliography

- [1] D. M. Pozar, *Microwave engineering*. John Wiley & Sons, 2011.
- [2] R. C. Dorf, *The engineering handbook*. CRC Press, 2018.
- [3] J. L. Bromberg, “Birth of the laser,” *Phys. Today;(United States)*, vol. 41, no. 10, 1988. DOI: 10.1063/1.881155.
- [4] G. Carpintero, E. Garcia-Munoz, H. Hartnagel, S. Preu, and A. Raisanen, *Semiconductor terahertz technology: devices and systems at room temperature operation*. John Wiley & Sons, 2015.
- [5] D. Pavlidis, *Fundamentals of Terahertz Devices and Applications*. John Wiley & Sons, 2021.
- [6] P. H. Siegel, “Thz instruments for space,” *IEEE Transactions on Antennas and Propagation*, vol. 55, no. 11, pp. 2957–2965, 2007. DOI: 10.1109/TAP.2007.908557.
- [7] D. Samanta, M. Karthikeyan, D. Agarwal, A. Biswas, A. Acharyya, and A. Banerjee, “Trends in terahertz biomedical applications,” *Generation, Detection and Processing of Terahertz Signals*, pp. 285–299, 2022. DOI: 10.1007/978-981-16-4947-9_19.
- [8] M. Seo and H.-R. Park, “Terahertz biochemical molecule-specific sensors,” *Advanced Optical Materials*, vol. 8, no. 3, p. 1900662, 2020. DOI: 10.1002/adom.201900662.
- [9] S. W. Harmer, S. E. Cole, N. J. Bowring, N. D. Rezgui, and D. Andrews, “On body concealed weapon detection using a phased antenna array,” *Progress In Electromagnetics Research*, vol. 124, pp. 187–210, 2012. DOI: 10.2528/PIER11112105.
- [10] T. Ikari, Y. Sasaki, and C. Otani, “Development of terahertz walk-through body scanner using 300 GHz FMCW radar,” in *2022 47th International Conference on Infrared, Millimeter and Terahertz Waves (IRMMW-THz)*, IEEE, 2022, pp. 1–4. DOI: 10.1109/IRMMW-THz50927.2022.9895879.

- [11] F. Rutz, M. Koch, S. Khare, M. Moneke, H. Richter, and U. Ewert, "Terahertz quality control of polymeric products," *International Journal of Infrared and Millimeter Waves*, vol. 27, no. 4, pp. 547–556, 2006. DOI: 10.1007/s10762-006-9106-7.
- [12] S. K. Mathanker, P. R. Weckler, and N. Wang, "Terahertz (thz) applications in food and agriculture: A review," *Transactions of the ASABE*, vol. 56, no. 3, pp. 1213–1226, 2013. DOI: 10.13031/trans.56.9390.
- [13] M. Polese, J. M. Jornet, T. Melodia, and M. Zorzi, "Toward end-to-end, full-stack 6g terahertz networks," *IEEE Communications Magazine*, vol. 58, no. 11, pp. 48–54, 2020. DOI: 10.1109/MCOM.001.2000224.
- [14] D. Cimbri, J. Wang, A. Al-Khalidi, and E. Wasige, "Resonant tunnelling diodes high-speed terahertz wireless communications-a review," *IEEE Transactions on Terahertz Science and Technology*, 2022. DOI: 10.1109/TTHZ.2022.3142965.
- [15] N. W. Ashcroft and N. D. Mermin, *Solid state physics* (Holt-Saunders international editions), eng. New York, NY [u.a.]: Holt, Rinehart and Winston, 1976, ISBN: 0030839939.
- [16] B. S. Williams, "Terahertz quantum-cascade lasers," *Nature photonics*, vol. 1, no. 9, pp. 517–525, 2007. DOI: 10.1038/nphoton.2007.166.
- [17] M. A. Kainz, S. Schonhuber, A. M. Andrews, *et al.*, "Barrier height tuning of terahertz quantum cascade lasers for high-temperature operation," *ACS photonics*, vol. 5, no. 11, pp. 4687–4693, 2018. DOI: 10.1021/acsp Photonics.8b01280.
- [18] M. Tonouchi, "Cutting-edge terahertz technology," *Nature photonics*, vol. 1, no. 2, pp. 97–105, 2007. DOI: 10.1038/nphoton.2007.3.
- [19] M. Asada and S. Suzuki, "Terahertz emitter using resonant-tunneling diode and applications," *Sensors*, vol. 21, no. 4, p. 1384, 2021. DOI: 10.3390/s21041384.
- [20] U. R. Pfeiffer, Y. Zhao, J. Grzyb, *et al.*, "A 0.53 thz reconfigurable source module with up to 1 mw radiated power for diffuse illumination in terahertz imaging applications," *IEEE Journal of Solid-State Circuits*, vol. 49, no. 12, pp. 2938–2950, 2014. DOI: 10.1109/JSSC.2014.2358570.
- [21] Z. Hu, M. Kaynak, and R. Han, "High-power radiation at 1 thz in silicon: A fully scalable array using a multi-functional radiating mesh structure," *IEEE Journal of Solid-State Circuits*, vol. 53, no. 5, pp. 1313–1327, 2018. DOI: 10.1109/JSSC.2017.2786682.
- [22] M. Urteaga, Z. Griffith, M. Seo, J. Hacker, and M. J. Rodwell, "Inp hbt technologies for thz integrated circuits," *Proceedings of the IEEE*, vol. 105, no. 6, pp. 1051–1067, 2017. DOI: 10.1109/JPROC.2017.2692178.

- [23] N. Buadana, S. Jameson, and E. Socher, “A multiport chip-scale dielectric resonator antenna for cmos thz transmitters,” *IEEE Transactions on Microwave Theory and Techniques*, vol. 68, no. 9, pp. 3621–3632, 2020. DOI: 10.1109/TMTT.2020.2993845.
- [24] K. Fujita, S. Hayashi, A. Ito, T. Dougakiuchi, M. Hitaka, and A. Nakanishi, “Broadly tunable lens-coupled nonlinear quantum cascade lasers in the sub-thz to thz frequency range,” *Photonics Research*, vol. 10, no. 3, pp. 703–710, 2022. DOI: 10.1364/PRJ.443819.
- [25] Q. Y. Lu, N. Bandyopadhyay, S. Slivken, Y. Bai, and M. Razeghi, “Continuous operation of a monolithic semiconductor terahertz source at room temperature,” *Applied Physics Letters*, vol. 104, no. 22, p. 221 105, 2014. DOI: 10.1063/1.4881182.
- [26] M. A. Kainz, M. P. Semtsiv, G. Tsianos, *et al.*, “Thermoelectric-cooled terahertz quantum cascade lasers,” *Opt. Express*, vol. 27, no. 15, pp. 20 688–20 693, Jul. 2019. DOI: 10.1364/OE.27.020688.
- [27] A. Khalatpour, A. K. Paulsen, C. Deimert, Z. R. Wasilewski, and Q. Hu, “High-power portable terahertz laser systems,” *Nature Photonics*, vol. 15, no. 1, pp. 16–20, 2021. DOI: 10.1038/s41566-020-00707-5.
- [28] Y. Jin, J. L. Reno, and S. Kumar, “Phase-locked terahertz plasmonic laser array with 2 w output power in a single spectral mode,” *Optica*, vol. 7, no. 6, pp. 708–715, Jun. 2020. DOI: 10.1364/OPTICA.390852.
- [29] L. Li, L. Chen, J. Freeman, *et al.*, “Multi-watt high-power thz frequency quantum cascade lasers,” *Electronics Letters*, vol. 53, no. 12, pp. 799–800, 2017. DOI: 10.1049/el.2017.0662.
- [30] R. Izumi, S. Suzuki, and M. Asada, “1.98 thz resonant-tunneling-diode oscillator with reduced conduction loss by thick antenna electrode,” in *2017 42nd International Conference on Infrared, Millimeter, and Terahertz Waves (IRMMW-THz)*, IEEE, 2017, pp. 1–2. DOI: 10.1109/IRMMW-THz.2017.8066877.
- [31] K. Kasagi, S. Suzuki, and M. Asada, “Large-scale array of resonant-tunneling-diode terahertz oscillators for high output power at 1 thz,” *Journal of Applied Physics*, vol. 125, no. 15, p. 151 601, 2019. DOI: 10.1063/1.5051007.
- [32] Y. Koyama, Y. Kitazawa, K. Yukimasa, *et al.*, “A high-power terahertz source over 10 mw at 0.45 thz using an active antenna array with integrated patch antennas and resonant-tunneling diodes,” *IEEE Transactions on Terahertz Science and Technology*, 2022. DOI: 10.1109/TTHZ.2022.3180492.
- [33] A. Al-Khalidi, K. H. Alharbi, J. Wang, *et al.*, “Resonant tunneling diode terahertz sources with up to 1 mw output power in the j-band,” *IEEE Transactions on Terahertz Science and Technology*, vol. 10, no. 2, pp. 150–157, 2019. DOI: 10.1109/TTHZ.2019.2959210.

- [34] J. Nishizawa, P. Plotka, T. Kurabayashi, and H. Makabe, “706-ghz gaas cw fundamental-mode tunnel diodes fabricated with molecular layer epitaxy,” *physica status solidi c*, vol. 5, no. 9, pp. 2802–2804, 2008. DOI: 10.1002/pssc.200779256.
- [35] H. Eisele, “Third-harmonic power extraction from inp gunn devices up to 455 ghz,” *IEEE Microwave and Wireless Components Letters*, vol. 19, no. 6, pp. 416–418, 2009. DOI: 10.1109/LMWC.2009.2020044.
- [36] P. Plotka, J. Nishizawa, T. Kurabayashi, and H. Makabe, “240-325-ghz gaas cw fundamental-mode tunnel diodes fabricated with molecular layer epitaxy,” *IEEE Transactions on Electron Devices*, vol. 50, no. 4, pp. 867–873, 2003. DOI: 10.1109/TED.2003.812103.
- [37] H. Eisele, “480 ghz oscillator with an inp gunn device,” *Electronics letters*, vol. 46, no. 6, pp. 422–423, 2010. DOI: 10.1049/el.2010.3362.
- [38] H. Eisele and R. Kamoua, “Submillimeter-wave inp gunn devices,” *IEEE Transactions on Microwave Theory and Techniques*, vol. 52, no. 10, pp. 2371–2378, 2004. DOI: 10.1109/TMTT.2004.835974.
- [39] H. S. Sommers, “Tunnel diodes as high-frequency devices,” *Proceedings of the IRE*, vol. 47, no. 7, pp. 1201–1206, 1959. DOI: 10.1109/JRPROC.1959.287351.
- [40] C. A. Burrus, “Gallium arsenide esaki diodes for high-frequency applications,” *Journal of Applied Physics*, vol. 32, no. 6, pp. 1031–1036, 1961. DOI: 10.1063/1.1736154.
- [41] D. Young, C. Burrus, and R. Shaw, “High efficiency millimeter-wave tunnel-diode oscillators,” *Proceedings of the IEEE*, vol. 52, no. 10, pp. 1260–1261, 1964. DOI: 10.1109/PROC.1964.3338.
- [42] Z. Gribnikov, R. Bashirov, and V. Mitin, “Negative effective mass mechanism of negative differential drift velocity and terahertz generation,” *IEEE Journal of Selected Topics in Quantum Electronics*, vol. 7, no. 4, pp. 630–640, 2001. DOI: 10.1109/2944.974235.
- [43] S. M. Sze, Y. Li, and K. K. Ng, *Physics of semiconductor devices*. John Wiley & sons, 2021.
- [44] G. D. Vendelin, A. M. Pavio, U. L. Rohde, and M. Rudolph, *Microwave circuit design using linear and nonlinear techniques*. John Wiley & Sons, 2021.
- [45] Y. Yao, A. J. Hoffman, and C. F. Gmachl, “Mid-infrared quantum cascade lasers,” *Nature Photonics*, vol. 6, no. 7, pp. 432–439, 2012. DOI: 10.1038/nphoton.2012.143.
- [46] B. Wen and D. Ban, “High-temperature terahertz quantum cascade lasers,” *Progress in Quantum Electronics*, vol. 80, p. 100363, 2021. DOI: 10.1016/j.pquantelec.2021.100363.

- [47] M. A. Belkin, F. Capasso, A. Belyanin, *et al.*, “Terahertz quantum-cascade-laser source based on intracavity difference-frequency generation,” *Nature Photonics*, vol. 1, no. 5, pp. 288–292, 2007. DOI: 10.1038/nphoton.2007.70.
- [48] A. Maestrini, B. Thomas, H. Wang, *et al.*, “Schottky diode-based terahertz frequency multipliers and mixers,” *Comptes Rendus Physique*, vol. 11, no. 7-8, pp. 480–495, 2010. DOI: 10.1016/j.crhy.2010.05.002.
- [49] I. Mehdi, J. V. Siles, C. Lee, and E. Schlecht, “Thz diode technology: Status, prospects, and applications,” *Proceedings of the IEEE*, vol. 105, no. 6, pp. 990–1007, 2017. DOI: 10.1109/JPROC.2017.2650235.
- [50] S. Preu, G. Döhler, S. Malzer, L. Wang, and A. Gossard, “Tunable, continuous-wave terahertz photomixer sources and applications,” *Journal of Applied Physics*, vol. 109, no. 6, p. 4, 2011. DOI: 10.1063/1.3552291.
- [51] J. Neu and C. A. Schmuttenmaer, “Tutorial: An introduction to terahertz time domain spectroscopy (thz-tds),” *Journal of Applied Physics*, vol. 124, no. 23, p. 231 101, 2018. DOI: 10.1063/1.5047659.
- [52] S. O. Pearson and H. S. G. Anson, “The neon tube as a means of producing intermittent currents,” *Proceedings of the Physical Society of London*, vol. 34, no. 1, pp. 204–212, Dec. 1921. DOI: 10.1088/1478-7814/34/1/341.
- [53] K. Karashima, R. Yokoyama, M. Shiraishi, S. Suzuki, S. Aoki, and M. Asada, “Measurement of oscillation frequency and spectral linewidth of sub-terahertz inp-based resonant tunneling diode oscillators using ni–inp schottky barrier diode,” *Japanese Journal of Applied Physics*, vol. 49, no. 2R, p. 020 208, 2010. DOI: 10.1143/JJAP.49.020208.
- [54] T. Hiraoka, T. Arikawa, H. Yasuda, *et al.*, “Injection locking and noise reduction of resonant tunneling diode terahertz oscillator,” *APL Photonics*, vol. 6, no. 2, p. 021 301, 2021. DOI: 10.1063/5.0033459.
- [55] K. Ogino, S. Suzuki, and M. Asada, “Spectral narrowing of a varactor-integrated resonant-tunneling-diode terahertz oscillator by phase-locked loop,” *Journal of Infrared, Millimeter, and Terahertz Waves*, vol. 38, no. 12, pp. 1477–1486, 2017. DOI: 10.1007/s10762-017-0439-1.
- [56] J. Lee, M. Kim, and K. Yang, “A 1.52 thz rtd triple-push oscillator with a μW -level output power,” *IEEE Transactions on Terahertz Science and Technology*, vol. 6, no. 2, pp. 336–340, 2015. DOI: 10.1109/TTHZ.2015.2509358.
- [57] A. Dobroiu, Y. Shirakawa, S. Suzuki, M. Asada, and H. Ito, “Subcarrier frequency-modulated continuous-wave radar in the terahertz range based on a resonant-tunneling-diode oscillator,” *Sensors*, vol. 20, no. 23, p. 6848, 2020. DOI: 10.3390/s20236848.

- [58] P. Ourednik, G. Picco, and M. Feiginov, "Chip-size resonant-tunneling-diode oscillator as a fmcw and oct source," in *2022 47th International Conference on Infrared, Millimeter and Terahertz Waves (IRMMW-THz)*, 2022, pp. 1–2. DOI: 10.1109/IRMMW-THz50927.2022.9896064.
- [59] S. Diebold, K. Nishio, Y. Nishida, *et al.*, "High-speed error-free wireless data transmission using a terahertz resonant tunnelling diode transmitter and receiver," *Electronics Letters*, vol. 52, no. 24, pp. 1999–2001, 2016. DOI: 10.1049/e1.2016.2941.
- [60] Y. Nishida, N. Nishigami, S. Diebold, J. Kim, M. Fujita, and T. Nagatsuma, "Terahertz coherent receiver using a single resonant tunnelling diode," *Scientific reports*, vol. 9, no. 1, pp. 1–9, 2019. DOI: 10.1038/s41598-019-54627-8.
- [61] L. Yi, R. Kaname, Y. Nishida, X. Yu, M. Fujita, and T. Nagatsuma, "Imaging applications with a single resonant tunneling diode transceiver in 300-ghz band," in *2020 International Topical Meeting on Microwave Photonics (MWP)*, 2020, pp. 120–123. DOI: 10.23919/MWP48676.2020.9314482.
- [62] A. Dobroiu, K. Asama, S. Suzuki, M. Asada, and H. Ito, "Terahertz-wave three-dimensional imaging using a resonant-tunneling-diode oscillator," *Journal of Infrared, Millimeter, and Terahertz Waves*, vol. 43, no. 5, pp. 464–478, 2022. DOI: 10.1007/s10762-022-00863-5.
- [63] T. Hiraoka, Y. Inose, T. Arikawa, H. Ito, and K. Tanaka, "Passive mode-locking and terahertz frequency comb generation in resonant-tunneling-diode oscillator," *Nature communications*, vol. 13, no. 1, pp. 1–8, 2022. DOI: 10.1038/s41467-022-31071-3.
- [64] L. Iogansen, "Resonance tunneling of electrons in crystals," *Soviet Phys. JETP*, 1965. [Online]. Available: www.jetp.ras.ru/cgi-bin/dn/e_020_01_0180.pdf.
- [65] L. Chang, L. Esaki, W. Howard, R. Ludeke, and G. Schul, "Structures grown by molecular beam epitaxy," *Journal of Vacuum Science and Technology*, vol. 10, no. 5, pp. 655–662, 1973. DOI: 10.1116/1.1318408.
- [66] R. Tsu and L. Esaki, "Tunneling in a finite superlattice," *Applied Physics Letters*, vol. 22, no. 11, pp. 562–564, 1973. DOI: 10.1063/1.1654509.
- [67] L. Chang, L. Esaki, and R. Tsu, "Resonant tunneling in semiconductor double barriers," *Applied physics letters*, vol. 24, no. 12, pp. 593–595, 1974. DOI: 10.1063/1.1655067.
- [68] T. Shewchuk, P. Chapin, P. Coleman, W. Kopp, R. Fischer, and H. Morkoc, "Resonant tunneling oscillations in a $\text{GaAs-Al}_x\text{Ga}_{1-x}\text{As}$ heterostructure at room temperature," *Applied physics letters*, vol. 46, no. 5, pp. 508–510, 1985. DOI: 10.1063/1.95574.
- [69] D. Bohm, *Quantum theory*. Courier Corporation, 2012.

- [70] S. Datta, *Electronic transport in mesoscopic systems*. Cambridge university press, 1997.
- [71] M. Feiginov, “Frequency limitations of resonant-tunnelling diodes in sub-thz and thz oscillators and detectors,” *Journal of infrared, millimeter, and terahertz waves*, vol. 40, no. 4, pp. 365–394, 2019. DOI: 10.1007/s10762-019-00573-5.
- [72] P. Roblin, R. C. Potter, and A. Fathimulla, “Interface roughness scattering in alas/ingaas resonant tunneling diodes with an inas subwell,” *Journal of Applied Physics*, vol. 79, no. 5, pp. 2502–2508, 1996. DOI: 10.1063/1.361104.
- [73] M. Shur, *Physics of Semiconductor Devices* (Prentice-Hall series in solid state physical electronics). Prentice Hall, 1990, ISBN: 9780136664963.
- [74] S. Suzuki, A. Teranishi, K. Hinata, M. Asada, H. Sugiyama, and H. Yokoyama, “Fundamental oscillation of up to 831 ghz in gainas/alas resonant tunneling diode,” *Applied Physics Express*, vol. 2, no. 5, p. 054 501, 2009. DOI: 10.1143/APEX.2.054501.
- [75] T. A. Growden, W. Zhang, E. R. Brown, *et al.*, “431 ka/cm² peak tunneling current density in gan/aln resonant tunneling diodes,” *Applied Physics Letters*, vol. 112, no. 3, p. 033 508, 2018.
- [76] T. A. Growden, D. F. Storm, E. M. Cornuelle, *et al.*, “Superior growth, yield, repeatability, and switching performance in gan-based resonant tunneling diodes,” *Applied Physics Letters*, vol. 116, no. 11, p. 113 501, 2020. DOI: 10.1063/1.5139219.
- [77] J. Encomendero, R. Yan, A. Verma, *et al.*, “Room temperature microwave oscillations in gan/aln resonant tunneling diodes with peak current densities up to 220 ka/cm²,” *Applied Physics Letters*, vol. 112, no. 10, p. 103 101, 2018. DOI: 10.1063/1.5016414.
- [78] W.-D. Zhang, T. A. Growden, D. F. Storm, D. J. Meyer, P. R. Berger, and E. R. Brown, “Investigation of switching time in gan/aln resonant tunneling diodes by experiments and p-spice models,” *IEEE Transactions on Electron Devices*, vol. 67, no. 1, pp. 75–79, 2020. DOI: 10.1109/TED.2019.2955360.
- [79] S. Lin, D. Wang, Y. Tong, B. Shen, and X. Wang, “Iii-nitrides based resonant tunneling diodes,” *Journal of Physics D: Applied Physics*, vol. 53, no. 25, p. 253 002, Apr. 2020. DOI: 10.1088/1361-6463/ab7f71.
- [80] P. Ourednik, T. Hackl, C. Spudat, D. Tuan Nguyen, and M. Feiginov, “Double-resonant-tunneling-diode patch-antenna oscillators,” *Applied Physics Letters*, vol. 119, no. 26, p. 263 509, 2021. DOI: 10.1063/5.0068114.
- [81] E. Brown, O. McMahan, L. Mahoney, and K. Molvar, “Spice model of the resonant-tunnelling diode,” *Electronics Letters*, vol. 32, no. 10, pp. 938–940, 1996. DOI: 10.1049/e1:19960576.

- [82] R. Sekiguchi, Y. Koyama, and T. Ouchi, "Subterahertz oscillations from triple-barrier resonant tunneling diodes with integrated patch antennas," *Applied Physics Letters*, vol. 96, no. 6, p. 062 115, 2010. DOI: 10.1063/1.3315868.
- [83] T. Maekawa, H. Kanaya, S. Suzuki, and M. Asada, "Oscillation up to 1.92 thz in resonant tunneling diode by reduced conduction loss," *Applied physics express*, vol. 9, no. 2, p. 024 101, 2016. DOI: 10.7567/APEX.9.024101.
- [84] M. Feiginov, H. Kanaya, S. Suzuki, and M. Asada, "Operation of resonant-tunneling diodes with strong back injection from the collector at frequencies up to 1.46 thz," *Applied Physics Letters*, vol. 104, no. 24, p. 243 509, 2014. DOI: 10.1063/1.4884602.
- [85] T. Maekawa, H. Kanaya, S. Suzuki, and M. Asada, "Frequency increase in terahertz oscillation of resonant tunnelling diode up to 1.55 thz by reduced slot-antenna length," *Electronics Letters*, vol. 50, no. 17, pp. 1214–1216, 2014. DOI: 10.1049/el.2014.2362.
- [86] H. Kanaya, H. Shibayama, R. Sogabe, S. Suzuki, and M. Asada, "Fundamental oscillation up to 1.31 thz in resonant tunneling diodes with thin well and barriers," *Applied Physics Express*, vol. 5, no. 12, p. 124 101, 2012. DOI: 10.1143/APEX.5.124101.
- [87] S. Suzuki, M. Shiraishi, H. Shibayama, and M. Asada, "High-power operation of terahertz oscillators with resonant tunneling diodes using impedance-matched antennas and array configuration," *IEEE Journal of Selected Topics in Quantum Electronics*, vol. 19, no. 1, pp. 8 500 108–8 500 108, 2012. DOI: 10.1109/JSTQE.2012.2215017.
- [88] K. Urayama, S. Aoki, S. Suzuki, M. Asada, H. Sugiyama, and H. Yokoyama, "Sub-terahertz resonant tunneling diode oscillators integrated with tapered slot antennas for horizontal radiation," *Applied physics express*, vol. 2, no. 4, p. 044 501, 2009. DOI: 10.1143/APEX.2.044501.
- [89] P. Ourednik and M. Feiginov, "Double-resonant-tunneling-diode bridge-less patch-antenna oscillators operating up to 1.09 thz," *Applied Physics Letters*, vol. 120, no. 18, p. 183 501, 2022. DOI: 10.1063/5.0090519.
- [90] M. Feiginov, C. Sydlo, O. Cojocari, and P. Meissner, "Resonant-tunnelling-diode oscillators operating at frequencies above 1.1 thz," *Applied Physics Letters*, vol. 99, no. 23, p. 233 506, 2011. DOI: 10.1063/1.3667191.
- [91] J. Lee, M. Kim, and J. Lee, "692 ghz high-efficiency compact-size inp-based fundamental rtd oscillator," *IEEE Transactions on Terahertz Science and Technology*, vol. 11, no. 6, pp. 716–719, 2021. DOI: 10.1109/TTHZ.2021.3108431.
- [92] E. R. Brown, J. Söderström, C. Parker, L. Mahoney, K. Molvar, and T. McGill, "Oscillations up to 712 ghz in inas/alsb resonant-tunneling diodes," *Applied Physics Letters*, vol. 58, no. 20, pp. 2291–2293, 1991. DOI: 10.1063/1.104902.

- [93] T. Sollner, P. Tannenwald, D. Peck, and W. Goodhue, “Quantum well oscillators,” *Applied physics letters*, vol. 45, no. 12, pp. 1319–1321, 1984. DOI: 10.1063/1.95134.
- [94] E. Brown, W. Goodhue, and T. Sollner, “Fundamental oscillations up to 200 ghz in resonant tunneling diodes and new estimates of their maximum oscillation frequency from stationary-state tunneling theory,” *Journal of applied physics*, vol. 64, no. 3, pp. 1519–1529, 1988. DOI: 10.1063/1.341827.
- [95] E. Brown, T. Sollner, C. Parker, W. Goodhue, and C. Chen, “Oscillations up to 420 ghz in gaas/alas resonant tunneling diodes,” *Applied Physics Letters*, vol. 55, no. 17, pp. 1777–1779, 1989. DOI: 10.1063/1.102190.
- [96] D. Chow, J. Schulman, E. Özbay, and D. Bloom, “Investigation of in0.53ga0.47as/alas resonant tunneling diodes for high speed switching,” *Applied physics letters*, vol. 61, no. 14, pp. 1685–1687, 1992. DOI: 10.1063/1.108451.
- [97] M. Reddy, S. Martin, A. Molnar, *et al.*, “Monolithic schottky-collector resonant tunnel diode oscillator arrays to 650 ghz,” *IEEE Electron Device Letters*, vol. 18, no. 5, pp. 218–221, 1997. DOI: 10.1109/55.568771.
- [98] N. Orihashi, S. Hattori, and M. Asada, “Millimeter and submillimeter oscillators using resonant tunneling diodes with stacked-layer slot antennas,” *Japanese journal of applied physics*, vol. 43, no. 10A, p. L1309, 2004. DOI: 10.1143/JJAP.43.L1309.
- [99] S. Suzuki, M. Asada, A. Teranishi, H. Sugiyama, and H. Yokoyama, “Fundamental oscillation of resonant tunneling diodes above 1 thz at room temperature,” *Applied Physics Letters*, vol. 97, no. 24, p. 242 102, 2010. DOI: 10.1063/1.3525834.
- [100] M. Asada, S. Suzuki, and N. Kishimoto, “Resonant tunneling diodes for sub-terahertz and terahertz oscillators,” *Japanese Journal of Applied Physics*, vol. 47, no. 6R, p. 4375, 2008. DOI: 10.1143/JJAP.47.4375.
- [101] H. Kanaya, R. Sogabe, T. Maekawa, S. Suzuki, and M. Asada, “Fundamental oscillation up to 1.42 thz in resonant tunneling diodes by optimized collector spacer thickness,” *Journal of Infrared, Millimeter, and Terahertz Waves*, vol. 35, no. 5, pp. 425–431, 2014. DOI: 10.1007/s10762-014-0058-z.
- [102] M. N. Feiginov, “Effect of the coulomb interaction on the response time and impedance of the resonant-tunneling diodes,” *Applied Physics Letters*, vol. 76, no. 20, pp. 2904–2906, 2000. DOI: 10.1063/1.126512.
- [103] M. N. Feiginov, “Displacement currents and the real part of high-frequency conductance of the resonant-tunneling diode,” *Applied Physics Letters*, vol. 78, no. 21, pp. 3301–3303, 2001. DOI: 10.1063/1.1372357.
- [104] M. N. Feiginov and D. Roy Chowdhury, “Operation of resonant-tunneling diodes beyond resonant-state-lifetime limit,” *Applied Physics Letters*, vol. 91, no. 20, p. 203 501, 2007. DOI: 10.1063/1.2806922.

- [105] M. Feiginov, C. Sydlo, O. Cojocari, and P. Meissner, “High-frequency nonlinear characteristics of resonant-tunnelling diodes,” *Applied Physics Letters*, vol. 99, no. 13, p. 133 501, 2011. DOI: 10.1063/1.3644491.
- [106] M. Asada and S. Suzuki, “Room-temperature oscillation of resonant tunneling diodes close to 2 thz and their functions for various applications,” *Journal of Infrared, Millimeter, and Terahertz Waves*, vol. 37, no. 12, pp. 1185–1198, 2016. DOI: 10.1007/s10762-016-0321-6.
- [107] K. Kasagi, S. Suzuki, and M. Asada, “Array configuration using resonant-tunneling-diode terahertz oscillator integrated with patch antenna,” in *2015 40th International Conference on Infrared, Millimeter, and Terahertz waves (IRMMW-THz)*, IEEE, 2015, pp. 1–2. DOI: 10.1109/IRMMW-THz.2015.7327788.
- [108] D. Horikawa, Y. Chen, T. Koike, S. Suzuki, and M. Asada, “Resonant-tunneling-diode terahertz oscillator integrated with a radial line slot antenna for circularly polarized wave radiation,” *Semiconductor Science and Technology*, vol. 33, no. 11, p. 114 005, 2018. DOI: 10.1088/1361-6641/aae1ef.
- [109] F. Han, H. Fujikata, H. Tanaka, S. Suzuki, and M. Asada, “High-power cavity-type rtd thz oscillators integrated with impedance-matched slot antenna,” in *2022 47th International Conference on Infrared, Millimeter and Terahertz Waves (IRMMW-THz)*, 2022, pp. 1–2. DOI: 10.1109/IRMMW-THz50927.2022.9895762.
- [110] K. Kobayashi, S. Suzuki, F. Han, H. Tanaka, H. Fujikata, and M. Asada, “Analysis of a high-power resonant-tunneling-diode terahertz oscillator integrated with a rectangular cavity resonator,” *Japanese Journal of Applied Physics*, vol. 59, no. 5, p. 050 907, 2020. DOI: 10.35848/1347-4065/ab8b40.
- [111] M. Feiginov, “Sub-terahertz and terahertz microstrip resonant-tunneling-diode oscillators,” *Applied Physics Letters*, vol. 107, no. 12, p. 123 504, 2015. DOI: 10.1063/1.4931727.
- [112] Z. Jéhn, “Simulation of traveling-wave resonant tunneling diode oscillator waveguides,” *Opt. Express*, vol. 30, no. 20, pp. 35 725–35 733, Sep. 2022. DOI: 10.1364/OE.466405.
- [113] Z. Jéhn and M. Feiginov, “Demonstration of sub-thz traveling-wave resonant-tunneling-diode oscillators,” *IEEE Transactions on Nanotechnology*, 2023, Under review.
- [114] H. Fujikata, H. Tanaka, F. Han, A. Ishikawa, S. Suzuki, and M. Asada, “Terahertz oscillator using rectangular-cavity resonator and large-area rtd with heat dissipation structure,” in *2022 47th International Conference on Infrared, Millimeter and Terahertz Waves (IRMMW-THz)*, 2022, pp. 1–2. DOI: 10.1109/IRMMW-THz50927.2022.9895508.

- [115] Z. Jéhn, “Cylindrical cavity optimization for resonant-tunneling diode oscillators,” *IEEE Transactions on Microwave Theory and Techniques*, vol. 70, no. 5, pp. 2658–2667, 2022. DOI: 10.1109/TMTT.2022.3150146.
- [116] R. Izumi, T. Sato, S. Suzuki, and M. Asada, “Resonant-tunneling-diode terahertz oscillator with a cylindrical cavity for high-frequency oscillation,” *AIP Advances*, vol. 9, no. 8, p. 085 020, 2019. DOI: 10.1063/1.5114963.
- [117] G. Stareev, H. Künzel, and G. Dortmann, “A controllable mechanism of forming extremely low-resistance nonalloyed ohmic contacts to group iii-v compound semiconductors,” *Journal of applied physics*, vol. 74, no. 12, pp. 7344–7356, 1993. DOI: doi.org/10.1063/1.355002.
- [118] S. Suzuki, A. Teranishi, K. Hinata, M. Asada, H. Sugiyama, and H. Yokoyama, “Fundamental oscillation of up to 831 ghz in gainas/alas resonant tunneling diode,” *Applied Physics Express*, vol. 2, no. 5, p. 054 501, 2009. DOI: 10.1143/APEX.2.054501.
- [119] J. D. Zimmerman, E. R. Brown, and A. C. Gossard, “Tunable all epitaxial semimetal-semiconductor schottky diode system: Eras on inalgaas,” *Journal of Vacuum Science & Technology B: Microelectronics and Nanometer Structures Processing, Measurement, and Phenomena*, vol. 23, no. 5, pp. 1929–1935, 2005. DOI: 10.1116/1.2013312.
- [120] K. Kajiyama, Y. Mizushima, and S. Sakata, “Schottky barrier height of n-in x gal- x as diodes,” *Applied Physics Letters*, vol. 23, no. 8, pp. 458–459, 1973. DOI: 10.1063/1.1654957.
- [121] N. Orihashi, S. Hattori, S. Suzuki, and M. Asada, “Experimental and theoretical characteristics of sub-terahertz and terahertz oscillations of resonant tunneling diodes integrated with slot antennas,” *Japanese Journal of Applied Physics*, vol. 44, no. 11R, p. 7809, 2005. DOI: 10.1143/JJAP.44.7809.
- [122] D. K. Schroder, *Semiconductor material and device characterization*. John Wiley & Sons, 2015.
- [123] G. Reeves, “Specific contact resistance using a circular transmission line model,” *Solid-State Electronics*, vol. 23, no. 5, pp. 487–490, 1980, ISSN: 0038-1101. DOI: 10.1016/0038-1101(80)90086-6.
- [124] G. Reeves and H. Harrison, “Obtaining the specific contact resistance from transmission line model measurements,” *IEEE Electron Device Letters*, vol. 3, no. 5, pp. 111–113, 1982. DOI: 10.1109/EDL.1982.25502.
- [125] M. N. Feiginov, “Does the quasibound-state lifetime restrict the high-frequency operation of resonant-tunnelling diodes?” *Nanotechnology*, vol. 11, no. 4, p. 359, 2000. DOI: 10.1088/0957-4484/11/4/333.
- [126] S. Luryi, “Frequency limit of double-barrier resonant-tunneling oscillators,” *Applied Physics Letters*, vol. 47, no. 5, pp. 490–492, 1985. DOI: 10.1063/1.96102.

- [127] P. Ourednik, G. Picco, D. Tuan Nguyen, C. Spudat, and M. Feiginov, “Large-signal dynamics of resonant-tunneling diodes,” *Journal of Applied Physics*, vol. 133, no. 1, p. 014 501, 2023. DOI: 10.1063/5.0134223.
- [128] W. Shockley, “Currents to conductors induced by a moving point charge,” *Journal of applied physics*, vol. 9, no. 10, pp. 635–636, 1938. DOI: 10.1063/1.1710367.
- [129] S. Ramo, “Currents induced by electron motion,” *Proceedings of the IRE*, vol. 27, no. 9, pp. 584–585, 1939. DOI: JRPROC.1939.228757.
- [130] C. Spudat, P. Ourednik, G. Picco, D. T. Nguyen, and M. Feiginov, “Limitations of output power and efficiency of simple resonant-tunneling-diode oscillators,” *IEEE Transactions on Terahertz Science and Technology*, vol. 13, no. 1, pp. 82–92, 2023. DOI: 10.1109/TTHZ.2022.3228069.
- [131] T. Lee and A. Hajimiri, “Oscillator phase noise: A tutorial,” *IEEE Journal of Solid-State Circuits*, vol. 35, no. 3, pp. 326–336, 2000. DOI: 10.1109/4.826814.
- [132] C. Kim and A. Brandli, “High-frequency high-power operation of tunnel diodes,” *IRE Transactions on Circuit Theory*, vol. 8, no. 4, pp. 416–425, 1961. DOI: 10.1109/TCT.1961.1086849.
- [133] M. Feiginov, C. Sydlo, O. Cojocari, and P. Meissner, “Operation of resonant-tunnelling oscillators beyond tunnel lifetime limit,” *EPL (Europhysics Letters)*, vol. 94, no. 4, p. 48 007, 2011. DOI: 10.1209/0295-5075/94/48007.
- [134] M. Feiginov, C. Sydlo, O. Cojocari, and P. Meissner, “Operation of resonant-tunnelling-diode oscillators beyond tunnel-lifetime limit at 564 ghz,” *EPL (Europhysics Letters)*, vol. 97, no. 5, p. 58 006, 2012. DOI: 10.1209/0295-5075/97/58006.
- [135] S. Sahin, N. K. Nahar, and K. Sertel, “Dielectric properties of low-loss polymers for mmw and thz applications,” *Journal of Infrared, Millimeter, and Terahertz Waves*, vol. 40, no. 5, pp. 557–573, 2019. DOI: 10.1007/s10762-019-00584-2.
- [136] S. Lucyszyn, “Comment: Terahertz time-domain spectroscopy of films fabricated from su-8,” *Electronics Letters*, vol. 37, no. 20, p. 1267, 2001. DOI: 10.1049/e1:20010847.
- [137] S. Kitagawa, S. Suzuki, and M. Asada, “Wide frequency-tunable resonant tunnelling diode terahertz oscillators using varactor diodes,” *Electronics Letters*, vol. 52, no. 6, pp. 479–481, 2016. DOI: 10.1049/e1.2015.3921.
- [138] M. Asada, “Theoretical analysis of subharmonic injection locking in resonant-tunneling-diode terahertz oscillators,” *Japanese Journal of Applied Physics*, vol. 59, no. 1, p. 018 001, 2019. DOI: 10.7567/1347-4065/ab600b.
- [139] C. C. Homes, G. L. Carr, R. P. S. M. Lobo, J. D. LaVeigne, and D. B. Tanner, “Silicon beam splitter for far-infrared and terahertz spectroscopy,” *Appl. Opt.*, vol. 46, no. 32, pp. 7884–7888, Nov. 2007. DOI: 10.1364/AO.46.007884.

- [140] E. Brown, C. Parker, and T. Sollner, “Effect of quasibound-state lifetime on the oscillation power of resonant tunneling diodes,” *Applied Physics Letters*, vol. 54, no. 10, pp. 934–936, 1989. DOI: 10.1063/1.100812.
- [141] J. Mattia, A. McWhorter, R. Aggarwal, F. Rana, E. Brown, and P. Maki, “Comparison of a rate-equation model with experiment for the resonant tunneling diode in the scattering-dominated regime,” *Journal of applied physics*, vol. 84, no. 2, pp. 1140–1148, 1998. DOI: 10.1063/1.368115.
- [142] S. Clochiatti, K. Aikawa, K. Arzi, *et al.*, “Large-signal modelling of sub-thz inp triple-barrier resonant tunneling diodes,” in *2020 Third International Workshop on Mobile Terahertz Systems (IWMTS)*, IEEE, 2020, pp. 1–5. DOI: IWMTS49292.2020.9166270.

List of publications

Publications in peer-review journals:

- [J1] P. **Ourednik**, T. Hackl, C. Spudat, D. Tuan Nguyen, and M. Feiginov, “Double-resonant-tunneling-diode patch-antenna oscillators,” *Applied Physics Letters*, vol. 119, no. 26, 263509, 2021. DOI: 10.1063/5.0068114.
- [J2] P. **Ourednik** and M. Feiginov, “Double-resonant-tunneling-diode bridge-less patch-antenna oscillators operating up to 1.09 thz,” *Applied Physics Letters*, vol. 120, no. 18, 183501, 2022. DOI: 10.1063/5.0090519.
- [J3] P. **Ourednik**, G. Picco, D. Tuan Nguyen, C. Spudat, and M. Feiginov, “Large-signal dynamics of resonant-tunneling diodes,” *Journal of Applied Physics*, vol. 133, no. 1, p. 014501, 2023. DOI: 10.1063/5.0134223.
- [J4] C. Spudat, P. **Ourednik**, G. Picco, D. T. Nguyen, and M. Feiginov, “Limitations of output power and efficiency of simple resonant-tunneling-diode oscillators,” *IEEE Transactions on Terahertz Science and Technology*, vol. 13, no. 1, pp. 82–92, 2023. DOI: 10.1109/TTHZ.2022.3228069.

Publications in conference proceedings:

- [C1] P. **Ourednik**, G. Picco, and M. Feiginov, “Chip-size resonant-tunneling-diode oscillator as a fmcw and oct source,” in *2022 47th International Conference on Infrared, Millimeter and Terahertz Waves (IRMMW-THz)*, 2022, pp. 1–2. DOI: 10.1109/IRMMW-THz50927.2022.9896064.
- [C2] P. **Ourednik** and M. Feiginov, “Chip-size double-resonant-tunneling-diode patch-antenna oscillators and their sub-thz application,” in *2022 15th UK-Europe-China Workshop on Millimetre-Waves and Terahertz Technologies (UCMMT)*, 2022, pp. 1–3. DOI: 10.1109/UCMMT56896.2022.9994843, Invited.

- [C3] M. Feiginov and P. **Ourednik**, “Sub-thz and thz double-resonant-tunnelling-diode patch-antenna oscillators,” in *2022 14th Topical Workshop on Heterostructure Microelectronics (TWHM)*, 2022, pp. 1–2, Invited.

External presentations:

- [P1] P. **Ourednik**, T. Hackl, C. Spudat, D. Tuan Nguyen, and M. Feiginov, *Double-resonant-tunneling-diode chip-size patch antenna oscillator*, International School on Terahertz photonics and electronics, Pisa, Italy, 9-13 May, 2022.
- [P2] P. **Ourednik** and M. Feiginov, *Double-resonant-tunneling-diode patch-antenna oscillators and their application*, FKE Seminar, TU Wien, 2022.
- [P3] M. Feiginov and P. **Ourednik**, *Sub-thz and thz double-resonant-tunnelling-diode patch-antenna oscillators*, Lecture in TiTech, Tokyo, Japan, 29 September, 2022.

Author’s publications not related to this thesis:

- [A1] P. **Ourednik** and Y. Gourdou, *Antenna and system for rf communications*, US Patent 11,031,672, Jun. 2021.
- [A2] P. **Ourednik** and L. Jelinek, *Wave-guiding part of a capacitor paradox*, 2018. DOI: 10.48550/ARXIV.1806.11507.
- [A3] P. **Ourednik**, V. Adler, and P. Hudec, “Trl-based measurement of active antennas and other more complex microwave structures,” in *2017 89th ARFTG Microwave Measurement Conference (ARFTG)*, 2017, pp. 1–4. DOI: 10.1109/ARFTG.2017.8000834.
- [A4] P. Hudec, P. Panek, and P. **Ourednik**, “Suppression of false targets from active defense radar sensors,” in *2017 European Radar Conference (EURAD)*, 2017, pp. 77–80. DOI: 10.23919/EURAD.2017.8249151.
- [A5] J. Dobes, J. Michal, F. Vejrazka, and P. **Ourednik**, “Novel method for noise figure measurement of antenna low noise amplifiers optimized for a trade-off between gain and noise properties,” in *2018 IEEE Asia-Pacific Conference on Antennas and Propagation (APCAP)*, 2018, pp. 372–373. DOI: 10.1109/APCAP.2018.8538100.
- [A6] P. **Ourednik** and P. Hudec, “Trl-based measurement of embedded circuits in microwave printed circuit boards including frequency conversion,” *Radioengineering*, vol. 27, no. 4, pp. 1077–1084, Dec. 2018. DOI: 10.13164/re.2018.1077.
- [A7] P. **Ourednik**, A. Zidkov, and P. Hudec, “Doppler frequency-shift unit for digital-analog automobile radar target simulator,” in *2019 European Microwave Conference in Central Europe (EuMCE)*, 2019, pp. 281–284.
- [A8] P. **Ourednik**, P. Hudec, and P. Panek, “A microwave interferometric sensor for measuring fast mechanical processes in demanding environments,” in *2019 European Microwave Conference in Central Europe (EuMCE)*, 2019, pp. 146–149.

Curriculum Vitae

Petr Ouředník

Date of birth: 14.12.1991
Nationality: Czech Republic

OBJECTIVE Candidate for the title: Doctor of Engineering Sciences, Dr. Ing., at the Department of Electrical Engineering and Information Technology, TU Wien

EDUCATION 2014
Bachelor Degree with Honors, Bc., in Communications, Multimedia, Electronics
Czech Technical University in Prague, Faculty of Electrical Engineering
Programme: Communication Technology

2016
Master Degree with Honors, Ing. (equivalent to Master of Science in Engineering), in Communications, Multimedia, Electronics
Czech Technical University in Prague, Faculty of Electrical Engineering
Programme: Wireless Communication
Thesis: Digital USB Oscilloscope

2018-present
Doctoral Study, in THz Electronics
Department of Electrical Engineering and Information Technology, TU Wien
Research Topic: THz and Sub-THz RTD Oscillators
Thesis: Advanced concepts of THz resonant-tunnelling-diode oscillators

EXPERIENCE 2015-2018
Application Engineer
Applications of RFID and NFC systems, ST Microelectronics, Prague, Czech Republic, EMEA

2016-2018
Junior Researcher
Microwave Circuits, Systems, and Measurements, Department of Electromagnetic Field, Faculty of Electrical Engineering, Czech Technical University in Prague